The Surface Ejection of Electrons by Laser Excited Metastables Spectroscopy of Acetylene

by

Kevin Laughton Cunningham

Submitted to the Department of Chemistry
in partial fulfillment of the requirements for the degree of

Doctor of Philosophy

at the

MASSACHUSETTS INSTITUTE OF TECHNOLOGY

July 2000

Author .....
Department of Chemistry
July 2000

Certified by .....
Robert W. Field
Professor
Thesis Supervisor

Accepted by .....
Robert W. Field
Chairman, Department Committee on Graduate Students

This doctoral thesis has been examined by a Committee of the Department of Chemistry that included

Professor Robert J. Silbey _____
(Chairperson)

Professor Andrei Tokmakoff _____

Professor Robert W. Field _____
(Thesis Supervisor)

The Surface Ejection of Electrons by Laser Excited Metastables Spectroscopy of Acetylene

by

Kevin Laughton Cunningham

Submitted to the Department of Chemistry
on July 2000, in partial fulfillment of the
requirements for the degree of
Doctor of Philosophy

Abstract

Surface Ejection of Electrons by Laser Excited Metastables (SEELEM) spectroscopy has been employed to observe the long-lived, highly excited states of acetylene. This molecular beam technique exploits a surface effect, the Auger effect, in which electronically excited molecules de-excite by interacting with a nearby metal detection surface. This results in the ejection of an easily detectable electron from the molecule-surface system. The use of LIF and SEELEM spectroscopies have provided these insights:

i) A small number of triplet vibrational states mediate the ISC of $3\nu_3$. These triplet "doorway" perturbers are assigned to the T_3 electronic surface. The coupling between $3\nu_3$ and one doorway triplet state is found to be 0.11(1) cm^{-1}.

ii) The SEELEM-detectable eigenstates may have lifetimes as long as 280 μs. This suggests that the electronic character of the SEELEM-detectable states is predominantly S_0. These states do have small fractional S_1 and triplet characters which provide the excitation probability, the Auger detectability, and the radiative decay of these states.

iii) SEELEM spectra recorded with different detection surfaces reveal few changes in the relative intensities of the spectral features despite large changes in surface work function. This suggests that the detectivity of these eigenstates may be dominated by their S_1 character. Two simulations were conducted that partly confirm this hypothesis.

In addition, a pattern recognition technique, Extended Auto Correlation (XAC), was developed that extracts patterns from a highly overlapped SEELEM spectrum. The application of this technique resulted in patterns the accuracy of which are limited only by the quality of the experimental data.

Metastable photofragments were observed by SEELEM at a number of excitation frequencies. Although it is not possible to identify the source of this signal, the number of candidates is narrowed.

Thesis Supervisor: Robert W. Field
Title: Professor

Acknowledgments

I would like to express my gratitude to all the people who have helped me.

Bob, thank you for your enthusiasm, for your good natured and abundant patience, and for giving me the freedom to define the direction of my research almost in its entirety. This was a gift, the true value of which I don't think I will be able to fully appreciate for many years.

Thanks to Peter Giunta for all the help throughout the years. Peter is the most professional and resourceful secretary I have ever worked with.

Thanks to Prof. Alec Wodtke at UCSB for inviting me into his lab and providing me opportunity to conduct the initial experiments upon which this thesis is based. Thanks also to then-Wodtke lab post-doc Susan Humphrey and graduate student Gabe Morgan for working with me on these experiments. Another serving of thanks to Gabe for his work here helping us set up our Auger detector.

Thanks to Dr. Ramachandra Dasari, Prof. Michael Feld, and all the other folks at the George R. Harrison Spectroscopy lab that provided space, equipment, and good advice.

Thanks to Prof. Peter Bernath for lending us the IR detector for such a long time.

Thanks to Dr. Joseph Ledbetter for inspiring me to become a chemist and being a great friend.

Thanks to Prof. Paul Alivisatos for providing me with my initial taste of scientific research. And to Paul, Dr. Susan Kegley and then Alivisatos students Vicki Colvin, Sarah Tolbert, and Joseph Shiang for encouraging me to come to graduate school and giving me lots of guidance.

I have had the good fortune to be surrounded by many brilliant and generous professors who have answered questions and taught me physical chemistry. My thanks to Profs. Moungi Bawendi, Irwin Oppenheim, Keith Nelson, Sylvia Ceyer, and Robert Silbey.

Thanks to acetylene for being the world's most fascinating molecule. World domination cannot be achieved without you.

Thanks to all of the people over the years that made this such a vibrant place to do research, including Prof. Will Polik, Prof. Curt Wittig, Ma Hui, Nicole Schneider, Zygmunt Jakubek, Amy Miller, Dave Moss, Manjula Canagaratna, Scott Witonsky, Ilia Dubinsky, and George Adamson. Thanks to Don Lucas and Susan Q. Lang, two of the all-time great UROPs. I wish you both well in graduate school. Thanks to Dr. Stephen Coy for a number of enlightening conversations, especially those on statistical pattern recognition and collisions.

Thanks to Chris Gittins for starting me out in spectroscopy and for all the support early in my career. Thanks to Stephani Solina for inspiration and overwhelming enthusiasm. Thanks to Jon O'Brien for getting the triplet project set up in Speclab and for all the humor and advice. Thanks to Sergey Panov for all the excellent experimental guidance and for discussions on politics and other interesting topics.

Thanks to Prof. Steve Drucker for teaching me about the triplet states of acetylene and for providing leadership during the first part of this work. Good luck at Eau

Claire, Professor!

Thanks to Matt Jacobson for helping me understand Extended Cross Correlation, for all the discussions about XAC, and for our experimental work together. Thanks also for showing the occasional frustration so that I could see that your success was not as easy for you as it might have appeared.

Thanks to Leah Ruslen for helping me understand the many difficulties inherent in absorption spectroscopy. Also, thanks for the bowling!

Thanks to Jason Clevenger for all the great conversations and commiseration. Jason's resourcefulness is only surpassed by his willingness to lend a hand. Thanks also for your superb Russian accent.

Thanks to Michelle Silva for adding so much vibrancy to the group and for the occasional conversation.

Thanks to Richard Duan for working with me on the DF experiments and for his good cheer and curiosity.

Good luck to the newest students "father" Ryan Thom and Xing Jiang. You are both well on your way to being excellent experimentalists. The group's research is going to be in very capable hands.

A Big Thank You to Selen Altunata for working with me through all of the difficult, frustrating problems involved in getting the Auger detector to work. She maintained good humor and spirits even when we were both feeling daunted.

If there is one thing that characterizes this generation of Field students, it is their determination in the face of persistent experimental difficulties.

Thanks to James, Dora, Kerstin, Rose, Henry, Ken, and the Southern Gentleman David Rovnyak for being a wonderfully cooperative group of first years. Our study sessions in the Amdur room and the graduate student talks were irreplaceable educational experiences.

Thanks to Jennifer Raye Blanchard for taking care of my friend David and being so cool. Good luck to you two!

Thanks to the folks at the 1369 Coffeehouse on Mass. Ave. This thesis was almost entirely written in the 1369. Thanks to Jackie, Courtney, Duncan, Jess, Linda (even though you threw a penny at me), Lauren, and everyone else whose names I never learned. You made it a wonderful place to work through a difficult task. Also thanks to Allie, Jimmy, Gehlen, Susan, and all the other patrons who me cheered on and cheered me up. Thank you, Diana.

Thanks to Mike for such an unexpected friendship.

Thanks to Anne for so many wonderful dinners.

Thanks to the Mighty Men of Andrew Street: David, Fred, Ken, Brett, and Doug. There was never a dull moment on Andrew Street. You are The Men!

Thanks to my friends at the Imill: Sean, Pat, Jeff, Mike, and Brett. I feel very lucky to have had such good friends for so long. Homestead mustangs rule!

Thanks to Kerry for being a loving friend.

Thanks to all my family. Thanks to cousin Nancy, Aunt Carolyn, and Uncle Bill. Thanks to Keithette, McKenzie, and Courtney. I didn't always (ever?) answer your emails, but I loved getting them. I am glad that I will be able to see you more from

now on. Thanks to Aunt Joyce and Uncle Burgie for the cards and for letting us stay so often. Thanks to Aunt Vera for your good humor.

Mom and Dad, thanks for always being supportive, for all the calls, cards, emails, and visits. Thank you for being excited. Thank you for being proud of me.

For Mom and Dad

and for my Grandmothers

Contents

List of Figures

List of Tables

Chapter 1

Introduction

1.1 Objective

The objective of this work is to understand the interactions between the singlet and triplet states of acetylene. These interactions govern the intersystem crossing (ISC) from the laser-accessible singlet manifold to the triplet manifold. Once a molecule is excited to a triplet state, it will remain in the triplet manifold for a chemically significant time (~ 1 ms) because radiative decay from the triplet states to the ground singlet state is spin-forbidden. So, large amounts of electronic energy can be sequestered in these states. This energy can be released during a collision, initiating a chemical reaction. Laser-Induced Fluorescence and Surface Ejection of Electrons by Laser Excited Metastable (SEELEM) spectroscopies are employed to seek spectral features that are indicative of ISC.

Acetylene is a good test molecule for our experimental and analytical techniques. It is an inexpensive, permanent gas, and minimal preparation is required. Our research group and others have extensively studied the vibrational states of the electronic ground state (the $\tilde{X}$-state)[2, 4, 178, 136, 81, 83, 84], the first excited singlet state (the $\tilde{A}$-state)[205, 34, 35, 3, 4, 161, 59, 60, 127, 128, 48, 50, 51, 49, 43] and some of the higher valence and Rydberg states.[9, 109, 185, 160, 110, 112] This provides us with a strong foundation of knowledge for the present studies.

Acetylene presents a significant advantage for studying ISC: low state density.

Some rules for ISC have been developed, as reviewed by Avouris, Gelbart, and El-Sayed, [12] and experimentally verified by, among others, Klemperer [73] and Sneh, Cheshnovsky, and co-workers.[14, 170, 171, 172, 173, 174, 175, 176, 177]. These rules work well for large molecules with high state densities, but the high state density prevents the development of a state-resolved quantum mechanical description of ISC. The individual eigenstates cannot be experimentally resolved, so an effective Hamiltonian model cannot be developed. The low acetylene state density may permit the resolution of individual eigenstates by standard laser techniques, and an effective ISC Hamiltonian may be developed.

Finally, the triplet states of acetylene exemplify the long-lived, highly energetic states of many small molecules that have spin multiplicity different from that of the ground electronic state. By developing experimental and analysis techniques for the triplet states of acetylene, a foundation for the study of other molecules is provided.

1.2 The acetylene molecule

Acetylene has five electronic potential energy surfaces below its first dissociation limit, as shown in Fig. 1-1. These potential surfaces have been the subject of a good deal of theoretical work.[42, 209, 107, 214, 165, 198, 197, 38, 37, 113] Two of the electronic states are singlet, the S_0 and S_1 surfaces, and three are triplet, the T_1, T_2, and T_3 surfaces. The S_0 surface has a linear equilibrium geometry (the $\tilde{X}$-state) and a vinylidene well at $\sim$2 eV. The S_1, T_1, and T_2 surfaces have *trans*-bent, *cis*-bent, and vinylidene wells. The *trans* well of the S_1 surface is referred to as the $\tilde{A}$-state. The *cis* and *trans* wells of the T_1 surface are referred to as the $\tilde{a}$-state and the $\tilde{b}$-state, respectively. Similarly, *cis* and *trans* wells of the T_2 surface are referred to as the $\tilde{d}$- and $\tilde{c}$-states, respectively. These states are lettered according to their energy order. The equilibrium geometry of the T_3 state has not been calculated, but it likely has a C_1 symmetry.[42, 107, 38, 37]

Vibrational bands of the $\tilde{A}$-$\tilde{X}$ transition are referred to by the notation $V_b^a K_n^m$, where $\nu_4'' = b$, $\nu_3' = a$, $l'' = n$, and $K_a' = m$. A single prime refers to the upper state

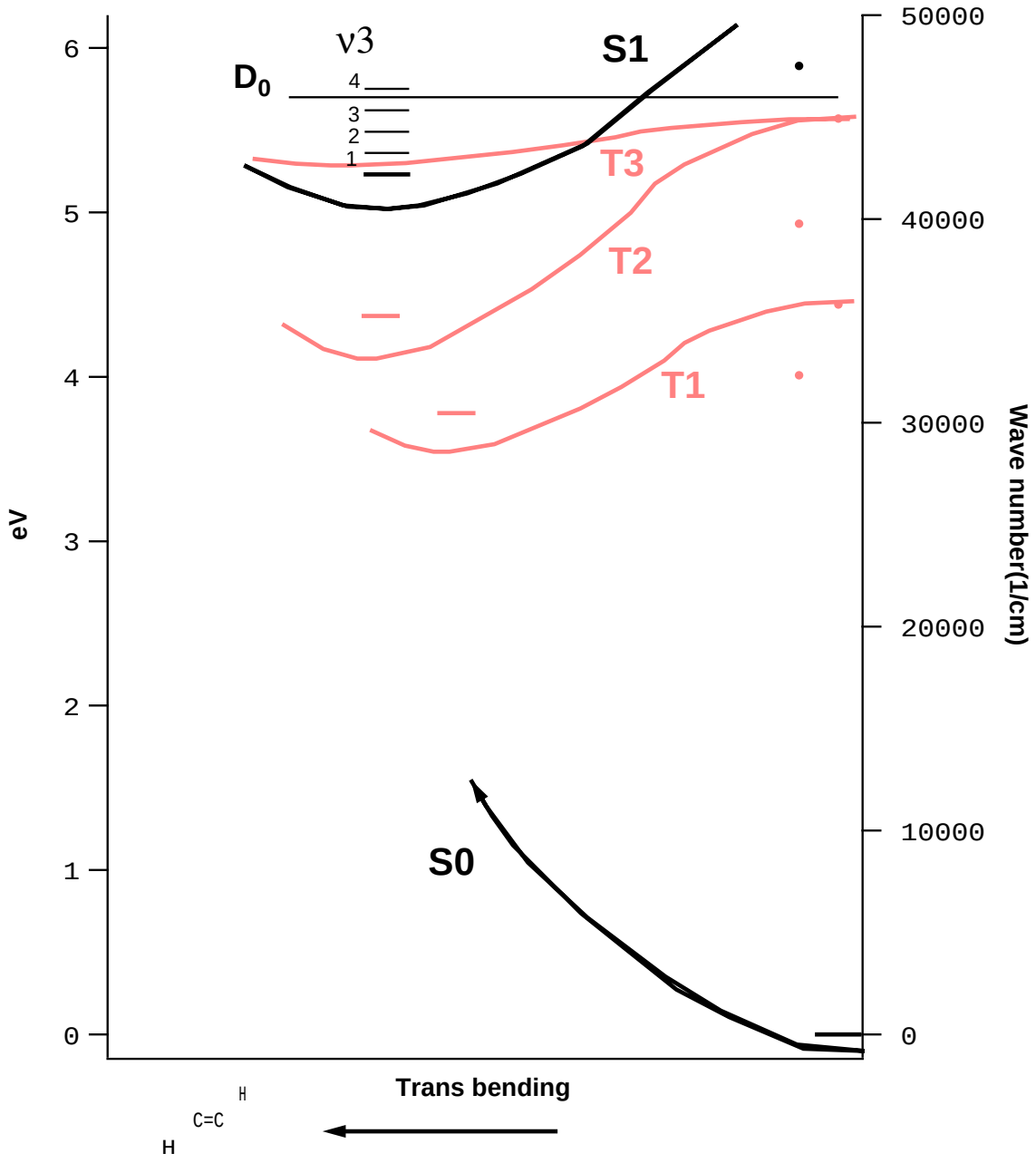

Figure 1-1: The potential energy surfaces of acetylene. This sketches a cut along the *trans* bending coordinate through each six-dimensional potential energy surface. The lowest dissociation limit is represented by the line marked D_0.

quantum numbers, and a double prime refers to the lower state quantum numbers. Normally, the notation would be $3_0^a 4_b^0$. The notation used for acetylene reflects the change in vibrational mode numbering with the change in equilibrium geometry from linear to *trans*-bent. The *trans*-bending mode is ν_4 in the $\tilde{X}$-state and ν_3 in the $\tilde{A}$-state. Because the *trans*-bending mode is the most Franck-Condon active mode, nearly every observed band involves changes in it. V_b^a refers to the change in *trans*-bending vibrational quanta.

1.3 Previous work on the singlet-triplet interactions in acetylene

A number of workers have contributed to our present understanding of the interactions between the $\tilde{A}$-state and the background triplet states. These studies show increasing coupling between the singlet states and the background states as a function of increasing *trans*-bending vibrational energy on the S_1 surface. And, with two exceptions, all of these studies use LIF as the observable.

The pure triplet states have been observed by optical spectroscopy only twice. Wendt, Hippler, and Hunziker observed a transition between ground vibrational levels of the *cis*-$\tilde{a}$-state on the T_1 surface and the *cis*-$\tilde{d}$-state on the T_2 surface.[207] This established the energy separation between the two vibrational states. Kanamori and co-workers observed the same transitions at much higher resolution and were able to fit most of the data to an effective Hamiltonian that provided a number of molecular constants for the ground vibrational levels of these states.[189, 190, 90]

The first LIF study of the $\tilde{A}$-state was conducted by Abramson, *et al.* [3]. They noted that the LIF-detectable states have long lifetimes (2-5 μs), large collisional quenching cross sections (17-23$\times 10^6$ s^{-1} $Torr^{-1}$, roughly twice the gas kinetic rate), and quantum beats on some of the fluorescence decays. These indicate that the electronically excited singlets are strongly coupled with the high density of long-lived background states.

Stephenson, Blazy, and King[181] measured the collisional quenching of LIF from the $\nu_3' = 0, 1, 2$ vibrational levels of the $\tilde{A}$-state. They used acetylene, oxygen, nitrogen, Ar, and He as colliding partners. The collisional quenching rate increased dramatically as a function of *trans*-bending vibrational energy of the excited acetylene molecule. For instance, the quenching rate with acetylene as a colliding partner increased 3-fold from the vibrationless level to $2\nu_3$, while the quenching rate with nitrogen as a colliding partner increased 30-fold from the vibrationless level to $2\nu_3$. They suggested that a curve crossing near $2\nu_3$ could generate a stronger mixing with the non-fluorescing background states and account for the higher rate of fluorescence-quenching collisions.

Ochi and Tsuchiya[137, 138] recorded the LIF spectra of the $V_0^2K_0^1$, $V_0^3K_0^1$, and $V_0^4K_0^1$ bands in a molecular beam with a resolution of 0.1 cm^{-1}. They noted the fractionation of individual rotational lines and recorded the fluorescence decay of many of these features. $3\nu_3$ is more fractionated than the other vibrational levels. Some decays exhibited quantum beats, so a magnetic field of as much as 300 Gauss was used to observe changes in the frequency and intensity of the beats. Some of LIF-detectable states split into Zeeman components, as do some of the states responsible for the zero-field beats. Other background states Zeeman tune through the LIF-detectable states.

The strong fractionation of $3\nu_3$ and the Zeeman splitting indicates that the LIF-detectable states have some triplet character. Ochi and Tsuchiya proposed that the singlet-triplet mixing is caused by a potential surface crossing between S_1 and T_3 that is calculated to occur in this energy region.[107, 38, 37] T_3 does not have the state density to account for these observations, so they proposed that the $3\nu_3$ state couples to T_2 states through T_3. They assigned the states responsible for the quantum beats to be predominantly S_0 with a small admixture of triplet character, probably T_1.

Drabbels, *et al.* [43] recorded high-resolution (18 MHz) LIF spectra of the $V_0^3K_0^1$ and $V_0^4K_0^1$ bands. These spectra provide the most detailed look at the LIF-detectable states to date. These experiments resolved numerous eigenstates that comprise each fractionated rotational transition. Drabbels, *et al.* used the Lawrance-Knight decon-

volution procedure[100, 101, 104] to arrive at couplings between the singlet "bright" states and the background "dark" states. This showed that few of the LIF-detectable states are pure singlet. An application of a magnetic field split the LIF-detectable states into Zeeman components, which demonstrated that the LIF-detectable states have triplet character. They observed a LIF-detectable state density that is comparable to the expected triplet density, so they concluded that most of the background T_2 and T_1 states that exist near a singlet state appear in the LIF spectrum.

Dai and co-workers studied LIF from acetylene-Ar clusters.[26, 27, 88] Features due to the clusters appear in the LIF spectrum 10-30 $cm^{-1}$to the red of features due to transitions in the monomer. The energy of the light goes into the electronic and vibrational coordinates of the acetylene molecule. The Ar atom is more bound to the $\tilde{A}$-state than it is to the $\tilde{X}$-state, so the features appear to the red of the monomer features. These features revealed information about the structure of the clusters. In addition, they showed that these features broadened with increasing *trans*-bending vibrational energy. The authors suggested that the Ar dissociates on a $\sim 10 - 50$ps time scale, followed by emission by the acetylene monomer. They suggest that the Ar dissociation induces IVR within the $\tilde{A}$-state, producing the fluorescence. It is possible that the Ar dissociation also induces ISC or internal conversion, but the experiment was not sensitive to products of these processes. Further, the authors showed that the apparent lifetimes of the clusters excited to the vibrationless level of the acetylene $\tilde{A}$-state are much shorter than the lifetimes of the monomer excited to the same vibrationless level. They suggested that the Ar atom induced ISC for this level. This lifetime shortening effect of the Ar atom was not observed in the higher vibrational states. This is odd because all the other experiments discussed here suggest that ISC increases with increasing *trans*-bending vibrational energy. Perhaps there is a more complicated explanation for this observation.

Dupré, Green, Field, and co-workers conducted a number of Zeeman anticrossing experiments on acetylene.[48, 50, 51, 49] When a long-lived background state Zeeman tunes into degeneracy and mixes with an LIF-detectable state, the mixed eigenstate lifetime will be longer than the zero-field lifetime of the LIF-detectable state. This

allows for more of the excited molecules to be collisionally quenched before they can emit, decreasing the total fluorescence. These decreases in LIF intensity are called Zeeman anticrossings. Because only triplet states shift in a magnetic field, thenumber of Zeeman anticrossings observed as the magnetic field is scanned is a measure of the density of coupled background states that have triplet character. The anticrossing widths (in Tesla) have a relationship to the coupling strength between the LIF-detectable state and the background state.

These Zeeman Anticrossing experiments demonstrated several things about the ISC of the $\tilde{A}$-state. The most important result was that the number of background states that couple with ro-vibrational states of the $\tilde{A}$-state increases with *trans*-bending vibrational energy. This increase vastly exceeds the growth in the background state density.[48] The significance of this is that the coupling between the $\tilde{A}$-state and the background states must be increasing, probably due to a curious potential surface feature. Dupré, *et al.*[48] proposed two possibilities. One feature they proposed was the potential surface crossing between the T_3 and S_1 surfaces, but the authors argued in favor of vibrational overlap between $\tilde{A}$-state vibrational levels and triplet vibrational amplitude that would accumulate over the *cis-trans* linear isomerization barrier on the T_2 electronic surface. $\tilde{A}$-state vibrational levels with increasingly more energy in the *trans* bending vibrational mode will have increasing amplitude at linearity and increasing overlap with triplet vibrational levels that are at an energy just above the linear *cis-trans* isomerization barrier. The authors preferred this explanation because the state density of T_3 is low, ~ 0.05 per cm^{-1}.[138] Perturbations due to T_3 would be too infrequent to explain the data.

Theoretical work by Vacek, *et al.*[197] and by Sherrill, *et al.*[165] predicted that the *cis-trans* linear isomerization geometry on T_2 (and T_3, the two states are degenerate at linearity) lies at 44940 cm^{-1}. This is very close to $3\nu_3$ at 45300 cm^{-1}. However, this geometry has four imaginary vibrational modes, two *cis* and two *trans*, so it is unlikely that significant vibrational amplitude will accumulate above such a geometry. Sherrill, *et al.*[165] explored the possibility that the non-linear *cis-trans* T_2 isomerization barrier would lie near $3\nu_3$. They calculated this geometry to lie ~ 4400

cm^{-1} below $3\nu_3$ which is too large a gap to be due to error in the calculation. They suggested that either the linear geometry or *cis-trans* non-linear isomerization barrier on the T_3 surface causes the increase in singlet-triplet coupling.

The Zeeman anticrossing work also demonstrated that the triplet states are more strongly coupled to the LIF-detectable S_1 states than they are with the S_0 states.[48] They showed that the triplet eigenstates have electronic character which includes contributions from more than one of the triplet potential surfaces.[51] They proposed that the coupling strengths between the electronic basis states have the following order: $T_2 \sim T_1 \gg S_1 \sim T \gg T \sim S_0 \gg S_1 \sim S_0$.[51] They also measured a number of couplings between LIF-detectable and background states that could be Zeeman tuned into degeneracy.[48, 50, 51]

Suzuki and co-workers have recently conducted sensitized phosphorescence experiments on the $\tilde{A}$-state vibrational levels.[186, 166] In these experiments, metastable acetylene in a molecular beam collides with a target surface coated with biacetyl. The acetylene transfers its energy to the biacetyl which, in turn, fluoresces. The emission is observed with a PMT. They recorded the spectrum of a number of vibrational lines. They also measured the decay constant of the metastable signal to be ~ 100 μs. These experiments demonstrated that long-lived, highly excited states can be accessed by laser radiation.

LIF was useful, but ultimately limited. The LIF data displayed diagnostically significant trends and isolated measurements in the singlet-triplet interactions. The background states are not observed directly but only through their impact on the LIF-detectable states. The information that is available in the LIF signal has been fully exploited. To learn more, we need an additional observable, something similar to that used by Suzuki. We want to implement a technique that observes the long-lived, highly energetic triplet states directly.

Molecules in electronic excited states can give up their energy to a nearby metal surface, which results in the ejection of electrons from the molecule-surface system. These electrons can be detected easily with standard pulse counting techniques. This is the additional observable. This surface phenomenon is called the Auger effect. This

effect will be discussed in detail in Chapter 2, including the distinction between this effect and the one exploited in Auger Electron Spectroscopy.

Molecular beam techniques have been developed to exploit the Auger effect. Snè and Cheshnovsky developed Surface Ejection of Electrons by Laser Excited Metastable (SEELEM) spectroscopy.[170] In SEELEM spectroscopy, a molecular beam is excited by a laser. The molecules then travel in the beam to a Auger detector with a specially prepared metal surface and electron detection electronics. Auger electrons produced at the detection surface are detected and recorded. A SEELEM spectrum is a record of the Auger electron intensity as a function of laser frequency. Only molecules in states with electronic energy exceeding the metal workfunction produce Auger electrons. Only molecules in states with long lifetimes can survive the flight time from the laser-molecular beam excitation region to the detector. SEELEM spectroscopy directly detects long-lived, highly-excited triplet states.

1.4 Accomplishments

The objective of this work was pursued by exploring what this additional observable would reveal about the long-lived, highly excited background states.

An Auger detector capable of detecting molecules in long-lived, highly energetic states was constructed. This was used to record SEELEM spectra. LIF spectra were recorded simultaneously.

The SEELEM and LIF spectra of the $V_0^3K_0^1$ bandreveal that a small number of background triplet states mediate the ISC of $3\nu_3$. These triplet perturbers are assigned to the T_3 electronic surface. We call this ISC mechanism Doorway-Mediated Intersystem Crossing, DMISC. The coupling between the $3\nu_3$ basis state and one "doorway" triplet state is found to be 0.11 cm^{-1}. The SEELEM spectrum is enhanced near the excitation energy of this T_3 doorway perturber.

This model of ISC may account for anomalous observations made in this research group of the fluorescence of the $2\nu_3$ and $3\nu_3$ states in a high applied electric field. [60, 59] The Stark splitting of the perturbing T_3 doorway state could simultaneously

account for the shorter apparent lifetimes, larger collisional quenching rates, and smaller fluorescence yield of these states.

The temporal behavior of the SEELEM signal was observed in several ways. The lifetimes of the SEELEM-detectable eigenstates may be as long as 280 μs. This indicates that the electronic character of the SEELEM-detectable states is predominantly S_0. These states have small fractional S_1 and triplet characters which provide the excitation probability, the Auger detectability, and the decay of these states.

SEELEM spectra recorded with different detection surfaces reveal few changes in the relative intensities of the spectral features despite large changes in surface work function. This suggests that the detectivity of these mixed-spin eigenstates may be dominated by the S_1 character. Two simulations were conducted to attempt to determine whether this hypothesis is correct. These show that at least a small fraction ($\sim$ 1 percent) of the molecules in SEELEM-detectable states will de-excite through their S_1 character at surface-molecule distances greater than those at which the de-excitation mechanism through the triplet character is significant ($\sim$ 3 Å). Although this is small, this fraction of the excited molecules may account for the SEELEM signal.

A pattern recognition technique, Extended Auto Correlation (XAC), was developed that extracts patterns from a highly overlapped SEELEM spectrum. The application of this technique resulted in patterns the accuracy of which are limited only by the quality of the experimental data.

Metastable photofragments were observed by SEELEM at a number of excitation frequencies. Although it is not possible to identify the metastable state or even the fragment that is responsible for this signal, the number of candidates is narrowed.

This thesis is available in pdf form at http://rwf.lms.mit.edu/group/theses.html.

Chapter 2

Experimental Apparatus

2.1 Auger effect

2.1.1 Introduction

The surface phenomenon that is exploited by SEELEM was first reported by Harold W. Webb, in 1924[206]. Webb's experimental apparatus consisted a cell with an electron emitting cathode, accelerating grids, and a photo-electric plate. The cell was filled with Hg vapor. The Hg atoms were excited by electrons emitted from the cathode and accelerated by the grids. This atomic excitation was carried to the photo-electric plate, where it resulted in electron emission signal. Webb considered the possibility that the signal was due to photons emitted from the Hg. At the Hg pressures used, photons would be emitted and re-absorbed repeatedly until they reached the photo-electric plate. However, the signal's dependence on the dimension of the cell and on the pressure was not consistent with this process. Instead, the data indicated that the excitation was physically carried to the photo-electric plate by excited atoms. Webb had discovered that metastable Hg, probably in the $^3P_{2,0}$ states, could excite electrons from a metal surface.

Later workers called this effect the "Auger effect" because it can be described with the same quantum mechanical treatment as can another effect that P. Auger reported in 1925 for a significantly different system.[146] Auger discovered that bombarding

a surface with x-rays produces electrons. The x-ray ejects an electron from a core atomic orbital, which leaves a vacancy in that orbital. The kinetic energy of this ejected electron is dependent on the radiation frequency. Another electron within the atom falls into the newly created vacancy. The energy released by this ejects a third electron. Because the energy difference between the core orbitals is fixed, the kinetic energy of the third electron is not dependent on the radiation frequency. Auger Electron Spectroscopy (AES) exploits this effect to determine the elemental composition of a surface. As will be shown, the Auger effect discovered by Webb is similar in that an orbital vacancy in a metastable atom is filled which results in the ejection of another electron from the metastable-surface system. For now, the term "Auger effect" shall refer to the phenomenon that Webb discovered.

Because of the confusion caused by the names of these two techniques, a number of other names have been used to describe experiments that exploit the Auger effect, including metastable quenching spectroscopy (MQS), metastable de-excitation spectroscopy (MDS)[213], metastable-atom electron spectroscopy (MAES)[119, 70], and metastable induced electron spectroscopy (MIES)[20]. Surface Ejection of Electrons by Laser Excited Metastable (SEELEM) spectroscopy was developed by Snè and Cheshnovsky[170] A molecular beam is excited by a laser and the resulting metastable molecules produce detectable Auger electrons at a detection surface.

Surface Penning Ionization electron spectroscopy [19], which is the surface variant of Penning Ionization, is a related technique. Penning Ionization [134] refers to the ionization of a atom or molecule by a metastable atom or molecule. For instance, metastable He($2\ ^3S$) with 19.8 eV of excited electronic energy can ionize a ground state H atom (IP = 13.6 eV). Surface Penning Ionization occurs when a metastable ionizes a molecule adsorbed to a surface. The Auger effect is distinct in that the metastable induces the removal of an electron from the metal surface itself. Of course, this distinction is not appropriate for all physical systems due to surface-adsorbate bonding. Metastable acetylene (5.6 eV of electronic excitation energy) is not energetically capable of ionizing any of the molecules that are likely to be adsorbed to our metastable detection surface.

A large number of workers have exploited the Auger effect to study surfaces. Early work is summarized in Cobas and Lamb[29], and Hagstrum[64]. Hagstrum wrote several definitive papers [62, 61, 63, 64, 65, 66, 67, 68]. More recent work includes that in refs. [31, 30, 164, 19, 213, 71]. Harada, *et al.* have written a nice review of these experiments.[70] These workers were interested in studying uncharacterized surfaces using well characterized metastable noble gas atoms. These experiments are very sensitive to surface conditions, because the metastable atom de-excites by interacting with only the top layer of surface atoms. The distribution of kinetic energies of the Auger electrons is related to the distribution of states at the metal surface.

Other workers have used the Auger effect to study metastable atoms or molecules. The observation of Auger electrons indicated the presence of metastable species in the beam. This includes early work of Lamb and Rutherford, who studied the fine structure of the hydrogen atom[87]. Freund and co-workers studied the metastable dissociation products that resulted from electron impact on O_2, N_2, and CO_2.[153, 154, 169] They observed long-lived Rydberg atoms. Klemperer and co-workers[73, 108] studied the production of metastable species by electron impact for a large number of molecules. Intersystem Crossing (ISC) was studied by Sneh, Cheshnovsky and co-workers[170, 171, 172, 173, 174, 175, 176, 177, 14] where the observation of Auger electrons indicated that the laser excited molecules undergo ISC instead of internal conversion. Wodtke and co-workers have studied the metastable NO($a\ ^4\Pi$) states as well as ketene dissociation by exciting the CO photoproduct to a metastable state and observing it with an Auger detector.[130, 131, 129]

This chapter will introduce the Auger effect and describe a number of experimentally important features of this effect. The experimental apparatus will then be detailed, which will include a description of the IR-UV cell experiments conducted on acetylene, the initial SEELEM experiment conducted at UC Santa Barbara, and the MIT apparatus. A large section of this chapter is devoted to the design and operation of the MIT Auger detector.

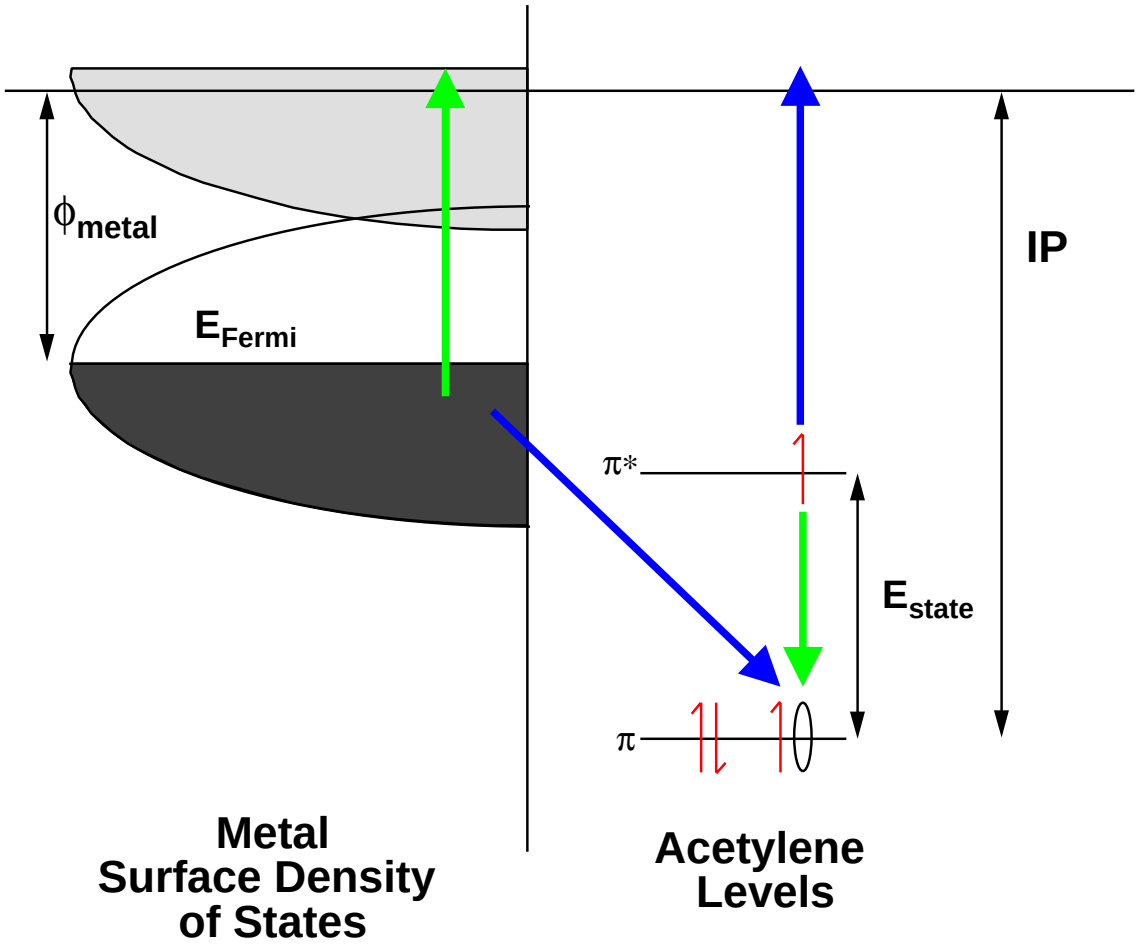

Figure 2-1: Auger de-excitation mechanism.

2.1.2 The mechanism of the Auger effect

As a metastable atom nears a metal surface, the electrostatic interactions among the electrons of the atom and metal increase. These interactions lead to the de-excitation of the metastable atom and, perhaps, to the ejection of an electron.

Figure 2-1 is an energy diagram of the metastable-surface system. The orbitals of the metastable species are shown on the right, along with an electron in an excited orbital and a vacancy in a lower orbital. The ionization potential is also shown. The metal surface density of states is represented on the left. The Fermi level is at the energy of the highest occupied metal orbital at T = 0 K. The energy required to remove an electron from the surface is called the work function, ϕ_{metal}, and is shown on the figure. The electronic states of the two systems can be aligned relative to each

other. An electron is free with no kinetic energy at the atomic ionization limit and at the energy of the metal work function. These two points are energetically equivalent.

Two simple mechanisms can account for Auger de-excitation of a metastable atom, also shown in Fig. 2-1. In the first mechanism, the excited electron fills the atomic vacancy, and the energy released excites a metal electron to a higher state within the metal band structure. If the energy of the metal electron exceeds the metal work function, the electron can leave the surface. In the second mechanism, an electron from the surface tunnels into the metastable atom, filling the vacancy. The energy released by this further excites the excited atomic electron. If the energy of the excited electron is greater than the ionization potential, the electron can leave the atom. Either way, an electron can be ejected from the metastable-surface system.

Clearly, there is an energy threshold for the creation of observable Auger electrons. The excited energy of the metastable atom must be greater than the metal work function to eject an electron from the metastable-surface system.

$$E_{state} > \phi_{metal} \tag{2.1}$$

If the excited energy of the metastable atom is smaller than the metal work function, then de-excitation via the first mechanism would produce an excited electron in the metal, but it would not have sufficient energy to escape the surface. De-excitation via second mechanism would result in an atomic anion with an electron below the ionization potential. The excited electron would tunnel into the degenerate, empty metal orbitals. The metastable atom would be de-excited in both cases without producing a detectable electron. Once the excited energy of the metastable atom exceeds the work function, some of the de-excitations result in ejected electrons. Although this energy threshold is straightforward for atoms, it is somewhat more complicated for molecules, as will be discussed.

2.1.3 Quantum mechanical Auger mechanism

Burhop[21], Hagstrum[64], and others[29, 117, 118] discuss a quantum mechanical description of the de-excitation that corresponds to the two simple mechanisms. Of all the electrostatic interactions among the electrons of the metastable species and metal, the simplest that can account for the de-excitation is the two-electron repulsion between an electron in the metal and the excited electron on the metastable. Just like the electron-electron repulsion term in a molecular Hamiltonian, this term has a "Coulomb" part and an "exchange" part. We will follow the discussion in Chapter 2 of Burhop[21].

The rate of Auger de-excitation (Burhop eq. 2.1 and Hagstrum eq. (7)) is

$$\Gamma_{Auger\ de-excitation} =$$

$$\frac{2\pi}{\hbar} \left| \int\int \psi^*_{free}(\mathbf{r_1})\ \psi^*_{ground}(\mathbf{r_2})\ \frac{e^2}{|\mathbf{r_1}-\mathbf{r_2}|}\ \psi_{excited}(\mathbf{r_2})\ \psi_{metal}(\mathbf{r_1}) d\mathbf{r_2}\ d\mathbf{r_1} \right|^2 \tag{2.2}$$

where the ψ_{free} is the wave function of the Auger electron, ψ_{ground} is the wave function in the ground atomic orbital, $\psi_{excited}$ is the wave function of the excited atomic orbital, and ψ_{metal} is the wave function of a metal electron. $\mathbf{r}_1$ and $\mathbf{r}_2$ represent the positions of electron 1 and electron 2. The wave functions must be antisymmetric with respect to exchange of electrons, so

$$\psi_i(\mathbf{r_1})\ \psi_j(\mathbf{r_2}) \tag{2.3}$$

is replaced by the wave function

$$2^{-\frac{1}{2}}\ [\psi_i(\mathbf{r_1})\ \psi_j(\mathbf{r_2}) - \psi_i(\mathbf{r_2})\ \psi_j(\mathbf{r_1})] \tag{2.4}$$

Eq. 2.2 becomes

$$\Gamma_{Auger\ de-excitation} = \frac{2\pi}{\hbar} \mid \gamma_{Coulomb} - \gamma_{exchange}|^2 \tag{2.5}$$

where

$$\gamma_{\ Coulomb} = \int\int \psi^*_{free}(\mathbf{r_1})\ \psi^*_{ground}(\mathbf{r_2})\ \frac{e^2}{|\mathbf{r_1} - \mathbf{r_2}|}\ \psi_{excited}(\mathbf{r_2})\ \psi_{metal}(\mathbf{r_1}) d\mathbf{r_2}\ d\mathbf{r_1} \tag{2.6}$$

$$\gamma_{\ exchange} = \int\int \psi^*_{free}(\mathbf{r_1})\ \psi^*_{ground}(\mathbf{r_2})\ \frac{e^2}{|\mathbf{r_1} - \mathbf{r_2}|}\ \psi_{excited}(\mathbf{r_1})\ \psi_{metal}(\mathbf{r_2}) d\mathbf{r_2}\ d\mathbf{r_1} \tag{2.7}$$

These two expressions correspond to the simple pictures above. In the Coulomb term, electron 1 initially occupies a metal orbital and is free after the de-excitation. Electron 2 initially occupies the excited atomic orbital and, after the de-excitation, occupies the ground atomic orbital. This corresponds to the first mechanism. The exchange term corresponds to the second mechanism for similar reasons.

In reality, these quantities are only the leading terms in the set of interactions between the metastable and the atoms of the surface, but they indicate that the mechanisms are distinct in two ways. The first distinction is that the Coulomb mechanism is stronger at larger molecule-surface distances than is the exchange mechanism. At long range, the Coulomb mechanism reduces to the emission of a photon by the excited species. The photon is absorbed by the surface, which ejects an electron via the photoelectric effect. In contrast, the exchange mechanism requires significant overlap between the metal and ground state wave functions. The rate of the exchange mechanism does not become large until the metastable is very close to the surface, on the order of the radius of a molecular wave function.

This is not to say that Coulomb mechanism always dominates the exchange mechanism. The de-excitation rate via the Coulomb mechanism may turn on first as a metastable nears the surface, but may not become large enough to de-excite the ma-

jority of molecules before the rate via the exchange mechanism becomes comparable. Determining which of these mechanisms dominates the de-excitation is the subject of Chapter 7.

It should be mentioned that the Coulomb mechanism does not have the same wave vector conservation constraints as does photoabsorption on surfaces. Ashcroft and Mermin discuss photoabsorption by surfaces in Chapter 15.[8] Only photons with frequencies that correspond to vertical transitions on a band diagram (transitions that preserve the wave vector of the metal electron) are possible in metal surfaces (without assistance from a phonon). When a metastable atom interacts with a metal electron, the interactions do not constrain the momentum transfer. As described in C. B. Harris, *et al.*,[202], the charge density oscillations on the surface induced by an excited atom can have high wave vector components. The wave vector components transferred to the surface are high because the size of the perturbing field of the excited atom is more compact than the field of a photon.

The second distinction between the two mechanisms is that the Coulomb mechanism can only take place if the excited electron in the metastable atom has the same spin orientation as the vacancy in the ground orbital, which has a well-defined spin orientation. The electron that fills the vacancy must have the same spin orientation because the operator in the Coulomb integral 2.6 does not operate on spin coordinates. In contrast, the electron that fills the vacancy in the exchange mechanism comes from the metal. The spin of the excited electron, which is ejected, can be of either orientation. Metastables that have a spin multiplicity different from that of the ground state are limited to the exchange mechanism for de-excitation. This spin-conserving effect has been observed. Spin-polarized He($2\ ^3S$) atoms produce spin-polarized Auger electrons.[71]

This implies that triplet acetylene and singlet acetylene have different de-excitation quantum yields, as will be discussed in Chapter 7. Triplets can only be de-excited by the exchange mechanism, while singlets can be de-excited by both mechanisms. However, it is not clear whether the de-excitation rate through the singlet character of an eigenstate will dominate the rate through the triplet character.

2.1.4 The Auger electron kinetic energy distribution

Hagstrum wrote a particularly clear and thorough description on the mechanism of the Auger effect.[64] The intent of Hagstrum's paper is, in part, to derive an "Auger transform," an expression that would transform an experimentally determined Auger electron kinetic energy distribution into the metal surface density of states. Hagstrum did not attempt to derive the Auger electron kinetic energy distribution from equations 2.6 and 2.7. Instead, he introduced several factors needed to arrive at reasonable expressions for the Auger electron kinetic energy distribution. His discussion is inductive. Each consideration is added to the one before it until he arrives at a distribution similar to his data and consistent with physical intuition. Several theses have summarized this paper, including Papaliolios[148], Freund[56], and Stern[182].

The factors Hagstrum discussed include the initial metal density of states, the metal density of states at the final energy for the ejected electron, and the direction of the motion of the excited metal electron within the metal. To account for broadening of the kinetic energy distribution, Hagstrum included the effects of atomic level shifts as the metastable atom approaches the surface and the effects of the finite lifetimes of the initial and final states. The "final state" of the Auger de-excitation leaves a vacancy somewhere in the metal band structure, which will eventually be filled.

The metal surface density of states (SDOS) is the dominant factor that determines the Auger electron kinetic energy distribution. The metastable atom can, in principle, excite any electron in the conduction band structure of the metal surface, as shown in Fig. 2-1. This results in a kinetic energy distribution of the excited electron within the metal that is similar to the SDOS from which the electron originated. The SDOS are related to the metal density of states in the bulk. The bands are narrower but similar to the bulk bands.[179] Surface plasmons, which are surface charge oscillations, can also be observed.[213] The portion of this distribution that exceeds the metal work function, that exceeds the energy threshold shown in eq. 2.1, becomes the Auger electron kinetic energy distribution after being transformed by several other factors,

which include the density of excited metal states and the density of free electron states. As a result, we can conclude that the quantum yield of Auger electrons is dependent on the excitation energy in excess of the work function and the energy depth of the conduction band.

Auger de-excitation is somewhat biased toward the surface electrons near the Fermi level because these electrons extend farther from the surface than do electrons lower in the conduction band. The Sommerfeld model predicts an exponential fall of metal electron density outside the surface of $e^{-(\sqrt{(E_B s)})}$,[213] where s is the distance outside the surface, and E_B is the binding energy. So, the electron in a metastable atom will interact most strongly with electrons near the Fermi level. This bias has been observed in a He($2\,^3S$)-Cs surface experiment by Woratschek, *et al.*[213].

This picture of Auger de-excitation is further complicated by changes in the metastable electronic states caused by the surface. Hagstrum discussed, in sections VIII and IX of ref. [64], how atomic level shifts will broaden the Auger electron kinetic energy distribution. As the metastable atom approaches the surface, E_{state} from eq. 2.1 may change. Since it is likely that E_{state} will be changing as the metastable approaches the surface, the Auger electron kinetic energy distribution will be broadened as different molecules de-excite at different distances, different E_{state}

In acetylene, the surface would not merely shift the levels. Acetylene bonds to many surfaces, so the electronic wave functions may completely rehybridize.[215] This would radically alter the electronic energy of the excited states, which makes it difficult to know what the energy of an excited electron would be. Fortunately, Hagstrum shows, in section XIII of ref. [64], that that the impact of level shifts on the Auger electron kinetic energy distribution would be limited. Hagstrum arrives at phenomenological expressions for the metastable-surface distance dependent Auger de-excitation rate (Hagstrum's equation (35)):

$$\Gamma_{Auger\ de-excitation} = Ae^{-as} \tag{2.8}$$

The metastable-surface distance is s. Hagstrum calculates values for A and a through

a fit to data. This clearly shows that the vast majority of the metastable atoms Auger de-excited before they arrive at the surface. The Auger de-excitation rate increases rapidly as the metal and atomic wave functions begin to overlap due to the exchange term (eq. 2.7). De-excitation will be complete shortly after the onset of rehybridization, so large alterations of the electronic structure of acetylene will not occur until after the Auger de-excitation has taken place.

2.1.5 Molecular Auger electron energy threshold

While the Auger electron energy threshold in eq. 2.1 is correct for atoms, it is too simple for molecules. The variation of electronic energy with molecular geometry means that the energy gap between an excited potential surface and the ground potential surface will depend on the vibrational state of the excited molecule. Auger de-excitation will cause a molecule to make a transition from a vibrational state on the excited molecular potential surface to a vibrational level on the ground molecular potential surface. If the energy gap between these two states is larger than the metal work function, Auger electrons can be produced. The work function of Au is 5.1 eV[106], so the Auger electron yield should be proportional to the fraction of the total fluorescence (see Fig. 4-3) at energies exceeding 41,000 cm^{-1} (5.1 eV).

As a rule, Auger electrons will be produced when the vertical energy gap between the excited potential surface and the ground potential surface at the geometries of the classical turning points of the initial vibrational state are greater than the metal work function.

$$E_{\ turning\ point} > \phi_{metal} \tag{2.9}$$

This energy threshold rule will not be exact, as in the case of $3\nu_3$. The vertical energy gap between the near-linear turning point of $3\nu_3$ and the S_0 surface is $\sim$5 eV while the work function of Au is 5.1 eV. Significant Franck-Condon factors from $3\nu_3$ to low-lying S_0 vibrational states allow for the production of Auger electrons.

The T_3 potential surface lies at energies similar to the S_1 potential surface [38, 37], so T_3 character in eigenstates near $3\nu_3$ may also contribute significantly to the

SEELEM signal. However, the potential surfaces of S_1 and T_3 have very different shapes, and little is known about the vibrational nature of the T_3 perturbers to $3\nu_3$.

Because the T_2 and T_1 potential surfaces lie much lower than either S_1 or T_3 at most geometries, we believe that these states do not significantly contribute to the Au-SEELEM signal. The vertical energy gaps between these surfaces and S_0 are smaller than the Au work function at all geometries for T_1 and all but linear geometry for T_2. The linear geometry of T_2 is calculated to have four imaginary frequencies, so this is not a true transition state (with one imaginary frequency) over which significant vibrational amplitude might accumulate.[38] It is possible, but not likely, that T_2 vibrational character in an eigenstate near $3\nu_3$ would be SEELEM-detectable.

It should be noted that the influence of the vibrational state of the metastable molecule on Auger electron yield has not been experimentally verified.

2.1.6 Surface conditions and Auger de-excitation

It might seem tempting to choose a low work function metal to maximize the Auger electron quantum yield. However, poor surface conditions can more than offset any increase due to a lower work function. This includes adsorbates and oxides, which are easily formed on low work function surfaces. Because the metastable species interacts with only a very small area of the metal surface, the Auger effect is very sensitive to surface conditions.

The work function represents a barrier to escape for metal electrons. As discussed in Chapter 5 of Somorjai[179] and in Chapter 18 of Ashcroft and Mermin[8], the barrier is formed by surface electrons. The wave functions of these electrons extend away from the surface into the vacuum. This creates a layer of negative charge just outside the surface nuclei, which form a positive layer of charge. The energy an electron requires to traverse this "double layer" is the work function.

The work function can be altered by surface adsorbates which will almost certainly exist on our detection surface. Although atomically clean surfaces can be formed, our detection surface will not be clean because the chamber pressure is too high. Our experiments are conducted at $\sim 2 \times 10^{-5}$ Torr, and our chamber has a base pressure

of 3×10^{-7}. The time required to form a monolayer of adsorbates on a clean surface is discussed in Chapter 29 of Atkins[11]. As a rule, one monolayer is formed in 3 s at 1×10^{-6} Torr. There must be some amount of surface adsorbates, even on a relatively clean detection surface like Au.

A molecule adsorbed to a surface can form a dipole with that surface either through polarization or charge transfer, and this can disrupt the double layer. If the negative end of the resulting dipole points away from the surface, the work function will increase because the local double layer increases. Adsorbed oxygen exemplifies this effect. If the dipole opposes the double layer, the work function will decrease. NH_3 can decrease the work function of a metal. Table 5.3 in Somorjai[179], covers many adsorbates and their effects on the work function. Somorjai discusses the Helmholtz equation (and a variation by Topping) that describes the change in work function due to adsorbate coverage. Acetylene is not mentioned. No observable work function change ($\Delta\phi < 0.1$ eV) was observed in the ultraviolet photoelectron spectrum of acetylene on Pd(111).[164] The effect of acetylene adsorption may be minor. Alkali metals dramatically decrease the work function. This is due to partial ionization (charge transfer) of the alkali by a surface with a larger work function. The alkali atom on the surface with a partial positive charge disrupts the negative layer. Andersson and Jostell decreased the work function of a Ni(100) surface ($\phi = 5.22$[106]) to ~ 2 eV by coating with a sub-monolayer of Na or K.[159] (This work was done at very low pressure, 1×10^{-10} Torr, so this would not be applicable under our conditions.)

Adsorbed acetylene will not entirely prevent metastable acetylene from de-exciting through the metal electrons. This is important because metastable acetylene ($\sim$5.6 eV) does not have sufficient excitation energy to surface Penning ionize surface bound acetylene, which probably has an ionization potential near that of free acetylene (11.4 eV). If acetylene is shielded from the surface by adsorbates, the origin of our Auger signal would be unclear. Sesselmann, *et al.*,[164] reported the Auger electron kinetic energy distributions of metastable He on adsorbate covered Cu and Pd surfaces. While adsorbates like CO shielded the surface from the metastable atom, acetylene did not. The Auger electron kinetic energy distribution of metastable He(^1S) on

1×10^{-7} Torr acetylene on a 300 K Pd(111) surface indicated that the metastable was able to de-excite by interacting with the metal.

Different faces of single crystals have different work functions. The work function of polycrystalline surfaces will vary with the degree of surface roughness. Besocke, *et al.* showed that the work function decreases linearly with increased step density on a single crystal Au surface.[16] The work function decreases by several tenths of an eV. The dipole associated with edge Au atoms is not as large as those of a Au atom in a flat surface. As a result, increased edge Au atom density decreases the effective work function.

The Auger electron quantum yield is sensitive to surface temperature. Surface temperature can alter the apparent work function by increasing the number of electrons that occupy high lying states in the conduction band. This effect is small, typically -1×10^{-4} eV/C.[218] The other, more significant effect of temperature is that it can thermally desorb adsorbates. A cleaner surface can significantly increase the Auger electron quantum yield, as will be demonstrated in section 2.3.3.

High temperatures can also drive off an oxide layer, but this requires low pressures and high temperatures. Dushman and Lafferty, Chapter 11 of ref. [52], presented a thermodynamic equation for predicting the loss of an oxide surface from a metal. They present data for many common metals, mostly from the first row of the d-block. H_2 and CO can be used as reducing agents. H_2 is preferred because CO can make volatile and unstable carbonyl complexes. The solid metals we use as detection surfaces require $\sim$1000° C to remove an oxide layer.

If a surface gets hot enough, it will emit electrons thermally. These electrons will be indistinguishable from Auger electrons formed at the same surface. Thermionic emission is described by the Richardson-Dushman equation.[8] This requires much higher temperatures than we use for the our solid metal detection surfaces.

Acetylene surface chemistry will certainly affect the surface conditions, but predicting how this will affect Auger de-excitation is difficult. Acetylene surface chemistry is heavily dependent on the surface material, surface temperature, and acetylene pressure.[215, 114, 133] The rate of each of the many reactions has a unique temper-

ature dependence. Because of these complications, as well as the uncharacterized nature of our polycrystalline detection surface and the high operating pressures of our experiments, it will be difficult to draw conclusions from a detailed look at this issue.

2.1.7 Other considerations

Molecules in high-lying vibrational states of the ground S_0 potential surface do not excite electrons from a surface.[73] Vibrational energy can impart excitation to metal electrons,[92] but the transfer is strongest when one vibrational quantum is transferred to the surface at a time. This can be thought of as a residual effect of the vibrational selection rule. It is unlikely that a single metal electron will be the recipient of sufficient vibrational energy to be ejected from the surface. Evidence that vibrational energy is not Auger detectable was provided by Klemperer and co-workers [73] and Snè and Cheshnovsky.[170, 171]

The translational energy of metastable species has been shown to have no effect on the Auger electron quantum yield at typical molecular beam velocities.[130, 131] It should be noted that acetylene moving at 1 mm/μs (a typical velocity in our experiments) has only 0.12 eV of translational energy.

Hagstrum discusses other surface-atom interactions[64]. If an ion approaches a surface, an electron can neutralize the ion (filling the vacancy) and the energy released by this can excite another metal electron above the work function. Hagstrum discusses this process, called Auger neutralization, in section III and Fig. 2 of ref. [64]. He also discusses resonance processes. The energy of the excited electron of a metastable atom can lie above the Fermi level of the surface. The electron will be resonant with empty metal states and can tunnel into these states, which leaves an ion behind. This ion is then Auger neutralized. Hagstrum discusses this process, called resonance de-excitation, in section II and IX and Fig. 1 of ref. [64]. This is how long-lived Rydberg states are likely to de-excite on all surfaces but those with the lowest work functions.[87, 153, 154, 169]

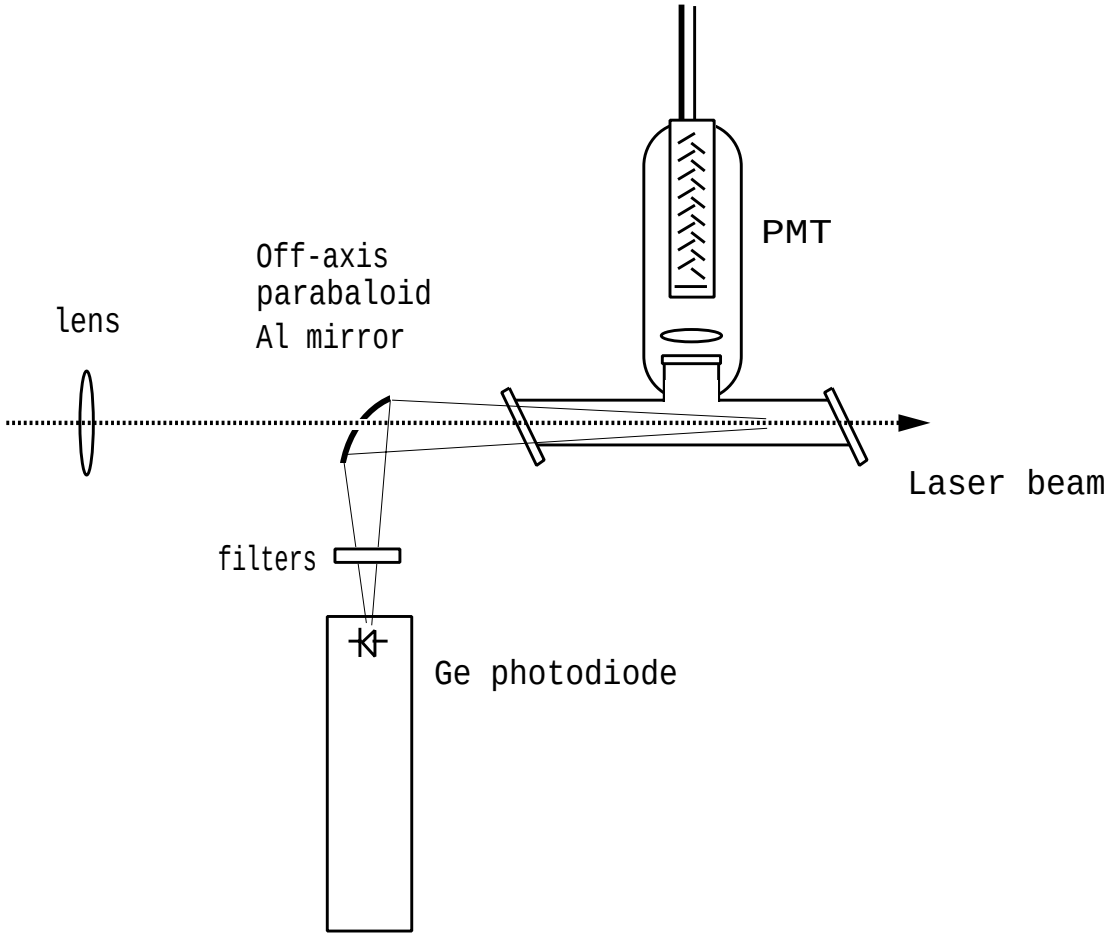

Figure 2-2: IR-UV LIF static cell experimental set up.

2.2 Experimental details

Three experimental apparatuses were used in this work. An IR-UV emission experiment on acetylene was carried out in a cell. The initial SEELEM experiment was conducted in UCSB. An apparatus was constructed at MIT which was used to record IR-LIF, UV-LIF and SEELEM spectra.

2.2.1 Infrared LIF static cell experiments

A series of LIF experiments were carried out on acetylene in a static gas cell. IR-LIF and UV-LIF spectra were simultaneously acquired as a laser scanned the regions of the $V_0^3K_0^1$ and $V_0^2K_0^1$ bands. The experimental set up is shown in Fig. 2-2.

The cell was filled with 150 mTorr of acetylene. Acetylene cylinders contain acetone to stabilize the acetylene as well as some air. Acetylene from a cylinder was frozen with liquid nitrogen and the non-condensable gases like oxygen and nitrogen were removed with a diffusion pump. The acetylene was then thawed, and the process was repeated. The acetylene was then flowed through a trap cooled to the pentane freezing point by a pentane/liquid nitrogen slurry to remove the acetone.

The acetylene was excited by frequency doubled radiation from a Lambda Physik FL3002 dye laser with intracavity etalon. The dye laser is pumped by the third harmonic (355 nm) of a Continuum NY-61 Nd:YAG laser at 20 Hz. The laser was pressure tuned with SF_6. The dyes used were Coumarin 440 and 450. UV light was generated by doubling the dye laser output with a β-BBO crystal. The doubled light was separated from the fundamental light with two 60° prisms. The light was focused by a 50 cm quartz lens, so that the focal point was at a hole in the center of the off-axis paraboloid mirror. As a result, the laser beam expanded as it traveled through the cell.

The laser power was limited to 5-10 μJ to avoid the formation of polyacetylene on the widows. This was a persistent problem. With time, the windows would be coated with polyacetylene, which absorb the IR emission. Particularly strong laser pulses (> 10 μJ) would create a visible piece of white junk on the entrance window, which would interfere with the laser beam and emit strongly in the IR. The windows had to be removed and cleaned with CeO polishing power.

A PMT (RCA 4501-V4) collected acetylene UV fluorescence through a S1-UV window in the side of the cell. The collection optics were S1-UV. The PMT output was amplified (LeCroy VW100B pre-amplifier) and sampled by a boxcar integrator (Stanford Research Systems SR 250, gated over only 70-79 ns). The averaged (10 shot) boxcar output was acquired by a computer.

A Ge photodiode (EO-817A North Coast Scientific, now Edinburgh Instruments, 800-1700 nm, 0.2 ms time constant) collected acetylene IR fluorescence through S1-UV laser beam entrance window on the end of the cell. The fluorescence was reflected by an off-axis paraboloid mirror toward the Ge detector. The fluorescence was filtered

by a long pass interference filter followed by a long-pass color filter (1000 nm cutoff, Oriel) to minimize the impact of laser scatter and UV fluorescence on the IR-LIF spectrum. A boxcar integrator (Stanford Research Systems SR 250) sampled the detector signal. The averaged (10 shot) boxcar output was acquired by a computer. It should be noted that the Ge detector was very sensitive to IR emission from the Nd-YAG laser.

The radiation frequency was calibrated with a Tellurium absorption cell.[24] A back reflection off of the first frequency-separating 60° prism was directed through neutral density filters and then to a $^{130}Te_2$ cell. The cell was inside an oven that heated the cell to 520° C. The light that emerged from the cell fell on a photodiode. A boxcar integrator (Stanford Research Systems SR 250) sampled the photodiode signal. The averaged (10 shot) boxcar output was acquired by a computer.

The IR and UV fluorescence signals were recorded as functions of laser power. To acquire laser power data, the transducer was removed from an Ophir PE-10 power head and positioned to intercept the laser beam after it exited the cell. The resulting signal from it was sampled by a boxcar (Stanford Research Systems SR 250). The averaged (10 shot) boxcar output was acquired by a computer.

2.2.2 UCSB experimental apparatus

The experimental apparatus in the UCSB laboratory of Prof. Alec Wodtke was used for the preliminary SEELEM experiments. It consisted of a doubly-differentially pumped vacuum chamber, an excimer pumped dye laser, and a pulsed nozzle mounted to a goniometer. It is similar to that used by Wodtke and co-workers for other experiments.[44, 130, 131] This work is reported in Humphrey, Morgan, Wodtke, Cunningham, Drucker, and Field[79].

Acetylene (Matheson) was flowed through a trap at $-100°$ C to remove acetone and then mixed with H_2, He, or Ne at a concentration of 6-8 percent. Each mixture also contained ~ 0.2 percent CO for diagnostic purposes. The mixture at 2 atm. was passed through a 1 mm diameter pulsed nozzle (General Valve), operating at 10 Hz, into a diffusion pumped vacuum chamber at $\sim 2 \times 10^{-5}$ Torr. The molecular beam

was collimated 3 cm downstream from the nozzle by a 3.5 mm diameter electroformed skimmer.

The molecular beam was excited by a XeCl-excimer pumped frequency-doubled dye laser (20-ns pulses tunable between 227 and 206 nm, $\sim$ 2 mJ, 0.35 cm-1 bandwidth). The light crossed the molecular beam 2-3 cm after the skimmer. 5 cm downstream from the laser-molecular beam excitation region, the molecular beam passed through a 1-cm-diameter aperture into a differentially pumped detector chamber at 5×10^{-7} Torr.

The molecular beam enters the homemade Auger detector.[130, 131, 129]. Biased plates, mounted on either side of the Auger detection entrance, prevented ions the entering the detector. They had a potential difference of 100 Volts. The Au surface, heated to 250° C, was located 21 cm downstream of the laser-molecular beam excitation region. The Auger electrons were steered by a repeller plate (-1000 V) onto a stack of 3 micro-channel plates, which operate in saturated gain mode and amplify the ejected electrons. A discriminator converts the signals to TTL pulses. A multichannel scalar (MCS-II, Tennelec, now Oxford Instruments) records the delay of the TTL pulses with respect to the laser pulse. In this way the time-of-flight (TOF) profile of the detected metastables was recorded. This is also called a "TOF spectrum," but we shall refer to it as a "TOF profile" to distinguish it from spectra we record as a function of laser frequency.

The TOF profile is used to distinguish between signals resulting from metastable acetylene and metastable photofragments. First, the laser excites the $R_2(0)$ transition in the $a\ ^3\Pi(v=0) \leftarrow X\ ^1\Sigma^+(v=0)$ absorption band of the trace CO in the sample-gas mixture. CO($a\ ^3\Pi$) has a lifetime on the order of 3 ms and was detected at the Au surface as previously reported.[151] CO does not dissociate at this excitation energy, so its TOF profile provides a measure of the molecular beam velocity distribution. The portion of the acetylene TOF profile that coincides with the CO TOF profile is intact metastable acetylene. If there is a peak in the acetylene TOF spectrum earlier than the CO peak, it is due to dissociation products moving ahead of the intact molecules in the beam. Due to the Jacobian transformation from the frame of the

molecules in the expansion to the laboratory frame, one normally observes only those fragments that move faster than the molecular beam velocity.

Metastable photofragments were selectively detected by redirecting the molecular beam away from the Auger detector. The nozzle and skimmer were mounted on a goniometer. The goniometer's axis of rotation lies along the laser beam, so the location of the laser-molecular beam excitation region remains fixed, but the molecular beam is rotated away from the detector. When the photofragments recoil from the molecular beam, the off-axis velocity due to translational energy release of the dissociation may redirect the photofragments toward the detector. Using a beam of CO, we can determine the molecular beam rotation needed to prevent detection of intact metastable acetylene. Any remaining peaks in the TOF spectrum must be due to metastable photofragments.

For SEELEM spectra, a section of the TOF profile resulting from a set number of laser shots was integrated and recorded. Then the laser frequency was stepped and the process was repeated. Metastable photofragments could confound analysis of these spectra, but were easily discriminated against by integrating the TOF profile over a range of arrival times close to that of the peak in the CO TOF profile. We did this to ensure that the SEELEM spectra are not contaminated by multiphoton processes, but this points out the danger of attempting such a metastable quenching experiment without velocity resolved methods.

LIF and SEELEM spectra were recorded simultaneously. A Hamamatsu 215R PMT was placed to detect UV fluorescence perpendicular to the molecular and laser beams. A Schott UG-11 filter was used to reduce scattered laser light. The fluorescence signal was processed by a boxcar integrator (SRS 250 gated from 270 ns to 1.53 μs), acquired by computer.

The lifetimes of the metastable states were measured by comparing SEELEM intensities for molecular beams with different speeds. The lifetime of the metastables will affect the signal strength if the lifetime is similar to the flight time. H_2 and He were used for the $V_0^3K_0^1$ transition, and He and Ne for other $\tilde{A}$-state transitions. The LIF signal is used to normalize the metastable signal. The efficiency of transport of

the metastables to the detector is assumed to be identical for the two molecular beams. Recent CO metastable imaging experiments show a negligible difference in the angular divergence of a He vs. Ne seeded CO beam[86]. Acetylene, with a similar mass, is assumed to behave similarly. The Auger electron ejection efficiency is assumed to be independent of velocity, a result which has been verified for CO[130, 131]. These results are discussed in Chapter 6.

2.2.3 MIT experiment

The Auger detector

This section will discuss the previous Auger detector designs, the design issues we considered, and the final detector design.

Previous Auger detector designs

Three Auger detector designs have been used to detect molecules: solid metal heated to the thermionic limit, alkali metals, and clean solid metals. Other designs, especially ones designed to accurately measure the Auger electron kinetic energy distribution, will not be discussed. Refs.[217, 75] are very good reviews of Auger detector design.

One of the simplest designs was one developed in the Klemperer group.[182] In one case, the first dynode of an electron multiplier acted as an Auger detection surface.[153] In a second case, a Ta filament was incorporated into the entrance of a Bendix Model 306-1 Magnetic Electron Multiplier. Once Auger electrons were produced, they were amplified by the electron multiplier. A large current was applied to the Ta filament, heating it to 900 K by virtue of the filament's resistance. The temperature could be raised to the thermionic limit, the temperature where the metal starts emitting electrons thermally. Elaborate heat sinking was necessary to keep the multiplier from overheating. Freund sent us one of these multipliers. The design is simple, and the surface temperature can be quite high, but the surface size is small. Also, the large heating current created large magnetic fields that interfere with the Auger electron collection.

A more complicated variant of this design is called the "Venetian blind" detector.

[154, 218, 116] An array of thin metal strips are positioned like half-open Venetian blinds, so each strip is at a 45° angle to the molecular beam. Auger electrons are guided through the strips to an electron multiplier behind the array of strips. Again, a current is applied to the array of strips to raise the temperature. Building this detector is harder than other designs, and the surface material cannot be changed. It does have a large detection area and collecting the Auger electrons is easy. The heating current can be run through the strips in alternating directions to minimize the effects of the magnetic fields on Auger electron collection.

The Klemperer group built a detector that used alkali metals as detection surfaces[73, 72, 108]. Cs or Na was evaporated from an oven onto one side of a rotating Cu rod ∼5 mm in diameter. A molecular beam impinges on the opposite side of the rod. Electrons formed at this surface were guided into a channeltron electron multiplier. Thermal electron emission is a problem, so the rod was in thermal contact with a liquid nitrogen cooling block. We have the parts of one of these detectors acquired from the Klemperer group. The alkali metal provides a low work function detection surface, but the surface is small.

The Cheshnovsky group also built an Auger detector using alkali metal as detection surfaces.[174, 176] The central design concept was a detection surface angled with respect to the molecular beam. An alkali metal oven was mounted under the detection surface. An effusive beam of alkali atoms continuously coated the detection surface. The molecular beam entered the detector at a right angle to the alkali beam. The Auger electrons were accelerated toward the microchannel plate electron multiplier at right angles to both the alkali and molecular beams. The detection surface had to be angled with respect to all three axes to intercept both beams and give off electrons directly into the electron multiplier. A large, low work function surface is provided. However, the slanted surface broadens the TOF profile.

The Wodtke group studied dissociation using a solid metal Auger detector mentioned above.[130, 131, 129] They selected a Ni detection surface based on its intrinsic cleanliness. The 25 mm diameter detection surface was placed in a Cu mount that was heated by a cartridge heater to $\sim 300°$ C. Auger electrons are accelerated into a

set of microchannel plates. This design is simple, but the surface temperature is limited. The microchannel plates were not thermally isolated from the detection surface and would get hot enough to thermally emit electrons. This also requires operating pressures less than 1×10^{-6} Torr.

The quantum yield of detection varies considerably with Auger detector design and metastable species.[217, 75] In a stainless steel cell especially designed for high quantum yield, Dunning, *et al.,* achieved quantum yields of 0.7 for He($2\,^3S$).[47] Other detectors have much smaller quantum yields. Lisy estimated that the Klemperer Cs detector has a quantum yield of 1×10^{-2} to 1×10^{-4} for a large number of small molecules.[108] Sneh and Cheshnovsky report that their alkali metal detector had a quantum yield of 5×10^{-2} to 1×10^{-3}, with triplet pyrazine giving the highest yield[173, 174].

The design of the MIT Auger detector

One of the important design objectives was to provide a way to switch solid metal detector surfaces without opening the chamber. The solution was the use of a wheel with four positions for 25 mm diameter detection surfaces, as shown in Figs. 2-3. During an experiment, one of the four surfaces is in a position to intercept the metastable molecules in the free jet. The wheel could be rotated from the exterior of the vacuum chamber, allowing the operator to change the detection surface quickly. The wheel is made of oxygen-free high-conductivity (OFHC) Cu. The large detection surfaces can collect a large fraction of the solid angle of the free jet. Figures 2-4 and 2-5 show the important components of the detector in the solid metal configuration. Most of the supporting framework is not shown. Au, Ag, Cu, Y, Gd, and Sm have been used as detection surfaces. Cu has the largest observed yields for metastable acetylene.

A second design objective was to provide a way to use alkali metals as detection surfaces. Alkali metals must be continuously evaporated onto the detection surface. The solution was the use of another wheel, shown in Fig. 2-6, which is a solid piece of OFHC Cu upon which we plated Cs. During operation, the wheel is rotated, and Cs is continuously plated on the wheel. Figs. 2-7 and 2-8 show the important components of the detector in the alkali metal configuration. Most of the supporting framework

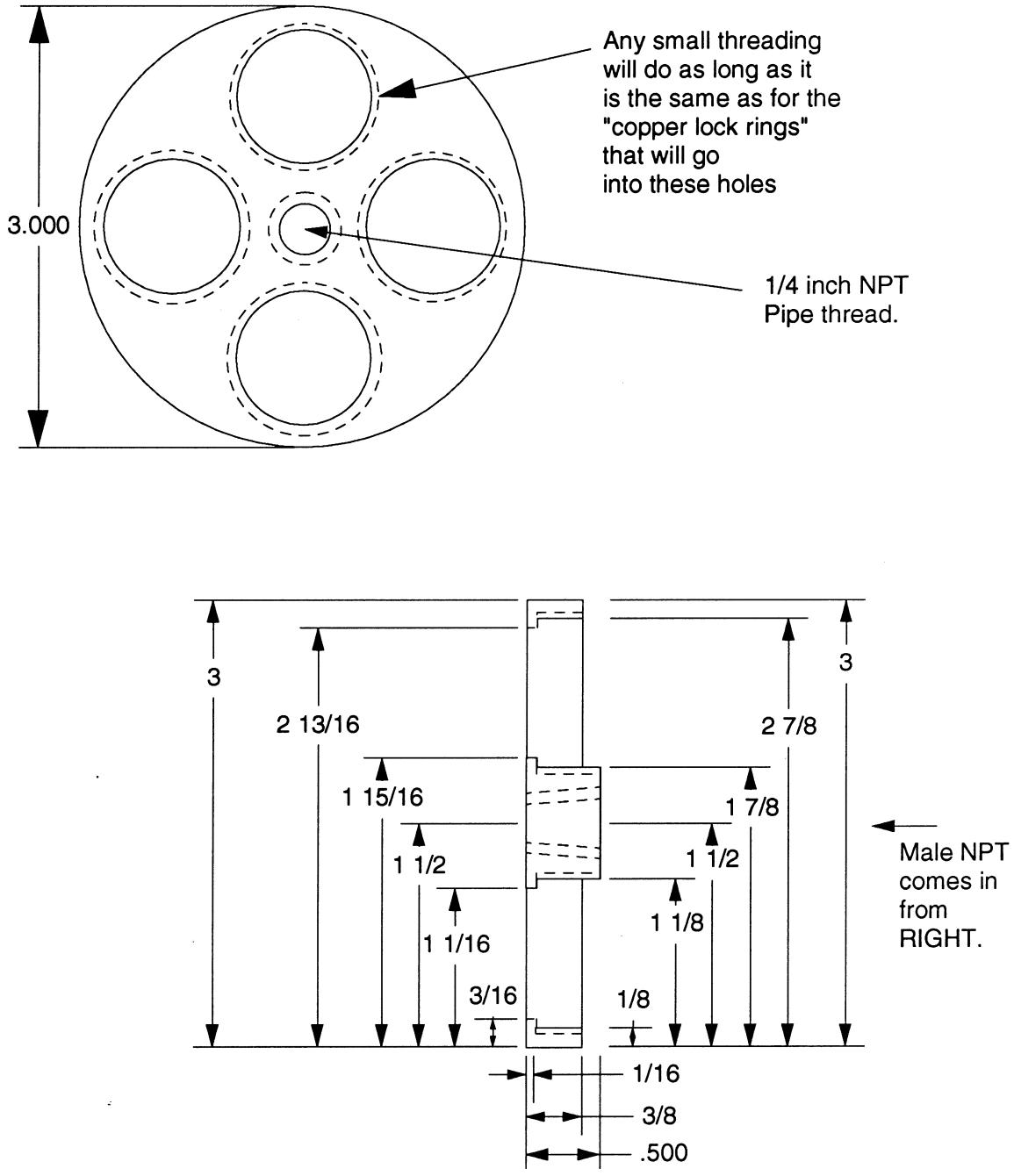

Figure 2-3: Wheel with positions for four solid metal detection surfaces.

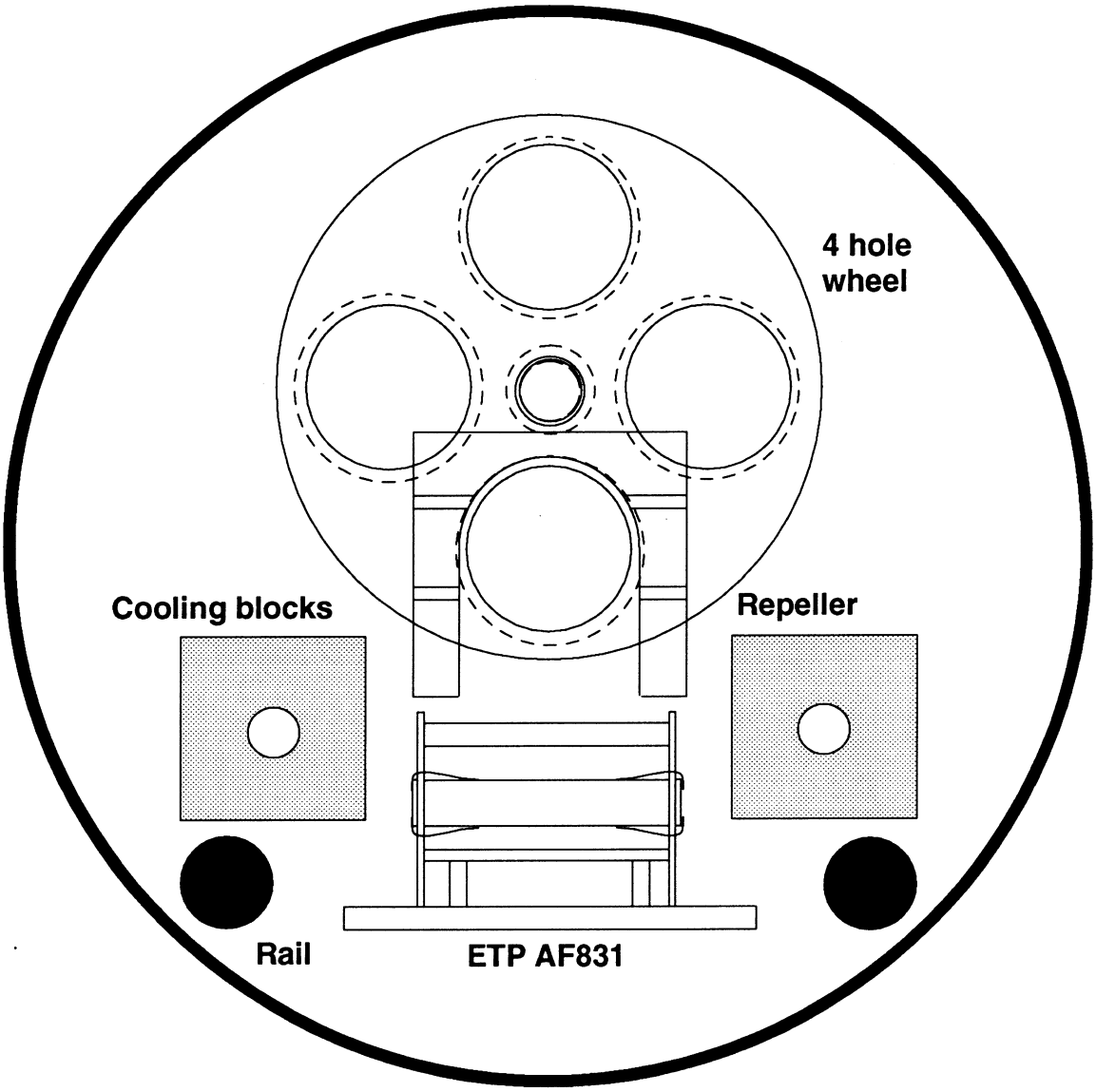

Figure 2-4: Front view of Auger detector.

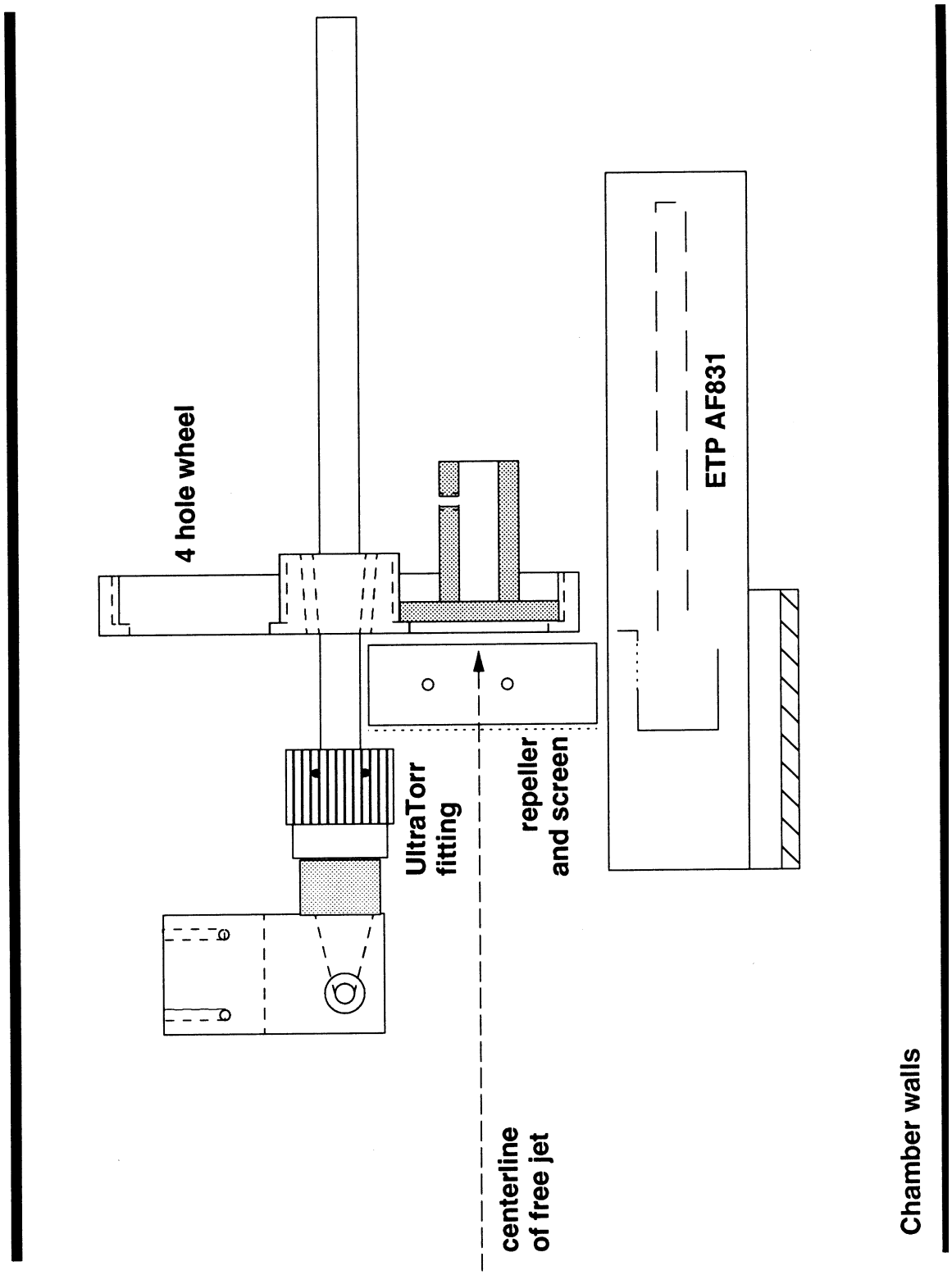

Figure 2-5: Side view of Auger detector.

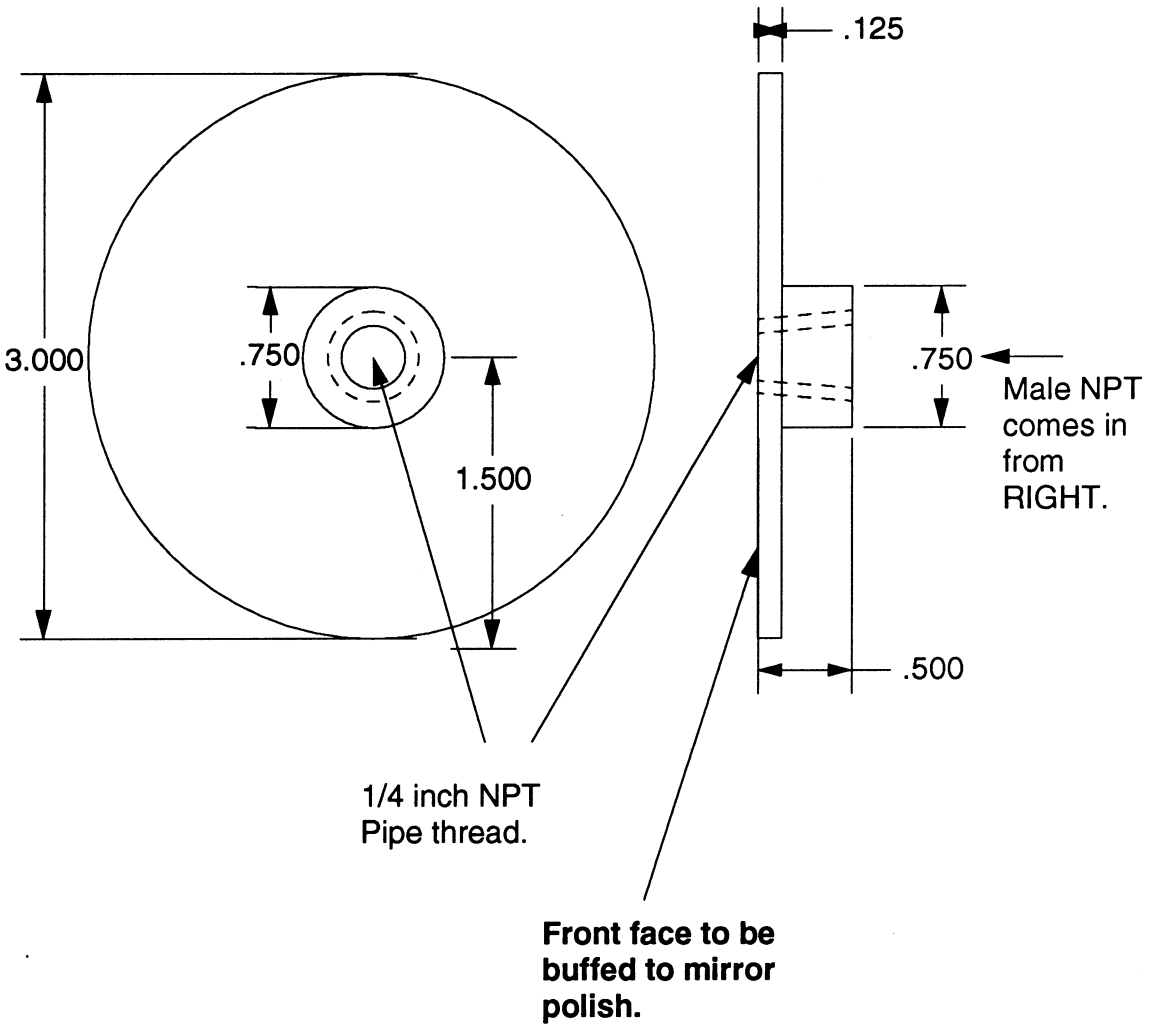

Figure 2-6: Wheel upon which alkali metals can be plated.

is not shown. We can switch from a solid metal detection surface to an alkali metal detection surface without having to alter the rest of the detector.

Each wheel is supported on a 1/4 inch stainless steel tube that serves many purposes. The wheel is attached to the tube by a stainless steel fitting. One end of the tube is held in an Ultratorr fitting, and the other end exits the back of the chamber. This tube supports the wheel and provides a way of rotating the wheel. This allows one to select which solid metal foil acts as the detection surface when the chamber is evacuated. Also, it allows for continuous rotation during Cs plating. The distance between the detector and the nozzle can be adjusted by pushing or pulling on this tube. The cooling water exited the detector through this tube, which serves as a source of cooling for the wheel.

While the tube provided exceptional control and flexibility, it also has a weakness. The continuous rotation during Cs plating wears out the Viton o-ring in the Ultratorr fitting. Within a few days of experiments, it would begin to leak, which caused background signal that varied with wheel position. The background signal is probably due to oxygen anions formed at the surface from water that leaks through the o-ring. Anion formation will be discussed in section 2.3.4. This is the part of the detector most in need of improvement.

The solid metal detection surfaces are heated by a cartridge heater (Omega CIR-1014/120) up to 300° C. This temperature is well below the thermionic limit of the solid metals we use. The temperature was monitored with a K-type thermocouple attached to the back of the wheel. To allow for rapid equilibration, the surface was cooled through the tube. Simultaneously heating and cooling the wheel speeds thermal equilibrium of the wheel. The heater is positioned behind the solid metals in a holder shown in Fig. 2-9.

Cs was evaporated onto the Cu wheel by an oven, as shown in Fig. 2-10. The oven is heated by cartridge heater. A thermocouple attached to the middle of the oven monitored the temperature. Originally, the oven was in contact with cooling surfaces at both its front face and back. This cooled the oven too much and too unevenly. Contact at the back was eliminated, and surfaces on the oven holder that contact the

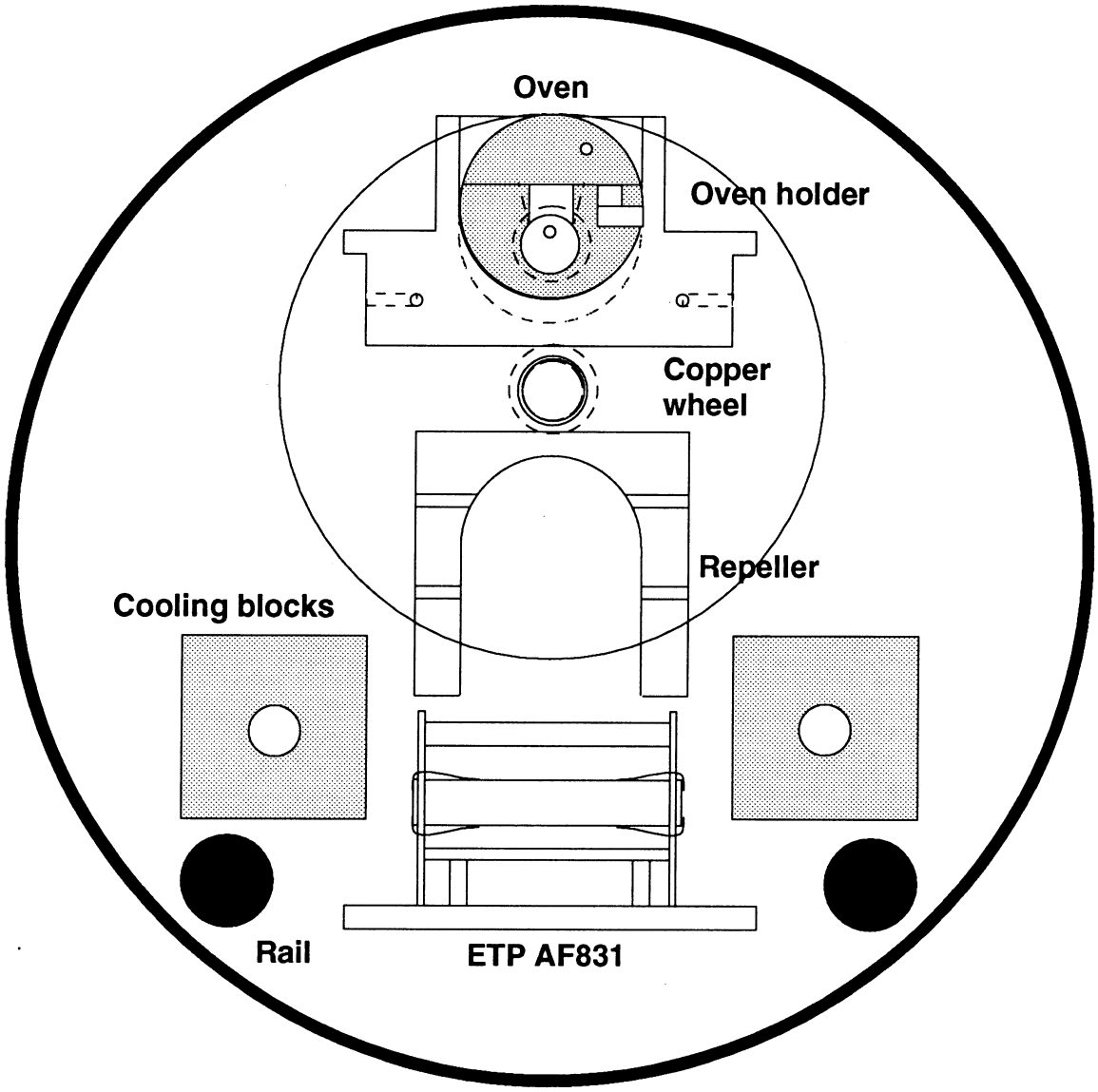

Figure 2-7: Front view of Auger detector in the alkali metal configuration.

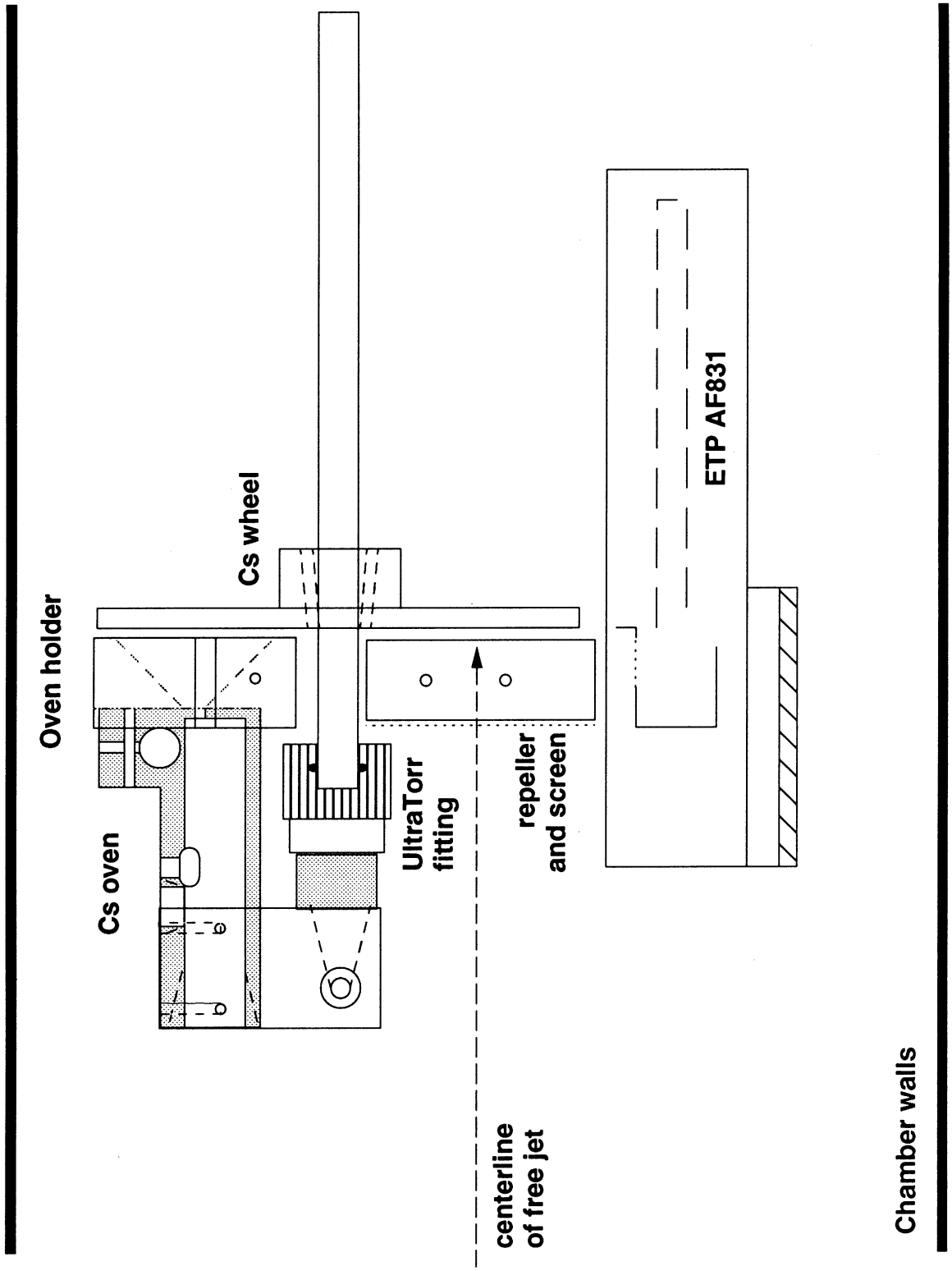

Figure 2-8: Side view of Auger detector in the alkali metal configuration.

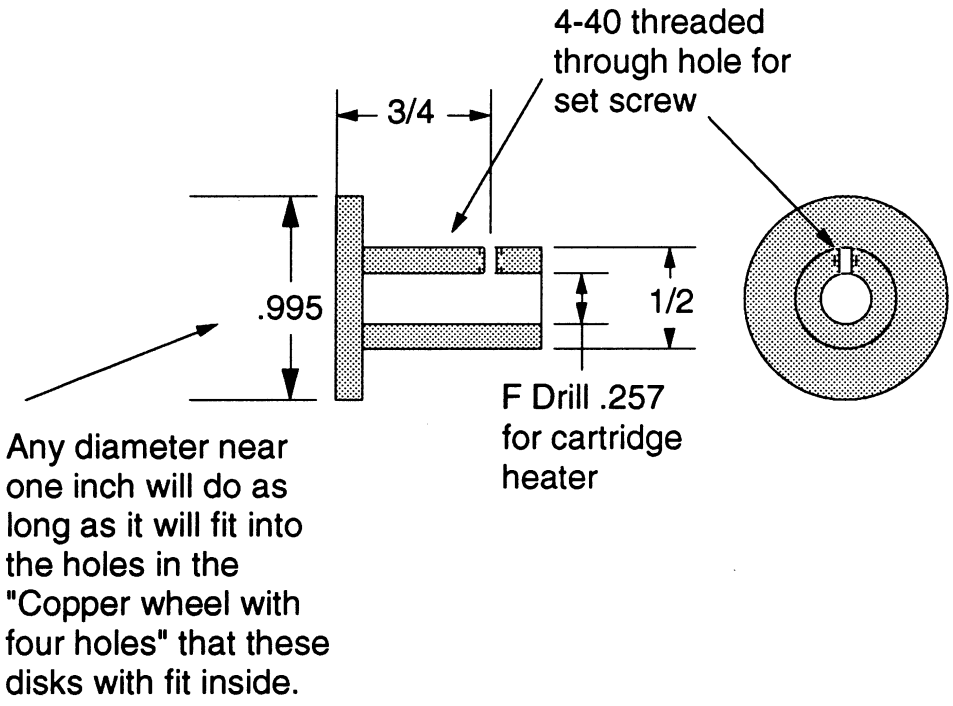

Figure 2-9: Cartridge heater holder.

oven were milled away to reduce cooling through the front of the oven. The SEELEM signal is a sensitive function of the oven temperature. Oven temperatures of 130° C are optimum. Temperatures over 170° C empty the oven quickly. Refs.[6] and [139] discuss the properties of alkali metals.

The oven is designed so that a 1 g ampoule of Cs can be loaded by simply breaking off the top of the ampoule and inserting the Cs, ampoule and all, into the oven. The oven is loaded in a nitrogen-filled glove box because the Cs will oxidize very quickly.

We were able to observe the Cs plating through a window in the chamber. The Cs appeared as a black coating with a few sliver specks. CsO is black. It is not clear whether the Auger electrons were being emitted from the Cs metal specks or the CsO. CsO can have a low work function and is used as a photocathode material in IR-sensitive PMTs.

Excess Cs must be removed from the detector after Cs experiments. The chamber is purged with nitrogen. The oven is removed from the chamber and placed in a desiccator. The oven is then transported to a hood and placed for a time in a large

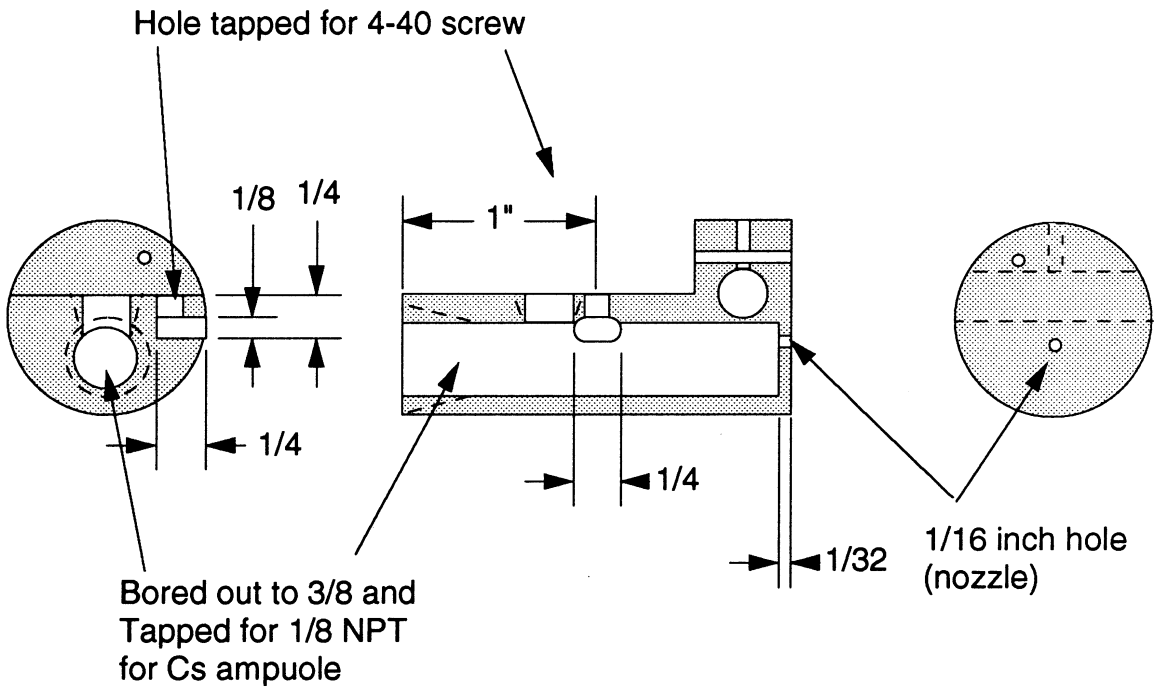

Figure 2-10: Cs oven

glass crystallizing dish to slowly oxidize the residual Cs in air. Later, water is slowly sprayed on the oven. The Cs will oxidize to CsOH, giving off hydrogen gas. A large concentration of hydrogen gas will explode spontaneously, so the hood sash was kept as low as possible and the water was added slowly. The oven is clean when there is no visible residue. The rest of the detector was moved to the hood and treated similarly. Sand was kept on hand in the event of a Cs metal fire.

Two plates, called ion deflectors, are placed in front of the detection surface and electron optics. A voltage is applied to these plates (± 10 volts) to deflect changed particles from the free jet before they reach the detection surface.

The electron optics were designed to effectively guide electrons from the 25 mm diameter detector surface to the electron multiplier mounted below. A series of simulations were run with a software package called SIMion. Using the results of these simulations, a horseshoe shaped repeller which surrounds three sides of the surface was designed. A small negative voltage (-1 V) is placed on the repeller to push electrons toward the multiplier. The repeller imposes a "stadium" electrostatic potential. Electrons escaping the surface travel toward the center and down. A screen has been

placed in front of the repeller to keep the electrons from escaping.

The Auger electrons are amplified by a discrete dynode electron multiplier (ETP AF831), which was selected because it can function at high pressure, because it has a high bias current, and because it provides a large entrance aperture. The detector is used in a single chamber vacuum system with pressure of $\sim 1 \times 10^{-5}$ Torr. This ruled out microchannel plates, which leaves three options: discrete dynode (ETP), channeltron (Galileo Corporation), and microsphere plates (El-Mul Technologies). The discrete dynode electron multiplier was selected because it has the highest current ($\sim$ 1 mA) and, therefore the highest count rates. The higher the count rate, the more signal can be processed without saturating the detection system.[1] The multiplier was heated to 50° C with a cartridge heater (Omega CIR-1014/120) to desorb adsorbates from the dynodes. Adsorbates that are struck by electrons flowing through the multiplier can poison the dynode surfaces and reduce the amplification of the multiplier. The multiplier has a maximum voltage of 3000 Volts. Typically, the voltage was 2700-3000 Volts. The multiplier has a maximum operating pressure of 1×10^{-4} Torr. A Ni box covers the multiplier on five sides. The back is left open for the signal connections.

The output of the multiplier was fed into the circuits shown in Fig. 2-11 a) and b). The first circuit resulted in 10 ns FWHM pulses with a lot of ringing. The second peak was $\sim$1/3 the size of the first peak. The ringing was caused by the long cable needed to carry the signal out of the vacuum chamber. The second, improved circuit produced single pulses with a 4 ns FWHM.

The pulses are recorded by one of two pulse counting systems. The first system consisted of a Stanford Research Systems SR400 photon counter. This has a discriminator, which converts pulses of a sufficient magnitude to TTL pulses, and a

[1]The maximum count rate can be determined by calculating the signal current as a fraction of the bias current flowing through the multiplier resistor network. The signal current is equal to the product of the charge of one electron, the gain, and the number of electrons per second (the count rate). When this is larger than $\sim$15 percent of the bias current, the gain of the multiplier starts to decrease. So, at some count rate, the size of the pulses due to a single Auger electron fall below the discriminator level, and the number of counts stops increasing with the number of Auger electrons produced. The higher the bias current, the higher the maximum count rate.

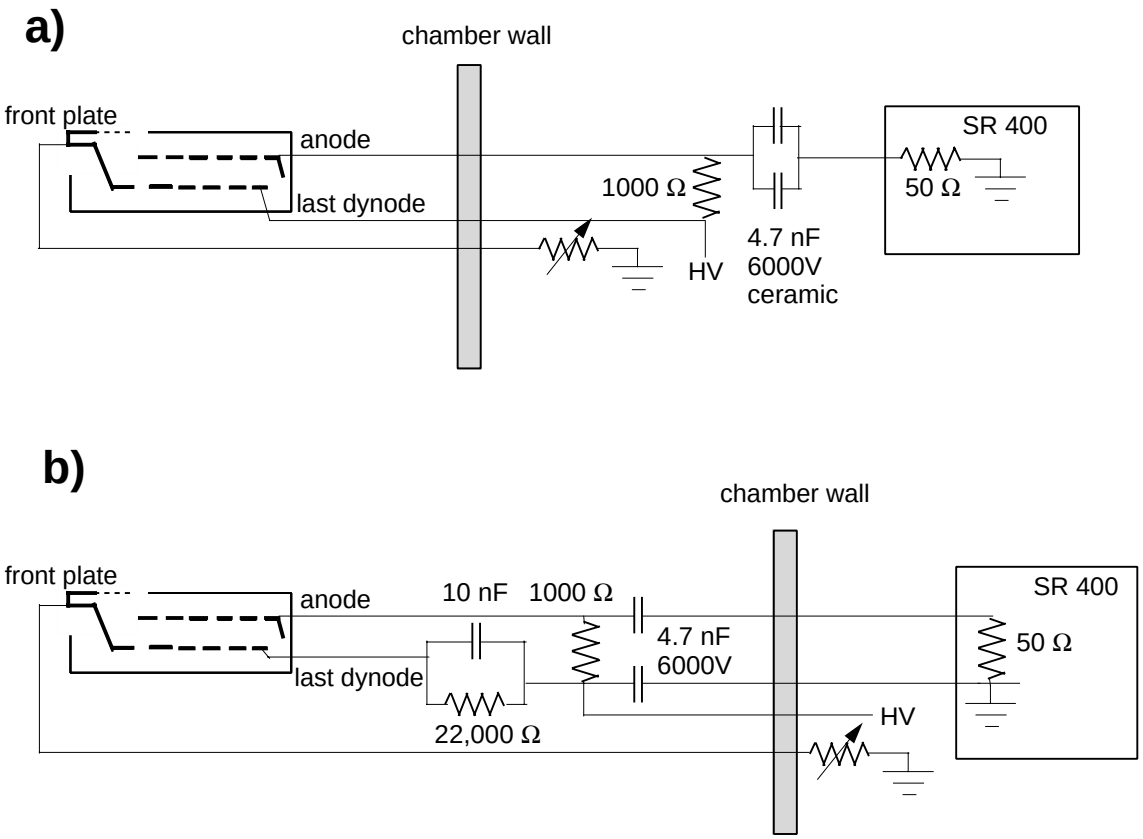

Figure 2-11: Circuits that couple pulses from the electron multiplier to the pulse counting electronics

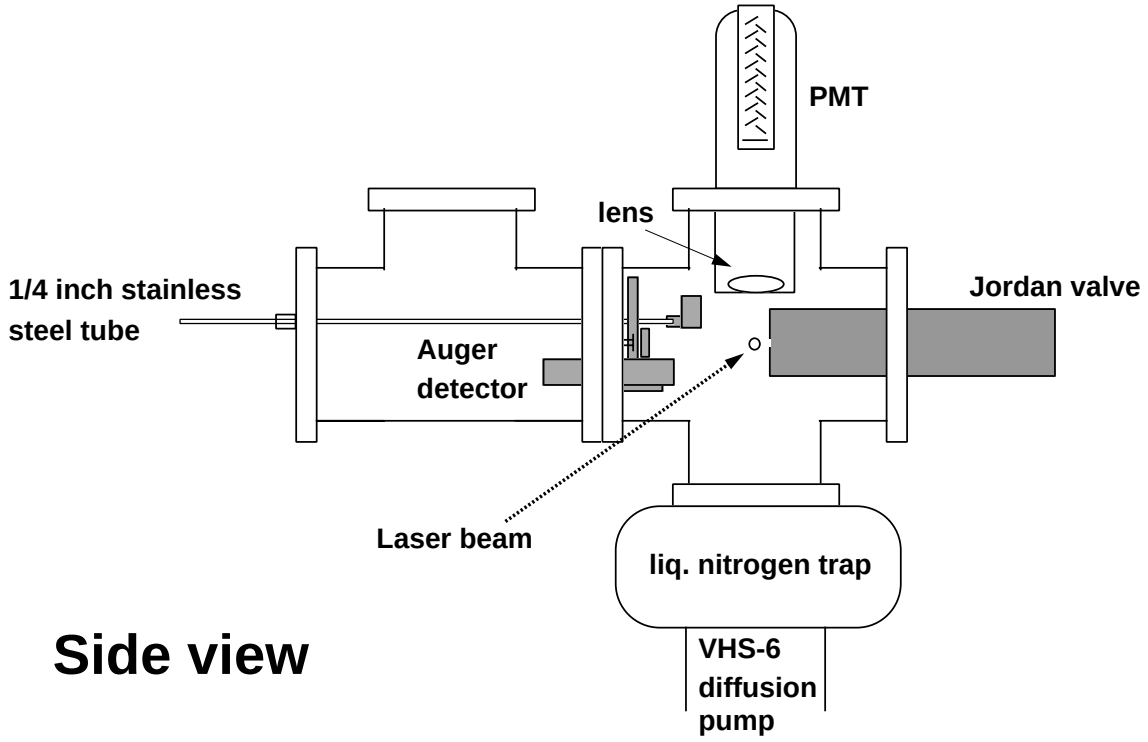

Figure 2-12: Side view of vacuum chamber and essential components.

pulse counter. The number of counts was recorded by computer. The second system (installed April 26, 1999) consists of a Ortec 9302 discriminator and a Tennelec multichannel scaler (MCS-II, Tennelec is now owned by Oxford Instruments). This system is superior because it acquires a full TOF profile each shot and because it records the number of counts in many regions of the TOF profile simultaneously.

Water cooling isolated the rest of the detector from the hot detection surface or oven. Water was circulated from an ice-filled reservoir through the detector.

The body of the detector was made of brass because of its relative strength and thermal conductivity. This was a mistake because brass has ∼35 percent Zn[125], which will have a vapor pressure of $\sim 1 \times 10^{-8}$ Torr if heated to $\sim 100^{\circ}$ C[156]. Al would have been a better choice.

The detector was typically positioned so that the detection surface was 10-20 cm from the laser-free jet excitation region.

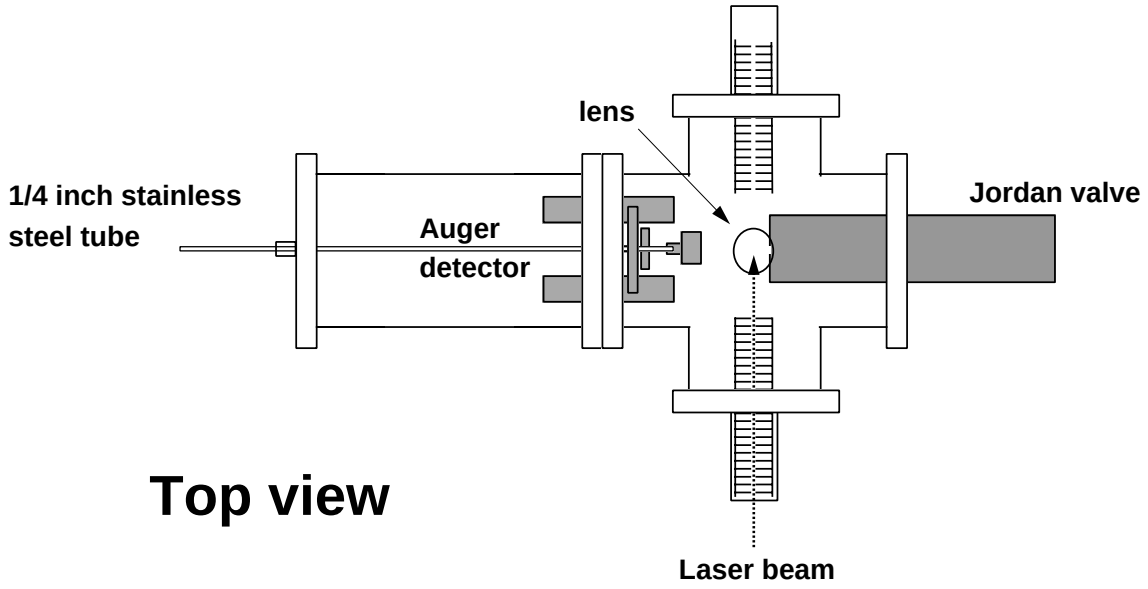

Figure 2-13: Top view of vacuum chamber and essential components.

Vacuum chamber

The vacuum chamber consists of only a single chamber, as shown in Figs. 2-12 and 2-13 in its final configuration with the Gentry-type pulsed valve. The chamber is pumped by a single diffusion pump (Varian VHS-6) with liquid nitrogen trap (Varian 362-6). We use Santovac pumping fluid in the diffusion pump. The diffusion pump is backed with a Welch 1374 mechanical pump through $\sim$11 m of 10 cm diameter vacuum line.

The chamber base pressure is 3×10^{-7} Torr as measured with a Bayard-Alpert ionization gauge. Pressures of 4×10^{-8} Torr could be reached with baking.

There is no skimmer in the chamber. No molecular beam is formed; we simply have a free jet.

Molecules

Acetylene (BOC, atomic absorption grade 2.6) is used as is or was mixed with Helium. Acetylene cylinders contain acetone to stabilize the acetylene and a trace of air. For the Cs-SEELEM experiments (spring of 1999), the acetylene is frozen with liquid nitrogen and the non-condensable gases like oxygen were removed with a diffusion

pump. The acetylene is then thawed, and the process is repeated. To remove the acetone, the acetylene is then flowed through a trap cooled to -75° C by an ethanol/liquid nitrogen slurry.

Two pulsed nozzles were used to expand the acetylene into the vacuum chamber. Initially, a General Valve Series 9 pulsed nozzle was used. It uses a solenoid to open the nozzle. It has a minimum open time of 270 μs and a 1 mm diameter orifice. With the nozzle running, the typical chamber pressure was 8×10^{-6} Torr with a He-acetylene mix at 4 atm. backing pressure and was 1×10^{-5} Torr at 2 atm. of pure acetylene. The chamber pressure appears lower with the He-acetylene mix because the Bayard-Alpert ionization gauge has a low sensitivity to He. The typical foreline pressure was 15 mTorr with a He-acetylene mix at 4 atm. and 6 mTorr at 2 atm. of pure acetylene.

A Gentry-style [200] pulsed valve (R. M. Jordan) was installed (December 12, 1998). The nozzle is opened when a large current (up to 5000 Amps) is pulsed through a "hairpin," a folded, flat piece of metal. The magnetic field induced by the current in one half of the hairpin opposes the magnetic field induced in the other half, which pushes the hairpin apart. This is positioned to open a 0.5 mm orifice for as little at 60 μs. With the nozzle running, the typical chamber pressure was 1×10^{-5} Torr with a He-acetylene mix at 2 atm. backing pressure and was 2×10^{-5} Torr with 2 atm. of pure acetylene. The typical foreline pressure was 12 mTorr with a He-acetylene mix at 2 atm. and was 7 mTorr with 2 atm. of pure acetylene.

An expansion through the General Valve nozzle produced a rotational temperature of $\sim$13 K, although the intensities of the transitions could not be fit to a single temperature. Lower rotational levels had a larger fraction of the population than would be expected for a rotational temperature of 13 K. UV-LIF intensities of rotational lines that terminate on the same final state were compared to measure the relative populations of the initial states. For example, the intensity of R(0) was compared to the intensity of P(2). Both terminate on $J' = 1$. The intensities were adjusted to account for the different line strength factors of the transitions. The emission strengths of the lines are different because transitions populate a different set of M_J-

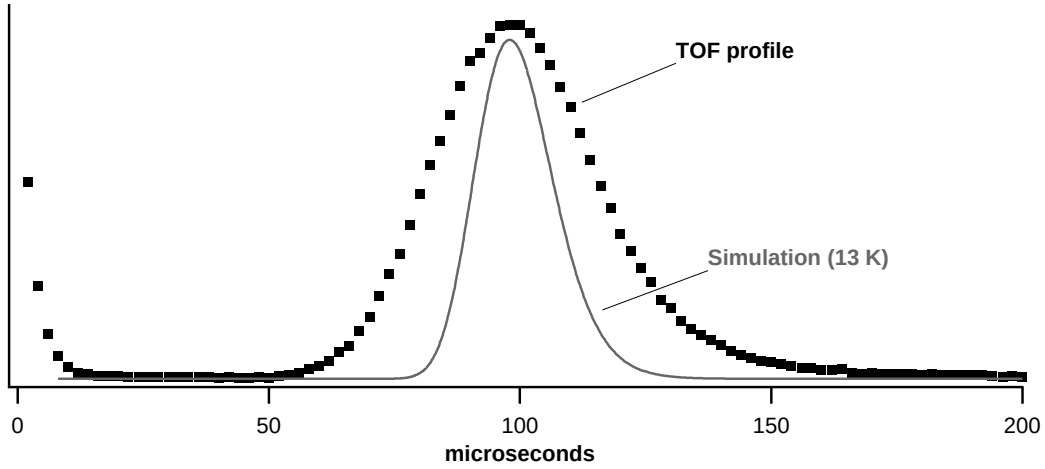

Figure 2-14: Velocity distribution of metastable acetylene compared to the expected velocity distribution.

components of the upper state and the PMT could only see light that was emitted along a particular lab axis. R(0) only populates the M=0 level, while P(2) populates all three M-components of $J' = 1$. The intensities were adjusted through the use of the appropriate direction cosine matrix elements taken from Hougen's monograph.[76] The comparison of R(0) and P(2) indicated that the rotational temperature was $\sim$5 K. Similar comparisons of higher Js indicated that the rotational temperature was warmer. The rotational temperatures leveled off at 13 K as J increased.

The velocity of the free jet could be modeled using the formulas presented by both Miller[121] and by Morse[132], but the velocity distribution as revealed in the SEELEM TOF profiles could not. As shown in Fig. 2-14, the TOF profile is much broader than a distribution based on a terminal beam temperature of 13 K, the rotational temperature. This is not due to detector saturation. As shown in Section 6.2, TOF profiles on peaks the intensities of which differ by a factor of 14 have the same widths. The explanation for the wide velocity distribution is not known, but may be due to the small size of the vacuum chamber and the lack of a skimmer.

As will be discussed in Chapter 8, extreme rotational populations could be produced. We optimized the expansion conditions so that J=4 was the most populated rotational state in the (00010) S_0 vibrational state. The backing pressure was 2 atmospheres of pure acetylene. The nozzle-laser delay was set to maximize the R(4)

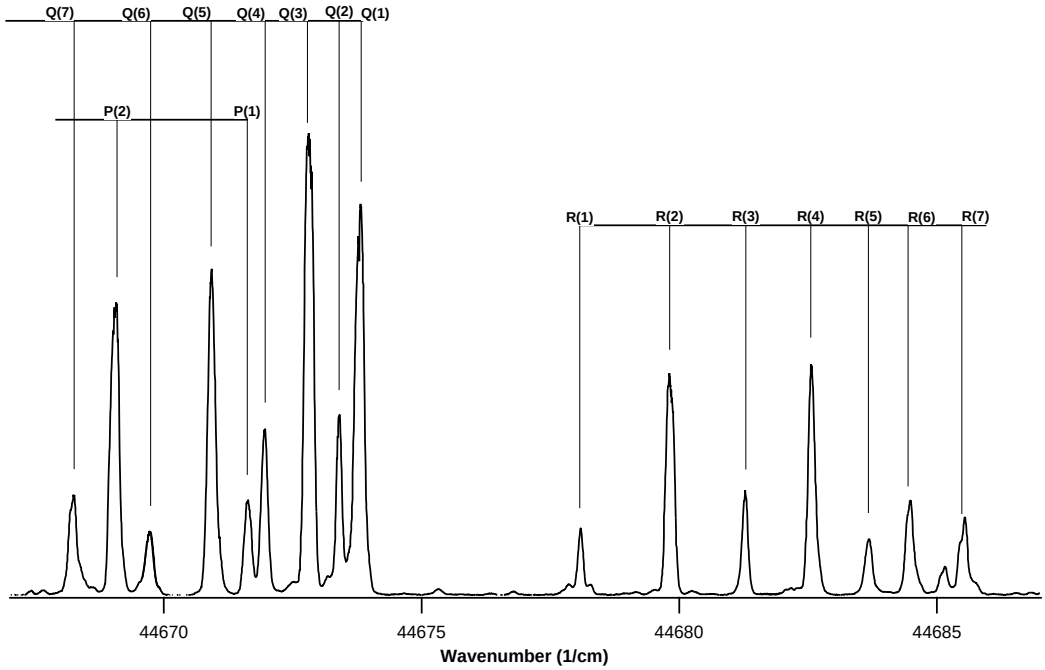

Figure 2-15: LIF signal of $V_1^3K_1^0$ under expansion conditions to enhance $J'' = 4$.

transition of $V_1^3K_1^0$. To increase the population of the (00010) vibrationally excited initial state, the flange the nozzle is mounted on was wrapped in heating tape and baked during the experiment at $\sim 60^\circ$ C. This produced a very warm rotational population distribution, as shown in Fig. 2-15.

Lasers

The excitation radiation was produced by a Lambda Physik FL3002 with intracavity etalon. The dye laser was pumped by the third harmonic (355 nm) of a Continuum NY-61 Nd:YAG laser. The dye used for most of this work was Coumarin 440. 2 L of dye solution was mixed with $\sim$2 grams of DABCO, which is a preservative for the dye[155]. It doubled the life of the dye. The DABCO was used as purchased without further preparation. The dye laser typically produced 1-2 mJ of light. The laser frequency was tuned by step-scanning the etalon and grating with steps as small as 0.001 cm^{-1}.

UV light was generated by doubling the dye laser output with a β-BBO crystal.

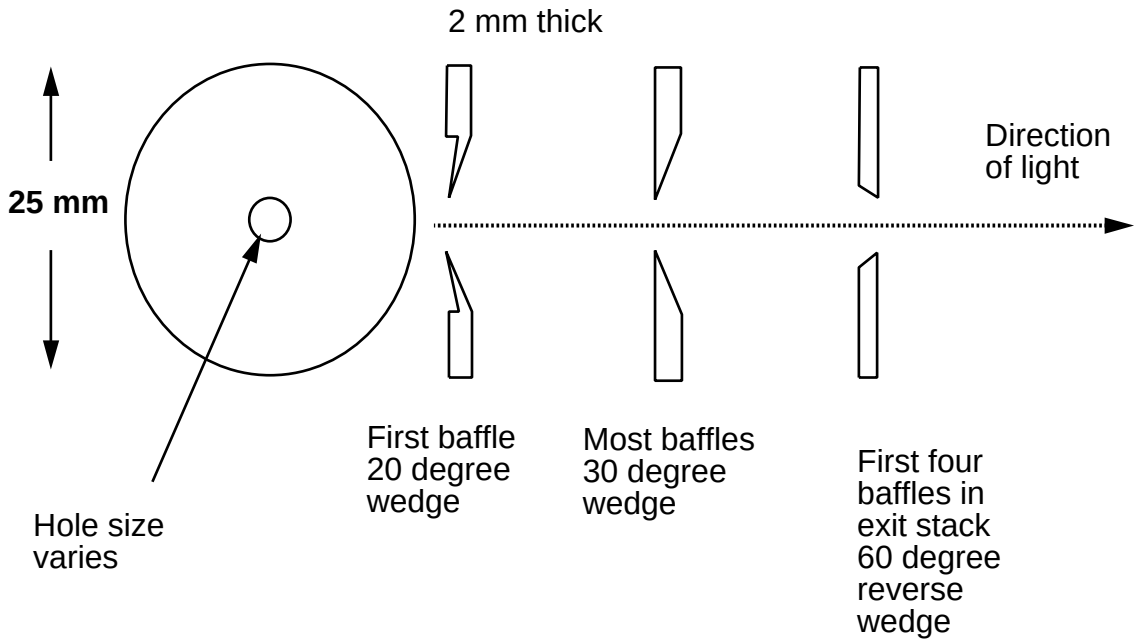

Figure 2-16: Scatter-suppressing baffles.

The doubled light was separated from the fundamental light with two 60° prisms. The light was focused by a 50 cm lens to reduce laser scatter. The lens was positioned so that the focal point was 12 cm behind the free jet centerline. The focal point was not placed at the axis of the jet to avoid multiphoton absorption. The laser passes through the free jet 1-2 cm from the nozzle orifice. 50-100 μJ of light (FWHM of 0.07 cm^{-1}) are produced by this method.

The radiation frequency was calibrated with a Tellurium absorption cell.[24] A back reflection off of the first frequency-separating 60° prism was directed through neutral density filters and then through the $^{130}Te_2$ cell. The cell was inside an oven that heated the cell to 520° C. The light that emerges from the cell falls on a photodiode. A boxcar integrator (Stanford Research Systems SR 250) samples the photodiode signal.

Scatter suppressing baffles were installed in the chamber (September 9, 1998). The laser scatter appears both on the PMT and the SEELEM detector. The baffle system, designed by Frank Stienkemeier, [184] reduced the scatter by $> 30\times$.The baffles, shown in Fig. 2-16, are 25 mm Al disks with holes drilled in them. Scattering

off the edges of the holes is minimized by bringing them to sharp edges. The back face of each baffle is angled at 30°, with the exception of five discs. The first baffle's front face is also angled at 10° to sharpen the edge. The front face of the first four exit baffles are angled at 60° and the back face was flat. This helps reflect the laser light back into the exit baffles. The disks are 2 mm thick and are separated from each other by 8 mm thick, 25 mm diameter rings. These rings are threaded on the inside to help trap light. The holes in the baffles are different sizes, and the order of the disks is critical. For the entrance baffle stack, the disk order is as follows (the dimensions are in mm): 4, 12, 6, 10, 6, 5, 6, 12, 5, 8, 5, 8, 5, 14, 5, 6, 6, 10, 6, 8, 7, 8. The smallest baffle should be first because its edges will generate the most scatter. The disk order of the exit baffle stack is as follows: 14, 12, 10, 8, 8, 8, 9, 9, 9, 9, 10, 10, 12, 12, 14, 14. The first and last baffle in each stack is painted with a black graphite paint (ElectroDag). It might have been better to make these out of brass or Cu because these metals absorb UV light better than does Al.

The Lambda Physik FL3002 is capable of generating "narrow" bandwidth ASE. This ASE can be readily doubled and has a bandwidth of approximately 4 cm^{-1}. This is due to the arrangement of the output coupling optics. As a consequence, a broad background appears in both the LIF and SEELEM spectra. It was necessary to rotate the pre-amplifier pump beam focus lens so that the pre-amp pump beam was slightly out of alignment with the laser beam. While this did reduce the laser power, it also de-tuned the ASE light from the laser light. If the crystal angle was set to double the laser frequency, it would then be at the wrong angle to double the ASE light. (The new generation of Lambda Physik dye lasers, the Scanmates, has different output coupling optics which overcomes this problem.) It has been subsequently discovered that the dye laser was being pumped with the incorrect polarization of 355 nm light. This may have contributed to the ASE.

UV-LIF detection

Excited acetylene emits in the ultraviolet, which can be detected with a photomultiplier tube. The fluorescence was collected at right angles to both the laser beam and

free jet by 5 cm diameter S1-UV lenses, which focused the emission on a PMT with high sensitivity in the UV (RCA 4501-V4). The PMT output was amplified (LeCroy VW100B pre-amplifier) and then sampled by a boxcar integrator (Stanford Research Systems SR 250). The unaveraged boxcar output (LAST SAMPLE) was acquired by a computer.

Before the scatter-suppressing baffles were installed (October 1998), the fluorescence was filtered with a Schott UG-11 filter. The boxcar gate opened 60 ns after the laser fired. Once the baffles were installed, the boxcar gate could open immediately after the laser fired. The filter was unnecessary at the ~ 150 μJ laser power levels we used. The LIF signal due to laser scatter was well below the noise level.

Due to the size and geometry of the collection optics, we were able to detect some fluorescence as much as 18 μs after the laser fired, as will be described in Chapter 6.

IR-LIF detection

Excited acetylene emits in the near-infrared, which can be detected with a Ge photodiode. The fluorescence was collected at right angles to both the laser beam and free jet through the same collection optics used for the UV fluorescence. The IR emission was focused onto a Ge photodiode (EO-817A North Coast Scientific, now Edinburgh Instruments, 800-1700 nm, 0.2 ms time constant, 25 mm^2 diameter active area). A boxcar integrator (Stanford Research Systems SR 250) sampled the photodiode signal. The unaveraged boxcar output (LAST SAMPLE) was acquired by a computer.

Laser power

To monitor the laser power, the light was directed to a Ophir Nova powermeter (with a PE-10 head) after the light exited the vacuum chamber. The powermeter output was amplified (PAR-113) by $10\times$ and acquired by computer. The power of each shot was used to power normalize both the LIF and SEELEM signal. The powermeter output requires ~ 50 ms to settle into a correct value. This delays the acquisition of the powermeter data by one shot.

DAQ

A data acquisition card (National Instruments Lab-PC+) acquired the analog output from the boxcar integrators that process the UV-LIF signal, IR-LIF signal, and the $^{130}Te_2$ oven absorption data for laser frequency calibration. It also acquired the amplified powermeter output. Each signal was differentially acquired; the signal and ground level from each device were separately acquired. These levels were subtracted on the board and recorded.

The BUSY output of the boxcar integrator with the longest gate triggers the acquisition of each shot. As mentioned, the powermeter data was delayed by one shot. When the card acquired the signals, it acquires the laser power level of the previous shot. This must be corrected during later data processing steps.

Timing

The timing of the laser relative to the nozzle was accomplished by a set of TTL circuits. Originally, the master clock based on the 555 chip was used. Delays were generated by a TTL circuit discussed in page 186 in Chapter 4 of ref. [96] and in ref. [191]. Eventually, a master clock that is synchronized with the 60 Hz power line frequency was installed, as shown in Fig. 4-8c of ref. [96] and Section 6.3 of George Adamson's thesis[5]. The 60 Hz was stepped down to 20 Hz. and 10 Hz with circuits discussed in Chapter 6 of ref. [96] and Section 6.3 of ref. [5]. This clock helped eliminate ground loop noise on the signals. Ground loop noise is discussed in section 6.9.6 of ref. [126]

The boxcar integrators were triggered by a photodiode inside the Nd-YAG laser case. The SR400 photon counter and the MCS-II were triggered with a photodiode outside the Nd-YAG laser. The laser step scanning was triggered by the SR400 photon counter or the MCS-II.

The experiments were always initiated by opening the Nd-YAG laser output shutter. The data acquisition of the boxcar integrator signals was started before the experiment began. When the laser shutter was opened, the powermeter and $^{130}Te_2$

calibration signal levels jumped, which indicated the beginning of the experiment for data recorded by the data acquisition card. The SR400 or the MCS began acquiring data with the first shot, which, in turn, began to trigger the dye laser step-scanning.

2.3 Auger detector performance

The SEELEM signal was sensitive to nozzle-laser delay, surface roughness, and surface temperature. The relative SEELEM intensities of a set of lines are insensitive to nozzle-laser delay, repeller voltage, and to nozzle backing pressures which give rise to chamber pressures between 2×10^{-5} to 2×10^{-6}. We have also observed signal on the detector from halogen-containing molecules in their ground electronic state.

2.3.1 Nozzle-laser delay

The SEELEM intensity is a function of the delay between the opening of the nozzle and the laser pulse. Figure 2-17 shows the UV-LIF and Au-SEELEM intensity of R(1) of the $V_0^3K_0^1$ band as a function of nozzle-laser delay. While the number of molecules excited is relatively constant, as revealed by the LIF intensity, the SEELEM intensity decreases by a factor of 3.

There are two possible explanations for the detectivity loss: surface poisoning and backscattering. Surface poisoning could occur when molecules in the expansion adsorb to the surface and interfere with metastable de-excitation. Or, molecules that backscatter off the detection surface could collide with incoming metastable molecules and de-excite them.

This loss of signal is observed in other experiments, and will be discussed in Chapter 6.

2.3.2 Surface roughness

Surface roughness has a significant effect on the SEELEM detectivity. Four OFHC Cu detection surfaces were prepared with different degrees of surface roughness. The

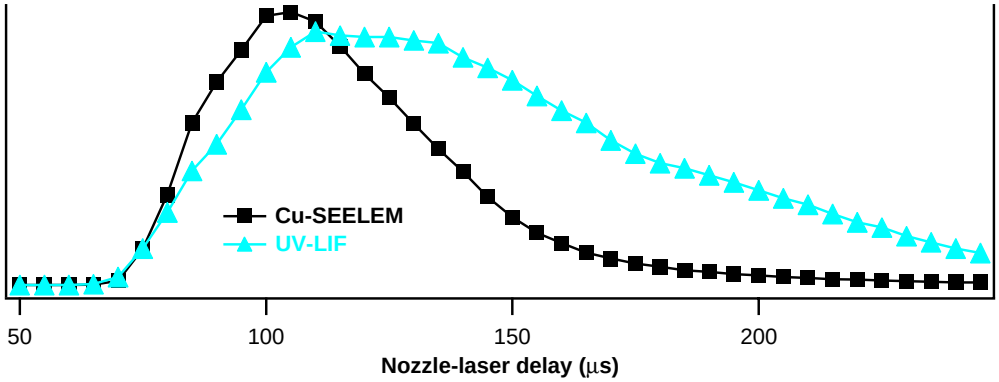

Figure 2-17: SEELEM and LIF signals as a function of nozzle-laser delay.

first two were polished with CeO, which is a powder used to clean excimer laser windows with a grain size of ~ 250 nm. One of these was then sanded with 320 grit sand paper. A third surface was sanded without CeO polishing. The fourth surface was used without preparation. The four surfaces were then washed with soap and thoroughly rinsed with de-ionized water. Finally, they were dried with a heat gun. The four surfaces were placed in the detector, and heated to 200° C. The spectra of R(1) in the $V_0^3K_0^1$ band were recorded on the four surfaces in rapid succession. The spectra are shown in Fig. 2-18.

Despite the crude surface preparation, the changes are dramatic. The polished surface had the poorest detectivity, and the sanded surfaces had a detectivity more than 4 times greater. This suggests that surface roughness may be critical to the creation of Auger electrons.

2.3.3 Surface temperature

Surface temperature also has a significant effect on the SEELEM detectivity. Figure 2-19 shows the SEELEM signal as a function of Au surface temperature. The laser was tuned to the maximum of R(1) in the $V_0^3K_0^1$ band. A large increase in the SEELEM detectivity occurs at 100° C. The SEELEM signal was relatively constant at higher temperature.

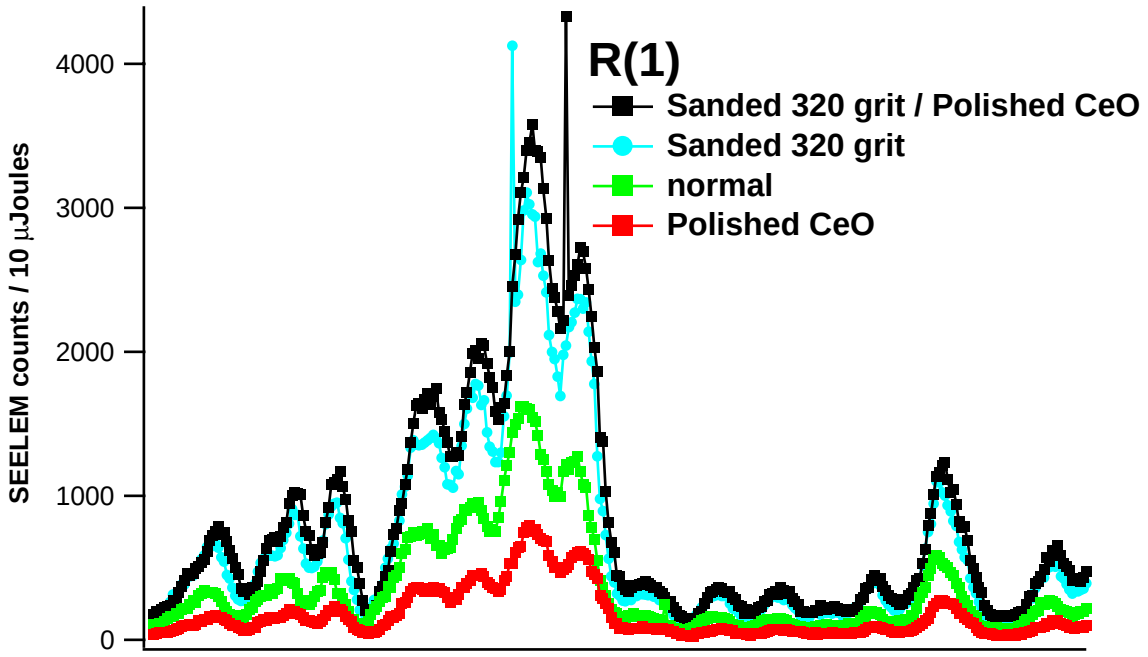

Figure 2-18: SEELEM signal of R(1) of the $V_0^3K_0^1$ band detected on four differently prepared Cu surfaces.

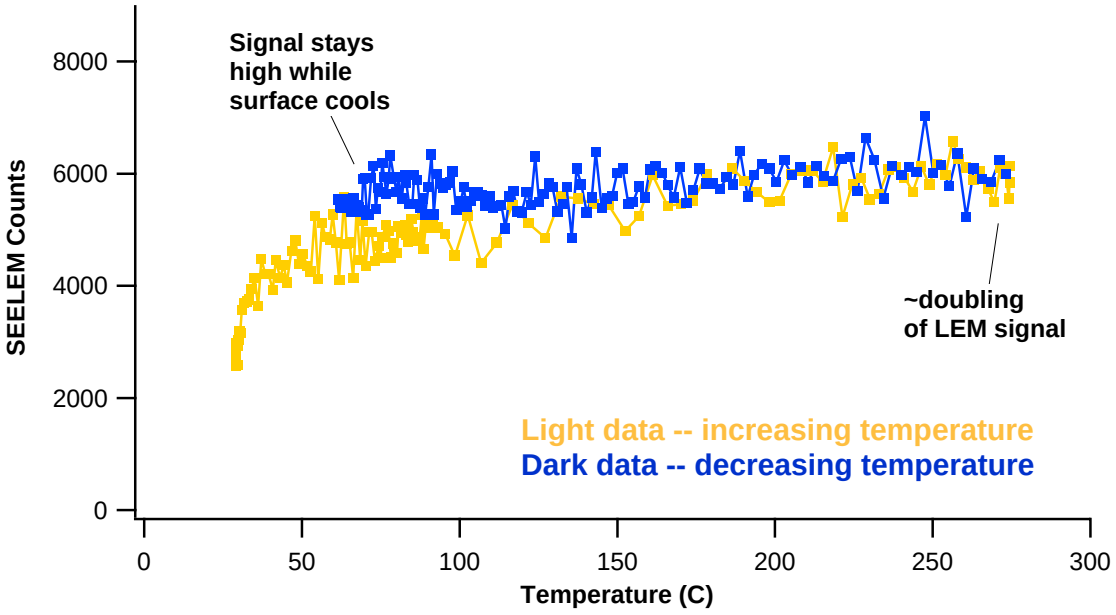

Figure 2-19: SEELEM intensity of R(1) in the $V_0^3K_0^1$ band as a function of temperature.

2.3.4 Negative ion formation at surfaces

Molecules with large electronegativities can produce a signal that interferes with the SEELEM signals[149]. Somorjai discusses the energetics of negative ion dissociation in section 5.4.1 of ref. [179]. Anion desorption can be thought of as occurring through the following process. A neutral atom thermally desorbs from the surface. Then an electron leaves the surface and combines with the atom, forming an anion.

$$E_{\ anion\ desorbtion} = E_{\ neutral\ desorbtion} + \phi_{\ metal} - E_{\ electron\ affinity} \tag{2.10}$$

If the work function is low, as is the case with Cs, and the electron affinity is large, as is the case with halogens and oxygen, anions are produced. The source of background signal in the Cs-SEELEM is probably oxygen atoms from water leaked into the chamber through the worn o-ring. Hemminger notes that compounds with halogen atoms or aromatic systems will generate a signal on a alkali metal detector[72]. While acetylene does not produce this signal, we have observed this effect with chloroform. Figure 2-20 shows a TOF profile of the electron capture signal from chloroform (a few percent seeded in He) on a Au surface. Perhaps chloroform dissociates on the surface and chlorine anions are produced. There was no laser excitation in this experiment.

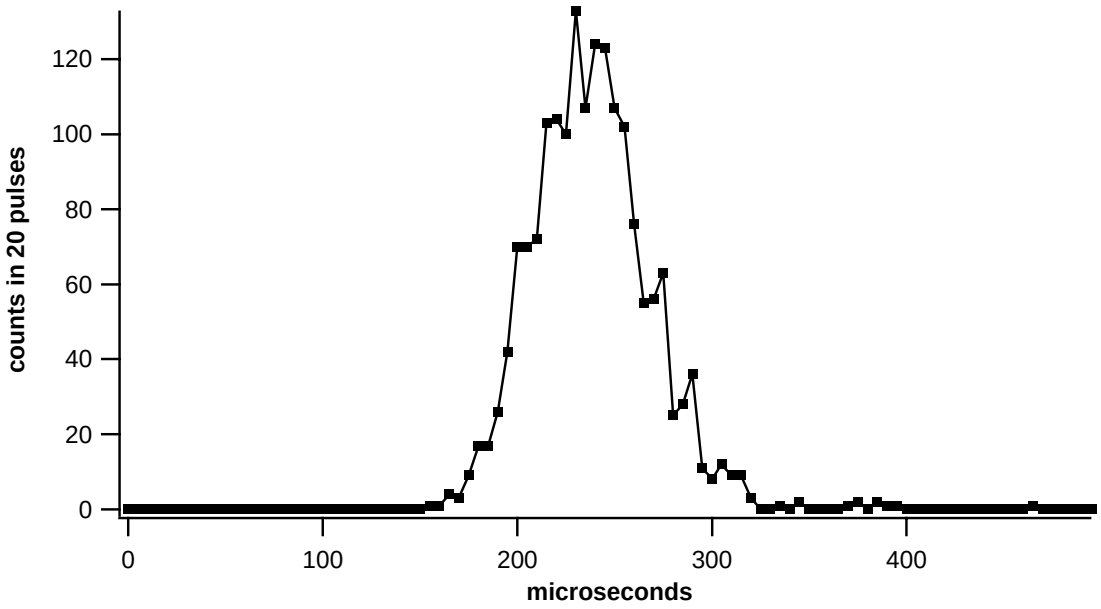

Figure 2-20: TOF profile of chloroform anion signal on a Au detection surface. No laser excitation was used in this experiment.

Chapter 3

SEELEM Intensity Estimation

This section will describe calculations that estimate the number of Auger electrons that will be produced at the detection surface by a given eigenstate. The three key quantities needed for the estimate: the number of molecules excited to an eigenstate, the eigenstate lifetime, and the detection quantum yield of the eigenstate. The estimate is possible because all three key quantities can be related to the fractional S_1 character in the mixed eigenstates. The number of Auger electrons will be calculated for a typical set of nozzle expansion conditions and laser power. The Hönl-London factor and initial population corresponding to R(1) of the $V_0^3K_0^1$ band will be used. R(1) is often the subject of study because it is one of the largest rotational transitions in the SEELEM spectrum of $V_0^3K_0^1$. The computer programs used to calculate each quantity are mentioned in the text so that calculations for other cases can be carried out.

3.1 Number of molecules excited to an eigenstate

The number of excited molecules can be calculated with a simple formula and a number of solid approximations. As we will show, the number of excited molecules is proportional to fractional S_1 character. Five factors, expressed in the following equation are required to estimate the number of molecules excited to a given eigenstate.

$$n_{excited} = n_{irradiated} \left(\frac{\sigma_{transition}(m^2\ rad/s) \cdot n_{photons}}{linewidth_{laser}(rad/s) \cdot \sigma_{laserbeam}(m^2)} \right) \tag{3.1}$$

where $n_{excited}$ is the number of excited molecules, $n_{irradiated}$ is the number of irradiated molecules, $n_{photons}$ is the number of photons, $\sigma_{transition}$ is the cross section of the transition, and $\sigma_{laserbeam}$ is the cross section of the laser beam.

To calculate $n_{irradiated}$, one requires an estimate of the density of acetylene at the point the laser beam crosses the free jet and the irradiated volume. The formulas presented by Morse (and also Miller) provide the density as a function of distance from the nozzle.[132, 121]. As Morse discusses, the expansion is modeled as being adiabatic and isentropic. The Mach number, the ratio of the jet velocity to the local speed of sound, is calculated as a function of distance from the nozzle. The required input quantities are the heat capacity ratio, the nozzle temperature, the backing pressure, and the nozzle diameter. The temperature, velocity, pressure, and density as functions of distance from the nozzle can then be calculated from the Mach number. No attempt was made in this calculation to determine at what distance from the nozzle the Mach number stops decreasing due to the transition from continuum to free-molecular flow or to take account of the pulsed nature of our expansion.

Commonly, the nozzle pressure is 760 Torr of pure acetylene at 300 K. The nozzle diameter for the Gentry-style R. M. Jordan valve is 0.5 mm. The heat capacity ratio, gamma, is equal to 7/5 which is correct for a rotating linear molecule with its vibrations frozen. This will be valid as long as there are no excited vibrational states within kT of the ground vibrational state. In acetylene the first excited vibrational state is at 612 cm^{-1}, or $\sim$3kT at 300 K. Vibrations will add little to the heat capacity. As the beam cools, the heat capacity ratio will remain at 7/5 until kT decreases below twice the rotational constant, B, which is 1.17 cm^{-1} for acetylene. The rotational temperature of the free jet has been measured to be $\sim$13 K. kT is 9 cm^{-1} which is much larger than $2B = 2.34$ cm^{-1}. So the heat capacity ratio will remain 7/5 over the entire expansion. If acetylene-seeded He is used, the heat capacity ratio would be 5/3. He has no rotational degrees of freedom, so its heat capacity ratio is larger.

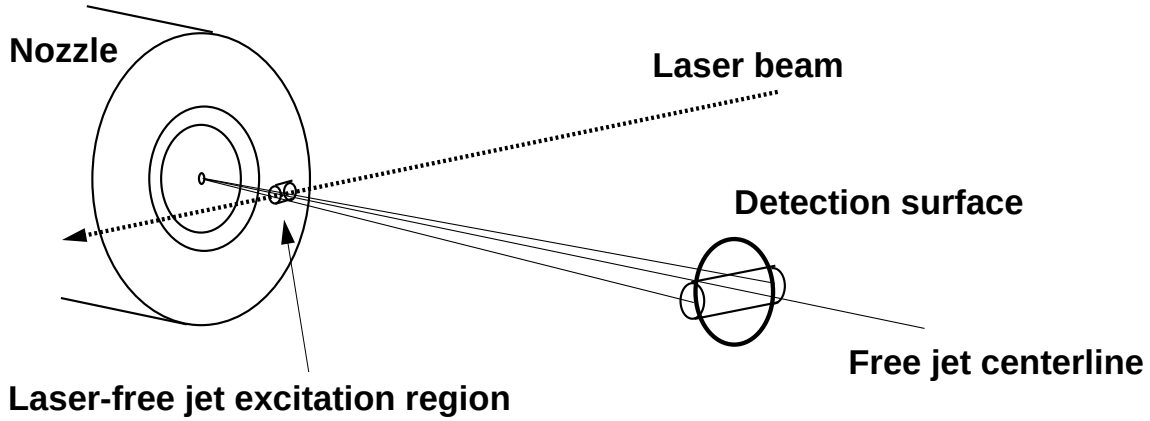

Figure 3-1: The "cylinder" of excited molecules formed by the laser at the laser-free jet excitation region expands both vertically and horizontally as it travels toward the detection surface.

Two other parameters are required to calculate the Mach number. These numbers are obtained from a fit to data.[10] They are dependent on the heat capacity ratio and are listed in Table I of Morse[132] and Table 2.1 of Miller[121]. The expansion parameters corresponding to the heat capacity ratio and nozzle diameter are $x_0 = 0.2$ mm and A=3.65. The meaning of these parameters is discussed in Miller[121]. For the present calculation, the laser-nozzle distance will be set to 20 mm. At this distance, the density is 1.35×10^{15} molecules/cm^3, which is equivalent to the density at 42 mTorr and 300 K. The file containing this calculation is P:/proj/trplts/Tools/Molecular Beam.pxp.

The irradiated volume is also required to calculate the number of irradiated molecules. The laser creates a "cylinder" of excited molecules in the free jet, as shown in Fig. 3-1. The laser spot size, 0.4 mm, defines the cross sectional area of the cylinder, which equals 1.25×10^{-7} m^2. This cylinder will expand as it travels toward the detector. The nozzle-detection surface distance is commonly 120 mm. Assuming the molecules expand linearly in the horizontal and vertical directions, as if they were originating from a point source, the length of the cylinder of molecules that will arrive at the 25 mm detector surface equals 25mm $\cdot$ (20 mm/120 mm) = 4.2 mm. Irradiated volume is 5.3810^{-10} m^3.

As the cylinder moves toward the detector, it expands in diameter as well as length.

It is possible for the cylinder diameter to exceed the diameter of the detection surface. At a nozzle-detector distance of 12 cm, the diameter only grows to 0.4 mm · (12 cm / 2 cm) = 2.4 mm. Because this is much smaller than the 25-mm diameter detector surface, loss due to expansion of the diameter of the cylinder is minimal and ignored in these calculations.

The density of molecules along this cylinder is treated as constant, but it is not. It decreases as a function of angle, θ, from the centerline of the expansion. The density decreases as $cos^4\theta$ as one moves out from the center line at a right angle. This comes from the $cos^2\theta$ dependence of density with the angle and an additional $cos^2\theta$ loss due to the $\frac{1}{r^2}$ loss with the additional distance. This last point might seem surprising, but the relationship is exact. See Fig. 3-2. So, the density at the ends of the 4.2 mm long cylinder is a factor of 0.978 lower than the density at the center. Because this effect is small, it is not included in the calculation.

So, the number of irradiated molecules is calculated as follows:

$$\begin{aligned} n_{irradiated} &= Volume \cdot Density \\ &= 5.3 \times 10^{-10} m^3 \cdot 1.35 \times 10^{15} molecules/cm^3 \cdot (1 \times 10^6 cm^3/m^3) \\ &= 7.2 \times 10^{11} molecules \end{aligned} \tag{3.2}$$

While this is the number of molecules that are irradiated, not all of these molecules are in the initial rotational-vibrational state of the desired transition. Using the partition function, the fraction of the population in a given initial state can be calculated. The fraction of molecules in J=1 is 0.51 based on a beam rotational temperature of 10 K. The program P:/proj/trplts/Tools/Population in a J.vi is used for this calculation. This value is a little high because the vibrational partition function is not included. It was not possible to calculate the vibrational partition function because no measure of the vibrational temperature has been made. If the vibrational temperature were 100 K, the vibrational partition function would be 1.00017. This is small enough to ignore.

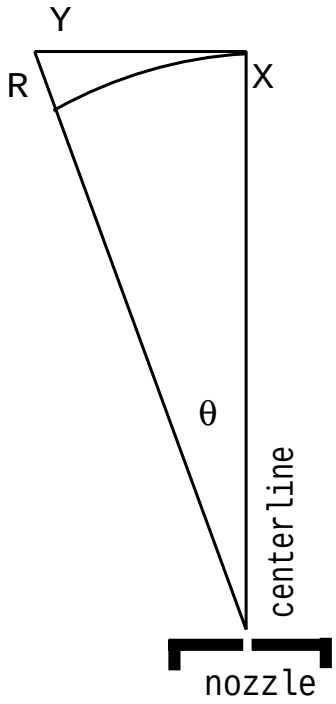

$X = R \cos \theta$
$Y = R \sin \theta$

The density of molecules decreases as $1/r^2$. So, the density at distance R will be less than the density at distance X by the following factor:

$(1/R^2) / (1/X^2) = X^2/R^2 = (\cos \theta)^2$

The density of molecules decreases with angle θ as $\cos^2\theta$, so the density decreases as $\cos^4\theta$ as a function of distance perpendicular to the centerline along Y.

Figure 3-2:

The total number of irradiated molecules in the selected initial state is 3.7×10^{11} molecules.

The number of 220 nm photons is set to 1.1×10^{13}, corresponding to 10 μJ of light. While the experiments are usually conducted with $\sim$ 100 μJ of light, the spectra are usually normalized to 10 μJ of light. The FWHM of the laser linewidth is $\sim$ 0.07 cm^{-1}.

$\sigma_{transition}$ can be calculated from Ingold and King's measurement of the oscillator strength of the $V_0^3K_0^1$ band. They measured an oscillator strength of 1.45×10^{-6}.[80] This is converted into a cross section using Hilborn's paper.[74] This was accomplished with a LabVIEW program (P:/proj/trplts/Tools/Hilborn OscStr f.vi), which results in a cross section of 2.410×10^{-11} m^2 rad/s. This is the cross section for the band, but what is the cross section for an individual line like R(1)? The oscillator strength is invariant with temperature. In other words, it is invariant with the population distribution of the molecules. If all the molecules were in J=1, the oscillator strength of the band would still be 1.45×10^{-6}. That oscillator strength would be split between the two possible transitions from this state, Q(1) and R(1). The Hönl-London factors for these transitions are the same, so the R(1) line possesses half the oscillator strength of the band, or 1.2×10^{-11} m^2 rad/s. The oscillator strength of a rotational line equals the oscillator strength of the band multiplied by the fraction of total line strength from the initial state.

This number is divided by the laser linewidth (in rad/s) to arrive at a cross section in m^2. This assumes that the laser linewidth (0.07 cm^{-1}) is larger than the Doppler-broadened absorption linewidth, which is true in our case. The width of the detection surface (25 mm) determines the observed Doppler broadening. The Doppler effect is largest for those molecules in the ends of the cylinder. These molecules travel at an angle of 5.9° from the free jet centerline. If they are moving 0.8 mm/microsecond, they will be moving $\pm$80 m/s in the direction of the laser beam. This changes the apparent wave number of the laser radiation by $(80 \ / \ 3 \times 10^8) \cdot 45300 = 0.012$ cm^{-1}, which is smaller than the laser linewidth.[15]

One of the characteristic features of the final states we study is that the singlet

basis states are fractionated into many eigenstates. This distribution of oscillator strength will not be incorporated into this calculation for an important reason. The oscillator strength calculated here is distributed over a number of eigenstates because the singlet basis state is coupled to many background states. Once the number of molecules excited to a pure singlet basis state is calculated, this quantity can be multiplied by the fractional singlet character in a given eigenstate to yield the number of excited molecules populating that eigenstate. In several forthcoming sections, simulations of the data are expressed in terms of fractional singlet character. This calculation gives a quantitative scaling factor for the number of excited molecules in any eigenstate.

The calculation shows that 1.87×10^{10} of the 3.7×10^{11} molecules in the initial state are excited, about 5 percent. This calculation was accomplished with a LabVIEW program (P:/proj/trplts/Tools/Molecules excited.vi). 1.87×10^{10} is a large number. Our experiments are usually conducted with 100 μJ of light, a factor of 10 more than this calculation. Under these conditions, roughly half the molecules would be excited. The transition would be saturated. We do not observe this because none of the transitions in the $V_0^3K_0^1$ band terminate in pure singlet states. The coupling to background states is so strong that few of the eigenstates have more than 20 percent S_1 character.[43] The number of molecules excited to any eigenstate under these conditions is:

$$n_{excited} = 1.87 \times 10^{10} \cdot (S_1)^2 \tag{3.3}$$

3.2 Lifetime of an eigenstate

We would like to have a simple way to predict the radiative lifetimes of the eigenstates. Fortunately, enough is known about acetylene to allow for reasonable predictions. The eigenstates will be composed of varying amounts of S_1, T_1, T_2, T_3, and S_0 characters. In principle, each basis state will make a contribution to the decay rate. We assume that external processes that might depopulate the state, such as collisions or a Stark

interaction from stray fields, are not present. As we will show, the decay due to the fractional S_1 character dominates the contribution to the decay due to the fractional T_2 and T_3 characters until the fractional S_1 character is smaller than ~ 0.001.

The S_1 character provides the eigenstate with spontaneous radiative decay to vibrational levels on the S_0 electronic surface. The S_1 character provides a decay rate equal to the decay rate of the pure S_1 basis state $\cdot$ the fractional S_1 character in the eigenstate. The decay rate of a pure S_1 state is the inverse of the lifetime. Ochi and Tsuchiya have estimated the lifetime of a pure S_1 state to be 270 ns based on a sum of the emission rates of the fractionated eigenstates derived from a single singlet basis state.[138] The rate of decay through the S_1 character is 3.7×10^6 (1/s) $\cdot$ $(S_1)^2$.

The S_0 character contributes radiative decay due to vibrational transitions. This sort of emission process is known to have a rate $\sim 3 \times 10^2$ (1/s). So the rate of decay due to S_0 character is 3×10^2 (1/s) $\cdot$ $(S_0)^2$.

T_1 character is spin-forbidden from contributing to emission to the S_0 electronic surface. The eigenstates near the bottom of the T_1 wells do decay slowly to the ground state, but the decay rate of these states is not due to the T_1 character. Oscillator strength from T_1 to the ground state is provided by a small amount of singlet character from remote perturbers mixed into the T_1 states by the spin-orbit interaction. The T_1 character only contributes to the decay rate through vibrational transitions to lower T_1 vibrational states. The rate of decay of the T_1 character is also $\sim 3 \times 10^2$ (1/s) $\cdot$ $(T_1)^2$.

The T_2 character provides oscillator strength to lower states with T_1 character. However, this emission is only symmetry-allowed in *cis*-bent geometry. All three triplet states have *u* symmetry in *trans*-bent and linear geometries. The emission rate between the lowest vibrational state in the *cis* well of the T_2 surface and the lowest vibrational state in the *cis* well of the T_1 surface has been measured to be 40-90 μs.[208] Using the shorter lifetime, the decay rate contributed to an eigenstate is equal to 2.5×10^4 (1/s) $\cdot$ $(T_2)^2$.

T_3 emission has never been observed, but the *g/u,* symmetries are the same as T_2. While T_3 and T_2 are calculated to differ in geometry, the two states are degenerate

at linear geometry. So it is likely that the two states are highly coupled and may behave similarly. The decay rate of T_3 to the lower surfaces will be assumed to be the same as the decay rate of T_2, 2.5×10^4 (1/s) $\cdot$ $(T_3)^2$.

Now that the decay rates of each of the basis states have been approximated, the next step is to determine whether the decay of the $3\nu_3$ eigenstates will be dominated by the character of a single basis state. In particular, the decay due to the S_1 character will compete with the decay due to the T_2 and T_3 characters. Which dominates? As a maximum, fractional T_2 and T_3 basis state characters could comprise almost all of a SEELEM-detectable eigenstate, with a small fractional S_1 character to account for the excitation probability of the eigenstate. The decay rate due to this maximal fractional T_2 and T_3 character would equal 2.5×10^4 (1/s). What fraction of S_1 character would provide a decay rate equivalent to the decay rare due to this maximal fractional T_2 and T_3 character? 2.5×10^4 / $3.7 \times 10^6 \cong 7 \times 10^{-3}$ S_1 character. The fraction of S_1 character in an eigenstate will dominate all other decay pathways at least until it descends to ~ 0.007. Above this value, the decay of the eigenstates may be approximated by 3.7×10^6 (1/s) $\cdot$ S_1 character. For eigenstates with fractional S_1 character nearing 0.007, this approximation will start to underestimate the decay rate. For an eigenstate with the maximal fractional T_2 and T_3 character and 0.007 S_1 character, the approximation will underestimate the decay rate by a factor of 2. As discussed in Chapter 6, the SEELEM-detectable eigenstates have dominant S_0 character, so S_1 character will dominate the decay at fractional S_1 characters well below 0.007.

The number of metastable molecules that exist at any point in the free jet can now be calculated. Under the standard conditions, the number of excited molecules would be $1.87 \times 10^{10} \cdot$ S_1 character. The number of molecules that would remain excited after a time, t, would be

$$n_{remaining} = 1.87 \times 10^{10} \cdot \ (S_1)^2 \cdot e^{-(3.7 \times 10^6 \cdot (S_1)^2 \cdot t)} \tag{3.4}$$

3.3 Auger electron quantum yield

The detection quantum yield of metastables at the detection surface will be proportional to several factors, as discussed in the Chapter 2. These factors include those involving the surface and those involving the molecular eigenstate. The surface factors are not entirely predictable, and we will assume that surface conditions have the same effect on the de-excitation of all eigenstates.

The detection quantum yield is proportional to that fraction of the eigenstate that is composed of electronic character with electronic energy exceeding the workfunction of the detection surface, as discussed in Section 2.1.5. In the case of Au, only S_1 and T_3 have sufficient electronic energy to remove an electron from the surface. So, the detection quantum yield on Au could be proportional to fractional S_1 and T_3 characters. Chapter 7 will discuss the possibility that the detection quantum yield is proportional only to S_1 character.

If we knew the detection quantum yield of a pure S_1 state and a pure T_3 state, we could quantitatively predict our SEELEM signal. Unfortunately, we do not have this information. In fact, it is likely that the yield of a pure S_1 state will be different from that of a pure T_3 state because they de-excite through different mechanisms, as discussed in Section 2.1.3.

Because we have insufficient information to determine which of these two possibilities is correct or to determine the relative detection quantum yield of pure S_1 and T_3 states, we can only calculate the number of Auger electrons that would be ejected with several different assumptions. Figs. 3-3, 3-4, 3-5, and 3-6 display the SEELEM signal under a number of possible detection quantum yield dependencies. In these figures, the numbers of Auger electrons are calculated as if the detection quantum yield were purely some function of the electronic character of the eigenstates. Each scenario is calculated at four flight times reflecting the four flight times used in the experiments discussed in Chapter 6 in Section 6.4. It assumes that the detection quantum yield of a pure S_1 or pure T_3 state is unity. So, some further factor, reflecting the detection quantum yield of a pure S_1 or pure T_3 state, is necessary to arrive at

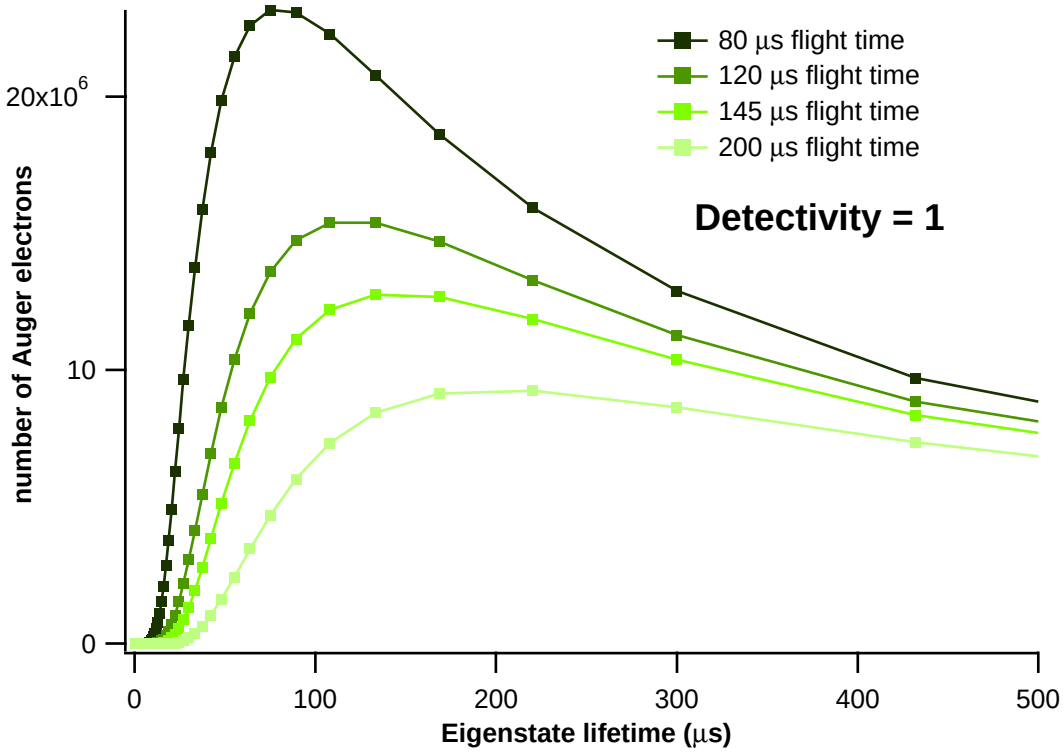

Figure 3-3: Number of Auger electrons that would be produced if all metastable acetylene molecules produce Auger electrons when they arrive at the detection surface. This is equivalent to the number of metastable molecules that reach the surface.

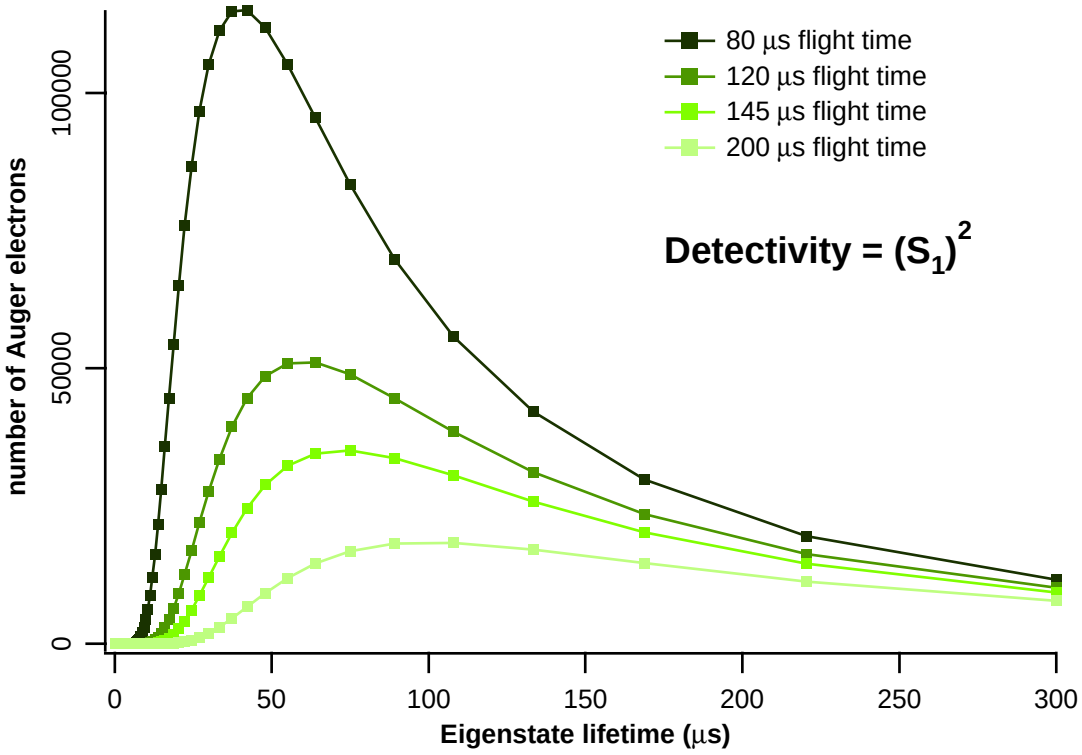

Figure 3-4: Number of Auger electrons assuming that the detection quantum yield is equal to fractional S_1 character.

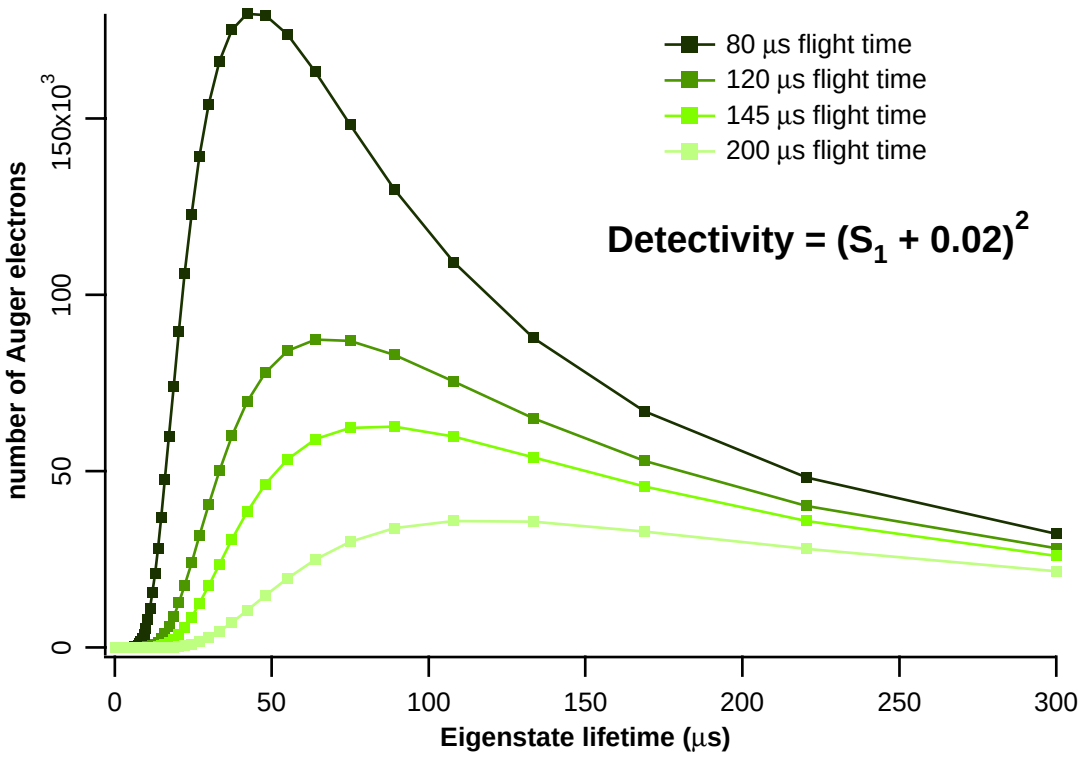

Figure 3-5: Number of Auger electrons assuming the detection quantum yield equals $(S_1+0.02)^2$. This simulates a small contribution to the detection from the T_3 character in the eigenstate.

a realistic estimate of the number of Auger electrons. These figures plot the number of Auger electrons as a function of eigenstate lifetime, which should be thought of as reflecting S_1 character in the eigenstate.

If the Auger detectivity is dominated by the fractional S_1 character in the eigenstate, then the SEELEM signal can be calculated with the following equation where Q_{S_1} is the detection quantum yield of a pure S_1 state:

$$I_{SEELEM} = 1.87 \times 10^{10} \cdot (S_1)^2 \cdot e^{-(3.7\times10^6\cdot(S_1)^2\cdot t)} \cdot Q_{S_1} \cdot (S_1)^2 \tag{3.5}$$

3.4 Observed Auger electron quantum yield

The quantum yield of electrons from the detector can be estimated by comparing the number of counts we observe to the calculated number of metastables that arrive at

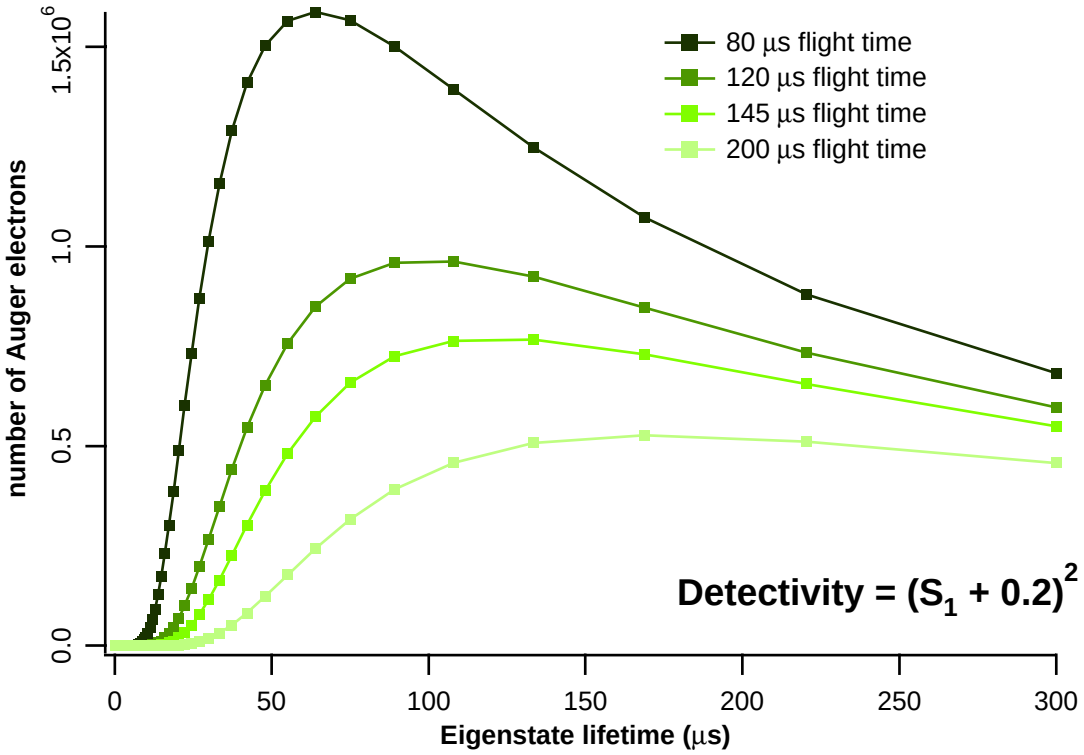

Figure 3-6: Number of ejected electrons assuming the detection quantum yield equals $(S_1+0.2)^2$. This simulates a large contribution to the detection from the T_3 character in the eigenstate.

the detection surface. The SEELEM-detectable states are shown in Chapter 6 to have ~ 0.001 singlet character, so use of eq. 3.4 shows that 1.4×10^7 metastable molecules will still exist when they arrive at the detector surface 80 μs later. SEELEM spectra of R(1) in $3\nu_3$ (8AUGb.cnt and 9AUGh.cnt) show that the largest peaks have 3500 counts / 10 μJ summed in 50 shots, or 70 counts per shot per 10 μJ. The detection quantum yield is 70 / $1.4 \times 10^7 = 5 \times 10^{-6}$.

Assuming the detectivity is proportional to fractional S_1 character, 1.4×10^7 metastable molecules with 0.001 S_1 character are equivalent to 1.4×10^4 molecules in pure S_1 states. The detection quantum yield of the pure S_1 state is 70 / $1.4 \times 10^4 = 5 \times 10^{-3}$. This is comparable to the detection quantum yields reported by others, as discussed in section 2.2.3.[108, 173, 174]

This assumes that the largest peak was due to only one state with a singlet character of 0.001 and a lifetime of 300 μs. Obviously, this is not something of which we are certain, so this detection quantum yield is approximate.

Chapter 4

Doorway Mediated Intersystem Crossing

4.1 Initial SEELEM spectrum

In our initial attempt to observe SEELEM signal at UCSB, we recorded the SEELEM and LIF spectra shown in Fig. 4-1. This spectrum is of the $V_0^3K_0^1$ band in the acetylene $\tilde{A}$-$\tilde{X}$ system, which terminates in a vibrational state with 3 quanta of the *trans*-bending mode, ν_3. Au was used as the SEELEM detection surface. The experimental resolution of the SEELEM and LIF spectrum is 0.2 cm^{-1} and 0.35 cm^{-1} respectively. We reported this work in Humphrey, *et al.*[79] This spectrum helps confirm a proposal made separately by Ochi and Tsuchiya[138] and by Dupré, *et al.*[48]. They each proposed that the Intersystem Crossing of $3\nu_3$ is mediated by a sparse manifold of states from the T_3 electronic surface. The SEELEM spectrum indicates that, in fact, the Intersystem Crossing of $3\nu_3$ may be mediated by a single T_3 vibrational state. The $3\nu_3$ singlet basis state is more strongly coupled to this T_3 vibrational state than to any other background states. Coupling of the $3\nu_3$ basis state to the other triplet states occurs primarily through this T_3 "doorway" state. This understanding is embodied in a model we called the "Gateway," or more properly "Doorway," Mediated Intersystem Crossing (DMISC) model. This chapter discusses three experiments conducted to further investigate this model.

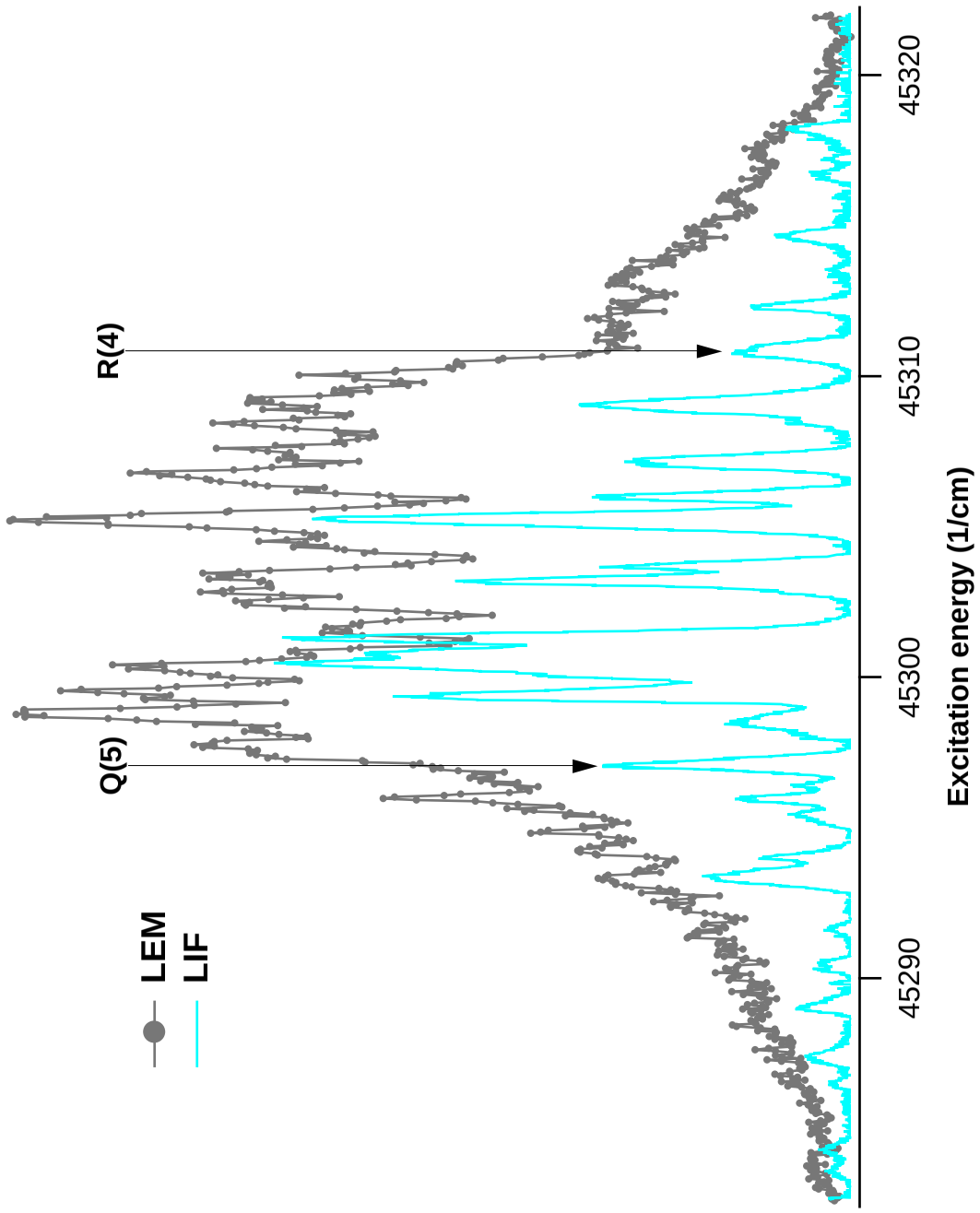

Figure 4-1: SEELEM and LIF spectra of $V_0^3K_0^1$ recorded at UCSB. The arrows mark the drops in SEELEM intensity at R(4) and Q(5).

The real Hamiltonian can be well approximated by a DMISC Hamiltonian:

$$H_{DMISC} = \begin{bmatrix} 3\nu_3 & H_{anharm} & H_{so} & 0 & 0 & 0 & 0 \\ H_{anharm} & 4\nu_b & 0 & 0 & 0 & 0 & 0 \\ H_{so} & 0 & T_3 & H_{T_3 \sim\ T_{2,1}} & \cdots & 0 & 0 \\ 0 & 0 & H_{T_3 \sim\ T_{2,1}} & T_{2,1} & ? & H_{so} & \cdots \\ 0 & 0 & \vdots & ? & \ddots & H_{so} & \cdots \\ 0 & 0 & 0 & H_{so} & H_{so} & S_0 & ? \\ 0 & 0 & 0 & \vdots & \vdots & ? & \ddots \end{bmatrix} \tag{4.1}$$

where $3\nu_3$ refers to the $3\nu_3$ basis state, T_3 refers to the T_3 doorway state, $T_{2,1}$ refers to vibrational levels of the T_2 and T_1 electronic surfaces, H_{so} are spin-orbit terms , and $H_{T_3 \sim\ T_{2,1}}$ are spin-orbit and non-Born-Oppenheimer terms. $4\nu_b$ and H_{anharm} refer to a singlet perturber and the anharmonic resonance that couples it to $3\nu_3$. The DMISC model does not bare on neither the coupling between the T_2 and T_1 states nor the coupling between the S_0 states, so these parts of the matrix left unspecified.

The initial suggestion that the ISC is mediated by a single state came from an intriguing feature of the SEELEM spectrum. The SEELEM intensity drops at two energies highlighted by arrows in Fig. 4-1. These crashes occur at the location of two transitions, Q(5) and R(4). Curiously, both transitions terminate on rotational states with J=5. Q(5) terminates on 5_{15}, and R(4) terminates on 5_{14}. If two basis states mix to form eigenstates and if both basis states are SEELEM-detectable, these two sources of SEELEM-detectability could interfere constructively and destructively. Using a simple expression for the detectivity, we showed in Humphrey, *et al.*[79] that the SEELEM intensity for a given background state, ψ_i, is

$$I_{SEELEM_i} \propto\ (S_1)^2\ \left[e^{-\left(\Delta t\ \frac{(S_1)^2}{\tau_{S_1}}\right)}\right]\ |S_1\ +\ T_3|^2 \tag{4.2}$$

$$\propto (S_1)^4\ \left[e^{-(\Delta t\ \frac{(S_1)^2}{\tau_{S_1}})}\right]\ \left[1 + [\alpha^2(1-\alpha^2)]^{-1/2}\ \left[\alpha^2 + \frac{E_i - E_{S_1}}{E_{S_1} - E_{T_3}}\right]^2\right] \tag{4.3}$$

where one basis states is S_1) and the other is T_3. $(S_1)^2$ is the fractional $3\nu_3$ character, $(T_3)^2$ is the fractional T_3 character, Δt is the flight time, τ_{S_1} is the lifetime of a pure $3\nu_3$ state, α is the mixing angle between the S_1 and T_3 basis states, E_{S_1} is the energy of the $3\nu_3$ basis state, E_{T_3} is the energy of the T_3 doorway basis state, and E_i is the energy of the background state, ψ_i. The last term shows the interference between the $3\nu_3$ basis state and the T_3 doorway basis state. When the T_3 doorway basis state tunes through the $3\nu_3$ basis state as a function of J, the sign of the denominator of the last term changes sign, which could create a significant change in the SEELEM intensity. The spectrum indicates that such a crossing takes place just before or just after J=5 in both parities and results in destructive interference of the detectivity term at higher J, decreasing the SEELEM intensity at Q(5) and R(4). The crash in SEELEM intensity as a function of J is consistent with a perturbation of $3\nu_3$ by a single vibrational state.

This doorway state is assigned to T_3 electronic state for several reasons. First, the T_3 state is SEELEM-detectable on Au. The workfunction for Au is 5.1 eV[106]. As discussed in Chapter 2, to eject an electron from a Au surface, a metastable molecule must have more than 5.1 eV of electronic energy. Neither T_2 nor T_1 have sufficient electronic energy to eject an electron from Au. T_3 provides the interfering SEELEM-detectability.

Second, the density of T_3 states is so low, about 0.05 per cm^{-1}[138], that one would not expect to see many interference effects in the spectrum. If states from the T_2 or T_1 manifolds could interfere in the SEELEM spectrum, many more interference effects should be evident because these states have a high density of states ($>$ 1 per cm^{-1}).[43]

Third, *ab initio* calculations predict the T_3 and the S_1 potential surfaces intersect near $3\nu_3$. This could lead to much larger coupling between S_1 and T_3 than between S_1 and the other triplets. The minimum of the seam of intersection of this crossing in the *trans* geometry is calculated to lie 100 cm^{-1} above the $3\nu_3$ state.[38, 37] While the uncertainty of these calculations is much larger than this energy difference[180], an intersection of the potential surfaces certainly occurs near $3\nu_3$. Vibrational states

at the energy of an intersection of potential surfaces can have large overlaps because they will have classical turning points at almost the same geometry, the geometry of the intersection. The vibrational overlap part of any interaction between these states will be much larger near the energy of the intersection than it would be below or far above the intersection. If the T_3 and S_1 states do cross just below $3\nu_3$, it could explain why the coupling between $3\nu_3$ and this T_3 doorway state is so strong. Further, it could explain why singlet-triplet coupling increases as a function of ν_3, as reported by Dupré, *et al.* [48], Ochi and Tsuchiya [138] and Drucker, *et al.* [45].

Finally, the T_3 state may be strongly coupled to the background triplet states. For a state to act as a doorway, it must be strongly coupled to the other background states in addition to being strongly coupled to the bright $3\nu_3$ state. The T_3 basis state can couple to the high density of T_2 and T_1 background states through spin-orbit and non-Born-Oppenheimer interactions. Some of these interactions can be thought of as Renner-Teller interactions because T_3 and T_2 are degenerate at linear geometry. A given T_2 vibrational state cannot be as strongly coupled as a T_3 vibrational state to the other triplet states. A T_2 vibrational state cannot couple to other T_2 vibrational states directly because of orthogonality. And T_2 states do not have large vibrational overlap with T_1 levels because the two potential surfaces are similar but offset. The T_3 potential surface is very different than those of T_2 and T_1. The T_3 character of the doorway state provides it with large coupling to both $3\nu_3$ and to the background states. The T_3 state "gregarious."

This model has implications about the appearance of the absorption spectrum, which will change as a function of resolution in ways that reveal the order of the various couplings. At low resolution, each rotational line would be a single peak in the spectrum. As the resolution was improved, the rotational lines would split into a main line and a line for each of the major perturbers. For the low J R-branch lines in $3\nu_3$, there are two perturbers, the T_3 doorway state and a singlet perturber assigned by Crim, *et al.* to $4\nu_b$.[194] The rotational transition would split into 3 lines, each of which would receive a fraction of the $3\nu_3$ basis state character. The phenomenon of the mixing of a basis state which carries oscillator strength from the ground state

(the "bright" state) into near-degenerate background states (the "dark" states) is called fractionation. The fractionation of a bright state results in a set of eigenstates possessing some fraction of bright basis state character. It is through these mixed states that a molecule in the singlet "system" can cross over into the triplet "system" and achieve Intersystem Crossing. Ochi and Tsuchiya,[138] and Scherer, Field, *et al.*[161], among others, have reported LIF spectra of this resolution. We will analyze a LIF spectrum of this resolution below.

A digression about the singlet perturber $4\nu_b$: $4\nu_b$ is a vibrational level in the $\tilde{A}$-state that has four quanta ν_b, a combination of ν_4, torsion, and ν_6, asymmetric in-plane bend. ν_4 and ν_6 have nearly identical harmonic frequencies, so they are profoundly mixed by anharmonic resonances .[194] Because of this mixing, the states are referred to as ν_b. $4\nu_b$ is associated with the five states that are comprised of the (ν_4, ν_6) basis states (0,4), (1,3), (2,2), (3,1), and (4,0). The three eigenstates comprised of (0,4), (2,2), and (4,0) have the correct vibrational symmetry to interact via anharmonic coupling with $3\nu_3$. One of these eigenstates is responsible for the "extra" lines.

If the resolution were improved further, the spectrum would reveal that each of the three lines splits into clumps of lines. In other words, the three lines would be fractionated by the high density of background T_2 and T_1 vibrational states. This fractionation would be dependent on the amount of T_3 doorway character in each of the three lines, because T_3 carries the coupling to the triplet background states. Drabbels, *et al.* reported a high-resolution spectrum (18 MHz) which reveals three clumps of lines for each rotational transition.[43] The density of lines in Drabbels' spectrum was comparable to the density of background triplets, indicating that this spectrum shows the fractionation of the $3\nu_3$ character into the triplet states. Drabbels, *et al.* analyzed their spectrum with a Hamiltonian that included many more states than we will use here but no special doorway state.

An experiment with a higher signal-to-noise ratio, and perhaps better resolution, would reveal the fractionation of the $3\nu_3$ bright character into the background vibrational states from the ground S_0 vibrational surface. Some of these states

have been observed in Zeeman Anti-Crossing experiments by Dupré, Green, and co-workers.[48, 50, 51, 49]

All of the previous work on the $\tilde{A}$-state has shown that the mixing of $\tilde{A}$-state vibrational levels to the background triplets increases with increasing quanta in ν_3.[181, 48, 50, 51, 49, 137, 138, 45] Dupré, Green, and co-workers showed that the increase in mixing far outpaces the growth in background density of states.[48] In a Fermi's Golden Rule sense, if the mixing is outpacing the density of states, the intrinsic coupling must be increasing. Dupré, *et al.* suggested that this increase in coupling was due to increased coupling between S_1 and either T_3 (because of the intersection of the potential surfaces) or T_2 (because of the linear *cis-trans* isomerization barrier which is near $3\nu_3$ in energy). Dupré, *et al.* preferred the later explanation because the T_3 density of states is so low. But either way, $3\nu_3$ mixes with the background states through one manifold of triplet states.

The significance of this work is to provide more evidence that the intersystem crossing of $3\nu_3$ is mediated by a doorway state. Dispersed fluorescence spectra of the perturbers that appear in the LIF fluorescence spectra of $3\nu_3$ show definitively that one perturber is triplet and the other is singlet. A simple Hamiltonian fit to the energies of the lines that appear in the LIF spectrum provides measures of the off-diagonal matrix elements between $3\nu_3$ and the perturbers. The SEELEM spectrum shows that the long-lived, highly energetic states are clearly influenced by the doorway state.

4.2 Experimental results

We have performed three types of experiments to investigate the perturbations to $3\nu_3$, Dispersed Fluorescence (DF) spectroscopy, Laser-Induced Fluorescence (LIF) spectroscopy, and Surface Ejection of Electrons by Laser Excited Metastable (SEELEM) spectroscopy. Most of these experiments have been discussed in Chapter 2, but a few details should be mentioned. The data that resulted from the experiments is presented.

As shown in the LIF spectrum in Fig. 4-2, two states clearly perturb the singlet state. The figure identifies three sets of peaks for each rotational transition. For the purposes of this paper, the basis states shall be referred to as the $3\nu_3$, $4\nu_b$, and T_3 doorway states. The eigenstates they form shall be referred to as the main, extra, and triplet states. In reality, these are not eigenstates, but intermediate basis states. Additional triplet and S_0 background states perturb these intermediate basis states and form the eigenstates of the real Hamiltonian.

The dispersed fluorescence experiment has been described in detail elsewhere.[136] Briefly, an excitation laser (excimer pumped Lambda Physik FL2002) is tuned to a rotational line in the $V_0^3K_0^1$ transition in acetylene($\tilde{A}\ ^1A_u$). The lines investigated are shown by arrows in Fig. 4-2. The laser radiation is directed though a cell containing 200 mTorr of acetylene. The fluorescence is imaged into a 0.75 m monochromator (SPEX 1700), which disperses the fluorescence across an ICCD (Princeton Instruments 576LDG/RB). The DF spectrum is frequency calibrated using the emission spectra from Hg, Fe, and Ne.

The DF spectra from the R(1) main and extra lines are shown in Fig. 4-3. Most remarkably, the extra lines have a distinctly different DF spectrum than that of the main lines. The DF spectra of the triplet lines show the same features as the DF spectrum of the main line emission. This shows that the triplet line receives its fluorescing character from the $3\nu_3$ basis state and not from the $4\nu_b$ basis state. It also shows that it provides no fluorescing character of its own. These perturbers cannot be singlet states.

The LIF spectra shown in Fig. 4-2 was recorded as described in Chapter 2. The frequency of an excitation laser (Nd:YAG pumped Lambda Physik 3002) was tuned through the $V_0^3K_0^1$ band. The laser radiation is directed into a vacuum chamber and through a free jet expansion of acetylene. The total fluorescence was collected at right angles to both the laser and free jet by a 5 cm diameter S1-UV lens onto a PMT. The large aperture collection optics allowed for detection of fluorescence as much as 18 μs after the laser fired. The PMT signal was fed into a boxcar integrator. The boxcar output was acquired each shot without averaging. A reading was acquired from a

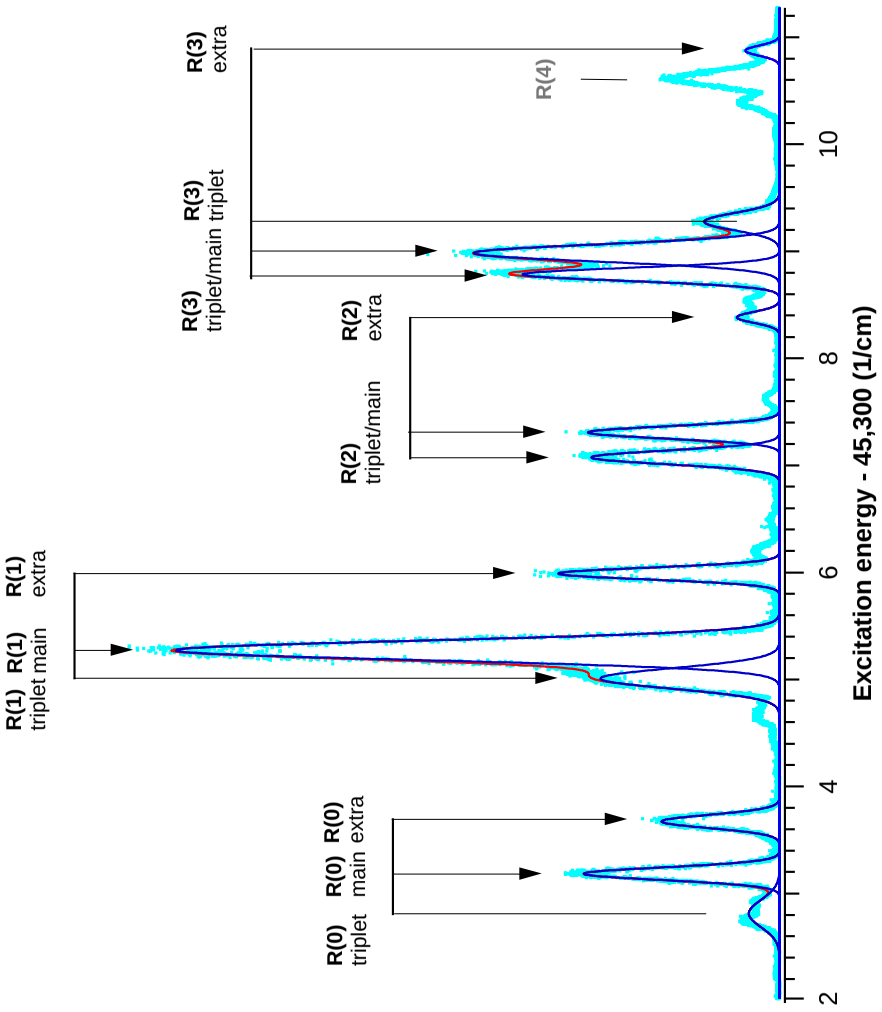

Figure 4-2: LIF spectrum of the R-branch of $V_0^3K_0^1$ with an experimental resolution of 0.12 cm^{-1}. The Gaussian fits to the transitions are shown along with the assignment of each transition.

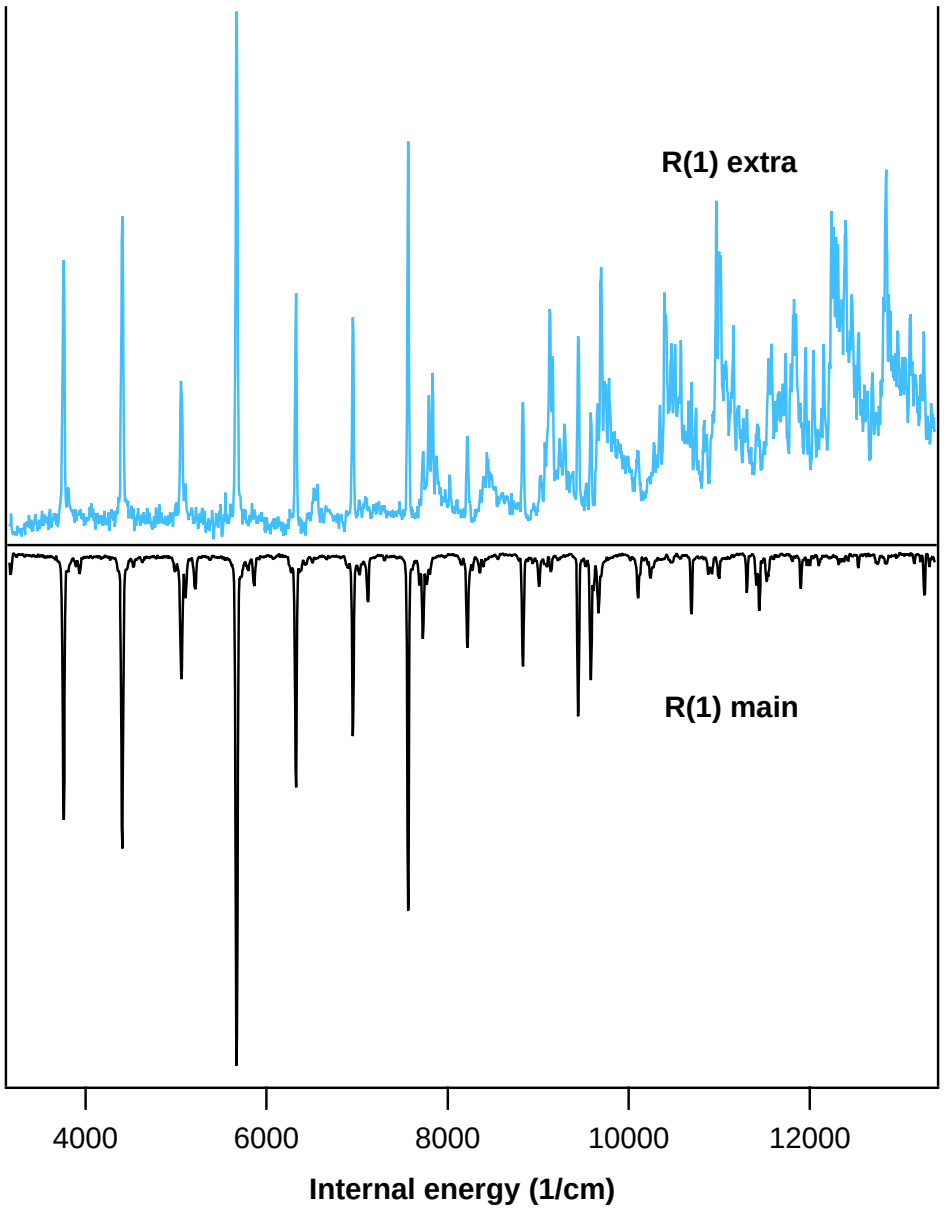

Figure 4-3: Dispersed fluorescence (DF) spectra of the main and extra lines of R(1). The DF spectrum of the triplet line of R(1) is the same as that of the main line.

powermeter each shot for power normalization.

While an absorption spectrum directly reflects the $3\nu 3$ character in the eigenstates, the LIF spectrum may not because not all of the fluorescence is collected. We performed the experiments under conditions that minimize the effects of several factors that could alter the LIF intensities of the lines. As mentioned, fluorescence could be detected many microseconds after the laser fired. This allowed us to use a boxcar gate of 12 μs and acquire as much of the exponential decay of the eigenstates as possible. The states excited in this study have lifetimes $< 7\mu$s. (see Chapter 6 and ref.[138]) With a 12 microsecond gate, more than 82 percent of the LIF intensity of a state with a 7 microsecond lifetime is collected. Also, the laser radiation enters and exits through a set of baffles[184] that effectively eliminates the contribution from scattered light. This allowed the boxcar to sample the fluorescence decay form the beginning.

The fluorescence was not wavelength filtered because the main line and the extra line have different emission frequencies.[161] The $4\nu_b$ basis state emits to S_0 vibrational states with greater internal energy than does the $3\nu_3$ state. So the emission from the $4\nu_b$ character of an eigenstate, which centers on 33,000 cm^{-1}, is red-shifted relative to that of the emission from the $3\nu_3$ character, which centers on 40,000 cm^{-1}. This can be seen in the DF spectra shown in Fig 4-3. Use of a filter would alter the true LIF intensity. The PMT photocathode quantum yield also affects the relative intensities of the main and extra lines because it is more efficient for the higher frequency main line emission. The extra lines should be $\sim$15 percent more intense than they appear.[152]
.

The LIF spectrum shows that the singlet state is perturbed by several other states. An example is the fractionation of the R(2) line in $3\nu_3$ shown in Fig. 4-4. The doublet is composed of the eigenstates formed from $3\nu_3$ and the T_3 doorway state which are nearly degenerate at $J' = 3$. The small peak at higher energy is a singlet perturber that has been investigated in the past.[161, 194] This is the "extra" line. The weak line between them is an unassigned triplet perturber.

The SEELEM spectrum was recorded in the same vacuum chamber as was the

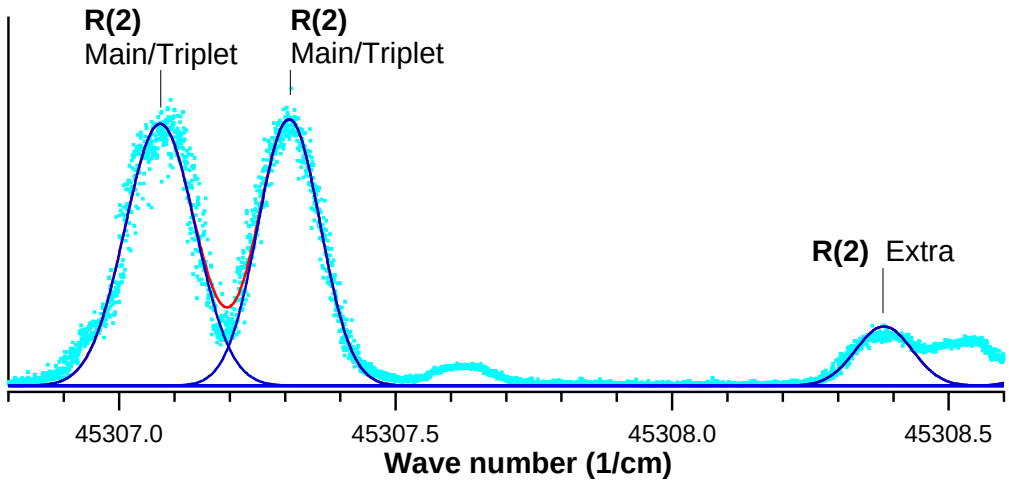

Figure 4-4: LIF spectrum of R(2) of $V_0^3K_0^1$. The Gaussian fits to the transition are shown.

LIF spectrum. These spectra are shown in Fig. 4-8. The detection surface was Cs. The resolution of this data is 0.08 cm^{-1}, compared to the 0.2 cm^{-1} resolution of the UCSB data. The resolution is improved because the dye laser at MIT was equipped with an intracavity etalon.

4.3 Discussion

Several conclusions can be drawn from the data. The DF experiments distinguish between singlet and triplet perturbers. The LIF spectrum provides the information needed to determine the magnitude of the coupling between the perturbers and $3\nu_3$. The SEELEM spectrum demonstrates that the T_3 doorway state determines frequencies at which long-lived highly energetic species are created.

4.3.1 Dispersed Fluorescence

DF spectra can distinguish between singlet and triplet perturbers. The dispersed fluorescence spectrum of the pure $3\nu_3$ state is well known. Molecules in this state emit to a progression of *trans*-bending vibrational states on the ground electronic surface. The intensity of each transition is governed by the Franck-Condon overlap between the

excited state vibrational wavefunction and the final vibrational wavefunction on the ground electronic surface. As a result, the intensity patterns in the DF spectrum are sensitive to the shape of the excited state vibrational wavefunction. If the perturbing state is singlet, the DF spectrum will be different than the unperturbed spectrum in a way that may identify the vibrational nature of the perturber. If a perturbing state is a triplet, the DF spectrum will have the same features as the DF spectrum of a pure singlet state because emission from the triplet states to the ground state is spin-forbidden.

The DF spectra clearly identify the perturber that is responsible for the extra line as $4\nu_b$, as suggested by Crim and co-workers.[194] There are two possible singlet vibrational states in this energy region with the correct symmetry. $4\nu_b$ is one. The other is ν_1, which has a frequency of ~ 3040 cm^{-1}[34]. The DF spectrum from ν_1 will consist of a similar pattern of peaks as would a DF spectrum from the vibrationless level of the $\tilde{A}$-state shifted up in energy by the ν_1 vibrational frequency in the ground state, ~ 3300 cm^{-1}. In other words, the DF spectrum of ν_1 will be a *trans*-bending progression built on 1 quantum of symmetric CH stretch. The $4\nu_b$ vibrational state is a mixture of *cis*-bending and torsional motion. The DF spectrum from $4\nu_b$ will show transitions to vibrational levels with large amounts of *cis*-bending character. The DF spectra of the extra lines do indeed show progressions to states with *cis*-bending character, which identifies the perturber at $4\nu_b$. The dispersed fluorescence spectrum of the triplet lines is the same as the DF spectra from the main lines. We can directly conclude that a triplet state is responsible for these perturbations.

4.3.2 Laser-Induced Fluorescence

The certainty about the triplet nature of the perturbers suggests that the triplet perturbers found in consecutive rotational lines in the LIF spectrum may be assignable to a single vibrational state. We assign one line in each rotational level to rotational levels of a single triplet vibrational state. We fit a model Hamiltonian to the data to measure the magnitudes of the couplings between the $3\nu_3$ basis state and the perturbing states. This model incorporates only a portion of the Hamiltonian in

equation 4.1. Although this simple model leaves out most of the real Hamiltonian, the model will provide a measure of the largest couplings that initiate Intersystem Crossing of $3\nu_3$. The fit will be evaluated for its ability to predict the intensities and degree of fractionation. The spin-orbit term between the $3\nu_3$ and T_3 doorway states is large. This result will be discussed.

The Fit

The data was fit to a model Hamiltonian is represented by a 3×3 matrix:

$$H = \begin{bmatrix} 3\nu_3 & H_{anharm} & H_{so} \\ H_{anharm} & 4\nu_b & 0 \\ H_{so} & 0 & T_3 \end{bmatrix} \tag{4.4}$$

The bright $3\nu_3$ state, the $4\nu_b$ perturber, and the T_3 doorway perturber are the three states that form the basis. The on-diagonal elements have the form

$$E_0 + B' \cdot J'(J'+1) - B(S_0) \cdot J'(J'-1) \tag{4.5}$$

The E_0 and B' terms were allowed to vary while the $B(S_0)$ term was held fixed at the value found by Palmer, *et al.* 1.176608 cm^{-1} .[147, 205]. H_{so} represents a spin-orbit term between the $3\nu_3$ state and the T_3 doorway perturber. H_{anharm} represents an anharmonic term between the $3\nu_3$ basis state and the $4\nu_b$ perturber. This rotational effective Hamiltonian matrix is for a prolate top where the $(A-B)\cdot K^2$ term is included in E_0. Of course, the "eigenstates" of this Hamiltonian are not eigenstates of the true Hamiltonian. These "eigenstates" form a new, intermediate basis. The eigenstates of the real Hamiltonian are formed when other, near-degenerate background states mix with these basis states.

The main, extra, and triplet lines that appear in Fig. 4-2 are partially fractionated by the background states, so the energies of these line cannot simply be read off the spectrum. To arrive at an estimate of the energies of the intermediate basis states, we fit each rotational transition to 3 Gaussians, one for the main line and one for

each perturber. While the 3 lines of each rotational transition are actually composed of several eigenstates, we view each line as a broadened "eigenstate." A Gaussian fit to a set of peaks corresponding to one of the three states provides a good estimate of the relative energy and intensity of each state in the absence of fractionation. The width of the Gaussians is related to the fractionation strength. Fig. 4-2. shows the fits, and Fig. 4-4. shows an expanded view of the fits to the R(2) lines.

Some of the relative energies and widths were held fixed in the Gaussian fit. The energy of the R(2) extra line is held fixed at the energy measured by Drabbels, *et al.*[43]. Similarly the R(3) extra line was held at the energy measured by Scherer, *et al.*[161]. The widths of both lines are also fixed at 0.12 cm^{-1}, the width resulting from the doppler broadening convolved with the laser linewidth. Only the intensity of each line was allowed to vary. The widths and energies of these two lines had to be held fixed because these lines are overlapped with other lines in the spectrum.

The main R(3) line is split by an unassigned triplet perturber that is not accounted for in the model Hamiltonian. Two Gaussians were fit to the main line. The area-weighted mean energy of the two Gaussians was used for the energy of R(3). The sum of the areas of the two Gaussians was used for the R(3) intensity.

The evolution of perturbations with J are clear in the reduced term value graph shown in Fig. 4-5. A reduced term value is equal to the state energy (not the transition energies) as determined in the Gaussian fit minus the rotational energy. These values are plotted against J(J+1). Usually the rotational energies will be unknown, but this is no problem. One chooses a value near the apparent real value, B_{guess}. B_{guess}· J(J+1) is subtracted from the state energies to arrive at the reduced term values.

$$\begin{aligned} reduced\ term\ value &= E_0 + B_{correct} \cdot J(J+1) - B_{guess} \cdot J(J+1) \\ &= E_0 + (B_{correct} - B_{guess}) \cdot J(J+1) \end{aligned} \tag{4.6}$$

E_0 is the vibrational and electronic energy, which is not dependent on rotational quantum number. When plotted against J(J+1), the reduced term values will lie

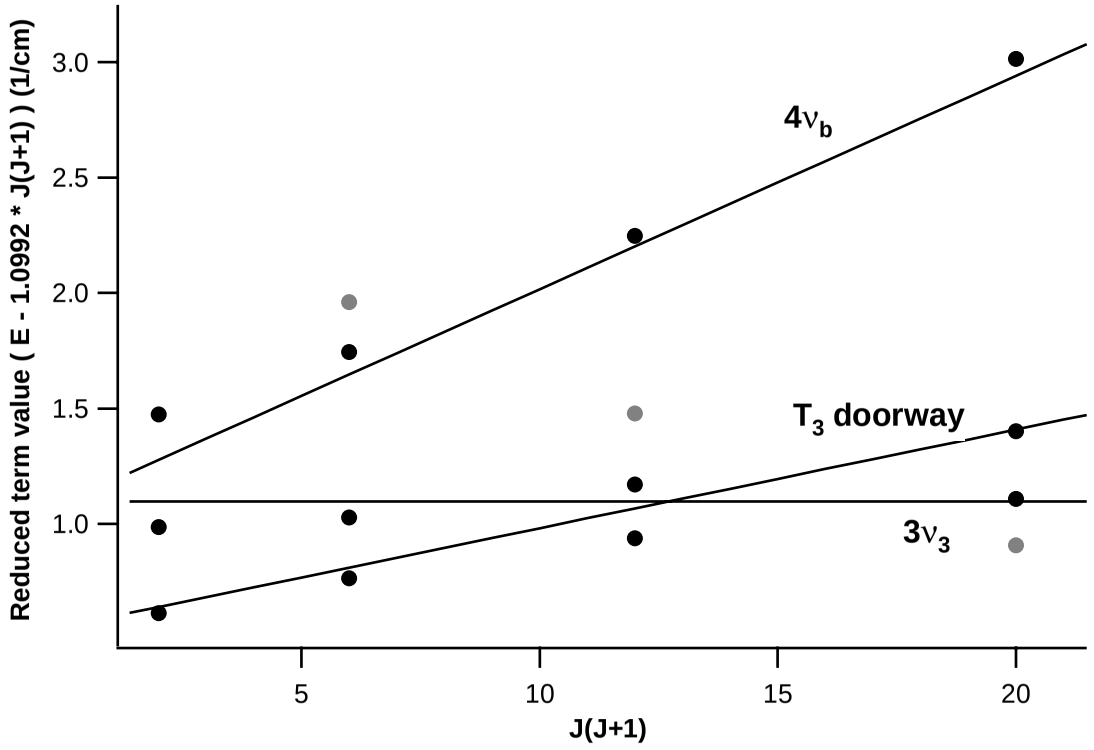

Figure 4-5: The reduced term values for the Gaussians as a function of $J(J+1)$. The lines represent the positions of the $3\nu_3$, $4\nu_b$, and T_3 doorway basis states calculated using the parameters from the Hamiltonian fit. The reduced term values of the unassigned triplet perturbers are shown in gray.

along a line with a slope of $(B_{correct} - B_{guess})$ and an intercept of E_0. Obviously, if one chooses the correct B value, the slope will be zero. Several things will cause the reduced term values to lie along a curve instead of a line, including centrifugal distortion and perturbations. As one can see in Fig. 4-5, the reduced term values of the three lines do not fall on straight lines due to interactions among them. Several other perturbers are also shown because it appears that they may be assignable to a single triplet vibrational state. We refer to them as "unassigned" perturbers.

The parameters in the Hamiltonian were fit to the energies of the Gaussians and reasonable results were obtained. The calculated energies are within 0.03 cm^{-1} of the observed energies except for the R(3) extra line, for which the calculated energy was 0.05 cm^{-1} too low. We consider this a good fit considering that the 12 "observations" are themselves approximations to the data. The random energies of the background

Table 4.1: Molecular constants from Hamiltonian fit

0.56(6)	E_{T_3}
1.09(4)	$E_{3\nu_3}$
1.10(3)	$E_{4\nu_b}$
1.142(4)	B_{T_3}
1.099(2)	$B_{3\nu_3}$
1.192(2)	$B_{4\nu_b}$
0.11(1)	H(so)
0.23(2)	H(anharm)

Table 4.2: Fractional basis state character in each eigenstate

transition		$3\nu_3$	T_3	$4\nu_b$	observed energies	obs. - calc.
R(0)	triplet	0.07	0.92	0.01	45302.81	0.00
	main	0.61	0.07	0.32	45303.18	0.03
	extra	0.32	0.01	0.67	45303.67	0.03
R(1)	triplet	0.14	0.85	0.01	45305.01	0.00
	main	0.74	0.15	0.11	45305.27	-0.02
	extra	0.12	0.00	0.88	45305.99	0.01
R(2)	triplet	0.53	0.45	0.02	45307.07	-0.01
	main	0.43	0.55	0.02	45307.31	0.01
	extra	0.04	0	0.96	45308.38	0.00
R(3)	triplet	0.07	0.92	0.00	45309.28	-0.03
	main	0.91	0.08	0.01	45308.91	0.01
	extra	0.02	0	0.99	45310.89	0.05

states make it inevitable that the energies measured with the use of the Gaussians are somewhat inaccurate. In other words, this fit is good considering how much of the real Hamiltonian is absent from the model. The molecular constants that resulted from the fit are displayed in Table 4.1. The fractional $3\nu_3, 4\nu_b$, and T_3 character in each eigenstate is displayed in Table 4.2. The deperturbed reduced term values of the basis states are shown in Fig. 4-5 as lines.

Assessment of the fit

The success of the model Hamiltonian will be assessed by examining the predicted relative intensities and degree of fractionation. The fit results in a large spin-orbit

term between the $3\nu_3$ and T_3 doorway states, which will be discussed, as will the magnitude of the H_{anharm} term between the $3\nu_3$ and $4\nu_b$ states.

In principle, the intensity should be proportional to the fractional $3\nu_3$ character in the eigenstate because $3\nu_3$ carries the oscillator strength from the ground state. Transitions to the triplet perturber are spin-forbidden, of course, and transitions to the $4\nu_b$ basis state are effectively Franck-Condon forbidden. The observed and calculated relative intensities are shown in Fig. 4-6. The observed intensity of the main R(3) line is the sum of the intensities of the two Gaussians that were fit to this line. The calculated relative intensities are very close to the relative intensities in the spectrum. Also, the qualitative trends of the calculation are correct. For instance, the relative intensities of the three R(2) lines are in the correct order although the extra line is a little too weak. Also, the fraction of $4\nu_b$ character predicted for each eigenstate is very close to the $4\nu_b$ fluorescence spectrum shown in Fig. 5 of Scherer, *et al.*[161]. The LIF in the Scherer LIF spectrum was filtered with a monochromator that passed only $4\nu_b$ emission to the detector.

Another way to assess the success of the model Hamiltonian is to compare the fractional T_3 character in each intermediate basis state to the fractionation of that state. T_3 doorway state character couples the intermediate basis states to the background triplet states, so the fractionation should be related to fractional T_3 character. The widths of the Gaussians should be proportional to a convolution of the experimental resolution with the width of the fractionation due to background states. A convolution of two Gaussians of widths w_1 and w_2 will result in a single Gaussian of width $\sqrt{(w_1^2 + w_2^2)}$. To the extent that the fractionation and experimental bandwidth are Gaussian, the widths of the LIF peaks can be approximated as

$$\begin{aligned} w_{peak} &\approx \sqrt{(w_{experiment}^2 + w_{fractionation}^2)} \\ &\approx \sqrt{((0.12\ cm^{-1})^2 + w_{fractionation}^2)} \end{aligned} \tag{4.7}$$

The $w_{fractionation}$ can be approximated with an expression derived by Bixon and

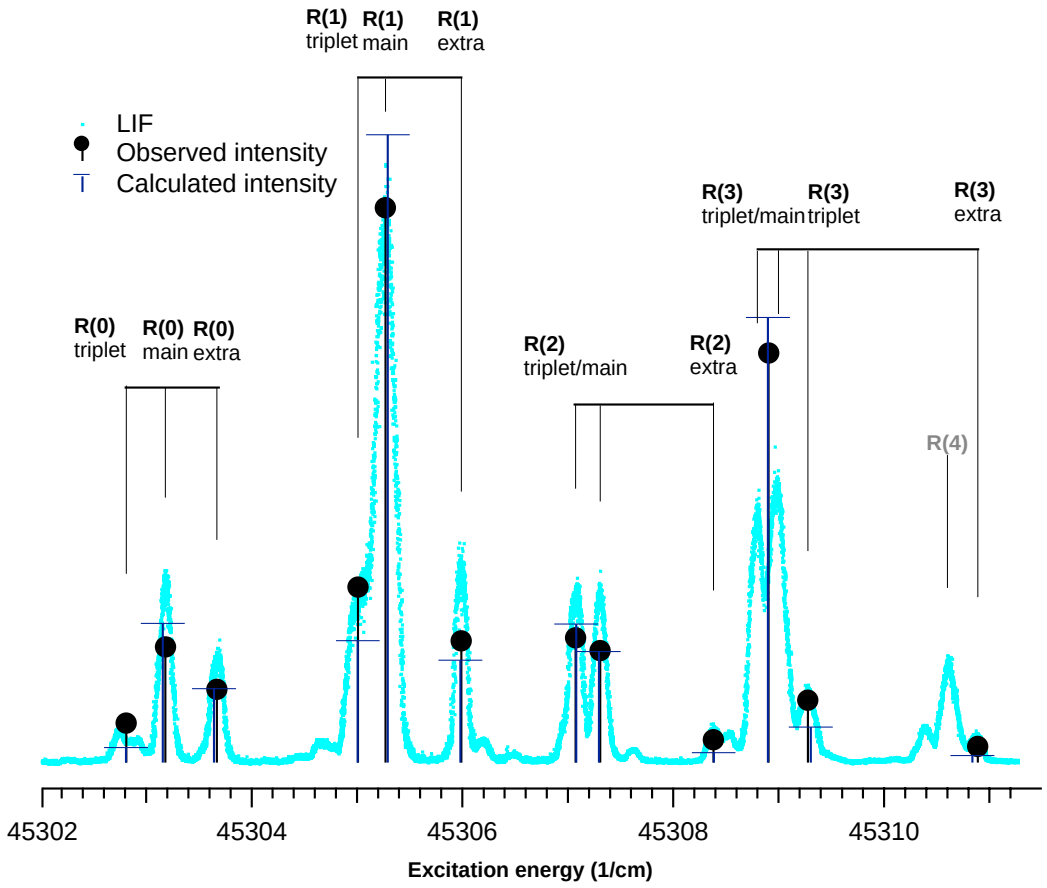

Figure 4-6: The observed intensity (areas of the fit Gaussians) and the intensity predicted from the fractional $3\nu_3$ character. The intensities have been adjusted for the overall intensity of the rotational transition.

Jortner[18]. They arrived at analytical expressions for the $w_{fractionation}$ of a very simple case: a single bright state coupled to a manifold of evenly spaced dark states. All the matrix elements between the bright state and the dark states are the same. There are no interactions among the dark states. These restrictions simplify the problem so that analytical expressions for the fraction of bright state character in each eigenstate can be derived. The fractional bright state character mixed into the dark states has a Lorentzian distribution centered on the energy of the bright state. Bixon and Jortner showed that the FWHM of this Lorentzian is $\pi \cdot (H_{T_3 \sim\ T_{2,1}})^2 \cdot \rho_{T_{2,1}}$. $H_{T_3 \sim\ T_{2,1}}$ is equal to $(\mathrm{T_3})^2\ \cdot\ <\ pure\ T_3\ |H|\ T_{2,1}\ >$, which represents the spin-orbit and non-Born-Oppenheimer terms between these states. $\rho_{T_{2,1}}$ represents the local density of $\mathrm{T_2}$ and $\mathrm{T_1}$ states. So, the fractionation of the intermediate basis state is expected to be proportional to the fractional $\mathrm{T_3}$ character, or

$$w_{fractionation} \sim\ \pi \cdot (T_3)^2 \cdot |< pure\ T_3 | H | T_{2,1} >|^2 \cdot \rho_{T_{2,1}} \tag{4.8}$$

The Hamiltonian model predicts the fractional $\mathrm{T_3}$ character in each intermediate basis state. If we knew the local density of background states and the couplings between $\mathrm{T_3}$ and the triplet background states, we could directly compare the predictions of the model and the LIF spectrum. Because the couplings and density have not been measured, Fig. 4-7 displays the fractional $\mathrm{T_3}$ character in each intermediate basis stated multiplied by 0.3 $\mathrm{cm^{-1}}$. This is equivalent to assuming that

$$\pi \cdot |< pure\ T_3 | H | T_{2,1} >|^2 \cdot \rho_{T_{2,1}} = 0.3\ cm^{-1} \tag{4.9}$$

Assuming $\rho_{T_{2,1}}$ equals 8.6 per $\mathrm{cm^{-1}}$ as calculated by Drabbels, *et al.*[43], this is equivalent to a $|< pure\ T_3\ |H|\ T_{2,1} >|$ of 0.1 $\mathrm{cm^{-1}}$. This should not be mistaken for a measurement. This coupling strength is only a value that makes the widths reasonably consistent with the $\mathrm{T_3}$ character in the eigenstates of the model Hamiltonian. The true average coupling between the $\mathrm{T_3}$ basis state and the background triplets could be very different and most likely vary considerably from rotational level to rotational level. Dupré, *et al.* proposed that the couplings between the triplets are larger than

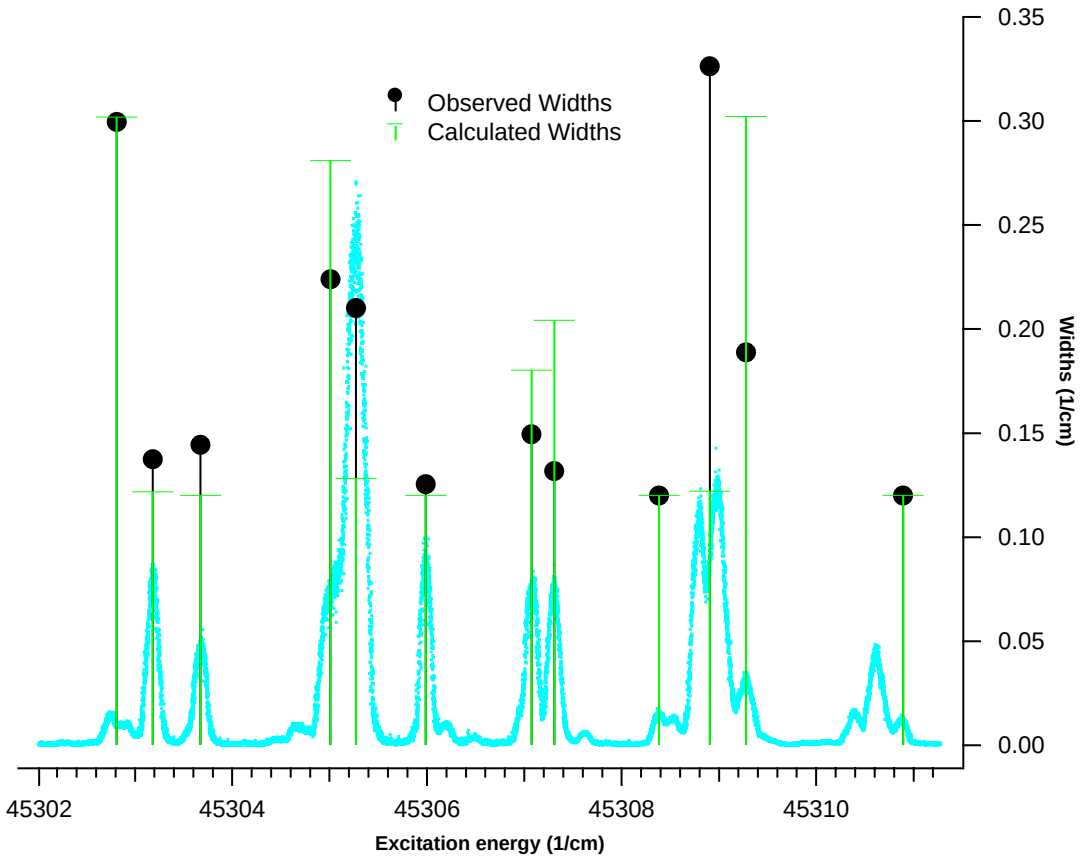

Figure 4-7: The observed widths of the fit Gaussians and the widths calculated as a function of fractional T_3 doorway state character.

coupling between S_1 states and the triplets. The value used here is approximately the same as the $S_1 \sim T_3$ coupling resulting from the fit.

The correlation between the T_3 doorway character and the width of the LIF features is not as strong as were $3\nu_3$ character and intensity, but broader states generally have more T_3 doorway character. The R(0) triplet line is broader than the other R(0) lines. The two R(2) main/triplet mixed lines have similar widths. The main R(3) line much broader than predicted by the calculation, but that is due to the effects of the unassigned perturber. The success of this comparison is susceptible to a breakdown of the Bixon-Jortner conditions: variations of the energies of the triplet background states and of the coupling strength between the states.

Our fit results in a small anharmonic resonance interaction of 0.23(2) cm^{-1} between the $3\nu_3$ state and the $4\nu_b$ state. It is the strength of a term exchanging 7

quanta of vibration, 3 quanta of *trans*-bend are exchanged for 4 quanta of ν_b. This anharmonic term is a septic term with a form of $Q_{\nu_3}^3 \cdot Q_{\nu_b}^4$, which is likely to be small.

The fit also results in a spin-orbit matrix element between $3\nu_3$ and T_3 of 0.11(1) cm^{-1}, which is large for a hydrocarbon. The molecular spin-orbit interaction can be thought of as the product of an electronic factor and a vibrational overlap factor. The electronic factor of the spin-orbit interaction between the S_1 and T_3 states where these potential surfaces intersect in C_{2h} symmetry has been calculated by *ab initio* methods to be 13.9 cm^{-1}.[38, 37] To generate a coupling of ~ 0.1 cm^{-1}, the vibrational overlap factor would need to be ~ 0.01 at this geometry. This is large for a molecule with six vibrational modes, but there is reason to believe this is the correct for $3\nu_3$. The geometry of the minimum of the seam of intersection restricted to C_{2h} symmetry is calculated to be similar to the *trans* S_1 equilibrium geometry. The CC bond distances are identical, and the CH bond distance at the intersection is calculated to be 0.019 Å smaller than the S_1 equilibrium CH bond distance. The CCH angle for the seam of intersection is 139.8° compared with 122.48° for the equilibrium geometry for the *trans* S_1 state.[78] However, the near-linear turning point of the $3\nu_3$ state has a bending angle that is very similar to the bending angle of the seam of intersection. Using the force constant for ν_3 derived in Scherer, *et al.*[161] and a vibrational frequency of 1047 cm^{-1}, the $3\nu_3$ vibrational wavefunction can be calculated. The maximum in the probability density at the near-linear turning point in this vibrational wavefunction is at 146.6°. In addition, the *trans* geometry of the minimum of the seam of intersection is calculated to lie only 100 cm^{-1} below $3\nu_3$.[38, 37] Although this energy difference is much smaller than the error in the calculations, this does demonstrate that the intersection of S_1 and T_3 is nearby in energy and at a similar geometry to $3\nu_3$, so it is reasonable that the vibrational overlap is large.

Three other singlet-triplet couplings of this magnitude in $3\nu_3$ have been observed. The splitting of the R(3) line shown in Fig. 4-2 is not due to the T_3 doorway state but the unassigned perturber. Since the splitting is ~ 0.2 cm^{-1}, the coupling between the $3\nu_3$ state and the additional perturber could be as large as ~ 0.1 cm^{-1}. This is because two degenerate basis states form eigenstates split in energy by two times the

coupling matrix element. This coupling is comparable to the coupling between the T_3 doorway perturber and $3\nu_3$.

Drabbels, *et al.* measured similar couplings for the LIF-detectable eigenstates that underlie the features we analyze here.[43] They used a Hamiltonian with off-diagonal elements between the $3\nu_3$ basis state and each background state. There were no elements between any of the background states. The values they obtained are equivalent to coupling of the $3\nu_3$ state to the $T_{2,1}$ through the T_3 doorway state. Accordingly, the couplings they obtain should be, and are, similar to what we obtain here.

Dupré and Green measured a coupling between the K=0 component of $3\nu_3$ and a triplet that has the same magnitude as the one we measure here.[50] They recorded LIF spectra of the P(1) line of the $V_1^3K_1^0$ band in the presence of a series of magnetic fields. A perturber passes through the P(1) line with a magnetic field strength at the crossing of 7.16(4) Tesla. Dupré and Green analyzed this avoided crossing in terms of a single triplet basis state crossing through the singlet state, which resulted in an interaction term of 3.3(4) GHz (0.11(1) cm^{-1}) and a g-value for the triplet perturber of 1.7(6). The g-value indicates that the perturbing state is a nearly pure $M_s = \pm 1$ triplet state, which is unmixed with other triplet or singlet basis states.

All of these observations may be assignable to the various spin and K-components of a single T_3 vibrational state. There are a number of good sources on the matrix elements and selection rules of the spin-orbit interaction.[199, 201, 183, 91] Using a form of the spin-orbit operator in equation 2.4.4 in Lefebvre-Brion and Field[103], the selection rules for this interaction are $\Delta J = 0$, $\Delta P = 0$, $\Delta K = +/-1, 0$, $\Delta K = -\Delta S$, where K has replaced Λ and P has replaced Ω in equation 2.4.5. Accordingly, several triplet rotational levels can interact with each singlet $3\nu_3$ rotational level. This might account of all of these strongly coupled triplet states. Alternatively, these observations may be caused by a sparse manifold of T_3 states.

4.3.3 SEELEM

The original SEELEM spectrum suggested that the doorway state crosses through the $3\nu_3$ state before $J' = 5$. The T_3 perturber included in the model Hamiltonian crosses at $J' = 3$ and the unassigned triplet perturber crosses at $J' = 4$. The interference effects in the SEELEM spectrum could switch from constructive to destructive at these crossings. The crashes in the UCSB SEELEM spectrum at $J' = 4$ are not apparent in the MIT SEELEM data, shown in Fig. 4-8, because the free jet used for this experiment has a lower rotational temperature ($\sim$ 10K) than the earlier work ($\sim$ 40K). At a rotational temperature of 10 K, there is little population in the initial states at $J'' > 4$.

One of the assertions of the DMISC Model is that the T_3 doorway state mediates the coupling of the bright $3\nu_3$ state to long-lived, highly energetic triplet background states. These are the states that appear in the SEELEM spectrum. As shown in Chapter 6 , these states have lifetimes as long as 280 μs and have partial electronic character with $\sim$5 eV of electronic energy. Fig. 4-8 shows that the SEELEM spectrum of each rotational transition is skewed to the side of the T_3 doorway perturber. R(0) and R(1) are skewed to lower energy, while R(3) is skewed to higher energy. At the crossing point, R(2), the SEELEM signal is unskewed. This shows that the T_3 doorway state does indeed provide access to long-lived, highly energetic states.

4.4 Conclusion

One conclusion is certain; a triplet perturber strongly mixes with the singlet $3\nu_3$ state. Whether or not this state can eventually be assigned to the T_3 electronic surface, it is clearly one of the most strongly coupled background states and is representative of a handful of states which initiate the coupling of the $3\nu_3$ basis states of the S_1 surface to the highly-excited, long-lived background states.

This understanding of the singlet-triplet mixing of these states makes them fertile ground for future work. The spectra of the low-J $3\nu_3$ states provide a set of observations upon which to test statistical techniques which identify and measure doorway

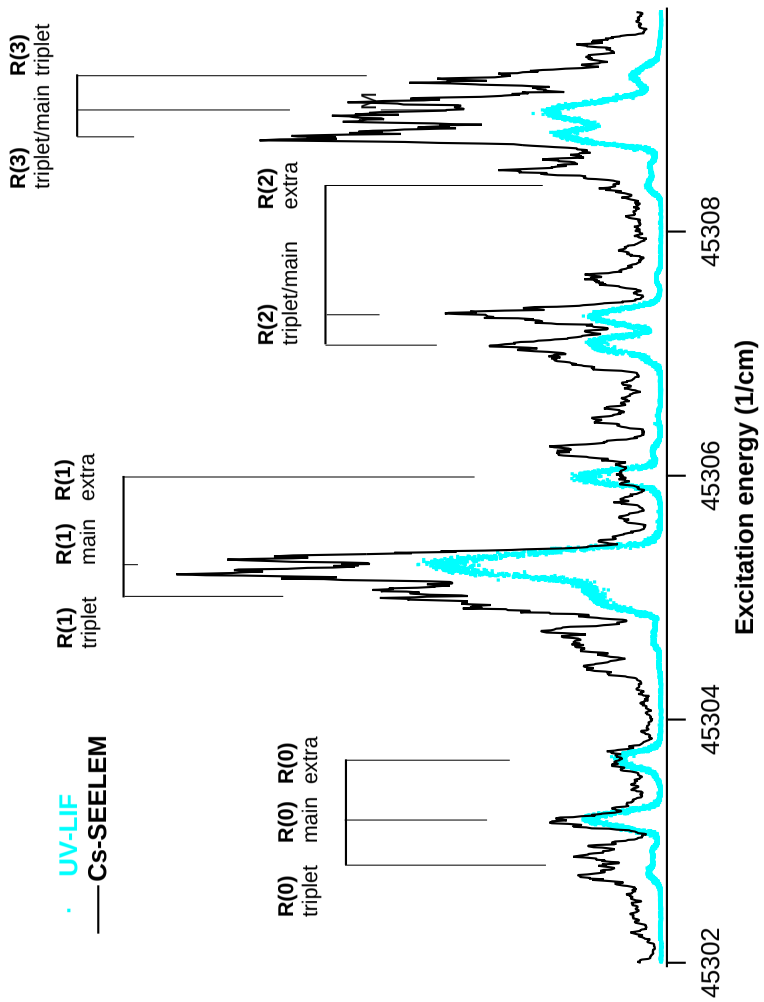

Figure 4-8: The SEELEM and LIF spectra of the R-branch of the $V_0^3K_0^1$ transition. The detection surface was Cs.

coupling. These states can serve as intermediates in experimental schemes probing other manifolds of states, such as the acetylene Rydberg states.

Chapter 5

The Effects of Electric Fields on the Doorway State

The T_3 doorway state that mediates the ISC of the $3\nu_3$ basis state into the background states also plays a central role in the response of the LIF-detectable states to an electric field. The DMISC model provides an explanation for the anomalous observations of acetylene at a field of 113,000 Volts/cm. This chapter will describe the data, survey the Stark interactions that are possible in acetylene, and discuss the role of the T_3 doorway state in the Stark response of the LIF-detectable states.

5.1 Introduction: anomalous electric field effects on acetylene

Peter Green, while a student in this research group, observed anomalous behavior of lifetimes and collisional quenching rates for LIF-detectable S_1 states in acetylene when a strong electric field (113,000 Volts / cm) was applied. The preferred interpretation of these odd results turned out to be incorrect. This behavior can now be understood as arising from the behavior of the T_3 doorway state in an electric field.

Naively, one might expect that the electric field would couple the LIF-detectable states with long-lived background states, which would dilute the S_1 character into

these dark states. This would lead to a lengthening of the lifetimes of the LIF-detectable states. The mixing of background state character into an LIF-detectable eigenstate could also lead to a larger collisional quenching cross section. This is because collisional cross sections are small for transitions that change the vibrational or electronic nature of a molecule. Enhanced background state character in the LIF-detectable eigenstates will lead to enhanced collisional cross section to the non-fluorescent background states. So, one expects that an increase in the lifetime would be accompanied by an increase in the effectiveness of collisional quenching.

Green observed this correlation for the lower vibrational states, but not for some rotational states belonging to $2\nu_3$ and $3\nu_3$, as shown here in Table 5.1 and in Green's thesis in Table 3.3 and Figs. 3.3b, 3.3c, and 3.3d.[59] Green observed states whose lifetimes decreased while the collisional cross section increased as the electric field was applied. In $2\nu_3$, Q(2), Q(4), and R(0) have this anomalous correlation. The other observed lines have the expected correlation, but the electric field induces more variation in the behavior of these states than in the rotational levels of the lower vibrational states. In some states, the collisional quenching cross section changes dramatically but the lifetime decreases only a small amount. Other states display the opposite behavior. Green observed decreases in total fluorescence yield with electric field on all of the observed lines in $2\nu_3$ and $3\nu_3$

In $3\nu_3$, all of the Q-branch lines have the anomalous correlation. This includes Q(2), Q(3), Q(5), Q(7), and the triplet perturbing line of Q(1) (mis-assigned at the time as $Q_e(2)$). Also, the total fluorescence of the Q-branch lines is reduced at high electric field, decreasing by as much as a factor of 13.5. The R-branch lines exhibit the expected correlation, although the R(1) line has a smaller collisional quenching cross section and a shorter lifetime. In fact, this is the only line in Green's data that displays this behavior. Despite this, R(1) suffers the largest electric field-induced decrease in total fluorescence of any of the four R-branch lines Green studied. The other lines are R(0), $R_e(0)$, and $R_e(1)$. Clearly, the Stark field induced perturbations become less monotonic with increasing vibrational energy. The local nature of these perturbations is characteristic of the Stark effect on these vibrational states and

Table 5.1: Effects of an electric field on selected rotational lines at 20 mTorr.

	Zero-field			**113,000 Volts/cm**			Calculated	Observed
	Radiative rate ($1/\mu$s)	Quenching rate ($1/\mu$s ·1/Torr)	Total rate at 20 mTorr	Radiative rate ($1/\mu$s)	Quenching rate ($1/\mu$s ·1/Torr)	Total rate at 20 mTorr	Q-yield ratio I_0/I_E	Q-yield ratio I_0/I_E
$3\nu_3$								
Re(1)	1.629	6.3	1.755	1.268	16.2	1.592	1.03	**3**
R(1)	0.624	19.5	1.014	1.021	12.2	1.265	0.99	5
Re(0)	1.283	10.6	1.495	0.604	42.7	1.458	2.01	1.25
R(0)	0.975	17.0	1.315	0.712	37.2	1.456	1.71	2.5
Qt(1)	0.975	15.2	1.279	1.010	21.9	1.448	1.27	13.5
Q(2)	1.213	12.0	1.453	1.340	20.2	1.744	1.36	3.25
Q(3)	0.952	15.8	1.268	0.997	23.1	1.459	1.30	12
Q(5)	1.260	36.4	1.988	1.550	42.2	2.394	1.25	4
Q(7)	0.626	19.5	1.016	0.838	24.0	1.318	1.32	12.5
$2\nu_3$								
R(7)	2.541	14.1	2.823	1.612	18.0	1.972	0.68	not measured
R(6)	1.744	17.7	2.098	1.830	10.5	2.040	0.89	not measured
R(5)	2.748	11.1	2.97	1.920	14.8	2.216	0.71	4
R(3)	1.407	19.4	1.795	1.546	15.5	1.856	0.98	4
R(2)	2.420	13.7	2.694	1.786	13.9	2.064	0.72	4
R(1)	1.675	19.0	2.055	1.478	22.7	1.932	0.98	3
R(0)	2.837	13.3	3.103	2.871	26.0	3.391	1.23	1.25
Q(1)	2.485	13.5	2.755	2.036	42.6	2.888	1.37	1.5
Q(2)	1.502	19.8	1.898	1.947	27.3	2.493	1.46	2
Q(3)	2.544	16.6	2.876	2.263	29.1	2.845	1.09	2
Q(4)	1.283	19.9	1.681	1.664	23.5	2.134	1.33	1.5
Q(5)	2.860	16.7	3.194	2.748	29.1	3.330	1.15	1.75
Q(6)	2.288	15.0	2.588	1.735	22.8	2.191	0.89	4.5
Q(7)	1.775	19.4	2.163	1.547	24.2	2.031	0.99	4.5
Q(9)	2.683	14.7	2.977	2.323	27.2	2.867	1.05	2.5
Q(10)	2.715	10.8	2.931	1.580	27.3	2.126	0.80	5.5

requires explanation.

The observed loss in total fluorescence yield is not simply due to the changes in the emission and collisional quenching rates. The quantum yield of fluorescence is

$$Q = \frac{k_{\ radiative}}{(k_{\ radiative} + k_{\ collisional\ quenching} \cdot [pressure])} \tag{5.1}$$

where $k_{\ radiative}$ is the zero-pressure rate of emission in $events\ /\ \mu$s, $k_{\ collisional\ quenching}$ is the collisional quenching rate in $events\ /\ \mu$s / Torr, and pressure is in Torr. Collisions and emission are the only two processes that can change the eigenstate of a molecule. The boxcar gate used to sample the LIF signal was started 150 ns after the laser fired to avoid laser scatter. Changes in the decay rate will result in changes in the observed total fluorescence yield. The fraction of the emission sampled is

$$F = 1/k_{\ total} \cdot e^{-(k_{total} \cdot 150\ ns)} \tag{5.2}$$

where $k_{\ total} = k_{\ radiative} + k_{\ collisional\ quenching}$. Green reported the ratio of the total emission at zero-field to the total emission at 113,000 volts/cm. This ratio should equal

$$\frac{I_0}{I_E} = \frac{Q(\ \ 0\ \ \frac{Volts}{cm})}{Q(113,000\ \frac{Volts}{cm})} \cdot \frac{F(\ \ 0\ \ \frac{Volts}{cm})}{F(113,000\ \frac{Volts}{cm})} \tag{5.3}$$

Using the radiative rates and collisional quenching rates measured by Green and a pressure of 20 mTorr, this ratio has been calculated and the results are shown in the last column of table 5.1. Clearly, the observed changes in the rates do not account for the loss in total fluorescence with electric field. The pressure used in Green's experiments was so low that dramatic changes in the collisional quenching rate had only a fractional change on the total fluorescence ratio.

Green and co-workers argue that the data could be consistent with a coupling of the LIF-detectable states to background states that are dissociative.[59, 60] The electric field mixes some S_0 states to the LIF-detectable S_1 states. If those S_0 states were dissociative, the lifetime would decrease because a new decay channel would have been introduced. The fluorescence yield would go down because more molecules

would dissociate rather than fluoresce when the electric field is applied. And the collisional quenching rate would go up because collisions could induce dissociation. This interpretation was put forward.[60] However, it is now firmly established that the first dissociation limit lies at higher energy than the states observed in Green's experiments.[127, 128] What other interpretation could explain Green's observations?

5.2 Survey of the interactions induced by an electric field

We will start to answer this question with a quick survey of the possible interactions induced by an electric field. An electric field introduces three types of couplings. Because the Stark effect has the same selection rules as electric dipole transitions, the three types of couplings introduced by an electric field are analogous to three types of electric dipole transitions in molecules: electronic, vibrational, and rotational. An electric field can couple rovibrational states of different electronic states if the transition between them is electric-dipole allowed. S_1 states can couple with S_0 states, but an electric field interaction between S_1 and the triplets is spin-forbidden. The strength of inter-electronic state interactions is proportional to the square of the vibrational overlap of the near-degenerate states, the Franck-Condon factor. The S_1 $3\nu_3$ state has maximum Franck-Condon factors with S_0 states with $\sim$5000 cm^{-1} of vibrational energy, but $3\nu_3$ is degenerate with S_0 states with 45300 cm^{-1} of vibrational energy. As a result, Stark interactions between S_1 and S_0 are strongly Franck-Condon forbidden. Significant $S_1 \sim S_0$ mixing will only occur between states that are nearly degenerate. The $S_1 \sim S_0$ interaction matrix elements have been measured to be a few MHz by Zeeman anticrossing experiments,[48, 50, 51, 49] but these are understood to be mediated by the near-degenerate triplet states. The direct $S_1 \sim S_0$ would be even smaller. The S_1 state would have to be within a MHz of the S_0 state to be strongly mixed by an electric field.

Stark couplings between the T_3 doorway state and states from the T_2 and T_1

surfaces will be larger than couplings between the singlet states because both the vibrational and electronic parts of the interaction may be large. The equilibrium geometry of the T_3 potential surface is calculated to have a C_1 symmetry equilibrium geometry,[38, 37] which is different than the T_2 and T_1 equilibrium geometries. The vibrational overlap between near-degenerate vibrational states from similarly shaped potential surfaces is small because a set of vibrational wavefunctions of one surface will be nearly orthogonal with the vibrational wavefunctions of the other. The difference in the energies of the potential surfaces ensures that the overlap integral between near-degenerate vibrational states will be near zero. Because T_3 has a different equilibrium geometry than T_2 or T_1, the Franck-Condon factors between near-degenerate vibrational levels of these states may be large. So, an electric field may mix T_3 with the near-degenerate T_2 and T_1 vibrational states. The electronic part of the interaction matrix element should also be enhanced because the T_3 state equilibrium geometry. In *trans* geometries, all three triplet states have u symmetry, so these states could not interact via an electric field without the assistance of *ungerade* vibrational excitation. Because T_3 does not have a *trans* equilibrium geometry, a Stark interaction between T_3 vibrational states and those of T_2 and T_1 will not be forbidden by g/u symmetry. Dupre, *et al.* have shown that the triplet states are substantially mixed at $2\nu_3$.[51] They have further argued that the couplings between the triplets are larger than the $S_1 \sim$ triplet couplings, the $S_0 \sim$ triplet couplings, or the $S_0 \sim S_1$ couplings, although they did not make the distinction we make here between the T_3 state and the T_2 and T_1 states. It is reasonable to conclude that the electric field will enhance the mixing among triplet states that are already significantly mixed.

An electric field can couple vibrational states within one electronic state with the same selection rules as are appropriate for vibrational transitions, most importantly Δ v $= \pm$ 1. This coupling is irrelevant to the present case because Stark-coupled vibrational states would necessarily be widely separated in energy. In a second-order perturbation theory sense, the Stark mixing between vibrational states is small because of a large energy denominator. Moreover, only a subset of the vibrational modes, those that change the molecular electric dipole moment, are Stark-active in

any case.

An electric field can mix rotational states within a vibrational state. These couplings have the same selection rules as do pure rotational transitions. The electronic state must have a permanent electric dipole moment. Neither the S_1 $3\nu_3$ nor $4\nu_b$ states have a dipole moment, so these states will not have Stark interactions between their rotational states. Theoretical calculations show that the T_3 state has a C_1 symmetry equilibrium geometry, which would imply the existence a permanent electric dipole moment.[38, 37] The exact equilibrium geometry for T_3 has not been determined by *ab initio* methods. Cui *et al.* have calculated the lowest energy structure for T_3 with a geometry search limited to C_2 symmetry.[38, 37] This structure is clearly not the equilibrium geometry because it has an imaginary vibrational mode with a frequency of 2465i and b symmetry. Antisymmetric CCH bend character dominates this vibrational mode. Motion along this mode carries the molecule into C_1 symmetry. This state will probably have a permanent electric dipole moment along all three rotational axes, so it will have Stark interactions analogous to the a-type, b-type, and c-type rotational transitions. Of these, the a-type are most important because they are $\Delta K_a = 0$. Acetylene is a near-prolate top, so the K_a levels are well separated in energy. Because the interacting states within one K_a have considerably smaller energy differences, a-type Stark interactions will result in larger level shifts and wavefunction mixing than b- and c-type Stark interactions. The a-type Stark interactions exist between the parity components of a rotational state. This mixing is dependent on the zero-field asymmetry splitting of the states and the Stark matrix element. Although the asymmetry splitting in the T_3 doorway state is unknown, the $3\nu_3$ splitting is $\sim 0.06\cdot$ J(J+1) cm^{-1}. The Stark coupling between the parity components, as discussed in refs. [85, 196, 195], is

$$\begin{aligned} \frac{\mu \cdot E \cdot K_a \cdot |M|}{J(J+1)} &= (0.017\ cm^{-1}) \cdot \frac{\mu(Debye) \cdot E(kVolts/cm) \cdot K_a \cdot |M|}{J(J+1)} \\ &= (1.9\ cm^{-1} \cdot \mu(Debye)) \cdot \frac{|M|}{J(J+1)} \end{aligned} \tag{5.4}$$

for $K_a = 1$ and 113 kVolts. This coupling will decrease with J proportional to $[J(J+1)]^2$.

To summarize, the electric field will have two significant effects. The electric field will mix rotational states of the T_3 doorway state by the "rotational" Stark effect. And the field will mix the T_3 doorway state with the background triplets by the "electronic" Stark effect. T_3 doorway state character will dominate the response of the observed eigenstates to an applied electric field.

5.3 Proposed explanation: Stark splitting of T_3 doorway state

We propose that Green's anomalous observations may be primarily a consequence of the splitting of the M_J-components of the T_3 doorway state. If the electric field is said to lie along the lab Z-axis, the T_3 state is split into its |M|-components because of the $\Delta M = 0$ selection rule. As a result, some of the T_3 |M|-components will Stark tune toward the nearby $3\nu_3$ basis state. Other |M|-components of the T_3 doorway state will Stark tune away from the $3\nu_3$ basis state, and some will maintain the zero-field energy separation. Stark interactions between the T_3 doorway state and $3\nu_3$ are spin-forbidden, but the spin-orbit interaction will mix the $3\nu_3$ and T_3 states as the T_3 state Stark tunes toward $3\nu_3$. The electric field will cause some of the |M|-components of the $3\nu_3$ state to become more mixed with the background triplet states. Some |M|-components will unmix with the triplets as the corresponding |M|-components of the T_3 doorway state Stark-shifts away from near-degeneracy. $3\nu_3$ |M|-components that maintain the zero-field energy separation from the T_3 |M|-components could also become more mixed with the triplet background states due to enhanced coupling between the T_3 doorway and the T_2 and T_1 states. The electric field will cause most of the |M|-components of the $3\nu_3$ state to increase their fractionation into the background states, which accounts for the loss of fluorescence intensity. A few of the |M|-components of the $3\nu_3$ states will unmix with the background states, which

accounts for the faster decay of the remaining LIF signal. The fluorescence from these |M|-components will strongly quench with pressure because a collisional transition into a slowly fluorescing state merely has to change the |M| of the state. The local nature of these anomalous observations is a result of variation in the energies of the T_3 |M|-components.

This cannot be quantitatively modeled at present because there is insufficient information about the rotational constants or orientation of the permanent dipole of the T_3 doorway state. The state of knowledge about the T_3 equilibrium geometry, which would lead to approximate rotational constants, has been discussed above. The magnitude of the electric dipole moment can be arrived at only within an order of magnitude. The magnitude of the dipole of acetylene in a number of geometries is reported by Schaefer and co-workers. The Cs symmetry isomerization transition state between the *cis* and *trans* wells on the S_1 surface has a dipole of $\sim$0.7 Debye.[198] The *cis* well on the T_1 surface has a dipole of $\sim$1.2 Debye, and the *cis* well on the T_2 surface has a dipole of $\sim$2.2 Debye.[214] The T_3 electronic state has a dipole that is somewhat smaller. The geometry at the stationary point in C_2 symmetry for the T_3 state is non-planar and bent with a dihedral angle of 104.7°.[37] This structure is more "*trans*" than "*cis*" so the T_3 equilibrium geometry is likely to have a smaller dipole than those of the *cis* wells. In fact, we know that the T_3 vibrational state that perturbs $3\nu_3$ must have a vibrational wavefunction with some amplitude at a *trans*-bent structure, a geometry with no dipole. So the dipole is probably a fraction of a Debye.

5.3.1 Loss of total fluorescence

The loss of total fluorescence could be explained by a striking increase in the fractionation of the $3\nu_3$ basis state. The $3\nu_3$ character mixed into a given background state may be so small that the resulting radiative decay rate cannot compete with the collisional quenching rate. These states would quench before they could significantly contribute to the total fluorescence and the fluorescence decays that Green recorded. However, they could account for the majority of $3\nu_3$ character.

Of the two significant effects of the applied electric field, only the increase in the coupling between the triplet states is most important. The rotational Stark effect may have very little effect on the total fluorescence. The field mixes the parity components of the T_3 rotational state. This mixing doubles the number of states with which the $3\nu_3$ basis state can couple, but the coupling between the states will decrease. This is because the spin-orbit interaction only couples a given $3\nu_3$ rotational state with the T_3 doorway character of the same rotational state. If the 1_{10} T_3 doorway state is 50/50 mixed with 1_{11} T_3 doorway state, the 1_{10} $3\nu_3$ state can now couple with both of the Stark-mixed eigenstates.

$$\phi_1 = \frac{1}{\sqrt{2}}(\psi_{T_3,1_{11}} + \psi_{T_3,1_{10}}) \tag{5.5}$$

$$\phi_2 = \frac{1}{\sqrt{2}}(\psi_{T_3,1_{11}} - \psi_{T_3,1_{10}}) \tag{5.6}$$

But, the coupling strength to each state will be reduced by one-half.

$$\begin{aligned} &|< 3\nu_3,\ 1_{10} \mid H_{so} \mid \phi_1 >|^2 \\ &|< 3\nu_3,\ 1_{10} \mid H_{so} \mid \frac{1}{\sqrt{2}}(\psi_{T_3,1_{11}} + \psi_{T_3,1_{10}}) >|^2 \\ &|< 3\nu_3,\ 1_{10} \mid H_{so} \mid \frac{1}{\sqrt{2}}\psi_{T_3,1_{10}} >|^2 \\ \frac{1}{2}&|< 3\nu_3,\ 1_{10} \mid H_{so} \mid \psi_{T_3,1_{10}} >|^2 \end{aligned} \tag{5.7}$$

Applying Fermi's Golden Rule to this case, the "rate" of fractionation is proportional to

$$\frac{1}{2}|< 3\nu_3,\ 1_{10} \mid H_{so} \mid \psi_{T_3,1_{10}} >|^2 \cdot 2 \cdot \rho_{zerofield} \tag{5.8}$$

When the field is applied, the Fermi's Golden Rule rate would stay approximately the same. Of course, this would strongly depend on the exact energies of the states, so this will be more important for some states than others.

The electric field-induced mixing between T_3, T_2 and T_1 increases the fractionation. As mentioned before, the field will increase the couplings between the triplets

states that are already somewhat mixed. We conclude that this is the dominant reason for the loss of total fluorescence, because it is the only effect universal enough to account for the ubiquitous loss.

5.3.2 Enhanced collisional quenching

The electric field enhances collisional quenching via ΔJ=0, ΔM= $\pm$1 collisional transitions. These kinds of collisions are common in acetylene. Coy, *et al.* have experimentally demonstrated the selection rules of collisional transitions relevant to this case.[32] In formaldehyde, Coy, *et al.* showed that there is a propensity rule against $\Delta J = 0$, $\Delta M = \pm 1$ collisional transitions at zero-field. Formaldehyde has a permanent electric dipole moment along the molecular a-axis. Collisions between two formaldehyde molecules can be described as a transient interaction between two dipoles. Coy, *et al.* showed that this interaction has the same selection rules as an electric dipole transition. The relevant constraint this places on colliding formaldehyde molecules is that the transition must change the parity of the molecular state. Coy, *et al.* studied the 1_{01} state in formaldehyde. Since all the Ms of a given J have the same parity in these $K_a = 0$ states, the collisions Coy, *et al.* studied should not cause $\Delta J = 0$, $\Delta M = \pm 1$ transitions. None were observed. Acetylene in $\tilde{A}$-state and in the ground state have no electric dipole moment, but they do have quadrupole moments. So acetylene collisions will have the same selection rules as an electric quadrupole transition Therefore, acetylene collisions have a propensity to *maintain* parity, allowing $\Delta J = 0$, $\Delta M = \pm 1$ collisional transitions.

At zero field, collisional transitions between the |M|-components result in no observable changes in total fluorescence because all the |M|-components behave identically. At 113 kVolts/cm, most of the |M|-components are heavily fractionated into non-fluorescing background states. Collisions from |M|-components with large fractional singlet character to weakly fluorescing |M|-components with the same J result in a dramatic loss of emission.

Dupre, Green, and Field have reported collisional quenching rates that corroborate this understanding.[51] Dupre, *et al.* showed that collisional transitions between

singlet rotational levels can be faster than fluorescence-quenching collisions to background states. In Fig. 13 of ref.[51], they show a Stern-Volmer plot of the decay rates vs. pressure of a single rotational level in $1\nu_3$. The figure compares the collisional quenching rate of the decay to the quenching rate of a quantum beat on this level. The quenching of the quantum beat is much faster than the quenching of the fluorescence. The quenching of the fluorescence is 6.25 μs^{-1} $Torr^{-1}$, which is comparable to the zero-field quenching rates Green observed. The quenching of the quantum beat is 32.9 μs^{-1} $Torr^{-1}$, which is similar to the rates Green observed at 113 kVolts. The reason the two rates are different is that a collisions that cause transitions to other singlet states (such as transitions to other M-component of the same J) will disrupt the beat without reducing the fluorescence, while a collisional transition to a non-fluorescing background state will eliminate fluorescence. As some |M|-components Stark mix at high electric field with the background triplets, the fluorescence quenching rate becomes similar to the quantum beat quenching rate because M-changing collisions can lead to fluorescence loss at high field.

5.4 Nuclear spin wavefunctions considerations

The nuclear spin wavefunctions may prohibit Stark interactions between parity components because the two parity components have different nuclear spin wavefunctions, but this will not affect the T_3 state. For electronic states with higher symmetry than that of T_3, the rotational wavefunctions of the two parity components have different nuclear spin wavefunctions, as shown by Lundberg.[111] This is true for all acetylene states with *cis* and *trans* geometries. Rotational wavefunctions with different symmetries must co-exist with different nuclear spin wavefunctions to arrive at a Complete Nuclear Permutation-Inversion (CNPI) symmetry of Sa+/- for the total wavefunction. An electric field does not affect the nuclear spin wavefunctions, so Stark interactions between states with different nuclear spin wavefunctions go to zero because of nuclear spin wavefunction orthogonality. When the geometry of the molecule becomes less symmetrical, the number of symmetry species decreases. The symmetry group for a

trans geometry is C_{2h} and has four irreducible representations. Each rotational level will be doubly degenerate. The two components will have separate CNPI symmetry labels. These states correspond to the two orientations of the carbon atoms relative to the H atoms. Since the inversion of the carbons without the inversion of the H atoms in a high energy event, the barrier for this inversion can be said to be infinite and the two states are degenerate. When the molecular symmetry changes to C_2, the number of symmetry labels is two. The number of states belonging to each rotational wavefunction is four, two corresponding to carbon atom inversion and two corresponding to inversion through a C_{2h} symmetry geometry. If the inversion barrier is high, the four states will be nearly degenerate. If the inversion barrier is low, the four states will be split into two groups of two states. Finally, when the molecular geometry is changed to C_1 symmetry, only one symmetry label exists. Eight states exist within each rotational level, because there can be inversion through the C_2 symmetry geometry. Each of these eight states corresponds to one of the eight possible CNPI symmetry labels. The two parity components will have the same rotational symmetries and so they will have the same nuclear wavefunctions. Stark interactions between the parity components will not be forbidden on the basis of nuclear wavefunction orthogonality.

While there are eight possible states, there can only be two of these that pair with the symmetry of the two nuclear spin wavefunctions to produce a CNPI symmetry of Sa+/- for the total wavefunction. The others have no statistical weight.

5.5 Other thoughts

It should be noted that the behavior of these states in an electric field would be different if there were no doorway state dominating the Intersystem Crossing. The other alternative explanation for Green's data would involve the T_2 or T_1 states. The electric field would split the T_2 and T_1 states, which have permanent dipoles in *cis*-geometry. These states would split the LIF-detectable states into |M|-components. However, the density of *cis*-T_2 and *cis*-T_1 states at the energy of $3\nu_3$ are 0.3 per cm^{-1}

and 4.7 per cm^{-1}, respectively.[43] With such a high density of states coupling to the LIF-detectable states, it is unlikely that any of the |M|-components would escape fractionation. Further, it is hard to imagine all of the triplets in a region tuning away from the LIF-detectable states to create the short lived states that appear in Green's data.

5.6 Conclusion

The Stark splitting of the perturbing T_3 doorway state could simultaneously account for the shorter apparent lifetimes, larger collisional quenching rates, and smaller fluorescence yield of the $2\nu_3$ and $3\nu_3$ states in an electric field. It could also explain the local nature of the perturbations.

5.7 Acknowledgments

Thanks to Dr. Stephen Coy for helpful discussion on the propensity rules for collisional transitions.

Chapter 6

Temporal Behavior of the SEELEM signal

The temporal behavior of the SEELEM signal is a function of both the lifetime of the eigenstates and the Auger electron quantum yield of the surface. Both of these processes are of interest. As discussed in Chapter 3, the lifetime of an eigenstate is related to its fractional S_1 character, because the decay of the eigenstate is dominated by emission to the ground S_0 state provided by the S_1 character. A measure of the lifetime of an eigenstate should provide a measure of its fractional S_1 character.

Measuring the lifetimes of the SEELEM-detectable states is complicated by variations in the Auger electron quantum yield, or the detectivity, of the surface. We will show here that a decrease in detectivity occurs over the course of a single pulsed expansion and that the decrease observed for metastable NO is different than it is for metastable acetylene. There are two possible explanations for the detectivity loss: surface poisoning and backscattering. Surface poisoning could occur when molecules in the expansion adsorb to the detection surface and interfere with metastable de-excitation. Or, molecules that backscatter off the detection surface could collide with incoming metastable molecules and de-excite them. This detectivity loss can be observed by varying the nozzle-laser delay, as mentioned in Section 2.3.1.

The temporal behavior of the SEELEM signal was measured using four experimental approaches. The four techniques are:

1) SEELEM intensity with different carrier gases. The different carrier gases create beams with different velocities. The decrease in SEELEM intensity with flight time is a measure of the SEELEM decay. However, it is not clear how the detectivity changes when the carrier gas is changed, so this technique may not give an accurate measure of the lifetime.

2) Comparison of TOF profiles of different metastables: The TOF profile should be the product of the velocity distribution and the decay of the SEELEM signal. Comparing the TOF profiles of different metastables can reveal differences between their SEELEM decay. In particular, it is an excellent way of observing the decay of the SEELEM detectivity, but not a good way of measuring the lifetimes of the SEELEM-detectable states.

3) Comparison of TOF profiles on different lines in the SEELEM spectrum: This provides a comparison of the lifetimes of the SEELEM-detectable states under the same expansion and detectivity conditions, but the differences may be small. The lifetimes of the LIF-detectable states can be measured simultaneously.

4) Comparison of SEELEM spectra recorded at different flight distances: This provides both relative and absolute measures of the SEELEM decay. The relative measure should provide information on the relative differences in eigenstate lifetimes. The absolute decrease in SEELEM intensity is vulnerable to detectivity variation, but provides an upper bound on the eigenstate lifetimes.

6.1 SEELEM intensity with different carrier gases

The first attempt to measure the temporal behavior of the SEELEM signal was made at UC Santa Barbara by recording the SEELEM intensity using two carrier gases, either H_2 or He. We report this work in Humphrey, *et al.*[79] H_2 generated a 92 ± 5 flight time, and He generated a 120 ± 5 μs flight time. The two SEELEM intensities provide sufficient information to calculate a decay constant with the assumption that the decay is exponential. This technique has the advantage that only the expansion gas changes. The detection surface collects the same solid angle of the molecular beam

for each carrier gas. The angular distribution of the expansion has been shown to be largely unaffected by a change in carrier gases.[86] However, the density of acetylene at the laser-molecular beam excitation region will be different with different carrier gases. To account for this, the SEELEM intensity was divided by the LIF intensity.

The decrease in the LIF-normalized $3\nu_3$ SEELEM intensity was recorded for a number of laser excitation frequencies within $3\nu_3$. This results in an exponential decay constant for the $3\nu_3$ state of 80 $\pm$ 30 μs. The error bounds are large because only two flight times were used. There was little variation with laser excitation frequency.

A simple calculation, discussed in Chapter 3, showed that this lifetime was reasonable. The calculation assumes that the SEELEM signal is proportional to the product of three factors as shown in eq. 3.5 and discussed in Chapter 3.

$$I_{SEELEM} \propto (S_1)^2 \cdot e^{-(3.7\times 10^6 \cdot (S_1)^2 \cdot t)} \cdot Q_{S_1} \cdot (S_1)^2 \tag{6.1}$$

The first factor is the number of molecules excited, which is proportional to the fractional S_1 character in the eigenstate, $(S_1)^2$. The second factor is the proportion of the excited molecules that survive the flight time to the detection surface. Since the decay of the excited eigenstate is dominated by radiative decay to the ground S_0 state, this will be a function of the S_1 character in the eigenstate. It is also a function of flight time, 120 μs, and pure S_1 lifetime, which has been estimated to be $\sim$ 270 ns.[138] The third factor is the detection probability, which we assume here to be proportional to the S_1 character. This is because the S_1 state meets the energy requirement for ejecting an electron from the detection surface, as discussed in Chapter 2. That fraction of the electronic wavefunction that is composed of S_1 character will create Auger electrons. The T_3 state also meets the energy requirement, however we leave this out of the present calculation because the fractional T_3 character in the eigenstates is unknown. Including some detectivity contribution from T_3 does not change the window of detectivity significantly.

Because this equation relates the eigenstate lifetime to SEELEM intensity, we can determine the most "detectable" lifetime. The SEELEM signal for an eigenstate

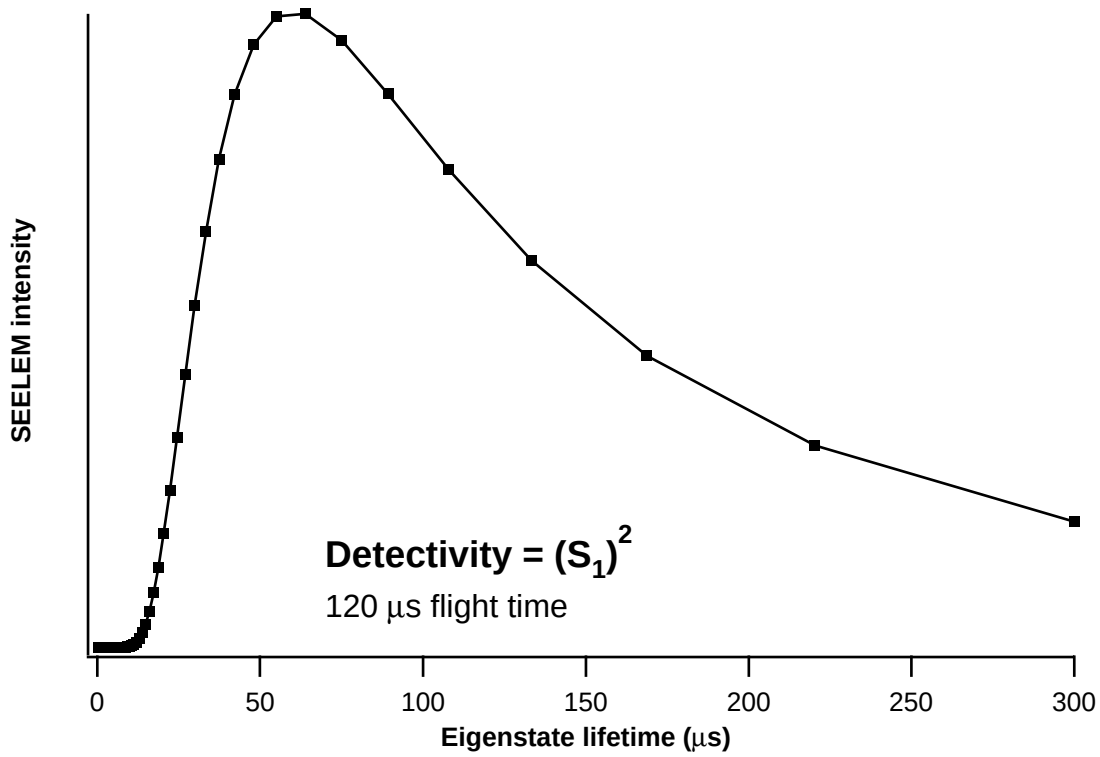

Figure 6-1: Expected SEELEM signal as a function of eigenstate lifetime.

calculated by eq. 6.1 as a function of lifetime in that eigenstate, (270 ns / $(S_1)^2$), is shown in Fig. 6-1. Clearly, there is a window of detectivity. Only eigenstates with lifetimes of 20-450 μs will have significant SEELEM detectability. This window exists because the three factors offset each other. If an eigenstate has a large amount of S_1 character, many molecules will populate this state. But few will arrive at the detector because the decay rate is so high. If an eigenstate has little S_1 character, few molecules will populate the state, but almost all of them will arrive at the detection surface. As shown in Fig. 6-1, the most detectable lifetime is $\sim$ 70 μs, showing that the detected lifetimes are reasonable.

However, this measurement may be affected by fluctuations in the detectivity. The two carrier gases may have different surface poisoning effects or different de-excitation probability for de-exciting backscattering collisions. Also, the dependency of detectivity on the nozzle-laser delay was not discovered until after this data was recorded. As discussed in Chapter 2, the SEELEM to LIF ratio is dependent on

the nozzle-laser delay, so dividing the SEELEM intensity by the LIF signal may not properly compensate for the change in acetylene density at the laser-molecular beam interaction region.

Suzuki and co-workers have also measured a metastable lifetime of $\sim 100 \pm 50 \mu$s for $3\nu_3$ using a somewhat different technique. They coated a surface with biacetyl. When metastable acetylene collides with this surface, the acetylene transfers its energy to the biacetyl, which then fluoresces. The emission is observed with a PMT. They compared the signal from experiments with two carrier gases, He and Ar, to arrive at the lifetime.[186, 166]

6.2 Comparison on TOF profiles of different metastables

Another approach to studying the decay of the SEELEM signal is to compare the TOF profile of acetylene with the velocity distribution of molecules in the beam as measured by the TOF profile of a metastable with a known lifetime. A TOF profile is the product of the velocity distribution and the decay of the SEELEM signal. The velocity of molecules in the beam has a Gaussian distribution,[57, 121, 132] so the TOF profile will be a Gaussian skewed by the exponential decay of the SEELEM signal. By independently measuring the velocity distribution, the decay of the SEELEM signal can be extracted.

We attempted to measure the velocity distribution of a free jet by recording the TOF profile for NO($a\ ^4\Pi$), the lifetime of which is calculated to be $\sim$ 100 ms.[102] This state can be accessed with a laser. The TOF profile of NO($a\ ^4\Pi$) is a measure of the velocity distribution because very little of the signal will decay in the $\sim$65 μs flight time of the experiment. Of course, the SEELEM detectivity may decrease during the pulsed expansion, but, as will be shown shortly, this is not as significant for NO($a\ ^4\Pi$) as it is for metastable acetylene.

We made up a gas mix that was $\sim$ 6 percent NO, $\sim$33 percent acetylene, and

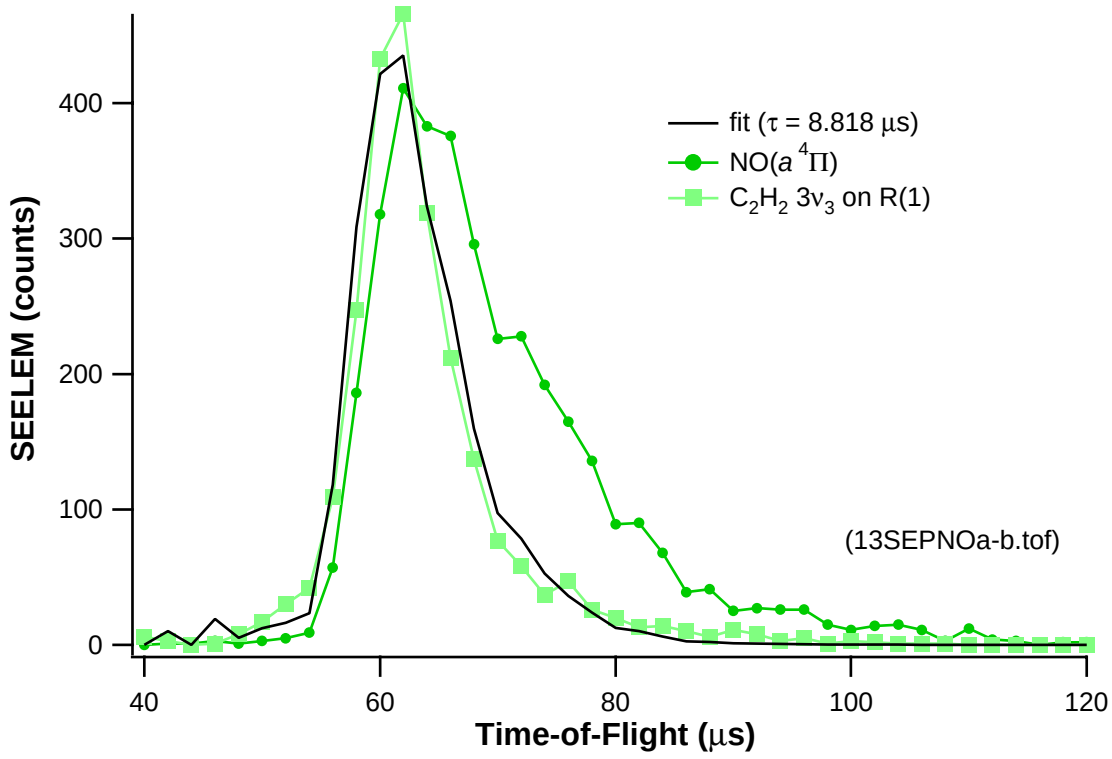

Figure 6-2: The TOF profiles of acetylene and NO($a\ ^4\Pi$), along with the fit.

the balance He. We could record the metastable NO($a\ ^4\Pi$) TOF profile and the metastable acetylene TOF profile simply by changing the laser frequency, leaving the expansion conditions and the nozzle-laser delay fixed. The velocity distribution of the co-expanded gases was determined by the He. A similar approach was used by Mason and Newell.[116]

The results of this experiment are shown in Fig. 6-2. The NO TOF spectrum multiplied by an exponential decay was fit to the acetylene TOF spectrum. The fit is also shown. This indicates that the exponential decay constant of the SEELEM-detectable signal is $< 10\ \mu$s. Clearly NO($a\ ^4\Pi$) behaves differently than does metastable acetylene. Is this difference due to the lifetimes of the eigenstates or the detectivity of eigenstates?

The difference is probably not due to the lifetimes of the SEELEM-detectable acetylene eigenstates. The other techniques discussed in this chapter all indicate that the metastable acetylene eigenstates have much longer lifetimes than 10 μs. Also,

the intensity calculation Chapter 3 shows that less than 700 molecules per pulse with lifetimes this short would arrive at the detector under typical experimental conditions. In the experimental Chapter 3, the detection quantum yield was shown to be $\sim 5 \times 10^{-6}$. States with 10 μs lifetimes should be completely undetectable.

Because this SEELEM signal decay constant is probably too large to be the result from the lifetimes of the eigenstates, the decay must be due to a decrease in SEELEM detectivity during the course of a single pulsed expansion. If this is the case, it indicates that NO($a\ ^4\Pi$) and metastable acetylene de-excite through mechanisms that have different sensitivities to surface conditions. NO($a\ ^4\Pi$) can only de-excite through the "exchange" mechanism discussed in Chapter 2, while metastable acetylene can be de-excited through the "Coulomb" mechanism, as discussed in Chapter 2. Although de-excitation is complicated, perhaps the "Coulomb" mechanism is more sensitive to surface poisoning. Alternatively, metastable acetylene may be more susceptible to collisional de-excitation by backscattering molecules. Acetylene does have a higher density of background states to serve as final states for collisional transitions than does NO.

Clearly, this technique is not a satisfactory way of measuring the lifetimes of the SEELEM detectable states, but it is a good way of observing the decrease in detectivity during the course of a single pulsed expansion.

6.3 Comparison of TOF profiles on different lines

The relative differences in eigenstate lifetime may be discernible in the TOF profiles of different acetylene lines for which the detectivity loss may be the same. The fluorescence decays of the LIF-detectable states can be simultaneously recorded to measure the lifetimes of these states.

6.3.1 SEELEM-detectable states

The TOF profiles of different SEELEM-detectable lines of a given band were analyzed to see if they reveal lifetime differences among the lines. Assuming the decay of the

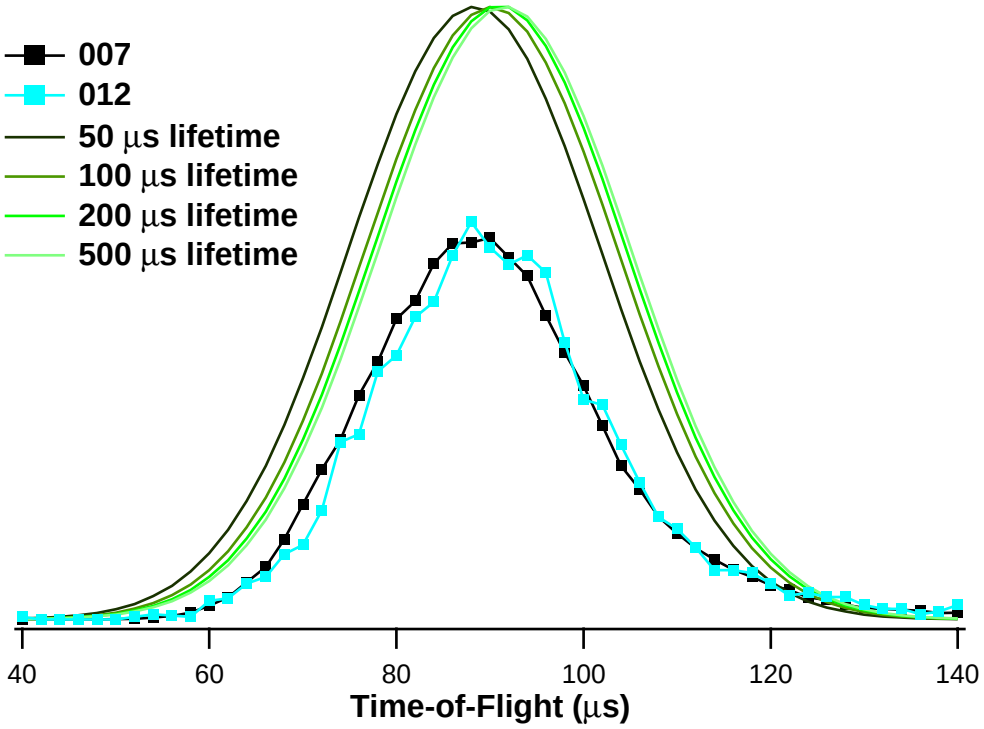

Figure 6-3: A simulation of the change in TOF profile with eigenstate lifetime and the observed TOF profiles of lines 007 and 012.

detectivity is the same for all of the lines, the only difference among the TOF profiles will be due to decay of the eigenstates. The expansion conditions and nozzle-laser delay do not change, so the velocity distribution and detectivity conditions should be the same for all TOF profiles.

Fig. 6-3 shows a simulation of TOF profiles with five different metastable lifetimes. The TOF profiles are the product of a Gaussian (mean = 110 μs, standard deviation = 19 μs), an exponential with a 10 μs decay constant to account for the loss of detectivity, and another exponential with decay constants that are 50 μs, 100 μs, 200 μs, or 500 μs. Clearly, the sensitivity of this technique is limited by the decrease in detectivity. Nonetheless, if the eigenstates have both i) lifetimes less than 200 μs and ii) lifetimes that vary by $\sim$ 50 μs, then we should be able to detect the impact of the lifetimes variation.

The SEELEM TOF profiles were collected for 14 fractionated lines belonging to R(1) of the $V_0^3K_0^1$ band, as shown in Fig. 6-4. We can detect many lines associated

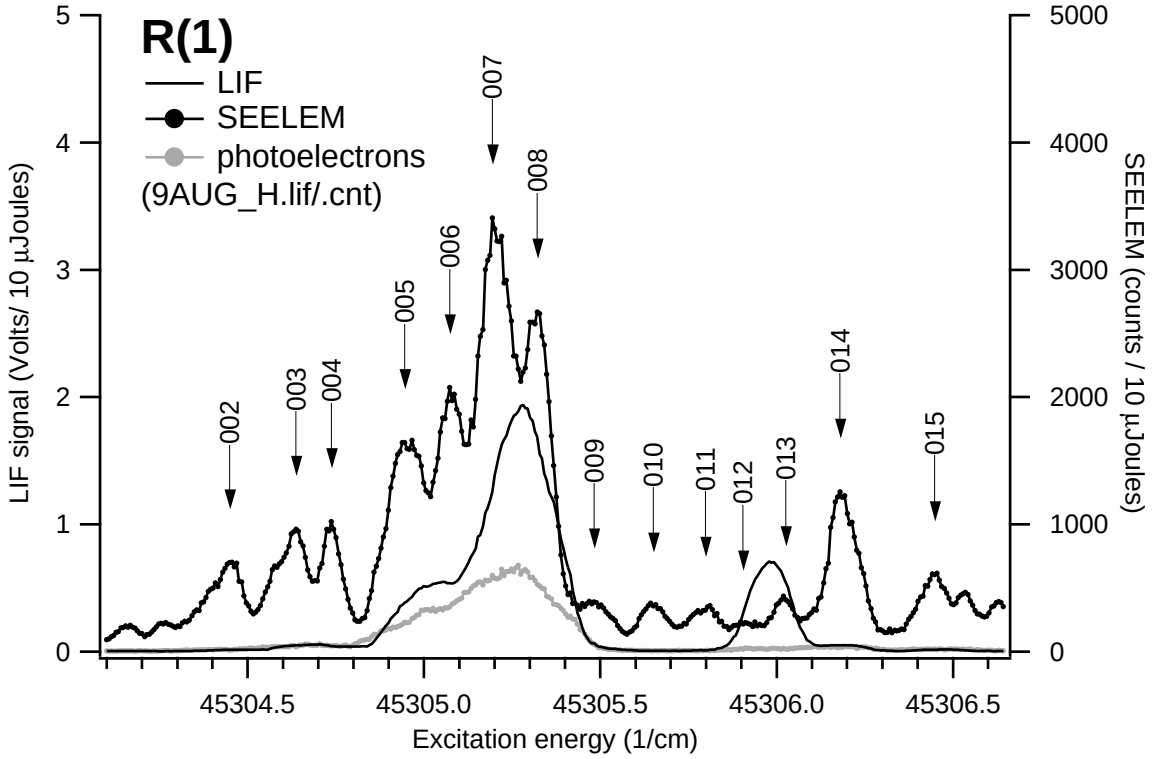

Figure 6-4: The SEELEM and LIF spectra of the R(1) transition of $V_0^3K_0^1$. TOF profiles and LIF decays were recorded at the positions marked by arrows. Also shown is the photoelectron signal produced on the detection surface by the LIF detectable states. The counts from 50 laser shots were summed to produce each point in the SEELEM and photoelectron spectra.

with R(1) because the $3\nu_3$ J=2 state is fractionated into several background states. This creates 14 distinct lines identifiable at this spectral resolution. R(1) was selected because it is one of the most intense rotational transitions in the SEELEM spectrum of this band, which provides a large number of SEELEM-detectable peaks. R(1) is also well separated from neighboring rotational transitions. A laser power study was conducted to ensure that the SEELEM detector was not saturated on the strongest peaks.

The TOF profiles for all 14 lines are nearly identical except for the overall intensity. Fig. 6-3 shows the TOF profile of lines 007 and 012 which differed the most. The TOF profiles of the other lines were intermediate between these two. The eigenstates excited at line 012 may have slightly longer lifetimes, but a strong conclusion is not justified by the small difference and the signal-to-noise ratio. We can come to one of two conclusions: the lifetimes of the SEELEM-detectable states are all similar, or the lifetimes of the SEELEM-detectable states are > 200 μs. We shall show in the next section that *both* conclusions may be correct.

6.3.2 UV-LIF-detectable states

Although this is a bit of a digression from the discussion of the SEELEM-detectable states, the lifetimes of the UV-LIF-detectable states were measured for each line in Fig. 6-4, which shows that these states are short-lived. The fluorescence decays of each line were recorded at the same time that the SEELEM TOF profiles were recorded. The SEELEM TOF profiles also contain information about the LIF-detectable states. A large, short-lived signal appears on the SEELEM detector immediately after the laser fires. This signal decays exponentially over ~ 20 μs. This signal is due to spontaneous emission from the LIF-detectable states that arrives at the SEELEM detection surface and generates electrons via the photoelectric effect. The decay of this signal provides another measure of the lifetimes of the LIF detectable states.

The two measures bracket the true decay of the LIF-detectable states because they have opposite geometric biases. LIF has a geometric bias that makes the observed decays appear shorter than the true decays. Although the molecules are excited in the

field of view of the PMT, the excited molecules in the free jet travel out of the optimal viewing region. This will cause the decays to appear shorter because the collection efficiency decreases with time. In the MIT experiment, the collection optics are 5 cm in diameter. Since the molecules were moving at $\sim$ 1 mm/μs, the molecules were expected to be in the viewing region for $>$ 10 μs. In fact, some fluorescence remained detectable 18 μs after the laser fired. The TOF profile has a different geometry that will make the lifetime appear longer than it is. The solid angle collected by the detection surface increases as the excited molecules travel toward the detection surface. Emission early in the decay is collected less efficiently than is emission later in the decay when the molecules are closer to the detection surface. This increase in the fraction of emission collected will make the observed decay look a little longer than the real decay of the eigenstates. Thus, the two observations bracket the true decay of the eigenstates.

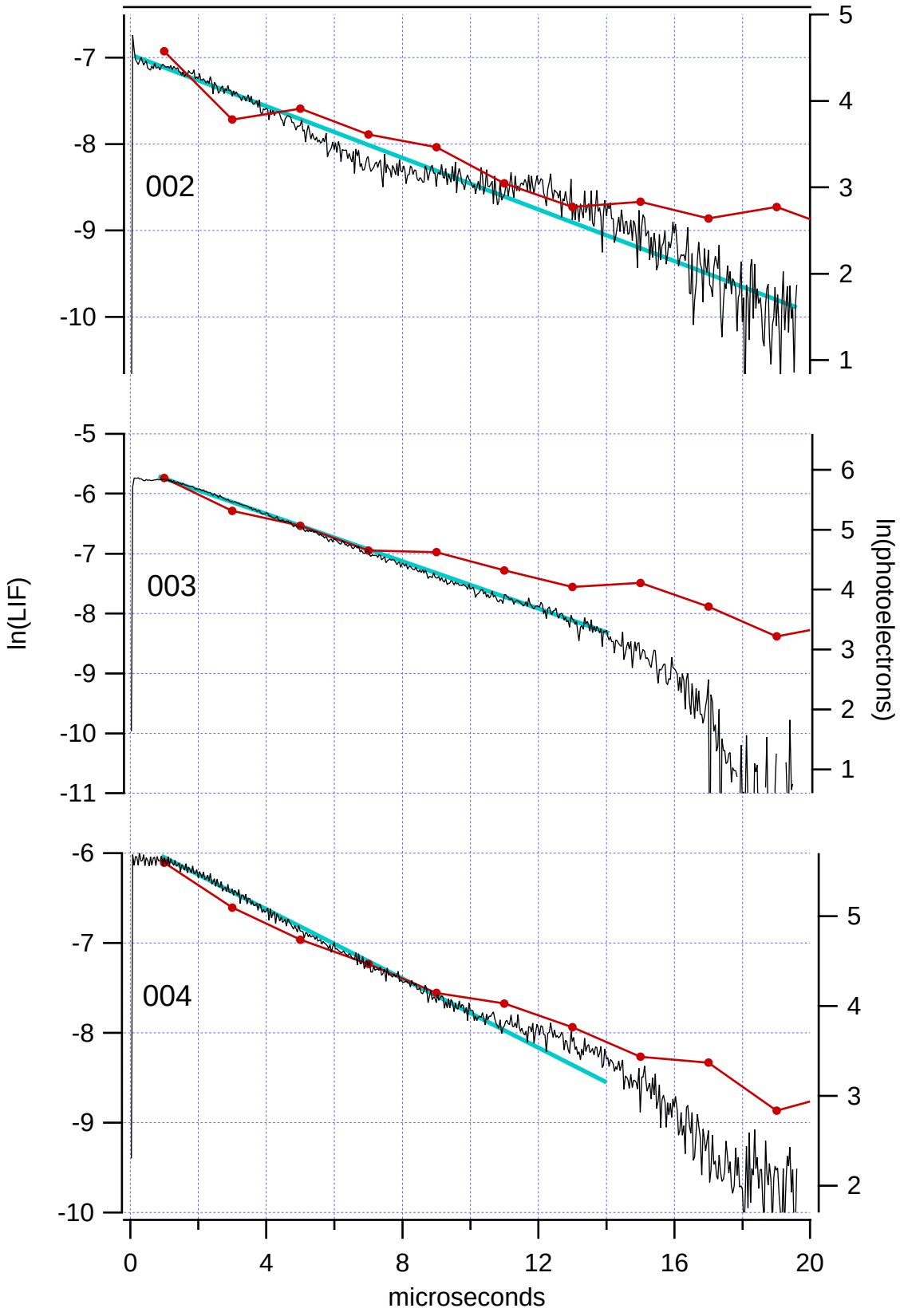
002
003
004
ln(LIF)
ln(photoelectrons)
microseconds
-7
-8
-9
-10
-5
-6
-11
0
4
8
12
16
20
5
4
3
2
1
6

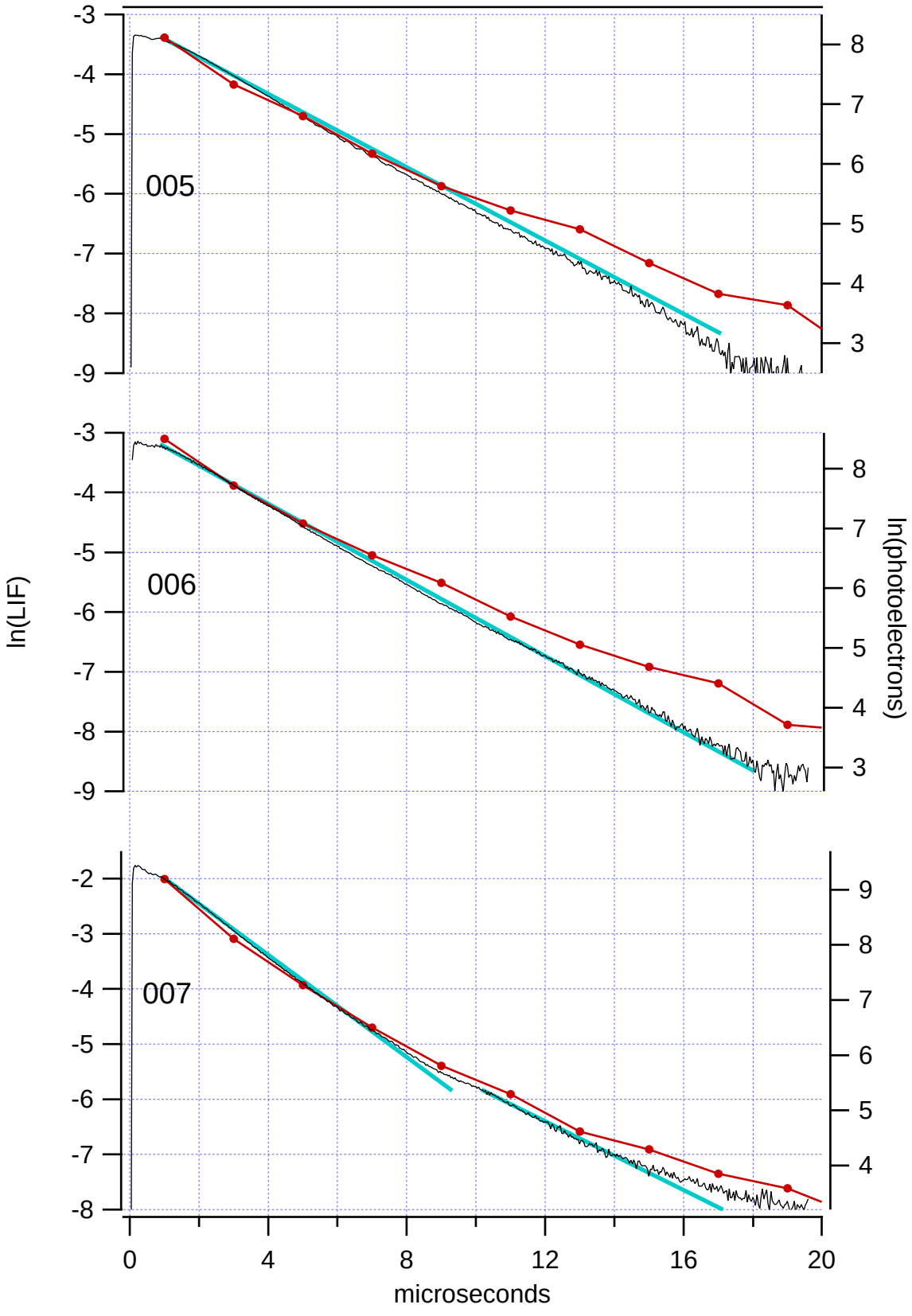
ln(LIF)
ln(photoelectrons)
005
006
007
microseconds
-3
-4
-5
-6
-7
-8
-9
-2
8
7
6
5
4
3
9
0
4
8
12
16
20

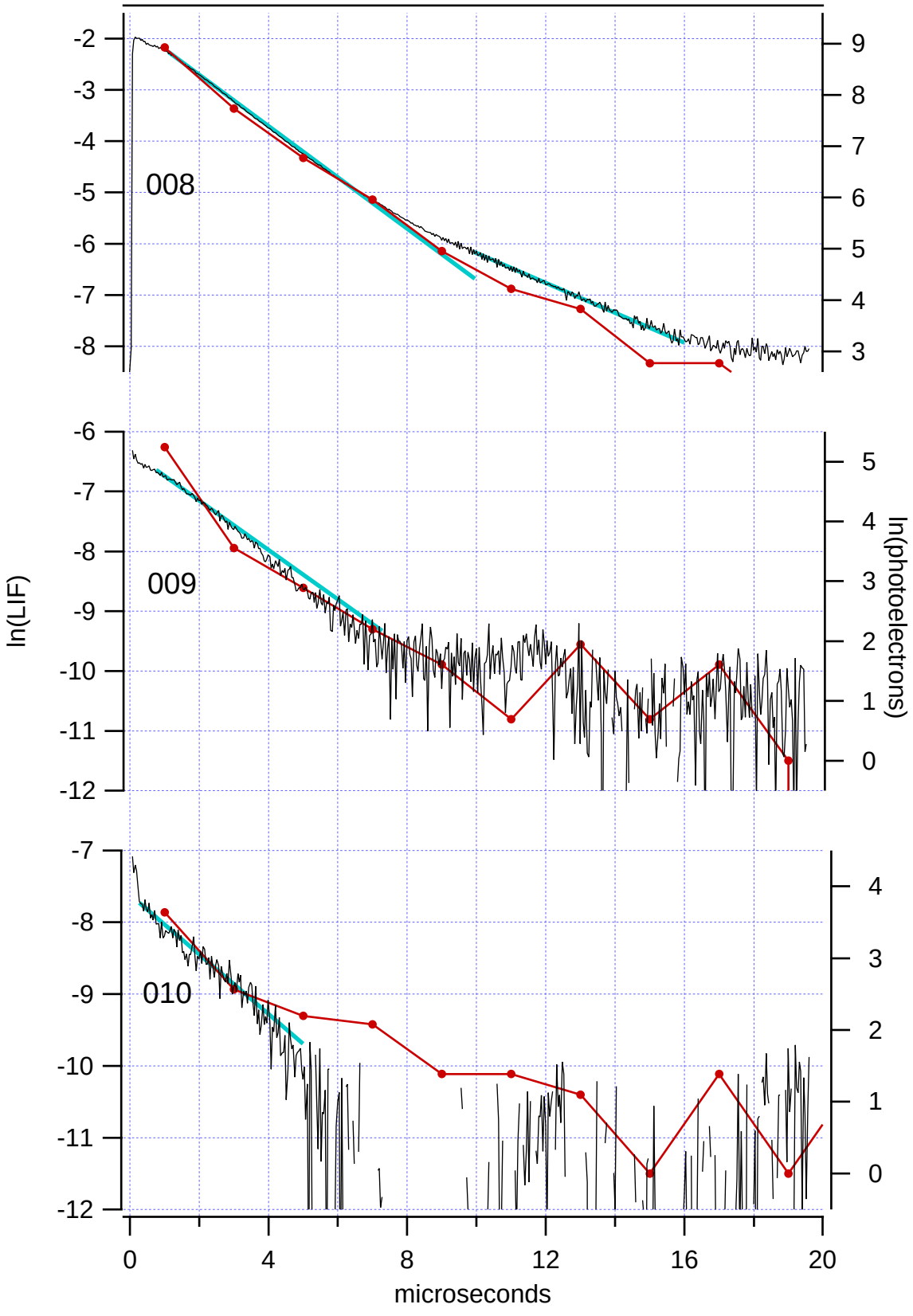
ln(LIF)
ln(photoelectrons)
008
009
010
microseconds
-2
-3
-4
-5
-6
-7
-8
9
8
7
6
5
4
3
-6
-7
-8
-9
-10
-11
-12
5
4
3
2
1
0
-7
-8
-9
-10
-11
-12
4
3
2
1
0
0
4
8
12
16
20

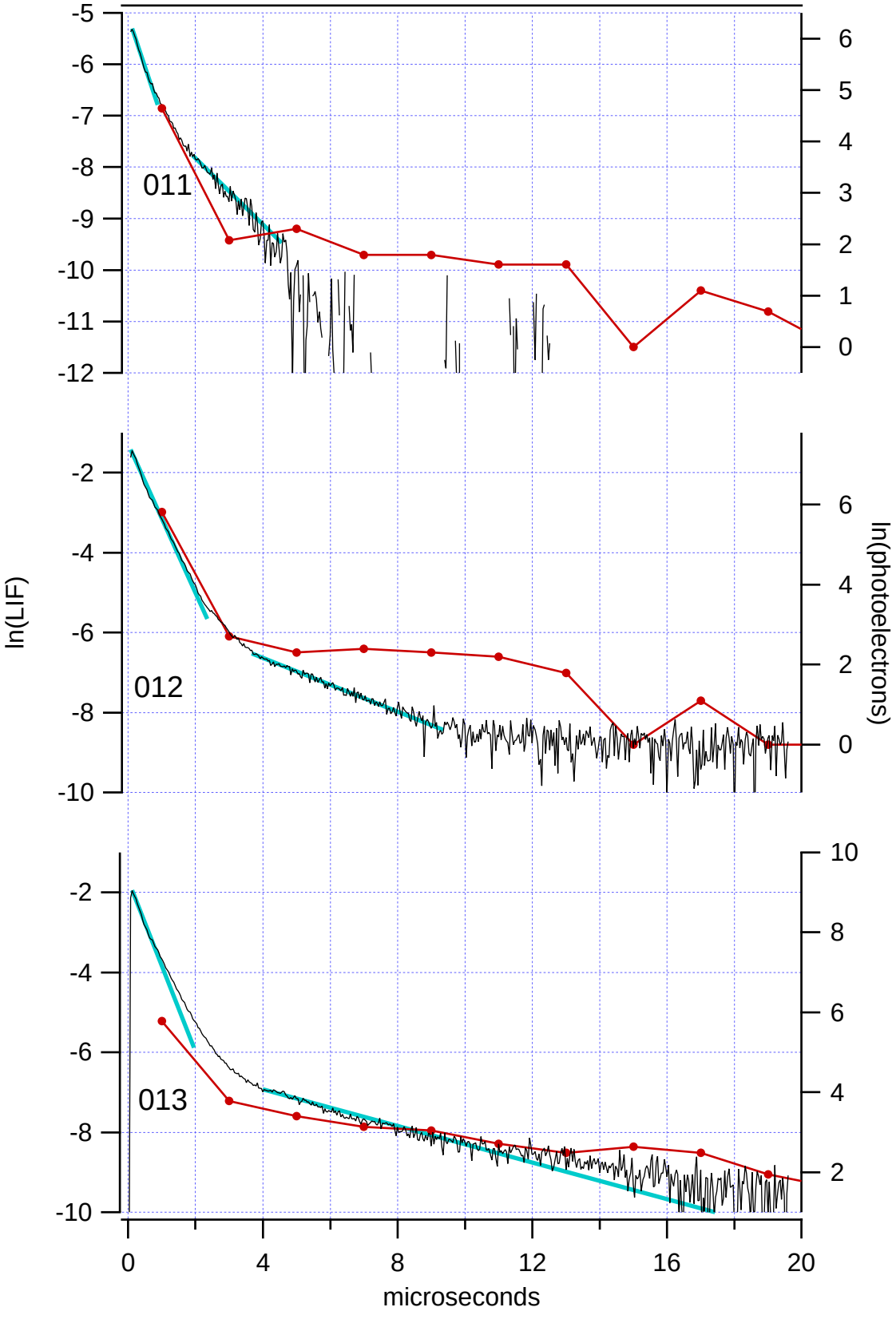
ln(LIF)
ln(photoelectrons)
microseconds
011
012
013
-5
-6
-7
-8
-9
-10
-11
-12
-2
-4
-6
-8
-10
-2
-4
-6
-8
-10
6
5
4
3
2
1
0
6
4
2
0
10
8
6
4
2
0
4
8
12
16
20

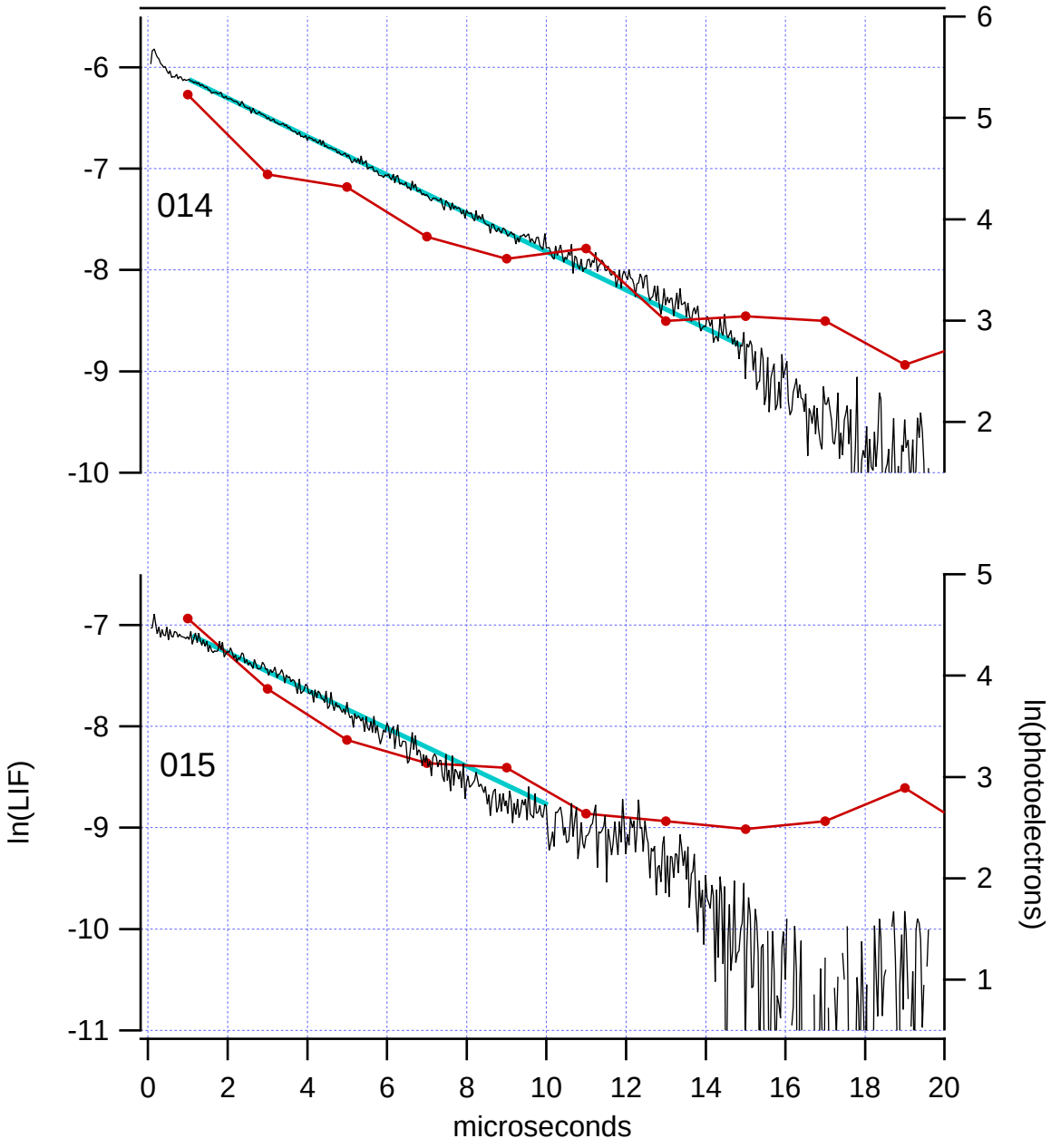

Figure 6-5: The natural log of the fluorescence of the LIF-detectable states detected by the PMT and by the photoelectrons from the detection surface. The fit to the PMT signal is shown.

Table 6.1: LIF decay constants in μs.

line	short component	long component	Ochi and Tsuchiya[138]
002	6.7(3)		-
003	5.1(3)		1.4(6)
004	5.2(3)		> 1
005	3.3(2)		> 1
006	3.1(2)		>1
007	2.2(1)	3.2(2)	1.3(5)
008	2.0(1)	3.4(2)	1.4(6)
009	2.4(1)		-
010	2.4(1)		-
011	0.51(3)	1.6(1)	-
012	0.54(3)	3.0(2)	0.4(3)
013	0.47(3)	4.4(3)	0.4(3)
014	5.3(3)		1.7(8)
015	5.4(3)		-

The lifetimes of the LIF-detectable states are short ($<$ 7 μs) and somewhat longer than those reported by Ochi and Tsuchiya.[138] The most significant errors in these decay constants is due to the systematic error introduced by the geometry of the collection optics. Fig. 6-5 shows the decays of the LIF-detectable states. The natural log of both LIF decays and SEELEM TOF profiles is shown. As expected, the LIF decays were usually a little shorter or the same as those observed from the photoelectrons on the SEELEM detector. The difference between these results and those reported by Ochi and Tsuchiya is probably due to the fluorescence collection optics. Clearly the lifetimes are short and vary over an order of magnitude.

The lifetimes of the LIF-detectable states can be determined by fitting the natural log of the decay to a straight line. The slope is equal to -1/(lifetime). The results are listed in Table 6.1. The lines were fit to a region of the data that was reasonably straight. In some cases, the decay was clearly bi-exponential, so lines were fit to two regions of the data. In most cases, the first microsecond of the decay was excluded to avoid an artifact in the decays caused by secondary ion feedback in the PMT. As discussed in appendix A of Peter Green's thesis,[59] He-atoms leak into a PMT

and can be ionized by electrons accelerated between the dynodes. The positive He ions go "backwards" through the multiplier and generate more electrons when they impact the dynodes. The magnitude of this is dependent on the fluorescence intensity and PMT voltage. We typically see secondary ion feedback signal a few hundreds of nanoseconds after the fluorescence begins. By fitting data after the first microsecond, we avoid this signal. The fits were weighted by the LIF intensity squared.[1]

6.4 Comparison of SEELEM spectra with different flight times

The decay of the SEELEM intensity for a line may be measured by observing the SEELEM intensity at a number of different flight times. One way of accomplishing this is to use different carrier gases. Another is to use the same expansion conditions and nozzle-laser delay and vary the laser-free jet excitation region-detector distance. The absolute decrease in a line's SEELEM intensity is not a direct measure of the eigenstate lifetime because, as usual, changes in detectivity affect the intensity. But the relative decrease in SEELEM intensity among lines should reveal variation in SEELEM-detectable state lifetime. This experiment is similar to one Sne and Cheshnovsky carried out.[171]

The absolute SEELEM intensity decrease of a line with increased excitation region-detector distance is due to the state's lifetime and two other factors. It is because of these two factors that the first technique, changing carrier gases, was attempted.

[1]Determining the approximate weighting of the fit is an exercise in propagation of errors. We want to know

$$\sigma^2(\ln(I_{LIF})) = \left(\frac{\partial(\ln(I_{LIF}))}{\partial(I_{LIF})}\right)^2 \cdot \sigma^2(I_{LIF}) = \left(\frac{1}{(I_{LIF})^2}\right) \cdot \sigma^2(I_{LIF}) \tag{6.2}$$

Since $w_i = \frac{1}{\sigma_i^2}$ and assuming $\sigma^2(I_{LIF}) =$ constant

$$w_i = (I_{LIF})^2 \tag{6.3}$$

This result is within a few percent of the true weights, but a more accurate expression is given by Cvetanovic and Singleton[39, 40] and by Deming on pages 191-203 of ref. [41].

First, the detectivity could be greater for the experiments done at larger excitation region-detector distances. Fewer molecules arrive at the surface, so less surface poisoning and/or backscattering can occur. This should not affect the relative intensities, assuming that the detectivity decrease is the same for all the excited eigenstates.

Second, as the detector is pulled back, the solid angle of the detection surface decreases. As a result, fewer excited molecules are collected. This geometric loss can be modeled, as shown in Fig. 3-1 and as discussed in Section 3.1. One might expect that the loss would be proportional to $\frac{1}{r^2}$, but this is not the case. The laser creates a "cylinder" of excited molecules as it passes horizontally through the free jet. The diameter of the cylinder is 0.4 mm. This cylinder will expand as it travels toward the detector. Assuming the molecules expand linearly in the horizontal and vertical directions, as if they were originating from a point source, the length of the cylinder of molecules that will arrive at the 25 mm detector surface equals 25 mm $\cdot$ (2 cm / 12 cm) = 4.2 mm. So a 4.2 mm length of the 0.4 mm cylinder expands to a diameter of 0.4mm $\cdot$ (12 cm / 2 cm) = 2.4 mm when it arrives at the detector. The 25 mm detector surface is under-filled vertically. If the detector is pulled back from 12 cm to 24 cm from the nozzle, the length of the initial cylinder of excited molecules decreases by one-half and the diameter of the cylinder increases to 4.8 mm at the detection surface. Still, the round detection surface is under-filled. There will be negligible loss in signal due to expansion in the vertical direction. The SEELEM signal will decline linearly with distance in the range of detector-nozzle distances used here.

The spectrum of the fractionated R(1) line of $V_0^3K_0^1$ was recorded at four excitation region-detector distances. Fig. 6-6 shows the TOF profiles at the four excitation region-detector distances. Fig. 6-7 shows the four SEELEM spectra. Very little variation in the relative intensities of the lines is apparent. This can be seen more clearly by plotting the spectrum recorded at one laser-nozzle distance against a spectrum recorded at another laser-nozzle distance. If the relative intensities are identical, then the data in this plot will form a line. Fig. 6-7 shows the three spectra recorded with longer laser-nozzle distances plotted against the spectrum with the shortest laser-

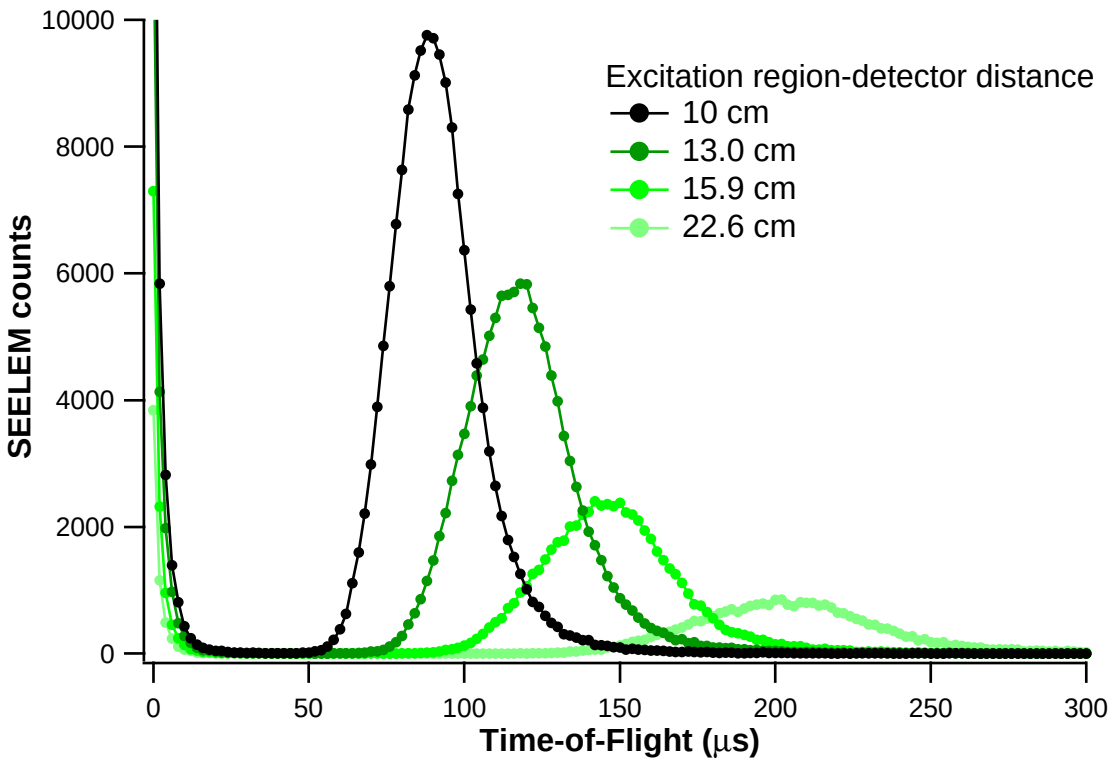

Figure 6-6: The TOF profiles of R(1) of C_2H_2 at 4 excitation region-detector distances.

nozzle distance. Clearly, the variation in the relative intensities is smaller than the noise level.

Lines can be fit to the data in this plot, and the slopes can be related to the decay of the SEELEM intensity for R(1) assuming an exponential decay. The decrease in the number of metastables collected by the detection surface can be factored out, but the change in the detectivity cannot. The SEELEM intensity decreases with a decay constant of $\sim 280 \pm 30$ μs. This constant reflects effects of both the lifetimes and detectivity changes. If, as anticipated, the detectivity increases with laser-nozzle distance, the lifetimes are shorter than 280 μs. This is an upper limit for the lifetimes of the SEELEM-detectable eigenstates.

As with the comparison of the TOF profiles, the lifetimes appear to be very similar. This may be a consequence of this technique's insensitivity to lifetime variation of states with lifetimes longer than the longest flight time. Figures 3-3, 3-4, 3-5, and 3-6 show that the expected SEELEM signal for the four different flight times used here.

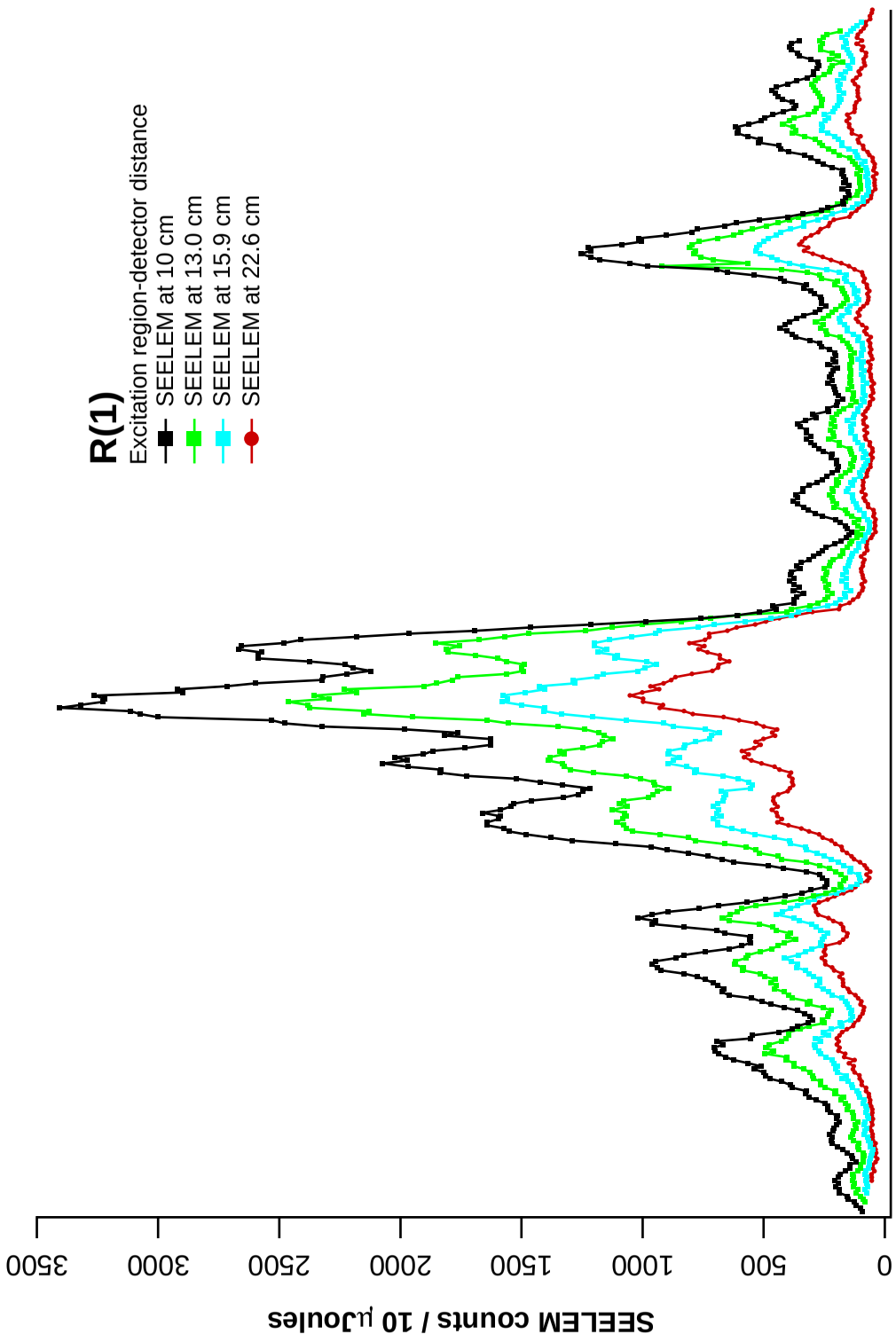

Figure 6-7: The SEELEM spectra of R(1) of C_2H_2 at four different excitation region-detector distances.

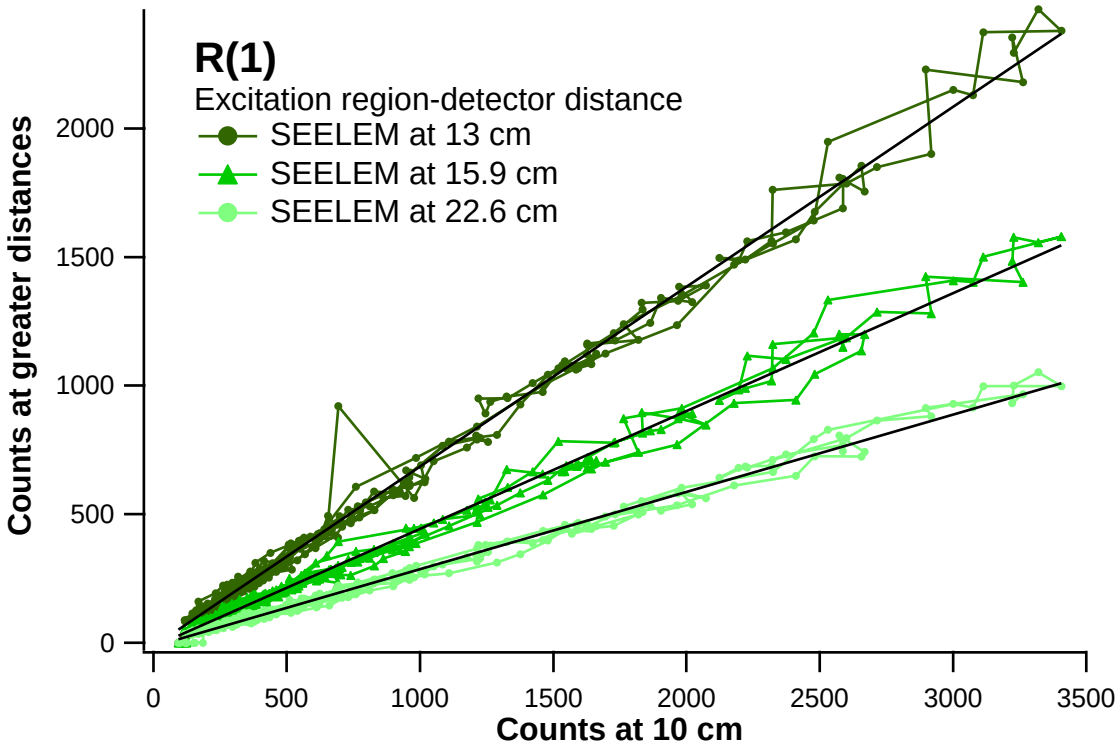

Figure 6-8: Three SEELEM spectra of R(1) plotted against the SEELEM spectrum of R(1) with the detector closest to the nozzle. The linear fits are shown.

The change in SEELEM signal for states with lifetimes varying around 300 μs will not be as dramatic as for states with lifetime varying around 100 μs. The variation may simply be masked by noise in this experiment. It would be interesting to repeat this experiment with flight times longer than 300 μs.

6.5 Discussion

We can conclude from the data that the SEELEM-detectable states have lifetimes no longer than 280 μs and probably no less than $\sim$ 80 μs. There is a gap between 20 and 80 μs where states should be SEELEM-detectable but no evidence for them exists. This indicates that all of the SEELEM-detectable eigenstates have small fractional S_1 characters. We can further conclude that all the lifetimes are similar. These conclusions are problematic. They require that all of the SEELEM-detectable states have similar fractional S_1 characters.

This is not an expected result because the fractional S_1 character in the eigenstates should be widely distributed due to strong variation in the coupling between the S_1 basis state and the background states. The vibrational wavefunctions of the background states should vary, which should result in fluctuations in the vibrational overlap factors between the S_1 and background states. The electronic characters of the background states are composed of differing amounts of T_3, T_2, T_1, and S_0 character, which will cause the electronic part of the coupling matrix element to vary. The energy difference between the S_1 state and the background states also varies. With so much variation in the factors that influence the coupling, one might expect a broad distribution in coupling strengths, which would result in a large range of S_1 characters in the eigenstates. The LIF-detectable states certainly show significant lifetime variation, as shown in Table 6.1.

The SEELEM-detectable states may have nearly uniform lifetimes because of the hierarchical nature of the coupling at this energy in acetylene. The coupling of the $3\nu_3$ basis states to the background states is mediated by a single T_3 "doorway" basis state, as shown in Chapter 4, to which $3\nu_3$ basis state is strongly coupled. The T_3

doorway state is, in turn, strongly coupled to other background triplet states from the T_2 and T_1 potential surfaces. The direct coupling of S_1 to these background triplet states is much weaker than is the coupling mediated by the T_3 doorway state. The coupling of the background triplets to the background S_0 states is small, but much larger than direct $S_1 \sim S_0$ couplings. In other words, there is a hierarchy of couplings, as suggested by Dupré, *et al.* [51] based on their work reported in refs. [48, 50, 51, 49]. They suggested that the coupling strengths between the electronic basis states have the following order: $T_2 \sim T_1 \gg S_1 \sim T \gg T \sim S_0 \gg S_0 \sim S_1$. The hierarchy of couplings results in a hierarchy of states, a hierarchy based on the fractional S_1 character in the eigenstates. Each class of states will have a different characteristic lifetime.

Neither LIF nor SEELEM can be used to observe the entire hierarchy because neither type of spectroscopy is sensitive to the full range of lifetimes in the eigenstates at these energies. LIF only detects states that have lifetimes ¡10 μs. SEELEM detects states with lifetimes > 20 μs. Because they observed states with different lifetimes, they reveal states with different fractional S_1 characters.

To which class of states is LIF sensitive? The density of background triplet states is ~ 9 per cm^{-1}. The density of states observed in the best resolved LIF spectrum, recorded by Drabbels, *et al.*, is also ~ 5 per cm^{-1}.[43] A large fraction, perhaps all, of the dominantly triplet eigenstates near-degenerate to a $3\nu_3$ state are detected in LIF. So, only the eigenstates that have S_0 dominant character remain. Is it possible that the SEELEM signal arises from molecules in these states?

At least one S_0 state would have to be near each LIF-detectable state, within the laser linewidth ($\sim$0.1 cm^{-1}). This is required because, at the resolution of this experiment, there is LIF signal at every excitation frequency at which there is SEELEM signal. The total density of S_0 background vibrational states is $\sim$1000 per cm^{-1}[48]. Sorting these by symmetry reduces the number of available states to $\sim$100 per cm^{-1}. On average, 10 S_0 states with the correct symmetry exist within the laser linewidth. So a few S_0 background states should be near each LIF-detectable state.

The observed lifetime of the SEELEM-detectable states limits the maximum frac-

tional S_1 character in the eigenstates. For example, if an LIF-detectable state has a lifetime of ~ 3 μs, then a near-degenerate S_0 background state must acquire two percent of the character from the nearby LIF-detectable state to have a lifetime of ~ 150 μs. The average separation between the LIF-detectable states and the closest near-degenerate S_0background state is 0.005 cm^{-1}. Using perturbation theory, the coupling between the LIF-detectable S_1 states and the S_0 background states would have to be < 0.0007 cm^{-1} (21 MHz). The Zeeman anti-crossing experiments[48, 51] show that this coupling is a few MHz. It is likely that the most strongly coupled near-degenerate background S_0 states would acquire enough S_1 character from the LIF-detectable states to account for the long lifetimes observed.

These lifetimes are a consequence of the hierarchy of couplings of $3\nu_3$. There are two classes of states with characteristic lifetimes 3 μs (LIF-detectable states) and perhaps 150 μs (SEELEM-detectable states). Few states at these excitation energies have lifetimes in between. If they existed, they would certainly be SEELEM-detectable, as one can see from Fig. 6-1. The apparent uniformity of the lifetimes of the SEELEM-detectable states may result from a lack of sensitivity to longer-lived states. We may only observe those S_0 background states with the largest fractional S_1 character. States with less S_1 character are simply less SEELEM-detectable.

6.6 Conclusions

The SEELEM-detectable states near $3\nu_3$ have dominant S_0 background basis state character with a small amount of S_1 and triplet character. This conclusion is based on the uniformity of the temporal behavior of a number of lines in the R(1) transition of the $V_0^3K_0^1$ band, the decrease in the SEELEM intensity with flight time, and previous estimates of the background density of states and measures of the couplings between these states.

6.7 Future work

This does leave us with one unanswered question: how can the SEELEM signal on $4\nu_3$ be explained? The $4\nu_3$ state lies above the first dissociation limit. All of the S_0 background states should dissociate rapidly. One might expect dissociation on the time scale of a vibrational period of the CH stretch, 3000 cm^{-1}, which corresponds to $\sim$10 fs. Clearly the eigenstates that do survive a $\sim$100 μs flight time must have very little S_0 character in them, $< 1 \times 10^{-7}$. At present, there is little information on the lifetimes of the SEELEM-detectable states at $4\nu_3$. An investigation of the temporal behavior of the $4\nu_3$ signal is required to answer this interesting question.

It may be possible to distinguish which of the two possible explanations for the detectivity decrease, backscattering and surface poisoning, is correct. Surface poisoning should be dependent on surface temperature. If the detection surface is hot enough, the molecules that poison the surface could be driven off the surface over the course of a single pulsed expansion. This would lead to a smaller decrease of signal in the TOF profile. The temperature dependence of this loss may lead to a mechanistic understanding of the poisoning. A sensitivity of the detectivity decrease to surface temperature (and other surface characteristics, like surface roughness and surface material) would indicate that poisoning is the cause, because backscattering is unlikely to be affected by these factors.

No distinction can be made based on nozzle backing pressure, because both will depend on the number of molecules in the beam. The surface poisoning is caused by molecules in the beam de-activating the detection surface, which would depend on the number of molecules that hit the surface. Backscattering from the surface would also depend on the number of molecules that strike the surface.

Chapter 7

De-excitation Mechanisms

7.1 Introduction

One of our most surprising and confounding results is that the relative intensities of the fractionation patterns in the SEELEM spectrum do not change when different metals are used as detection surfaces. Figure 7-1 shows the SEELEM spectra of the R-branch of the $V_0^3K_0^1$ band detected on Cs and Au detection surfaces. The same patterns appear in the SEELEM spectrum recorded with Ag or Cu surfaces. This is not what we expected. Our initial hypothesis was that the quantum yield of Auger electrons would be proportional to the fraction of the eigenstate composed of basis states whose electronic character has energy exceeding the metal work function, as discussed in Section 2.1.5. This would cause the relative SEELEM intensities of a set of lines to differ on different detection surfaces due to variation in the electronic characters of the eigenstates.

For example, the work function of Au is 5.1 eV.[106] Only the T_3 and S_1 electronic surfaces of acetylene have enough electronic energy to eject an electron from Au. Cs has a work function of 2 eV. All of the excited electronic states of acetylene can eject an electron from Cs. Consider two eigenstates with an identical but small fractional S_1 character. The states are distinct in that the first contains predominantly T_1 character and the second contains predominantly T_3 character.

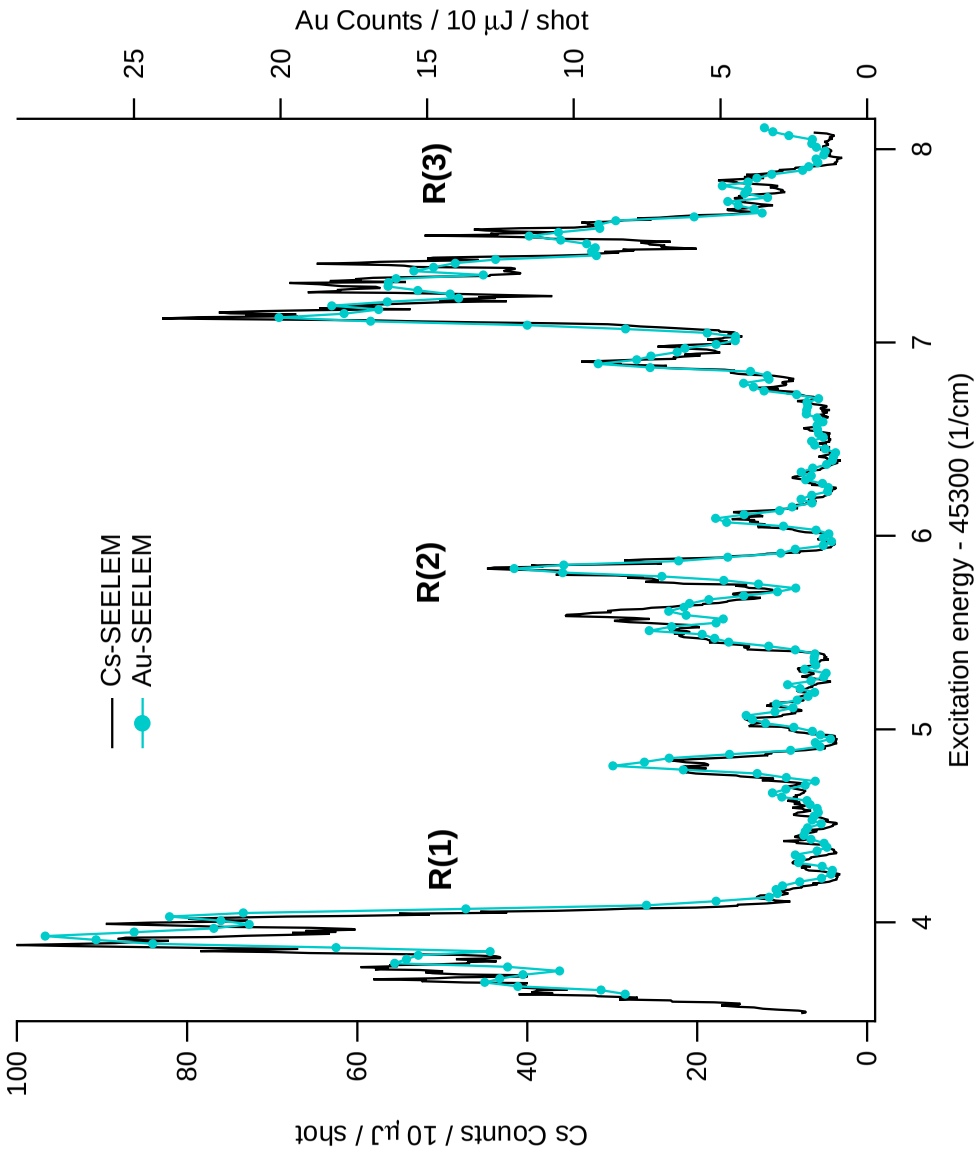

Figure 7-1: The SEELEM spectra of the R-branch of the $V_0^3K_0^1$ band. Negligible differences between the relative intensities are apparent.

$$\begin{aligned} \Psi_1 &= a^2\ \psi_{S_1} + b^2\ \psi_{T_1} \\ \Psi_2 &= a^2\ \psi_{S_1} + b^2\ \psi_{T_3} \end{aligned} \tag{7.1}$$

The S_1 character provides the excitation oscillator strength to these eigenstates, so the two states are equally populated by a laser. When molecules in Ψ_1 approach a Au surface, only the S_1 character will contribute to the ejection of electrons. In contrast, when molecules in Ψ_2 approach a Au surface, both the S_1 and T_3 components can provide enough energy to eject electrons from the surface. On a Cs surface, molecules in either state will be able to provide sufficient energy to eject electrons, so transitions to these two states should have the same SEELEM intensity. In the Au spectrum, the two states would have vastly different SEELEM intensities.

Accordingly, we expected that the relative intensities of lines in the SEELEM spectra would be different with different detection surfaces. This would provides us with information on the relative characters of various basis states in the SEELEM-detectable eigenstates. However, the Au and Cs $V_0^3K_0^1$ acetylene SEELEM spectra have the same relative intensities.

There are several possible explanations for the lack of variation of the relative intensities. Perhaps the S_1 and the T_3 characters are more Auger detectable than are T_2 and T_1. S_1 and the T_3 do have more excitation energy than do the lower states, so these states could excite a larger fraction of the electrons in the metal conduction band above the work function. This increase in Auger electron quantum yield is more important than the contribution of the two lower triplet states. However, this effect should be offset, at least in part, by the fact that the eigenstates should contain much more T_2 and T_1 character than S_1 and the T_3 character.

Another explanation is that the S_1 is the only basis state that contributes Auger detectability to an eigenstate. The de-excitation mechanism through an eigenstate's S_1 character is different than the mechanism through an eigenstate's triplet character, as discussed in Section 2.1.3. Because triplets have no oscillator strength to the S_0

surface, their de-excitation is dominated by an exchange of electrons with the metal. To de-excite through the exchange mechanism, the molecule must be near enough to the surface for significant overlap to exist between the molecular wavefunctions and metal electron wavefunctions. In contrast, singlets can de-excite when the metal surface enhances their inherent spontaneous emission probability. The singlet de-excitation mechanism can occur through long-range electric interactions. It is possible that most of the metastables have de-excited through their singlet character long before they are near enough to the surface to de-excite through their triplet character. If this is true, the relative intensities of lines in the SEELEM spectrum would not change because the SEELEM signal on any surface would be dependent only on the fractional S_1 character.

We will try two simple calculations to explore this hypothesis. The first calculation models the excited molecule as it approaches the metal as a classical oscillating dipole nearing a reflective surface, an approach introduced by Silbey and co-workers.[25] This model has successfully described increases in the decay rate of excited molecules near surfaces. The model is valid at molecule-surface distances as small as 10 Å. If this calculation shows that a significant fraction of the metastable molecules de-excite at this range, we can conclude that most of the de-excitation occurs through the state's fractional S_1 character. The second calculation reduces the problem to the simplest quantum mechanical interaction that can account for the de-excitation. Although the calculation is too simple to arrive at realistic results, it illustrates the elements of the calculation and the complications that must be addressed to arrive at an accurate result. These calculations address a problem which, to my knowledge, has not been addressed before: the de-excitation of a molecule in a state with mixed-spin character.

7.2 Classical oscillating dipole model

The classical oscillating dipole model was developed by Chance, Prock, and Silbey (hereafter referred to CPS)[25] to account for changes in lifetime and quantum yield of excited molecules near metal surfaces. As an electronically excited molecule ap-

proaches a metal surface, the molecule interacts with its image inside the metal. These long-range electric forces will alter the lifetime of the state. The model attempts to account for this change by representing the excited state as a classical oscillating dipole and the surface as a reflective mirror. An oscillating dipole is a good classical analogy for an excited molecule because they both radiate a dipolar field. The mirror is modeled using a dielectric constant appropriate for the metal. The radiation of energy from the dipolar field is calculated entirely with classical electrodynamics.

A number of experimental results have verified the model's predictive ability at a range of molecule-surface distances.[23, 211, 210, 7] Harris and co-workers have summarized the success of the CPS approach in ref. [202]. However, the CPS model underestimates the rate of emission when the molecule is closer than 10 Å to the surface. One of the reason for this will be discussed below.

This calculation will determine the number of the metastables that will be de-excited at molecule-surface distances greater than 10 Å. Only the S_1 character in the eigenstate provides oscillator strength to the ground state, so only the S_1 character is relevant to this process. Although the calculation's validity is limited to distances greater than 10 Å, the calculation is simple, and its interpretation is clear. This calculation will show whether these long-range interactions are responsible for the SEELEM signal.

There is oscillator strength from the T_3 and T_2 states to the T_1 state, but it will not compete with the emission from the singlet state. Triplet emission differs from singlet emission in two ways. The isolated molecule emission rate is likely to be lower for triplets, as was discussed in Chapter 3. In addition, the emission frequency of triplet is lower than for the singlet. The metal dielectric constant is dependent on the emission frequency. As a result, the emission rate of the dipole to the surface is enhanced if the dipole emits at higher frequencies. Both of these factors will lower the triplet emission rate near a surface relative to that for a singlet.

Although a complete discussion of the theoretical approach is in CPS, the following briefly outlines the calculation. The rate of emission is determined by calculating the energy flux of the dipolar radiation through two defined planes, one plane between

the dipole and the mirror and another plane above the dipole (CPS eq. 2.30). The energy flux is equivalent to the projection of the complex Poynting vector of the radiation normal to the defined plane integrated over the entire surface of the plane. The Poynting vector is rewritten in terms of Hertz electrodynamic potential vectors, which are defined for every point on the planes (CPS eq. 2.31). The expressions for the Hertz vectors are dependent on the distance of the dipole from the mirror and the dielectric constant of the mirror. The dielectric constant is, in turn, dependent on the relaxation time and plasmon frequency of the metal, and the dipole oscillation frequency. The Hertz vectors are Fourier transformed into wave vector space and divided by the wave vector of the oscillating dipolar field, yielding expressions in terms of a normalized wave vector (CPS eq. 2.9 and 2.10). After some manipulation, expressions for the energy flux through each plane are produced in terms of the normalized wave vector, the dielectric constant, and the dipole-mirror distance (CPS eq. 2.32).

A few additional steps provide convenient expressions for the rate of emission. The energy flux is divided by the energy of the dipole ($\frac{1}{2}\omega^2 m|\mu|^2/e^2$, where ω is the dipole oscillation frequency and μ is the magnitude of the dipole), which gives a rate (CPS eq. 2.35). The rate is divided by the rate of emission in the absence of the mirror, which gives a unitless quantity, the value of which is the amplification of the original rate. This is convenient because the emission rate of the eigenstate can be introduced at the end of the calculation. These expressions are integrated over the normalized wave vector to produce the amplification. The expressions used in this work appear in equations 2.36, 2.37, 2.39, and 2.40 of CPS.

These expressions can be used directly because the geometry of our system is simple – a metastable molecule in vacuum over a metal surface. We do not model surface roughness nor any oxide or other layers on the surface which have a dielectric constant different than that of the metal. Adjustments for these complications are discussed in refs. [25, 202].

The theory does not address what happens to the energy once it leaves the dipole and how likely it is that an electron will be ejected from the surface. Although no

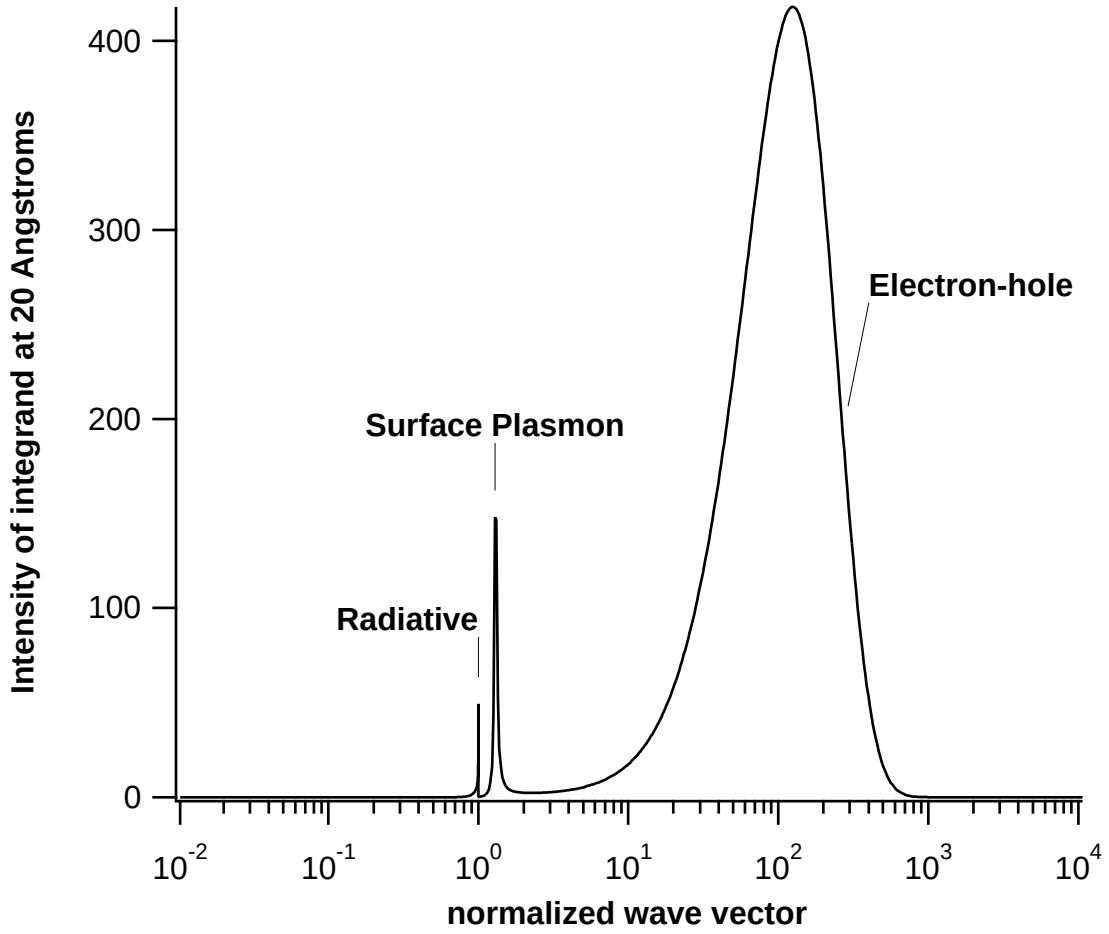

Figure 7-2: The value of the distance dependent integrand for a dipole perpendicular to the surface from CPS eq. 2.37. This shows the three wave vector regions responsible for de-excitation of the dipole. The wave vector is normalized so that the wave vector of the field radiated by the dipole is unity.

attempt shall be made to calculate the number of ejected electrons, the following discusses the various de-excitation mechanisms that one can distinguish in the CPS calculation. The normalized wave vector dependence of these expressions contains mechanistic information, as shown in Fig. 7-2. All of the mechanisms are likely to produce Auger electrons.

When the dipole is far from the surface, the only coupling is through wave vector components smaller than that of the radiated field. This is because the field emitted at an angle to the surface will create charge variation with the wave vector of the light, as shown in Fig. 7-3. The field emitted by the dipole directly toward the

surface will cause surface charge variation with a wavelength larger than the light. So the wave vector will be shorter. At long range, all the coupling is through wave vector components equal to or smaller than that corresponding to the frequency of the oscillating dipole. Some of the energy emitted will be absorbed by the surface which may eject electrons in a process similar to the photoelectric effect. This mechanism will be referred to as the radiative mechanism.

If the mirror-dipole distance is comparable to the wavelength of the emitted light, the dipole couples to the surface plasmon modes. This coupling is at wave vector components greater than that of the radiated field because the nearfield components of the dipole become strong at the surface. The nearfield refers to the region close to the dipole where there is rapid spatial variation of the emitted field, as shown in Fig. 7-3. As the dipole approaches close to the surface, the nearfield components begin to excite the resonance frequency of the surface charge density, creating surface plasmons. Surface plasmons in the metal have frequencies just greater than that of the oscillating dipole. Woratschek,*et al.*[213]observed electron emission due to surface plasmons, so this process man also produce ejected electrons.

When the dipole travels within ~ 50Å of the mirror, coupling through high wave vector components becomes strong. The nearfield induces increasingly higher wave vector components in the surface charge density as the distance becomes comparable to the dipole length. The coupling is strong because these high wave vector components impart enough momentum to the metal to excite excitons, excited electrons and holes in the metal. The simple quantum mechanical picture of the Auger effect introduced in Section 2.1.3 also results in the creation of excitons in the metal. So electron emission can presumably result from this process.

While all of these processes de-excite metastables, each process may not generate ejected electrons with the same quantum efficiency. Some additional theory would be needed to calculate the quantum yield of ejected electrons for each type of electron excitation. This calculation will not estimate the number of electrons that are ejected, but it will show whether the incoming population of metastables can be de-excited at a large distance from the surface. Presumably, some fraction of these de-excitation

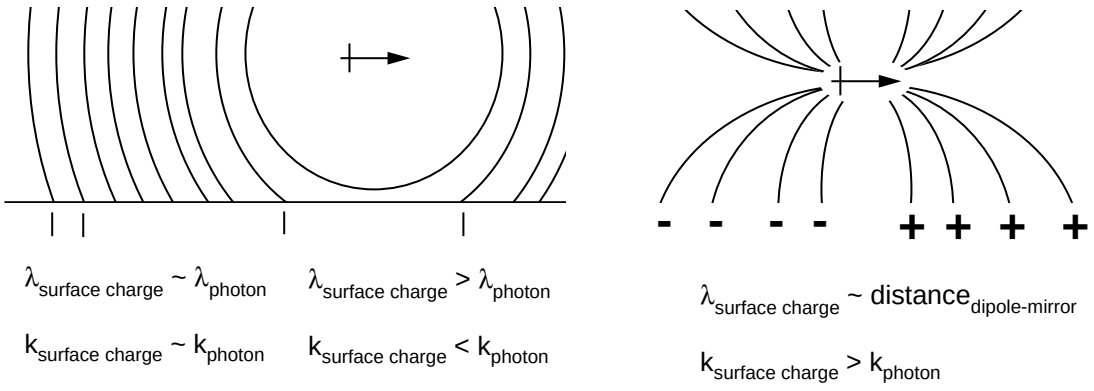

Figure 7-3: The spatial variation of surface charge due to the field emitted by the dipole has a similar or greater wavelength than that of the emitted field when the dipole is far from the surface. When the dipole nears the surface, the wavelength of the spatial variation becomes smaller than that of the field emitted by the dipole and nears the dimension of the dipole.

events result in ejected electrons.

The calculation requires a number of parameters. The metal relaxation time and plasma frequency are needed to calculate the dielectric constant and were taken from Ashcroft and Mermin.[8] The quantum yield was set to unity. The velocity of the dipole toward the surface, which is needed to calculate the survival probability, was set to 1000 m/s, which is the velocity of a pure acetylene in the free jet with 1 atmosphere backing pressure. The dipole oscillation frequency was set to 1.2×10^{15} 1/s, corresponding to 40,000 cm^{-1}. Excited acetylene emits at many frequencies, decreasing from 45,300 cm^{-1}. The emission strongest at 40,000 cm^{-1}. The radiative rate was varied from 3.7×10^6 1/s (270 ns lifetime) to 3.7×10^2 1/s (2.7 ms lifetime). This represents the range of rates possible in the SEELEM-detectable states.

The Drude dielectric constant with relaxation time (CPS, Section IV) is used in these calculations.

$$dielectric\ constant = 1 - ((\omega_{plasma})^2/(\omega_{dipole} \cdot (\omega_{dipole} + i/\gamma_{relaxation}))) \qquad (7.2)$$

where ω_{plasma} is the plasma frequency, ω_{dipole} is the frequency of the oscillating dipole, and $\gamma_{relaxation}$ is the metal relaxation time. The Drude model of metals is discussed in Ashcroft and Mermin.[8] Briefly, the Drude model treats electrons as a neutral gas. Like a gas, the electrons are said to have a mean free path and travel in straight lines between collisions despite the large amount of surrounding charge. The relaxation time is the time between collisions. As originally proposed, the collisions are between the electrons and the nuclei, but the relaxation time used in this calculation is phenomenological. The "collisions" are due to several scattering processes. The Drude model has been reasonably successful considering its simplicity. (See Ashcroft and Mermin[8] for a discussion of the model's applicability)

The Drude expression for the dielectric constant used in this calculation is valid as long as the spatial variation of the field is larger than the mean free path. If the field varies within a mean free path of the electron, the electrons will not travel in straight

lines. In other words, the "local" field must be constant for the expression of the dielectric constant to be valid. The local dielectric constant used in this calculation fails to properly describe the response of the surface electrons as the distance between the dipole and the surface becomes small, 10 Å. This is why this calculation underestimates the emission rate when the dipole is close to the surface. Using a non-local dielectric constant would result in a more realistic and larger coupling of the dipole to the surface at small dipole-mirror distances. (Non-local dielectric constants are discussed in several references in Harris and co-workers [202])

The CPS equations have a term that is distance dependent and one that is not. The distance independent term is due to radiative coupling to the surface and only contains wave vector components less than that of the radiated field. This term accounts for the emission of radiation that would take place in the absence of a surface. The distance dependent terms in the decay rate are due to the presence of the surface. These terms account for coupling at all wave vectors. By decomposing these terms into three characteristic regions of wave vector space, the rate of de-excitation due to each of the three mechanisms, radiation, surface-plasmon, and excitons, can be calculated separately.

The rates were calculated by integrating the expressions over the three regions of wave vector space corresponding to the three mechanisms. These rates were calculated over a range of dipole-surface distances 5000 to 0.1 Å, and the results are shown in Fig. 7-4. The oscillations in the rate are due to the reflected field constructively and destructively interfering with the dipole's oscillation, resulting in variation of the emission rate. Only the farfield interactions are clear on this scale. Figure 7-5 shows the results for a range of distances on the order of a wavelength of the oscillation frequency of the dipole. The coupling to the surface plasmons becomes significant for these distances. At shorter range Fig. 7-6 shows that coupling to excitons dominates the de-excitation.

The survival probability (Fig. 7-7) shows the proportion of incoming metastable molecules that remain excited at a given distance. At the beam velocity and radiative rate used here, approximately one percent of the incoming metastable molecules

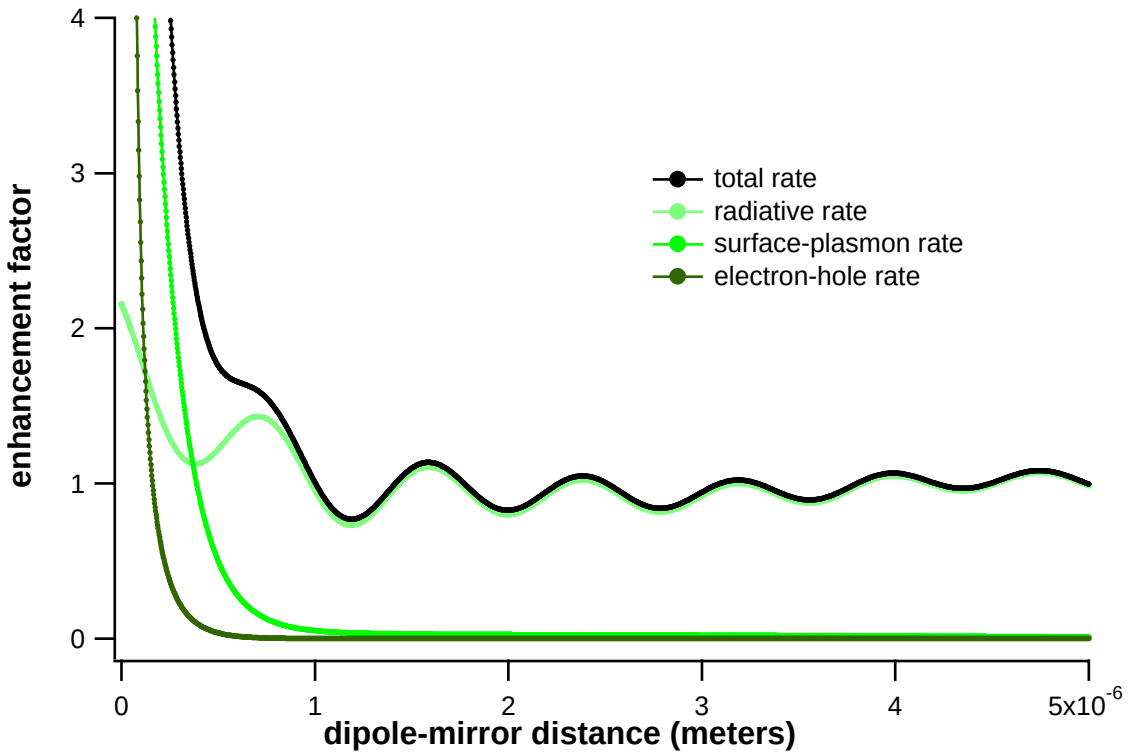

Figure 7-4: The modulation of the rate of emission due to the presence of the surface.

de-excite before they reach a distance where the calculation loses its validity. In particular, only ~ 0.1 percent of the molecules in states with lifetimes of 300 μs are de-excited by the time they are within 10 Å of the surface. The molecules in the free jet are moving too quickly to be de-excited at molecule-surface distances greater than 10 Å. The molecules are moving 1 Angstrom in $\sim 1 \times 10^{-13}$ s. For a significant number of metastables to be de-excited, the rate must be $\sim 1 \times 10^{11}$ or $\sim 1 \times 10^{12}$ for the final few Å from the surface. If the radiative rate in the absence on the surface were $\sim 1 \times 10^{4}$, this would require an enhancement of $\sim 1 \times 10^{7}$ or $\sim 1 \times 10^{8}$. The calculation does not predict this until well within the region where the calculation is no longer valid.

The review by Waldeck, Harris, *et al.* discusses many improvements on the original CPS theory.[202] These improvements include expressions that account for the effects of surface roughness (which affects the signal level, as shown in Section 2.3.2) and an expression for a more realistic, "non-local" dielectric constant. In addition, CPS

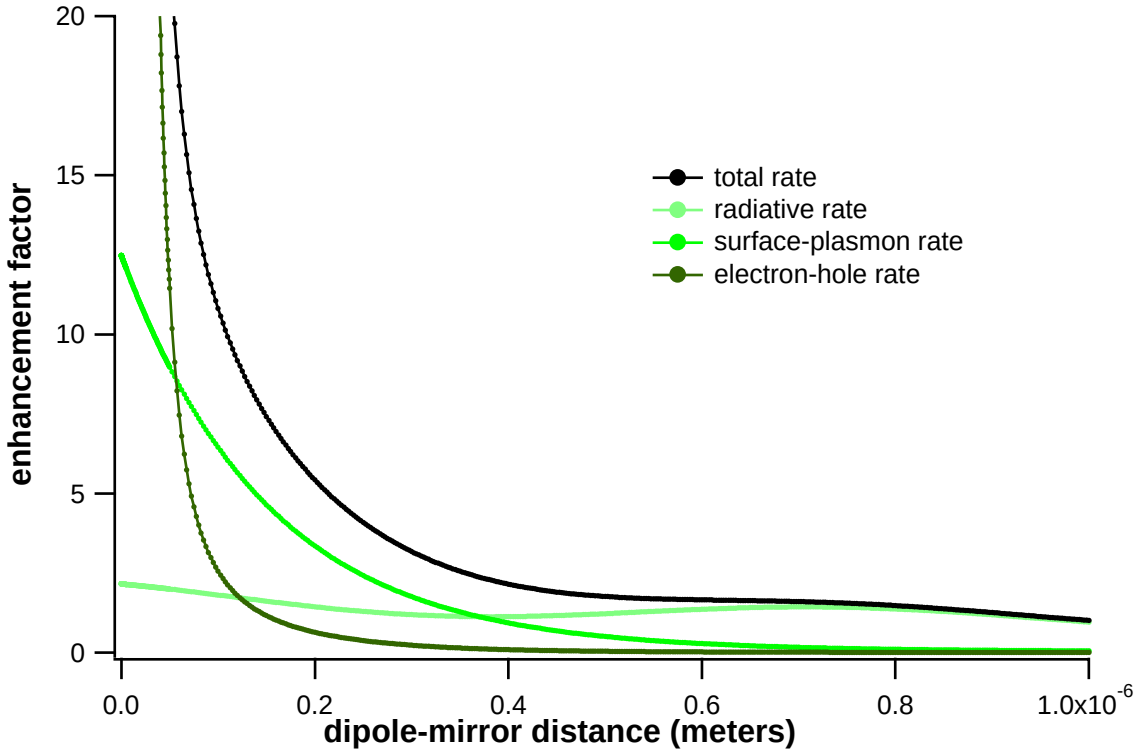

Figure 7-5: The enhancement of the rate of emission due to the presence of the surface. Coupling to the surface plasmons is now evident.

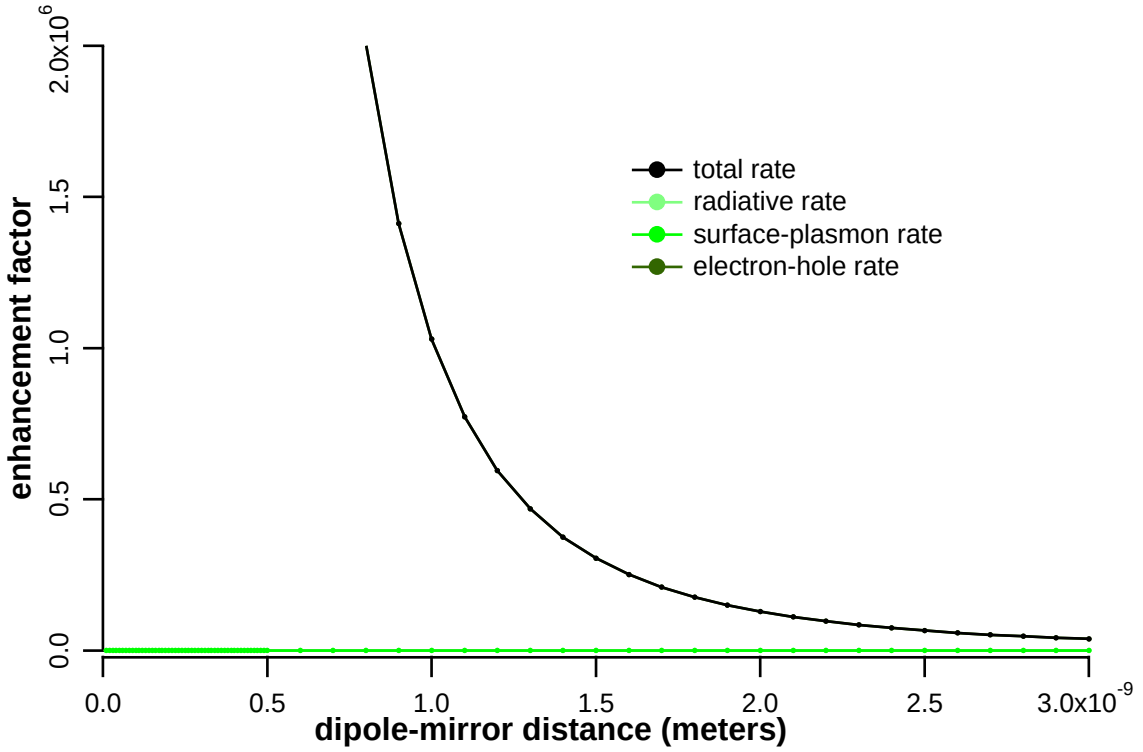

Figure 7-6: The enhancement of the rate of emission due to the presence of the surface. Coupling to excitons in the metal is now evident.

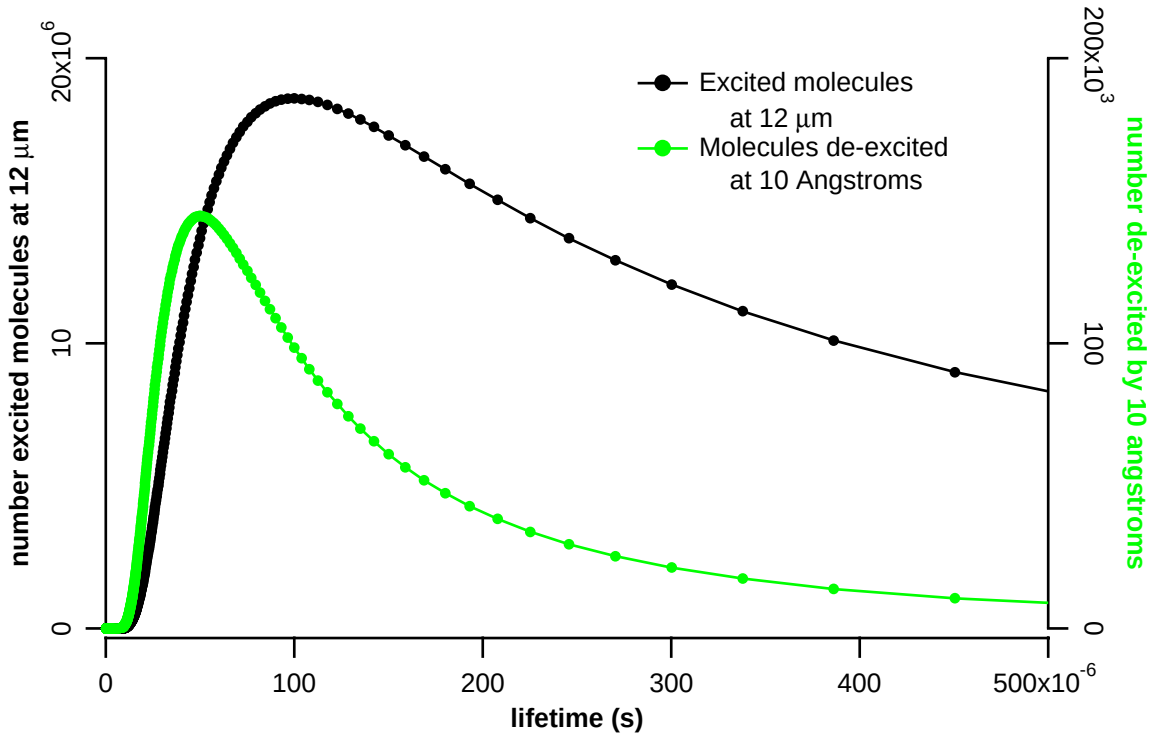

Figure 7-7: The number of metastable molecules that will be de-excited at 10 Å through their fractional S_1 character. Note that the right and left axes have different scales.

discusses the effect of layers on the surface that have a dielectric constant different than the metal.[25] This could account for an adsorbate layer on the surface. These improvements could lead to a faster calculated decay rate.

The hypothesis that S_1 basis state character dominates the de-excitation is certainly not confirmed by this calculation, but the hypothesis is not ruled out either. In fact, it is clear that at least some small fraction of the metastable molecules must be de-excited through their S_1 character at molecule-surface distances $>$ 10 Å. The Auger electron quantum yield is estimated to be $\sim 5 \times 10^{-6}$. So, de-excitation of 0.1 percent of the incoming metastable molecules could account for the signal if the probability of electron ejection by the metal after de-excitation is 0.005.

While it appears that the S_1 character cannot be responsible for the de-excitation of the majority of the metastables beyond 10 Å, it might still dominate the de-excitation within this distance. The following section will attempt to address this

question by discussing a quantum mechanical model.

7.3 Quantum mechanical approach

We would like to evaluate the integrals introduced in Section 2.1.3 and shown below. A few calculations of this kind have been made previously. The earliest were by Massey[117, 118] and by Cobas and Lamb[29]. Calculations of Penning ionization require the evaluation of similar integrals. Miller and co-workers conducted a number of successful early *ab initio,* calculations[122, 123, 124]. Wang and Ertl calculated the surface Penning ionization rate for a metastable He atom approaching a surface covered with a monolayer of CO[204]. More recent calculations include those of Penn and Apell[157]and those of Burrows, *et al.* [22]. Note that all of these calculation are for a relatively simple metastable atom. As will become apparent, evaluating these integrals is not a simple task.

$$\gamma_{\,Coulomb} = \int\int \psi^*_{free}(\mathbf{r_1})\ \psi^*_{ground}(\mathbf{r_2})\ \frac{e^2}{|\mathbf{r_1}-\mathbf{r_2}|}\ \psi_{excited}(\mathbf{r_2})\ \psi_{metal}(\mathbf{r_1}) d\mathbf{r_2}\ d\mathbf{r_1} \quad (7.3)$$

$$\gamma_{\,exchange} = \int\int \psi^*_{free}(\mathbf{r_1})\ \psi^*_{ground}(\mathbf{r_2})\ \frac{e^2}{|\mathbf{r_1}-\mathbf{r_2}|}\ \psi_{excited}(\mathbf{r_1})\ \psi_{metal}(\mathbf{r_2}) d\mathbf{r_2}\ d\mathbf{r_1} \quad (7.4)$$

In fact, the attempt to evaluate these integrals here is not satisfactory because the wave functions are too simple, the calculation is limited to one dimension, and the $\frac{1}{r_{12}}$ term is not handled with proper sophistication. But it does demonstrate the qualitative effects that we expect and the issues that need to be addressed to do a more realistic calculation.

To keep the calculation simple, the problem is reduced to a single dimension, that of the distance of the metastable from the surface. The four wave functions are one dimensional. ψ_{free} and ψ_{metal} are the solutions for the one dimensional potential step problem. The height of the step is the work function plus the band depth as

calculated from the free-electron, Drude metal expression in equation 2.25 of Ashcroft and Mermin.[8] The band depth is the energy between the Fermi level and the bottom of the conduction band. Ψ_{free} is the wave function for a particle 0.05 eV above the step. This wave function has a real and an imaginary part. Ψ_{metal} is the wave function of a particle 5.55 eV below the step (0.45 eV below the Fermi level). Since the calculations were only carried out for regions outside the surface, Ψ_{metal} is real and is consists only of an exponential decay of the wavefunction into the classically forbidden region. The wave functions are defined from the surface to 50 Å into the vacuum, with a grid spacing of 0.1 Å. The rates were recalculated with the electron starting at 0.05 eV below the Fermi level. There was very little change in the results. A more realistic calculation would evaluate the integrals for a range of metal electron energies that exist in the conduction band.

$\psi_{excited}$ and ψ_{ground} for acetylene are too complicated to replicate. The eigenstates we excite have heavily mixed electronic and vibrational character. The de-excitation will leave the molecule in one of a large number of S_0 vibrational states. In addition, the de-excitation probably has a dependence on the orientation of the molecule relative to the surface. If the π orbital containing the excited electron is oriented toward the surface, the rate might be different than if the molecule were approaching the surface end on. When the molecule is within a few Angstroms of the surface, the overlap between the molecular wavefunctions and those of this surface will begin to lead to acetylene orbital rehybridization. This is far beyond the scope of this calculation. These surface-molecule interactions may also tend to align or steer the molecule as it approaches. This calculation simply uses an exponential function with an average radius equal to the average radius of an ns hydrogenic wave function.

$$\begin{aligned} \psi_{ground}(x) &= \sqrt{\frac{1}{r_g}}\, e^{\left(\frac{-x}{r_g}\right)} \\ \psi_{excited}(x) &= \sqrt{\frac{1}{r_e}}\, e^{\left(\frac{-x}{r_e}\right)} \\ r &= \frac{3a_0}{2} \cdot \frac{R}{E_B} \end{aligned} \tag{7.5}$$

where R is the Rydberg constant, E_B is the binding energy (the ionization potential minus the excitation energy), a_0 is the Bohr radius, and r_g and r_e are the average radii of the states as calculated using the Rydberg formula. Obviously, these wave functions do not contain the complicated shape of the real wave functions, or even the radial nodal structure of the hydrogenic functions, but they do approximate the outer edge of the wave functions. This is the most important part, since the tunneling "exchange" term is governed by the initial overlap of ψ_{metal} with ψ_{ground}.

These wave functions are multiplied together to generate one-electron functions. For the "Coulomb" term, ψ_{ground} and $\psi_{excited}$ are multiplied for electron 1, while ψ_{metal} and ψ_{free} are multiplied for electron 2. The pairings of the wave functions are reversed for the "exchange" term.

To calculate the double integral over each electron, the vectors representing one-electron functions are multiplied to make a matrix. Element (r, q) of this matrix represents the joint probability of finding electron 1 at distance r and electron 2 and distance q.

Each point is multiplied by a value that is equal to the inverse of the point's distance to the diagonal. This results in the integrand for each point in the grid. The values of the matrix elements are summed to arrive at a value that is proportional to the integral. One difficulty arises because there are points of this integral where both electrons are at the same distance. The $\frac{1}{r_{12}}$ term is infinite at these points, of course. This integral diverges, which is unrealistic. Integrals of this type should converge. There are approaches that would lead to convergence of this integral. For instance, if all the wave functions could be approximated by Gaussians, the integral could be evaluated using the procedure in Appendix A of Szabo and Ostlund[187]. Miller evaluates an integral similar to this for the Penning ionization of hydrogen atom by He(^3S).[122] A better approach to this would improve the calculation in only a single way and was not pursued. In these calculations, the value of these points have been set to zero, as if the two electrons are never within one grid point. This simulates the phenomenon of electron correlation where two electrons tend to avoid each other.

To get some quantitative notion of the number of metastables de-excited, these

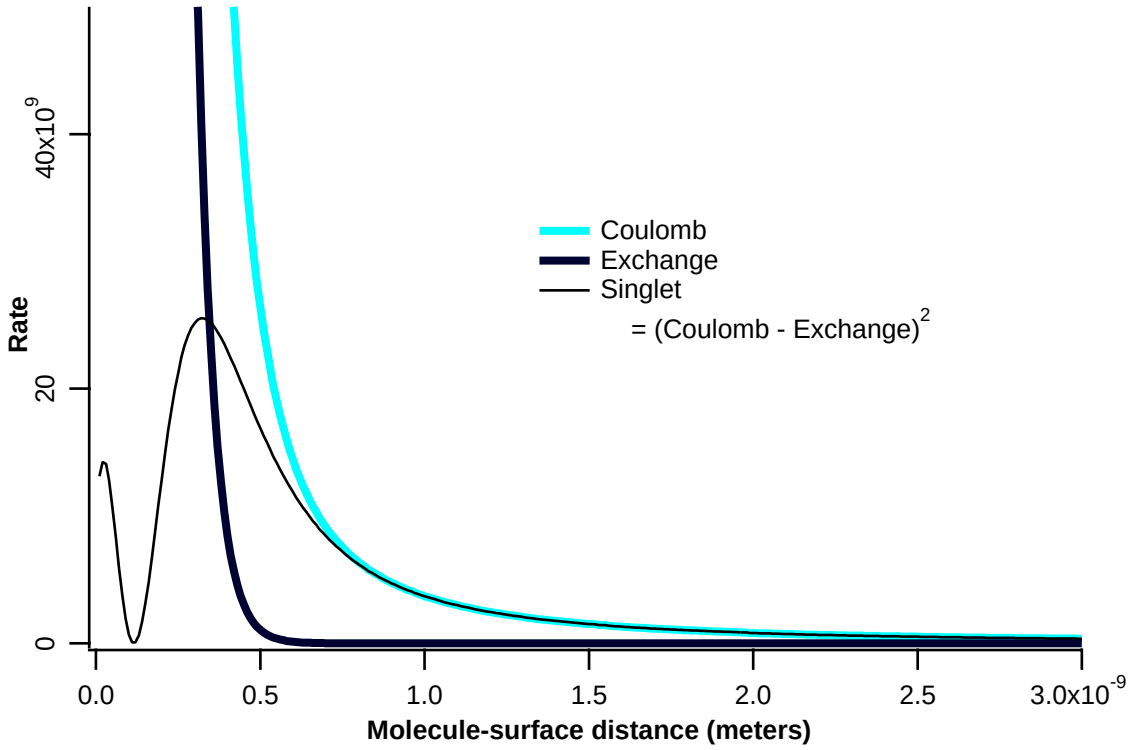

Figure 7-8: The rates of de-excitation. The de-excitation rate of a triplet will be that of the exchange mechanism.

results are scaled by the rate at 10 Å as calculated from the classical oscillating dipole model. Presumably, the classical rate at 10 Å is equal to the Coulomb mechanism at that distance. Figure 7-8 shows the de-excitation rates of a singlet state and of a triplet state. The rate for a singlet state was calculated as $\mid \gamma_{Coulomb} - \gamma_{exchange} \mid^2$, while the rate for a triplet state is calculated as $\mid \gamma_{exchange} \mid^2$.

The results of the integrals at each molecule-surface distance are the instantaneous rates. We would like to know the probability that an excited molecules survives to a given molecule-surface distance. The number of molecules de-excited at each distance with in 50 Å was calculated by using eq. 36 in Hagstrum[64]. For the singlet states, the number of excited molecules at 50 Å was calculated with eq. 3.4. For this calculation, the singlet de-excitation rate was multiplied by the fractional singlet character in the eigenstates. The results for the number of molecules de-excited at 1, 2, and 4 Å from the surface are shown in Fig. 7-10.

There is no correlation expected between triplet character and eigenstate lifetime,

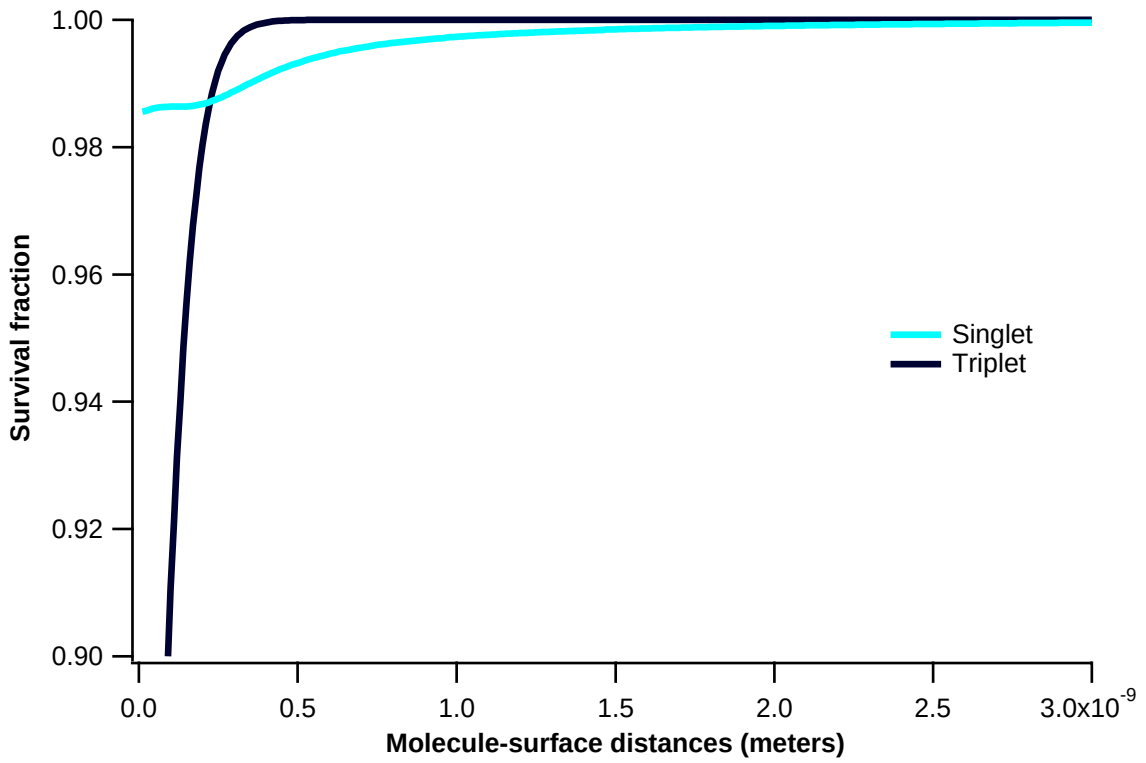

Figure 7-9: The survival probability. Only a few percent of the incoming molecules de-excite through the singlet route before the triplet mechanism becomes dominant at ~ 3 Å. The scale on the right has been expanded for clarity.

so the survival of the triplet states shown in Fig. 7-9 was calculated with two assumptions. First, the rate is assumed to be entirely dependent on triplet character, so the de-excitation rate equals the rate of the pure triplet multiplied by the fractional triplet character. Second, the number of molecules remaining at 50 Å is assumed to be the same for a given fractional triplet character as for a given fractional singlet character. This is equivalent to assuming that the fractional singlet and triplet character in a given eigenstate is the same. So, the number of triplets de-excited at 1 Å for a lifetime of 270 μs is equal to the number of molecules in eigenstates the de-excitation rate of which is dictated by the 0.001 fractional triplet character and a lifetime dictated by 0.001 singlet character. Although this is not a realistic situation, the calculation shows that the triplet mechanism is not important until the molecule is within a few Angstroms of the surface, at which point it dominates the de-excitation.

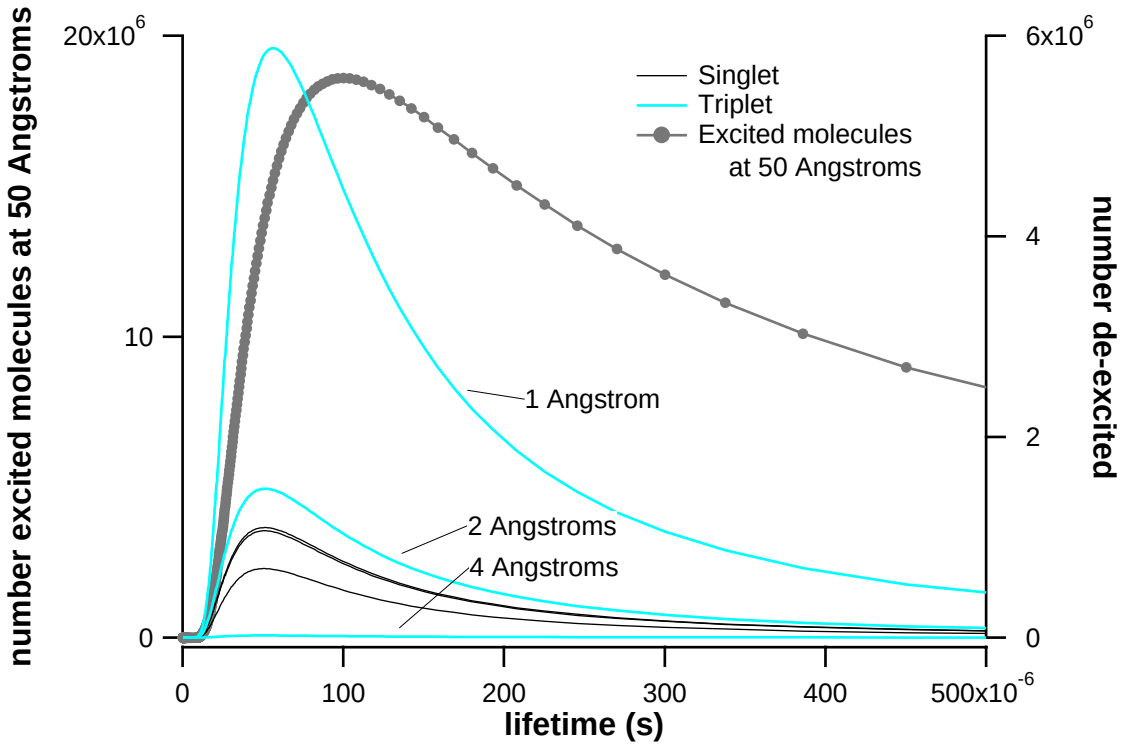

Figure 7-10: The number of metastable molecules that will be de-excited by 1, 2, and 4 Å. This number increases as the molecule draws near to the surface.

The calculation indicates that the triplet mechanism dominates the singlet mechanism once the metastable molecule is within a few Angstroms of the surface. As in the classical oscillating dipole model, the singlet de-excitation rate in this calculation simply does not grow large enough to de-excite the majority of excited molecules before the triplet exchange mechanism takes over. However, this small fraction of de-excited molecules could still account for the observed signal, as discussed above.

Clearly this calculation is suspect. Could it be biased against the singlet mechanism? The increase in the rate as the molecule nears the surface is not as fast for this model as it is in the classical oscillating dipole model. This is odd because the CPS model is supposed to yield rates that are increase too slowly as the molecule nears the surface. One would expect that a more realistic model would predict rates that grew more quickly than CPS as a function of molecule-surface distance. The fact that this simple quantum mechanical model does not do that indicates that it may not be a more realistic model. The effects of surface roughness and non-local effects on the dielectric constant may result in the CPS rate at 10 Å being much too low. An enhancement of this rate would lead to a de-excitation of a larger fraction of the metastable molecules via the singlet path before the triplet path becomes significant. In addition, treating the many complications more properly may result in a higher calculated singlet de-excitation rate.

In the end, the hypothesis is only partly confirmed. The CPS calculation shows that approximately one percent of the excited molecules de-excite through the singlet character of the eigenstate outside of 10 Å. This calculation indicates that additional excited molecules will be de-excited via the singlet character within 10 Å. So, a small fraction of the excited molecules certainly de-excite via the singlet character in the eigenstates, but it is not clear if this accounts for the observed signal.

Excited molecules may be prevented from de-exciting via the exchange mechanism because of surface conditions like an adsorbate layer. Before the excited molecule is sufficiently close to the surface to de-excite via the exchange mechanism, the excited molecule may collide an adsorbate molecule before and give up its energy via some process which does not result in an ejected electron.

7.4 Conclusions

The classical oscillating dipole model shows that approximately one percent of incoming metastables will be de-excited by the singlet path for the range of fractional singlet character that we expect to exist in our experiments. Because this model has been experimentally verified, this amounts to a low limit. It is possible that this small fraction of the excited molecules accounts for the SEELEM signal. More work is required to confirm this.

7.5 Acknowledgments

Thanks to Prof. Robert Silbey for several helpful discussions.

Chapter 8

Pattern Recognition by Extended Auto Correlation (XAC)

8.1 The problem

SEELEM spectroscopy is exquisitely sensitive to states that are weakly coupled to the S_1 basis states. Eigenstates with only ~ 0.002 fractional S_1 character are detected in a SEELEM spectrum, as discussed in Chapter 6. A given rotational transition, such as the R(2) transition in the $V_1^3K_1^0$ band shown in Fig. 8-2, may be fractionated into a set of background states. The $3\nu_3$ 3_{03} basis state is mixed with background states, which forms several SEELEM-detectable eigenstates. Analysis of the intensities and energies of this set of R(2) lines may reveal information about the interactions between the singlet state and the near-degenerate background states.

There is a problem to solve before these lines can be analyzed. We have to distinguish between lines belonging to R(2) and lines belonging to adjacent rotational transitions. As one can see in Fig. 8-1, the 3_{03} doublet pattern appears in P(4), Q(3), as well as R(2)., but the smaller lines could belong to several different rotational levels. The underlying pattern is invariant in each rotational transition, aside from the overall intensity, and reflects the interactions between the near-degenerate states. Combination differences alone are of limited use. We need a pattern recognition technique that can extract from the spectrum the spectral pattern formed by the set

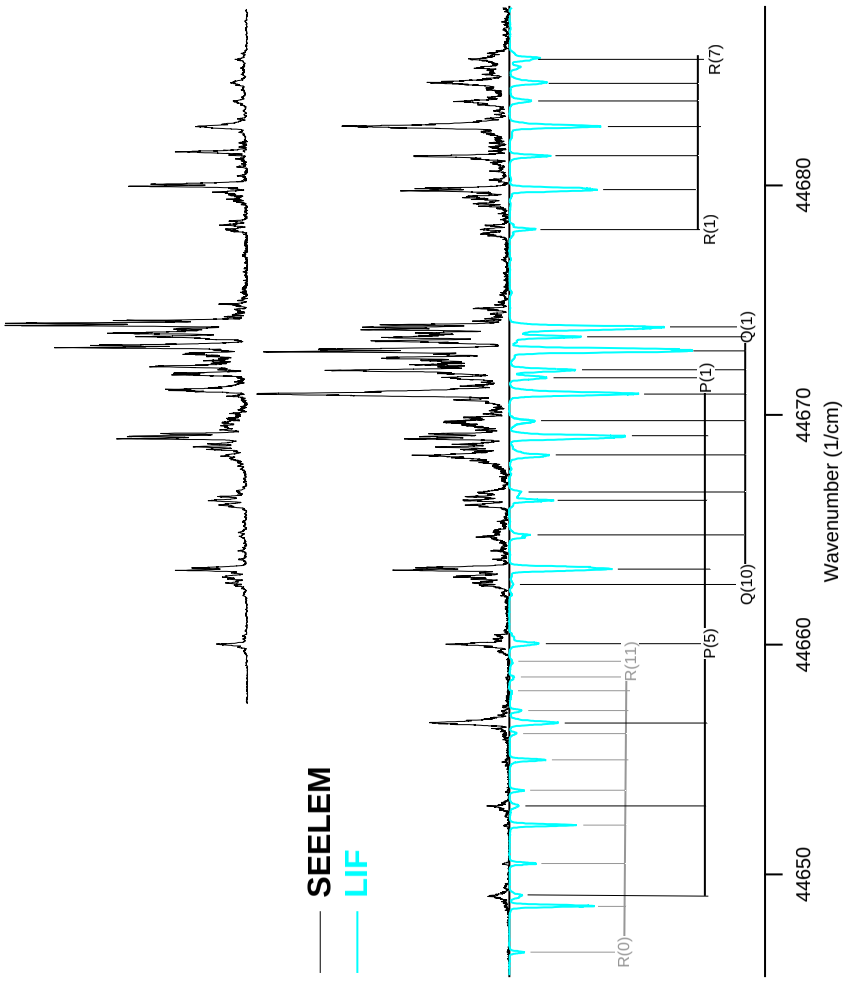

Figure 8-1: The two SEELEM spectra analyzed in this chapter. The LIF spectrum and the rotational assignments are also shown.

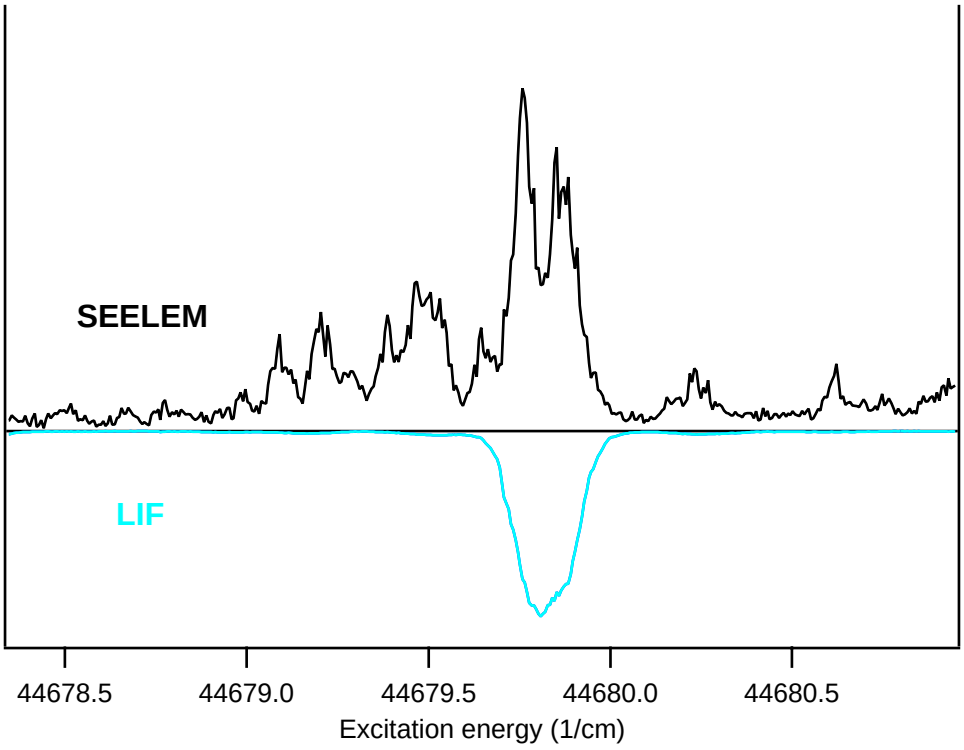

Figure 8-2: The SEELEM- and LIF-detectable eigenstates assignable to the R(2) line.

of lines assignable to a single rotational level.

Extended Auto Correlation, XAC, is a numerical pattern recognition technique that can entirely decompose the spectrum into the component patterns associated with each final rotational state. XAC takes advantage of several aspects of the spectrum that are known *a priori* or can be measured independently. This information is cast in a matrix that transforms the spectrum into the underlying patterns. Even those patterns that are significantly overlapped can be extracted. No assumptions are made about the shape of the underlying patterns, but we assume that all appearances of a pattern are identical except for the overall pattern intensity. The intensities of the spectrum are altered by changes in detectivity like saturation, XAC will not yield patterns that reflect reality. Also, the widths of the patterns are limited. Recording the SEELEM spectrum of the $V_1^3K_1^0$ band twice, with two different rotational temperatures, allowed us to observe each transition twice.

8.1.1 XCC

XAC is related to Extended Cross Correlation (XCC) developed by Jacobson, Coy, and Field.[82, 33] XCC has been applied to dispersed fluorescence spectra, which are generated by dispersing the fluorescence of a single S_1 ro-vibrational state onto an ICCD camera. The lines in these spectra form patterns, and these patterns overlap. The patterns reveal the couplings between the vibrational states of the S_0 potential surface. The overall intensity of a pattern can be changed by changing the vibrational nature of the fluorescing state, but the relative intensities within a pattern do not change. XCC can extract the overlapping patterns from the DF spectrum. XCC requires at least as many spectra as overlapping patterns that appear in the spectrum, because one needs as many measurements as unknowns. This can be seen in the following equations. Each point in a spectrum is composed of a point in each pattern multiplied by a intensity factor.

$$\begin{aligned} Spectrum_1 &= I_{P_1,S_1} \cdot Pattern_1 + I_{P_2,S_1} \cdot Pattern_2 + I_{P_3,S_1} \cdot Pattern_3 \\ Spectrum_2 &= I_{P_1,S_2} \cdot Pattern_1 + I_{P_2,S_2} \cdot Pattern_2 + I_{P_3,S_2} \cdot Pattern_3 \\ Spectrum_3 &= I_{P_1,S_3} \cdot Pattern_1 + I_{P_2,S_3} \cdot Pattern_2 + I_{P_3,S_3} \cdot Pattern_3 \end{aligned} \quad (8.1)$$

Since there are 3 unknown patterns, one requires 3 spectra. This assumes that the intensities can be measured independently. The intensities of the patterns must be different in each spectrum to maintain linear independence of the set of equations. These equations can be cast in a matrix, which is inverted. The spectrum is multiplied by the inverse matrix, which results in the patterns. If one requires multiple spectra to extract patterns, how can we extract overlapped patterns from a single SEELEM spectrum? While only one spectrum is recorded, the patterns appear a number times in SEELEM spectra, as opposed to only once in each DF spectrum. As will be shown, if the patterns appear enough times in a single spectrum, it is possible to extract the patterns.

8.2 XAC

8.2.1 How XAC works

To understand how XAC works, it is best to imagine it functioning in the reverse, to imagine that the patterns are known and a spectrum is to be generated. A simple example appears in Fig. 8-3. In this example, three patterns, corresponding to J′ = 1, J′ = 2, and J′ = 3, appear in the spectrum twice each, once in the R-branch and once in the P-branch. The spectrum is composed of 1000 points, and each pattern is composed of 200 points. Each appearance of a pattern is separated by the combination difference, the difference in energy of the initial states of the transitions. Each appearance has a different overall intensity. If the patterns, the combination differences, and the pattern intensities are known *a priori*, a matrix can be written that transforms the patterns into the spectrum. The matrix, M_{XAC} or simply M, is shown in Fig. 8-3. The intensity of the spectrum at each resolution element can be written as a vector, s_i. The patterns are concatenated end to end as a single vector. Three 200 point patterns make a single 600 point pattern vector, p_i. Each column of the matrix corresponds to a point in one of the patterns. And each row corresponds to a point in the spectrum. The diagonal lines represent the non-zero elements that project a pattern into the spectrum. All of the elements of a diagonal set have the same value, which reflects the intensity of the corresponding appearance of the pattern. Multiplying the pattern vector by the matrix generates the spectrum. The inverse of M_{XAC} can transform the spectrum into the underlying patterns.

8.2.2 Creating the XAC matrix

To create the XAC matrix, we need to know several things. Combination differences can be acquired from experimental observations of the initial states. The upper state rotational constant is needed to orient a set of appearances of one pattern with those of the others. The LIF spectrum provides the upper state rotational constant. Some limit needs to be placed on the pattern width. As a rule-of-thumb, pattern region

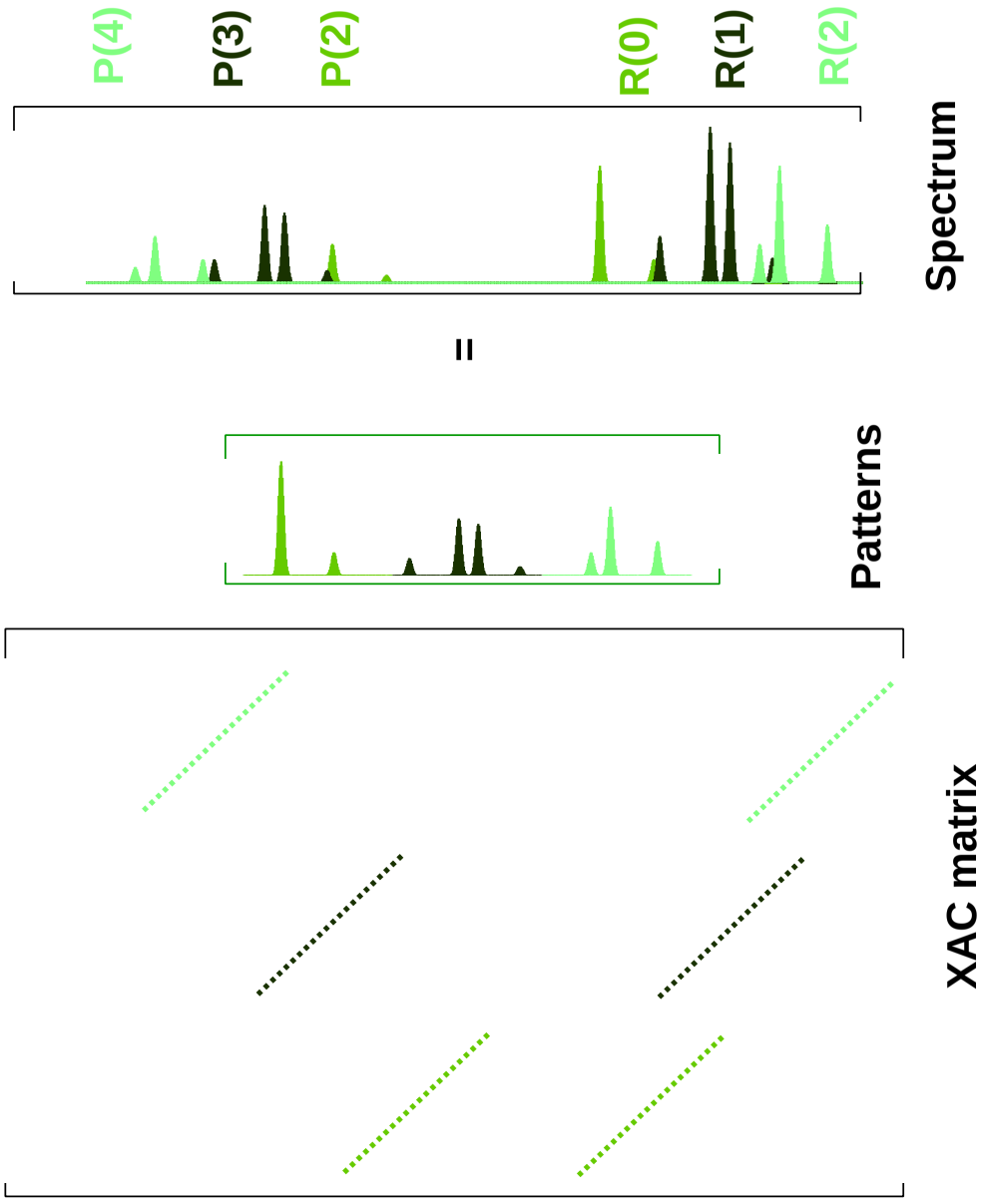

Figure 8-3: The XAC matrix. The patterns are projected into the spectrum by diagonal elements. All of the elements of a diagonal set have the same value, representing the relative intensity of this appearance of a pattern.

should be twice as large as the apparent pattern width. The width is limited because wider patterns correspond to more unknowns. If the patterns are too wide, M_{XAC} becomes under-determined, as will be shown below.

Finally, and most importantly, the intensities of each pattern appearance must be known. In principle, the intensity factors are calculable from the rotational line strength factors and rotational temperature. In our case, the populations of the initial rotational levels produced by the free jet expansion are not well described by a single temperature. The ratio must be measured in some other way.

We estimate the intensity factors by plotting the spectrum against itself shifted by a combination difference. This is called a recursion map. Fig. 8-4 shows the R(2) plotted against P(4). If one spectrum has a line at a given point but the other does not, this point will end up along the axis in the recursion map. If both spectra have a line at a given point, then the recursion map will have a set of points along a line into the first quadrant, as there is in the 3_{03} recursion map. Since the only difference between these two appearances of the pattern should be their relative intensity, all of these points will lie near a single line. The slope of this line is the relative intensity of the two appearances of the pattern. Only those regions of the spectrum which clearly contain some of the pattern are included in the linear fit. The larger features of the patterns in the real spectrum in Fig. 8-1 are obvious. R(2), Q(3), and P(4) all have a doublet. By plotting these regions against each other, the relative intensities of these lines can be estimated. The fit is not constrained to go through zero, because one or both of the appearances may be raised off the baseline by other, overlapping patterns.

If a pattern appears twice in a spectrum, a single recursion map will give you the relative intensity factors. If the pattern appears more than twice, then one can use multiple recursion maps to get the relative intensity factors. R(2) vs. Q(3) will give the first relative intensity factor. Q(3) vs. P(4) will give the second relative intensity factor.

While one must correctly measure the intensity for each appearance of a given pattern, one does not need perfect absolute intensity factors. For instance, a pattern

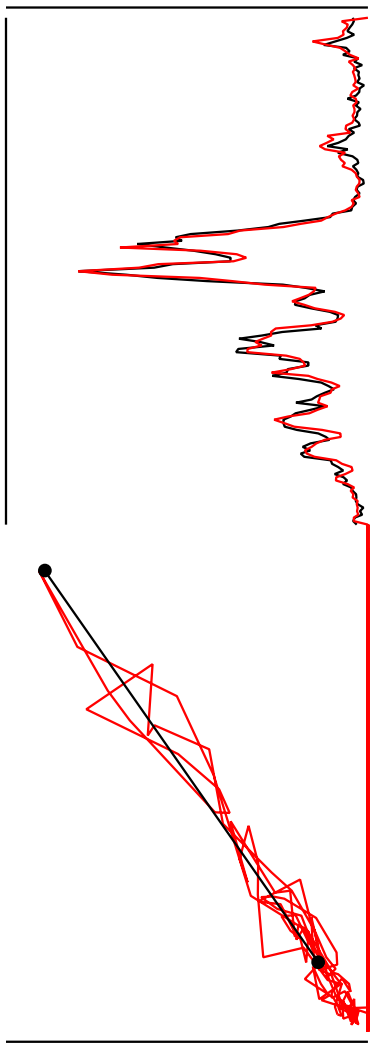

Figure 8-4: On the right, P(4) (black) is aligned with R(2) (gray). On the left, the recursion plot of P(4) vs. R(2).

with area equaling A results from an M_{XAC} with a given set of absolute intensity factors. If the absolute intensity factors for this pattern are halved, XAC will yield the same pattern with area of $2A$. The absolute intensity factors of the patterns are of interest. They are proportional to the overall intensity of the transition.

8.2.3 The degree of determination of the XAC matrix

How can we be sure that the matrix contains enough information to determine the patterns? Are there enough knowns to calculate all of the unknowns? In the example, the problem seems over over-determined, because there are 1000 observed points but only 600 unknown pattern points plus the 6 unknown intensities, for a total of 606 unknowns. This is not the correct way to assess the degree of determination of M_{XAC}. The matrix is block diagonal. Fig. 8-5 and eq. 8.2 illustrate that four points in the spectrum relate to one point from each pattern. Spectrum point 320 is composed of point 90 in the J=2 pattern and point 20 of the J=1 pattern. Spectrum point 900 is composed point 90 in the J=2 pattern (again) and point 30 in the J=3 pattern. The points in the J=1 and J=3 patterns themselves appear in the spectrum once more each, at spectrum point 680 and 80 respectively. So these three points in the patterns affect the spectrum 4 times, as shown in the following equations.

$$\begin{aligned}
Spectrum(80) &= I_{P(4)} \cdot Pattern_{J=3}(30) \\
Spectrum(320) &= I_{P(2)} \cdot Pattern_{J=1}(20) + I_{P(3)} \cdot Pattern_{J=2}(90) \\
Spectrum(680) &= I_{R(0)} \cdot Pattern_{J=1}(20) \\
Spectrum(900) &= I_{R(1)} \cdot Pattern_{J=2}(90) + I_{R(2)} \cdot Pattern_{J=3}(30) \qquad (8.2)
\end{aligned}$$

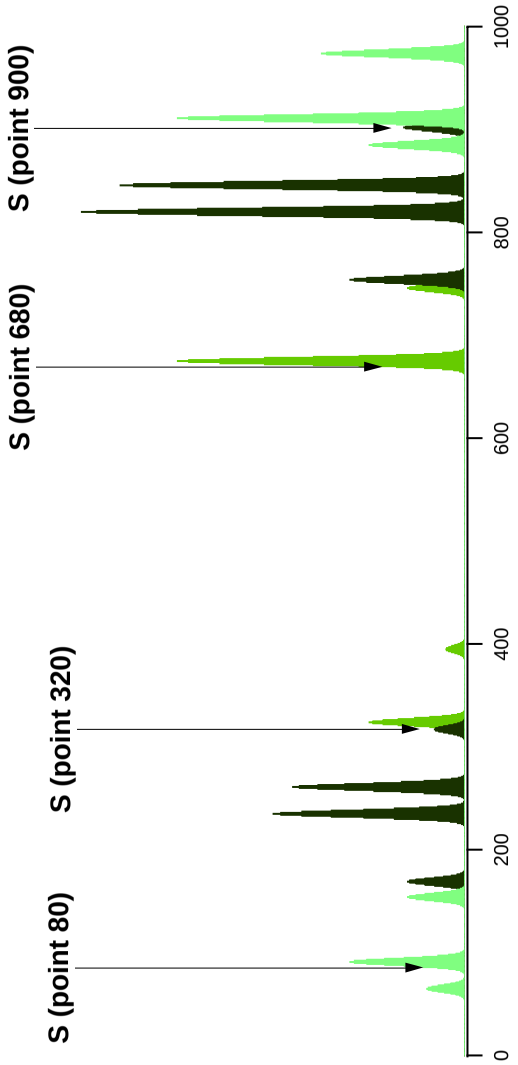

Figure 8-5: The example spectrum and the four spectral points that are related.

The matrix for this is

$$\begin{bmatrix} Spectrum(80) \\ Spectrum(320) \\ Spectrum(680) \\ Spectrum(900) \end{bmatrix} = \begin{bmatrix} 0 & 0 & I_{P(4)} \\ I_{P(2)} & I_{P(3)} & 0 \\ I_{R(0)} & 0 & 0 \\ 0 & I_{R(1)} & I_{R(2)} \end{bmatrix} \begin{bmatrix} Pattern_{J=1}(20) \\ Pattern_{J=2}(90) \\ Pattern_{J=3}(30) \end{bmatrix} \tag{8.3}$$

This 4×3 block is independent of the rest of the problem. There are four measurements and three unknowns–the problem is over-determined. The entire matrix must be checked to ensure that each of the blocks contains at least as many observed spectral points as unknown pattern points.

The fact that M_{XAC} is block diagonal suggests that the matrix inversion routine could be computationally simplified. Small blocks of the matrix could be inverted instead of the whole M_{XAC} at once, which would save computer time. Unfortunately, for the real spectrum shown in Fig. 8-1, there is so much pattern overlap that M_{XAC} has only one block.

8.2.4 Inverting the XAC matrix with SVD

Once the XAC matrix has been created, it can be inverted, and the spectrum can be multiplied by the inverse matrix to arrive at the pattern vector. A number of numerical routines can invert matrices. Numerical Recipes heavily recommends Singular Value Decomposition, SVD,[150] which is very successful this application. SVD results in three matrices, U, W, and V. Although, each of these matrices have specific statistical meaning, we use them only to create the matrix inverse.

$$M_{XAC} = U \cdot [diag(W_j)] \cdot V^T \tag{8.4}$$

$$M_{XAC}^{-1} = V \cdot [diag(1/W_j)] \cdot U^T \tag{8.5}$$

$diag(W_j)$ represents the diagonal elements of the matrix W. The last quantity is called the pseudo-inverse because the inverse of a non-square matrix cannot be exact. The quality of SVD on a matrix can be gauged by the condition number, as discussed

in Numerical Recipes [150]. The condition number is the ratio of the largest to the smallest diagonal element of matrix W. If the inverse of the condition number nears the machine precision, the results are suspect. Numerical Recipes discusses how to handle such an ill-conditioned matrix, but all the matrices discussed here are well conditioned because they are well-determined.

8.2.5 Noise in the spectrum

Real data has an additional pattern, which would be, in this example, 1000 points. This pattern is the noise that occurred as the data was being recorded. So, there are 1000 data points and 1606 unknowns. One might conclude that this would make XAC impossible, but in fact this is just the sort of problem SVD is good at solving. SVD is equivalent to a multi-dimensional least squares fit. Three non-co-linear points determine a plane. Solving a 3×3 would be like fitting a plane to three points. The fit would be perfect in the sense that there would be no residual; the plane would intersect all three points. All of the noise is incorporated into the patterns. In the case of a 4×3, we would be fitting a plane to four points in the least squared residual sense. Because of noise, it is unlikely that the four points all line in a plane. The fit plane would be the best least squares compromise between these four points. So, there is likely to be a residual for all four points, and some of the noise is not included in the patterns. Unsurprisingly, the more observations made of a given pattern, the closer the plane will be to reality. In the case of the example, SVD will fit 600 points of patterns to the 1000 points of data best in a least squares sense.

The patterns that result from the multiplication of the spectrum shown in Fig. 8-6, which includes some noise, with the inverse matrix, is shown in Fig. 8-7. The noise was Gaussian with a width that is the same size as the small line marked with an arrow. This line is not distinguishable in the spectrum, but it emerges in the pattern, demonstrating the ability of XAC to extract small lines in a pattern. This line would not be identifiable with combination differences.

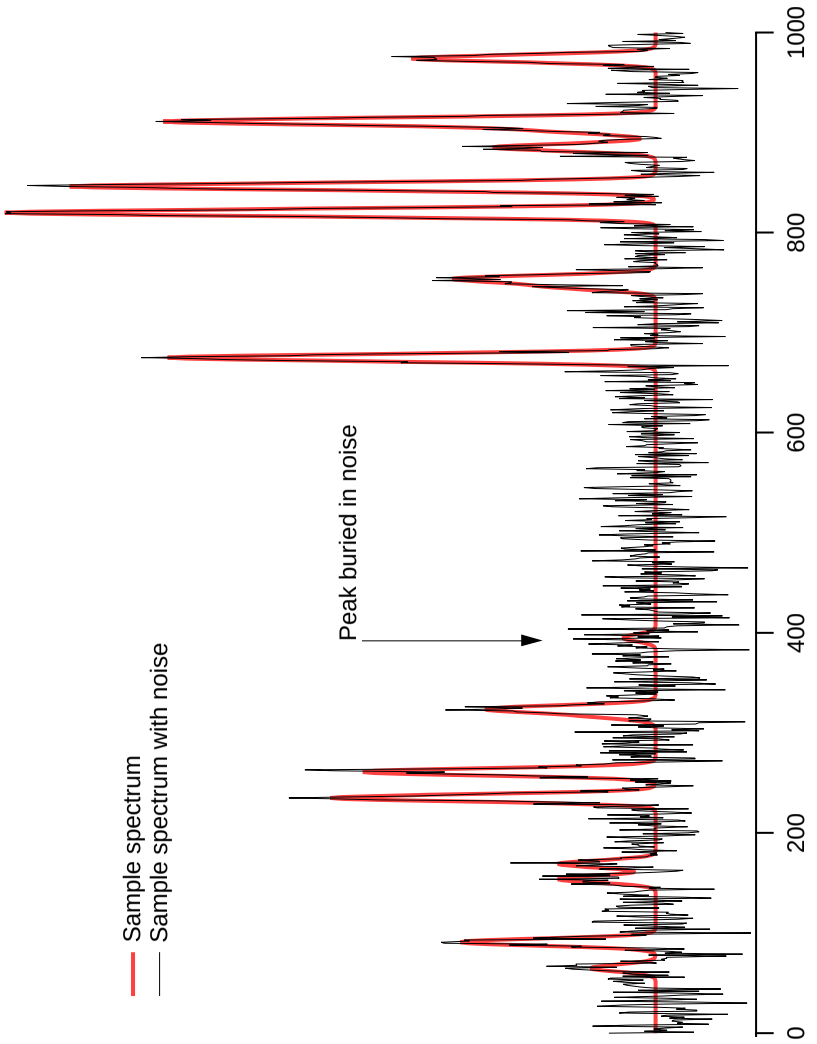

Figure 8-6: The sample spectrum with noise. Note that one of the small peaks is lost under the noise.

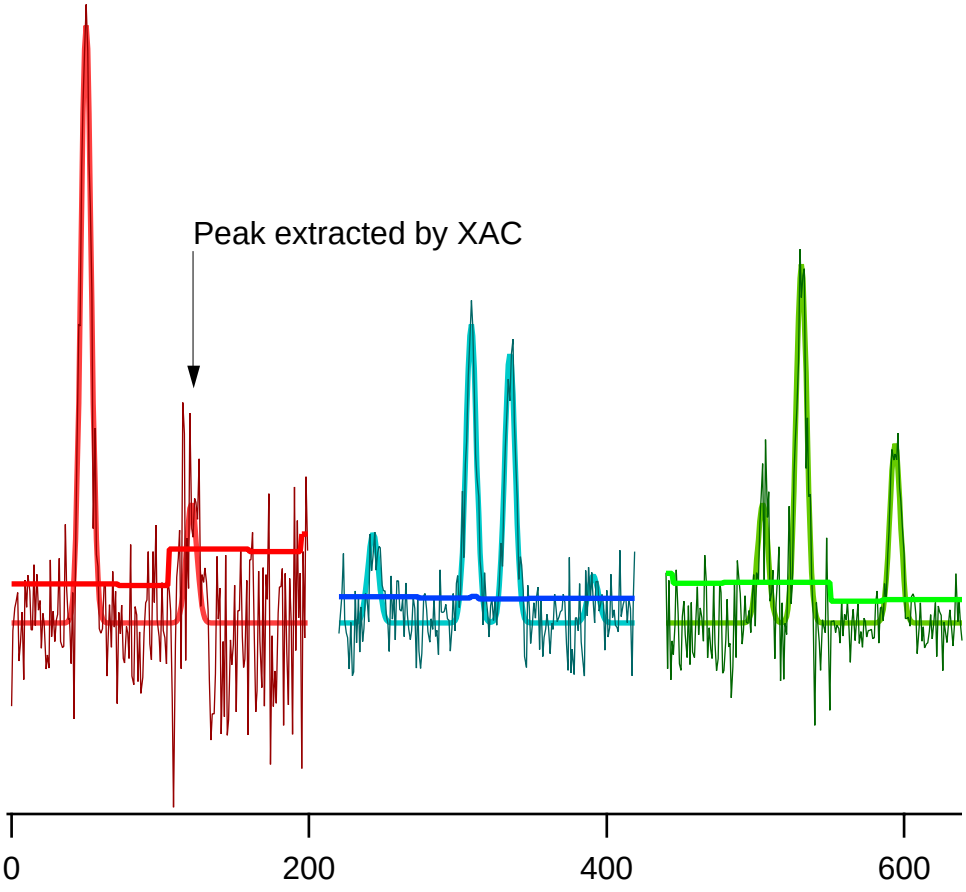

Figure 8-7: The patterns that result from XAC.

8.2.6 Uncertainty of the patterns

The noise in the spectrum leads to uncertainty in the patterns that result from XAC. This uncertainty can be determined from a simple propagation of errors treatment of M_{XAC}. As an example, consider the 4×3 M_{XAC} in eq. 8.3. Let the inversion of this matrix be

$$M_{XAC}^{-1} = \begin{bmatrix} T_{11} & T_{12} & T_{13} & T_{14} \\ T_{21} & T_{22} & T_{23} & T_{24} \\ T_{31} & T_{32} & T_{33} & T_{34} \end{bmatrix} \tag{8.6}$$

which leads to

$$\begin{bmatrix} T_{11} & T_{12} & T_{13} & T_{14} \\ T_{21} & T_{22} & T_{23} & T_{24} \\ T_{31} & T_{32} & T_{33} & T_{34} \end{bmatrix} \begin{bmatrix} Spectrum(80) \\ Spectrum(320) \\ Spectrum(680) \\ Spectrum(900) \end{bmatrix} = \begin{bmatrix} Pattern_{J=1}(20) \\ Pattern_{J=2}(90) \\ Pattern_{J=3}(30) \end{bmatrix} \tag{8.7}$$

Accordingly,

$$\begin{aligned} Pattern_{J=1}(20) \;\; = \;\; & T_{11} \cdot Spectrum(80) \;\; + \\ & T_{12} \cdot Spectrum(320) \;\; + \\ & T_{13} \cdot Spectrum(680) \;\; + \\ & T_{14} \cdot Spectrum(900) \end{aligned} \tag{8.8}$$

The error of $Pattern_{J=1}(20)$ can be calculated with propagation of errors.[167]

$$\begin{aligned} \sigma^2(Pattern_{J=1}(20)) \;\; = \;\; & \left(\frac{\partial Pattern_{J=1}(20)}{\partial Spectrum(80)} \right)^2 \cdot \;\; \sigma^2(Spectrum(80)) \\ & + \;\; \left(\frac{\partial Pattern_{J=1}(20)}{\partial Spectrum(320)} \right)^2 \cdot \;\; \sigma^2(Spectrum(320)) \end{aligned}$$

$$+ \left(\frac{\partial Pattern_{J=1}(20)}{\partial Spectrum(680)}\right)^2 \cdot \sigma^2(Spectrum(680))$$
$$+ \left(\frac{\partial Pattern_{J=1}(20)}{\partial Spectrum(900)}\right)^2 \cdot \sigma^2(Spectrum(900)) \tag{8.9}$$

$$\begin{aligned}\sigma^2(Pattern_{J=1}(20)) &= (T_{11})^2 \cdot \sigma^2(Spectrum(80)) + \\ &\quad (T_{12})^2 \cdot \sigma^2(Spectrum(320)) + \\ &\quad (T_{13})^2 \cdot \sigma^2(Spectrum(680)) + \\ &\quad (T_{14})^2 \cdot \sigma^2(Spectrum(900))\end{aligned} \tag{8.10}$$

So, elements of the inverted XAC matrix can be used along with the known errors of the data at each spectral point to calculate the errors in the patterns. This assumes that no error exists in the determination of the intensities. Including the uncertainties of the intensities could be accomplished with a similar approach.

$$\begin{aligned}\sigma^2(Pattern_{J=1}(20)) &= (T_{11})^2 \cdot \sigma^2(Spectrum(80)) + \\ &\quad (T_{12})^2 \cdot \sigma^2(Spectrum(320)) + \\ &\quad (T_{13})^2 \cdot \sigma^2(Spectrum(680)) + \\ &\quad (T_{14})^2 \cdot \sigma^2(Spectrum(900)) + \\ &\quad (Spectrum(80))^2 \cdot \sigma^2(T_{11}) + \\ &\quad (Spectrum(320))^2 \cdot \sigma^2(T_{12}) + \\ &\quad (Spectrum(680))^2 \cdot \sigma^2(T_{13}) + \\ &\quad (Spectrum(900))^2 \cdot \sigma^2(T_{14})\end{aligned} \tag{8.11}$$

The uncertainty in the patterns in Fig. 8-7 are shown by horizontal lines. The uncertainty shifts according to the degree of overlap of the pattern as it appears in

the spectrum.

8.2.7 The effect of bad intensities and non-linear fitting.

How important are the pattern intensities in M_{XAC}? What if a pattern appears in the spectrum that is unaccounted for in M_{XAC}? The short answer is that XAC will not work well. Imagine that a stray line appears in the spectrum in the middle of an appearance of a pattern, as shown in Fig. 8-8. XAC will compensate by placing the strong line into the pattern, as shown in the resulting patterns in Fig. 8-9. This causes a problem at other appearances of the pattern where the spectrum has no corresponding line. To compensate, XAC puts a negative line in another pattern that overlaps this region. These two patterns, when multiplied by their relative intensity factors and summed, will result in nearly zero for this spectral region. The negative line in the second pattern can be canceled in other appearances if a positive line can be placed in a third pattern. These stray lines can propagate throughout a set of patterns. An error in intensity causes similar problems. One could say that the stray line is a pattern assigned a intensity of zero. A pattern assigned an incorrect intensity will also result in negative lines propagating through the patterns.

The "down hill" direction of this propagation is toward patterns with smaller absolute intensities. Imagine that the patterns in eq. 8.3 were all zero at these points, which should produce 4 spectrum points that would also be zero. Further imagine that there is a stray line at $Spectrum(80)$. So the real matrix should look like this.

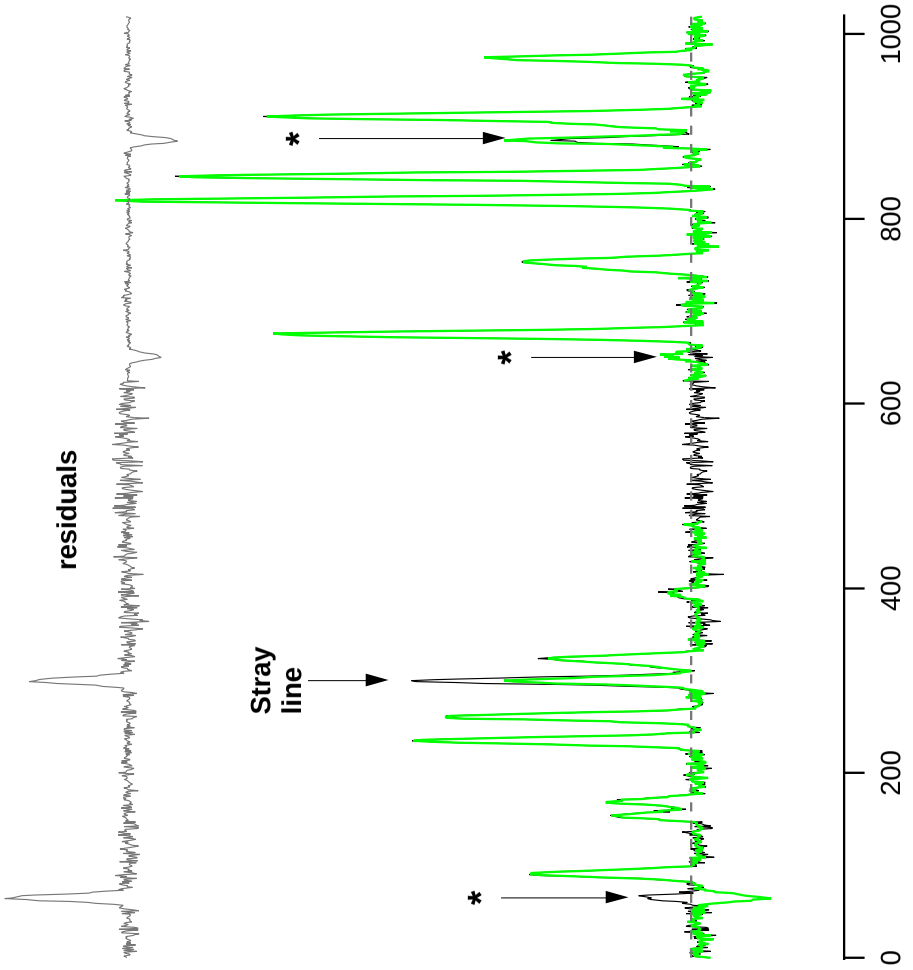

Figure 8-8: The sample spectrum with noise and a stray peak at point 300. The intensity of this peak propagates through the fit spectrum at locations marked by asterisks.

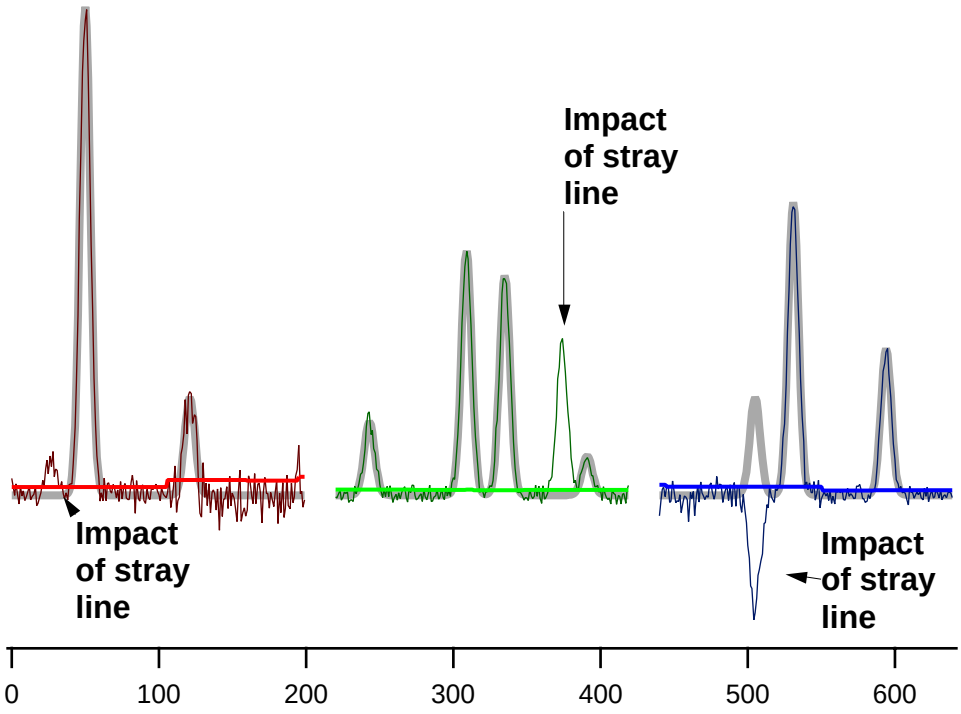

Figure 8-9: The patterns that result from the XAC of the spectrum shown in Fig. 8-8. All three patterns are affected by the intensity of the stray peak.

$$\begin{bmatrix} Spectrum(80) \\ Spectrum(320) \\ Spectrum(680) \\ Spectrum(900) \end{bmatrix} = \begin{bmatrix} 0 & 0 & I_{P(4)} & I_{stray} \\ I_{P(2)} & I_{P(3)} & 0 & 0 \\ I_{R(0)} & 0 & 0 & 0 \\ 0 & I_{R(1)} & I_{R(2)} & 0 \end{bmatrix} \begin{bmatrix} Pattern_{J=1}(20) \\ Pattern_{J=2}(90) \\ Pattern_{J=3}(30) \\ Pattern_{stray} \end{bmatrix} \tag{8.12}$$

$$\begin{bmatrix} Spectrum(80) \\ Spectrum(320) \\ Spectrum(680) \\ Spectrum(900) \end{bmatrix} = \begin{bmatrix} 1 \\ 0 \\ 0 \\ 0 \end{bmatrix} \tag{8.13}$$

If the matrix in eq. 8.3 is incorrectly applied to these spectral points, the intensity at $Spectrum(80)$ will be forced into $Pattern_{J=3}(30)$. This causes a problem at $Spectrum(900)$.

$$Spectrum(900) = I_{R(1)} \cdot Pattern_{J=2}(90) + I_{R(2)} \cdot Pattern_{J=3}(30) = 0 \tag{8.14}$$

$$\frac{Pattern_{J=2}(90)}{Pattern_{J=3}(30)} = \frac{-I_{R(2)}}{I_{R(1)}} \tag{8.15}$$

If $I_{R(2)} > I_{R(1)}$ then $Pattern_{J=2}(90) > Pattern_{J=3}(30)$ and $Pattern_{J=2}(90)$ will be negative. So the intensity of a stray line at $Spectrum(80)$ will propagate toward the patterns that appear smaller in the spectrum.

Negative lines in the patterns indicate that the intensities are wrong or that the spectrum contains patterns that are unaccounted for in M_{XAC}. The real SEELEM patterns cannot have negative values. The SEELEM signal is the number of observed Auger electrons, which is always a non-negative number. The patterns that result from XAC should have positive values beyond what might be expected from the noise level.

Large residuals also indicate that the intensities are wrong. Residuals should be calculated between the observed spectrum, s_i and the spectrum that results from multiplying M_{XAC} by the patterns that result from XAC, s_i'. Large residuals indicate that M_{XAC} has not properly accounted for all of the intensity in the spectrum.

Better intensities can be determined by a non-linear routine that minimizes the negative lines in the patterns and the large residuals in the calculated spectrum. No linear technique can be used to optimize the intensities because XAC contains terms like $I_{P(3)} \cdot Pattern_{J=2}(90)$. Since the unknowns are multiplied together, the problem is not linear in the fitted parameters. XAC is an attempt to "reduce" the non-linearity by separately estimating the relative intensity factors and the patterns using separate linear fitting approaches.

The merit function to be minimized is the sum of χ^2 and a penalty function for negative going features in the patterns.

$$\chi^2 = \sum_i \left(w_i \cdot (s_i - s_i')^2 \right) \tag{8.16}$$

$$F_{penalty} = 2 \sum_{p_i' < 0} \left(\frac{p_i'}{\sigma_{pattern}} \right)^2 \tag{8.17}$$

s_i is the intensity of the SEELEM spectrum, s_i' is the intensity in the spectrum resulting from XAC, p_i is the real pattern vector, p_i' is the pattern vector resulting from XAC, and w_i is the weight of each spectral point. The intensities were optimized using the expansion methods discussed in Section 8.5 of Bevington[17]. See also refs. [167, 150]. The Marquardt method was not implemented because each XAC iteration required intervention, which was necessary because of the size of M_{XAC} for the real data. The first and second derivatives of χ^2 and the $F_{penalty}$ are needed for the non-linear optimization. I_P and I_Q are the intensities of pattern P and Q, M is the XAC matrix, and M^{-1} is the inverse XAC matrix.

$$\begin{aligned}
\frac{\partial \chi^2}{\partial I_P} &= \frac{\partial \left(\sum_i w_i \cdot (s_i - s_i')^2 \right)}{\partial I_P} \\
&= 2 \sum_i w_i \cdot (s_i - s_i') \cdot \frac{\partial (s_i - s_i')}{\partial I_P} \\
&= -2 \sum_i w_i \cdot (s_i - s_i') \cdot \frac{\partial s_i'}{\partial I_P}
\end{aligned}$$

$$
\begin{aligned}
&= -2\sum_i w_i \cdot (s_i - s_i') \cdot \frac{\partial M \cdot p_i'}{\partial I_P} \\
&= -2\sum_i w_i \cdot (s_i - s_i') \cdot \left[\frac{\partial M}{\partial I_P} \cdot p_i' \ + \ M \cdot \frac{\partial p_i'}{\partial I_P}\right] \\
&= -2\sum_i w_i \cdot (s_i - s_i') \cdot \left[\frac{\partial M}{\partial I_P} \cdot p_i' \ + \ M \cdot \frac{\partial M^{-1} \cdot s_i}{\partial I_P}\right] \\
&= -2\sum_i w_i \cdot (s_i - s_i') \cdot \\
&\qquad \left[\frac{\partial M}{\partial I_P} \cdot p_i' \ + \ M \cdot \frac{\partial M^{-1}}{\partial I_P} \cdot s_i \ + \ M \cdot M^{-1} \cdot \frac{\partial \cdot s_i}{\partial I_P}\right] \\
&= -2\sum_i w_i \cdot (s_i - s_i') \cdot \\
&\qquad \left[\frac{\partial M}{\partial I_P} \cdot p_i' \ + \ M \cdot \frac{\partial M^{-1}}{\partial I_P} \cdot s_i\right] \\
&= -2\sum_i w_i \cdot (s_i - s_i') \cdot \\
&\qquad \left[\frac{\partial M}{\partial I_P} \cdot p_i' \ - \ M \cdot M^{-1} \cdot \frac{\partial M}{\partial I_P} \cdot M^{-1} \cdot s_i\right] \\
&= -2\sum_i w_i \cdot (s_i - s_i') \cdot \\
&\qquad \left[1 \ - \ M \cdot M^{-1}\right] \frac{\partial M}{\partial I_P} \cdot p_i'
\end{aligned}
\tag{8.18}
$$

using the following relations

$$
\begin{aligned}
s_i' &= M \cdot p_i' \\
p_i' &= M^{-1} \cdot s_i \\
\left(\frac{\partial s_i}{\partial I_P}\right) &= 0 \\
\left(\frac{\partial M^{-1}}{\partial I_P}\right) &= -M^{-1}\frac{\partial M}{\partial I_P}M^{-1}
\end{aligned}
\tag{8.19}
$$

The $M \cdot M^{-1}$ term is not equal to the identity matrix because M^{-1} is not the true inverse. $M \cdot M^{-1}$ reduces to $U \cdot U^T$, which may have some statistical meaning. The second derivative is needed as well.

$$\begin{aligned}
\frac{\partial^2\chi^2}{\partial I_P \partial I_Q} &= \frac{\partial}{\partial I_Q}\cdot\frac{\partial\chi^2}{\partial I_P} \\
&= \frac{\partial}{\partial I_Q}\left(2\sum_i w_i\cdot(s_i - s_i')\cdot\frac{\partial(s_i - s_i')}{\partial I_P}\right) \\
&= 2\sum_i w_i\cdot\left(\frac{\partial(s_i - s_i')}{\partial I_Q}\frac{\partial(s_i - s_i')}{\partial I_P} + (s_i - s_i')\frac{\partial^2(s_i - s_i')}{\partial I_P \partial I_Q}\right) \qquad (8.20)
\end{aligned}$$

Only the first term is used as is discussed in Numerical Recipes[150].

$$\begin{aligned}
\frac{\partial^2\chi^2}{\partial I_P \partial I_Q} &= \sum_i w_i\cdot\left(\left[1 - M\cdot M^{-1}\right]\frac{\partial M}{\partial I_P}\cdot M^{-1}\cdot s_i\right) \\
&\quad\cdot\left(\left[1 - M\cdot M^{-1}\right]\frac{\partial M}{\partial I_Q}\cdot M^{-1}\cdot s_i\right)
\end{aligned} \qquad (8.21)$$

The first and second derivatives of the penalty function are

$$\begin{aligned}
\frac{\partial F_{penalty}}{\partial I_P} &= \frac{\partial\left(2\sum_{p_i'<0}\left(\frac{p_i'}{\sigma_{pattern}}\right)^2\right)}{\partial I_P} \\
&= 2\sum_{p_i'<0}\frac{p_i'}{(\sigma_{pattern})^2}\frac{\partial p_i'}{\partial I_P} \\
&= -2\sum_{p_i'<0}\frac{p_i'}{(\sigma_{pattern})^2}\left[M^{-1}\cdot\frac{\partial M}{\partial I_P}\cdot M^{-1}\cdot s_i\right] \qquad (8.22)
\end{aligned}$$

$$\frac{\partial}{\partial I_Q} \cdot \frac{\partial F_{penalty}}{\partial I_P} = \frac{\partial}{\partial I_Q} \cdot \left(2 \sum_{p'_i<0} \frac{p'_i}{(\sigma_{pattern})^2} \frac{\partial p'_i}{\partial I_P} \right)$$

$$= 2 \sum_{p'_i<0} \left(\frac{1}{(\sigma_{pattern})^2} \frac{\partial p'_i}{\partial I_Q} \frac{\partial p'_i}{\partial I_P} + \frac{p'_i}{(\sigma_{pattern})^2} \frac{\partial^2 p'_i}{\partial I_P \partial I_Q} \right) \quad (8.23)$$

where

$$\frac{\partial p'_i}{\partial I_Q} = \left(M^{-1} \cdot \frac{\partial M}{\partial I_Q} \cdot M^{-1} s_i \right) \quad (8.24)$$

$$\frac{\partial p'_i}{\partial I_P} = \left(M^{-1} \cdot \frac{\partial M}{\partial I_P} \cdot M^{-1} s_i \right) \quad (8.25)$$

$$\frac{\partial^2 p'_i}{\partial I_P \partial I_Q} = M^{-1} \cdot \frac{\partial M}{\partial I_Q} \cdot M^{-1} \cdot \frac{\partial M}{\partial I_P} \cdot M^{-1} \cdot s_i + M^{-1} \cdot \frac{\partial M}{\partial I_P} \cdot M^{-1} \cdot \frac{\partial M}{\partial I_Q} \cdot M^{-1} \cdot s_i \quad (8.26)$$

8.2.8 Final note

XAC is related to a technique developed by Ruiz and Martin.[158] They had recorded a spectrum with lines with known energies and lineshapes. They wanted an accurate measure of the intensities. They created a matrix that contained the energy and lineshape information. A spectrum could be generated by multiplying this matrix by a vector containing intensity information. These authors used SVD to invert this matrix, multiplied the inverse by the spectrum, and arrived at a measure of the intensities of each line in the spectrum. There problem is the opposite of ours: they know the lineshape and want to measure the intensities, while we have a measure of the intensity and want to measure the fractionated lineshape.

8.3 Experimental details

Most of the experimental details are discussed in Chapter 2, but a few specifics should be mentioned. The LIF and SEELEM $V_1^3K_1^0$ spectra were recorded under two different

free jet expansion conditions and nozzle-laser delay settings. In one case, these were set to maximize the SEELEM intensity of the R(4) transition. 2 atmospheres of pure acetylene was used. In the other case, the conditions were set to maximize the SEELEM intensity of the Q(1) transition, using 10 percent acetylene in He for a total of 4 atmospheres pressure. Changing the conditions from one set to the other dramatically altered the relative intensities of the transitions. The nozzle temperature was raised to $\sim 60°$ C to increase the population of the vibrationally excited initial state. The average time of flight was 120 μs and 80 μs for pure acetylene and He carrier gas, respectively.

The SEELEM detector had a Au detection surface heated to 260° C. The multiplier was 2700 Volts, producing $\sim 3 \times 10^7$ multiplication, or output pulses of 20 mVolts across 50 Ohms. The signals were coupled out of the multiplier with the circuit shown in Fig. 2-11 a). A pulse counting integrator (Stanford Research Systems SR 400) processed this signal. The SEELEM intensity is the number of counts recorded in 50 shots. The laser frequency is scanned in 0.006 cm^{-1} steps.

The PMT was operated at 1700 V. Even with the baffles, the laser scatter signal at this voltage was too large for the boxcar gate to start when the laser fires. The boxcar sampled the fluorescence decay from 50 ns to 5 μs.

8.4 Results

The hot-band transition $V_1^3K_1^0$ was selected as a test for XAC because its spectrum has multiple copies of each pattern. The rotational transition structure is illustrated in Fig. 8-10. The final states of this transition are $K'_a = 0$. Each rotational level, J, has only one parity component (J_{0J}) where parity is $-1^{(K_c)}$. The initial states are $l'' = 1$ and have two parity components. The Q-branch transitions originate from one parity component and the R- and P-branch components originate from the other. But all three rotational transitions, P(J+1), Q(J), and R(J-1), terminate on the same (J_{0J}) state. The energies of the initial states are well known.[95] All of the congestion is due to the final states. Most of the patterns are repeated three times, once in

each branch. The pattern for $J' = 1$ is repeated only twice: in the P(2) and Q(1) transitions. It cannot be accessed by the R(0) transition since $l'' = 1$ has no $J'' = 0$ state. For similar reasons, the $J' = 0$ levels only appear once in the spectrum, in the P(1) transition. The fact that the pattern only appears once in the spectrum does not eliminate the possibility of using XAC to extract this pattern. M_{XAC} must be checked to determine if the spectrum contains enough information to extract this pattern. If the pattern for $J' = 0$ can be extracted, its uncertainty is likely to be high.

As mentioned, this spectrum was recorded twice under different expansion conditions. Generating spectra with maximally different rotational temperatures provides more spectral observations of the same unknown patterns. The inclusion of this data does not introduce any more overlap interactions or any additional patterns. It simply introduces more spectral points - more observations. The pattern intensities are different, so the information in the two spectra is linearly independent. This allows more pattern points to be determined, wider pattern areas, and better determination of the patterns. In a sense, the plane is fit to more points. Since the P(1) line only appears in the spectrum once, having observed it twice, once in each spectrum, allows for a more certain determination of the $J' = 0$ pattern.

XAC cannot be used on cold band transitions, like $V_0^3K_0^1$, which originate in $l'' = 0$ states with one parity component and terminate in $K_a' = 1$ with two parity components. The Q-branch transitions terminate in one parity component and the R- and P-branch transitions terminate in the other. The Q-branch patterns only appear once, which overlap each other and P-branch transitions. There is not enough information to extract the Q-branch patterns unless many spectra with differing intensities were recorded.

The region containing the P-branch of $V_1^3K_1^0$ also contains the R-branch of 2_0^1 $V_0^1K_0^1$. The intensity due to each rotational transition of the 2_0^1 $V_0^1K_0^1$ band was treated with a single pattern. This is possible because this vibrational state is not very SEELEM active. Only small, similarly shaped lines appeared in the spectrum at these transitions. Accordingly, a single, narrow pattern was used to account for all these lines. The intensities of the appearances of these lines were not varied in the

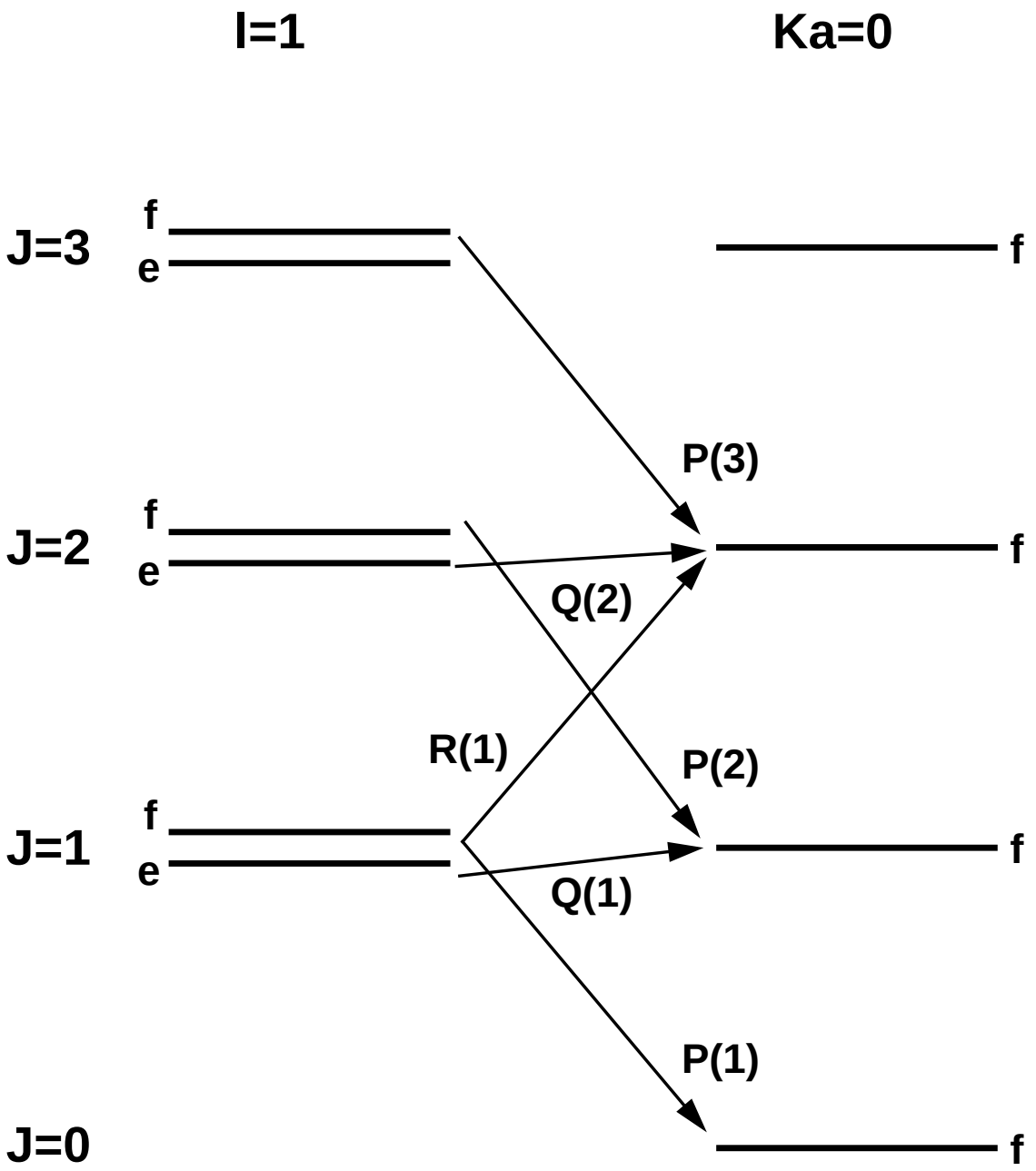

Figure 8-10: The rotational levels of the $l = 0$ initial state, on the left, and the $K_a = 0$ final state, on the right. $J' = 0$ can only be accessed through one transition, P(1). $J' = 1$ can be accessed through two transitions, P(2) and Q(1). Higher rotational levels can be accessed through three transitions.

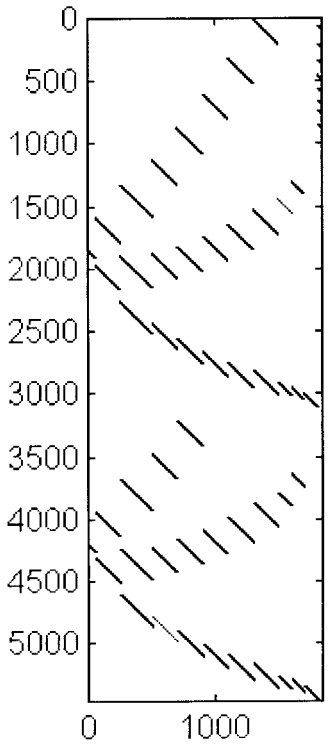

Figure 8-11: M_{XAC} for the spectra in Fig. 8-1. The R-, Q-, and P-branch transitions are clear. The lower part of the matrix is similar to the upper part because this matrix extracts patterns from both spectra simultaneously. The upper part corresponds to the lower SEELEM spectrum in Fig. 8-1, while the lower part corresponds to the upper spectrum in Fig. 8-1.

non-linear fit that will be discussed.

M_{XAC} for the SEELEM spectrum (Fig. 8-1) is shown in Fig. 8-11. The two SEELEM spectra were placed in a single spectrum vector. The lower rotational states appear the maximum number of times, but some of the higher J states were too small in the spectrum for all the appearances to be included. M_{XAC} was inverted with SVD using Matlab. M_{XAC}^{-1} was used to generate patterns, p_i', uncertainties in the patterns using eq. 8.10, and a calculated spectrum, s_i'. A non-linear fitting routine was used to minimize a merit functions by varying the intensities of each pattern appearance. The new intensities are used to create a new M_{XAC} for another iteration.

Many of the matrices in this calculation are large, so a large amount of memory was required for this calculation. M_{XAC}^{-1} has dimensions of 1842×5458, which requires

78 Mbytes to store. The SVD matrices also require a similarly large amount of memory. The $M \cdot M^{-1}$ term in eq. 8.18 has dimensions of 5458×5458. Terms like $\left(M^{-1} \cdot \frac{\partial M}{\partial I_Q} \cdot M^{-1} s_i\right)$ in eq. 8.23 do not take much memory because the $\frac{\partial M}{\partial I_Q}$ term is very simple. Only one of the diagonal lines in the matrix shown in Fig. 8-11 remains non-zero after the derivative is taken. Since $p_i' = M^{-1} \cdot s_i$, the $\frac{\partial M}{\partial I_Q}$ term merely defines a section of p_i' that will be multiplied by M^{-1}. The calculation was carried out on a 500 MHz PC with 500 Mbytes of RAM and 600 Mbytes of the hard drive assigned to virtual memory. The calculation takes 3 hours, and the computer must be restarted in the middle of the calculation to clear the memory.

Before XAC performed satisfactorily, the pattern widths had to be adjusted. Initially, all the patterns were the same width, approximately twice the width of the widest apparent patterns. However, the patterns with small intensities were too wide. This was also true of the J= 0 pattern. These patterns accumulated features belonging to other patterns. Non-linear fitting of the intensities of these patterns did not improve the results substantially. The widths of the patterns for J=0, 8, 9, and 10 were reduced as can be seen in Figs. 8-12 and 8-20 through 8-22.

Figures 8-12 through 8-22 shows the patterns that resulted from XAC using the intensities estimated with the recursion maps discussed in Section 8.2.2. These patterns are referred to as "recursion map" in the figures. These are fairly close to what would be expected from a look at the spectrum. There are a few negative going features in the patterns. The widths of the patterns are all broader than the extracted patterns. The uncertainties of these patterns is also shown. For most of the rotational transitions, the uncertainties for each pattern were very similar, so only the uncertainty for the "Third" pattern is shown. For $J'' = 0$, however, the uncertainties for all three patterns are shown and are in the same intensity order as the patterns. The calculated spectrum accounts for almost all the SEELEM intensity. Residuals are small. Nonetheless, non-linear fitting was used to obtain intensities that would result in less negative going features in the patterns and smaller residuals between the calculated and observed spectra.

The first attempt to fit the intensities was not successful. The key to an accurate

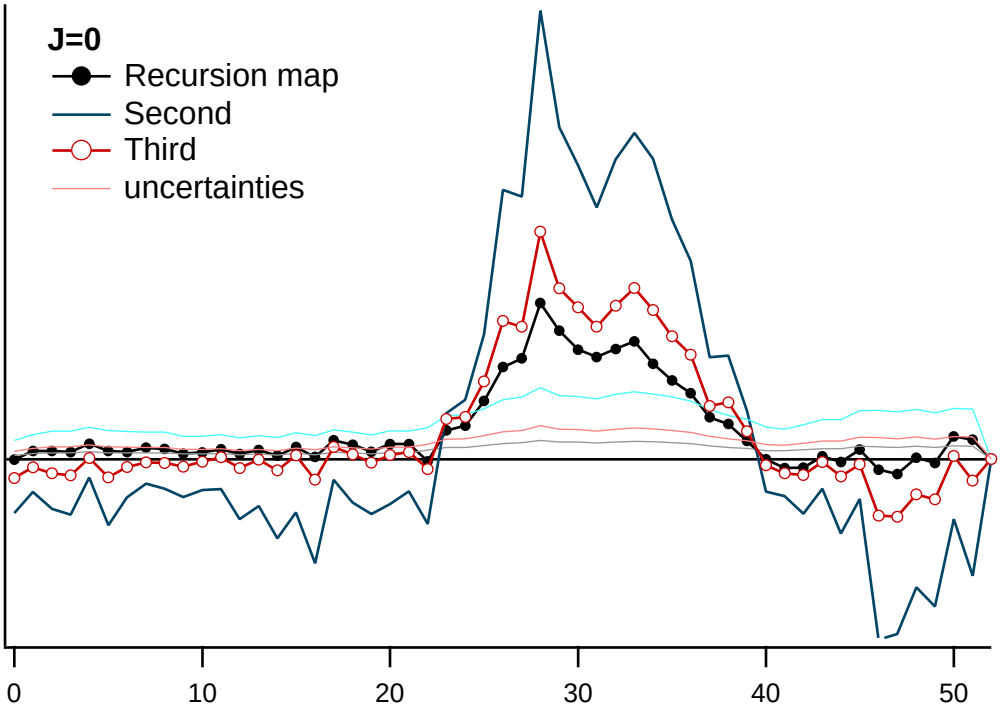

Figure 8-12: J=0 pattern. This pattern is narrow (52 points).

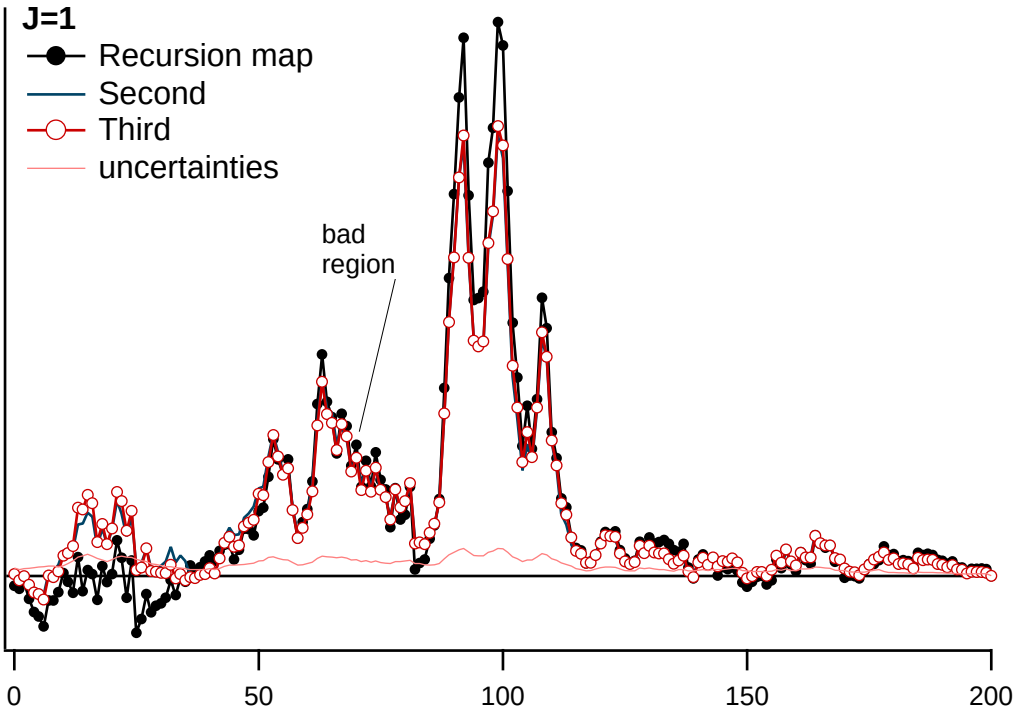

Figure 8-13: J=1 pattern.

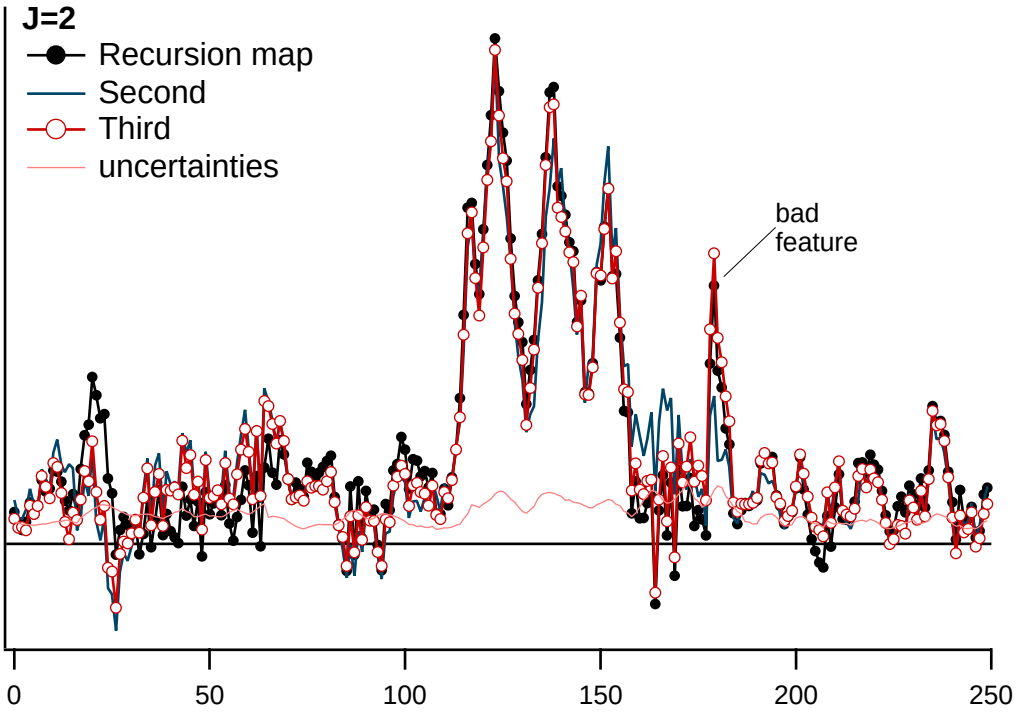

Figure 8-14: J=2 pattern. The feature on the right is not real.

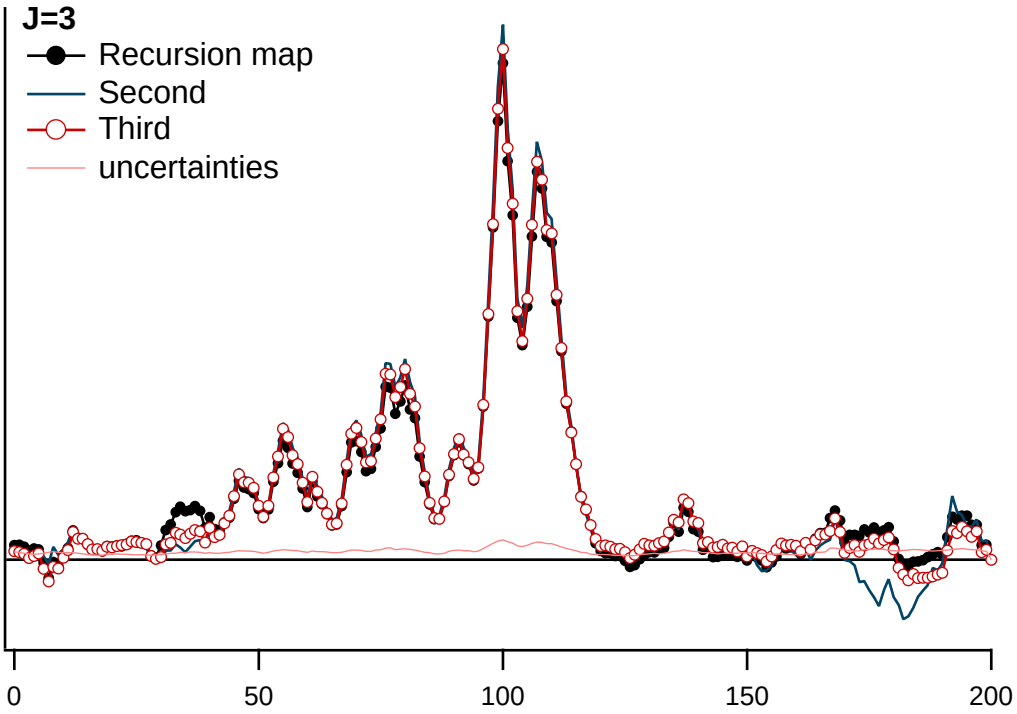

Figure 8-15: J=3 pattern.

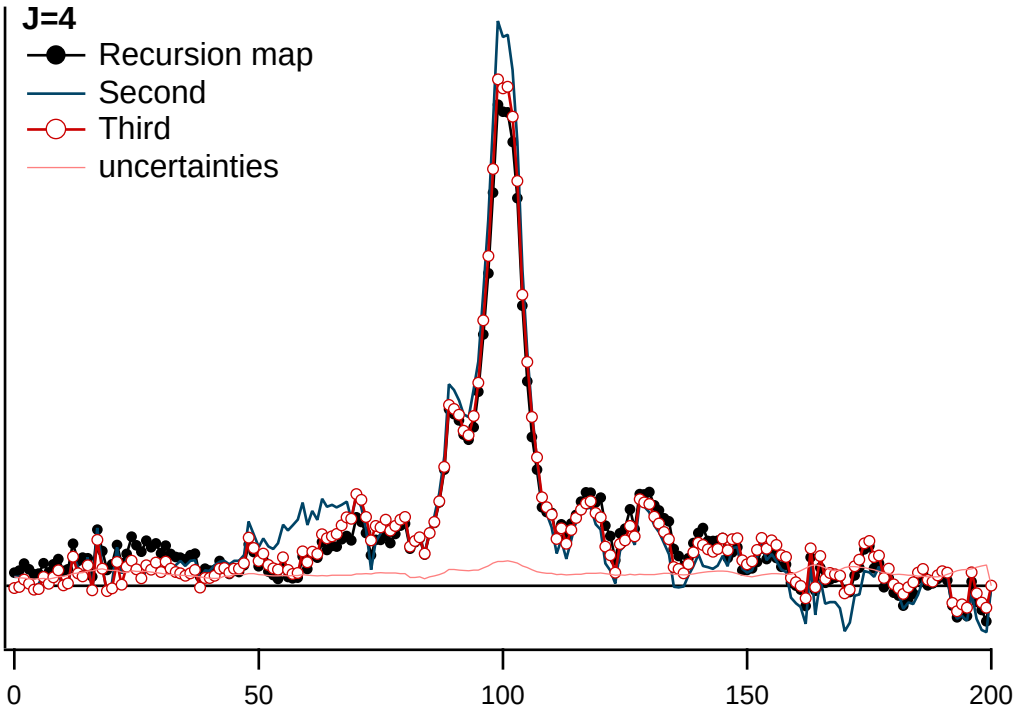

Figure 8-16: J=4 pattern.

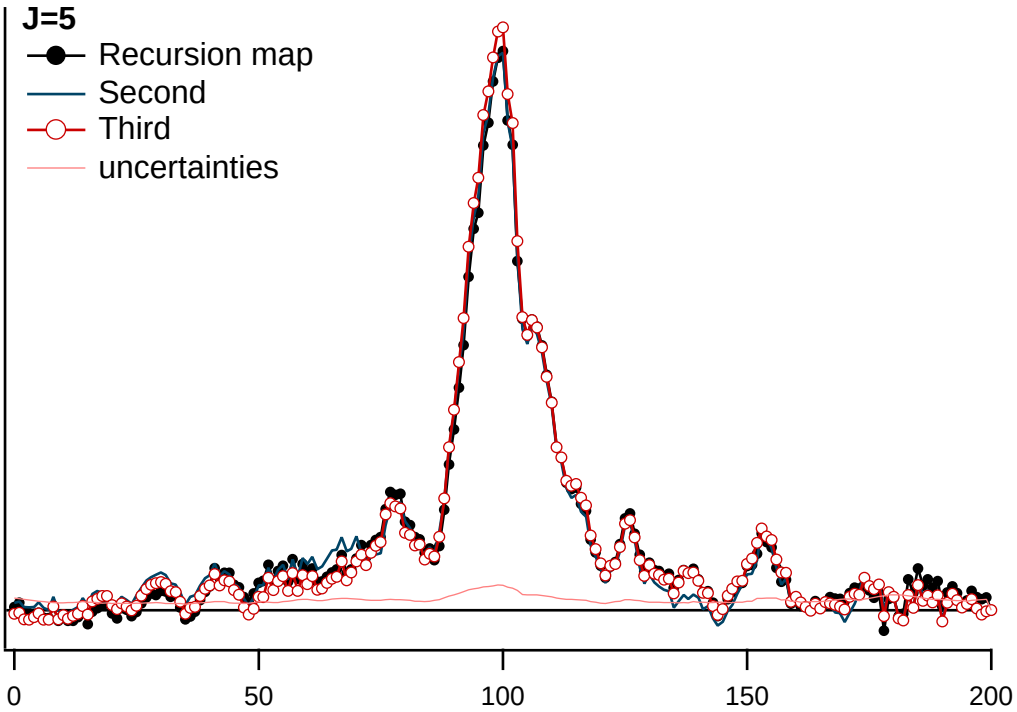

Figure 8-17: J=5 pattern.

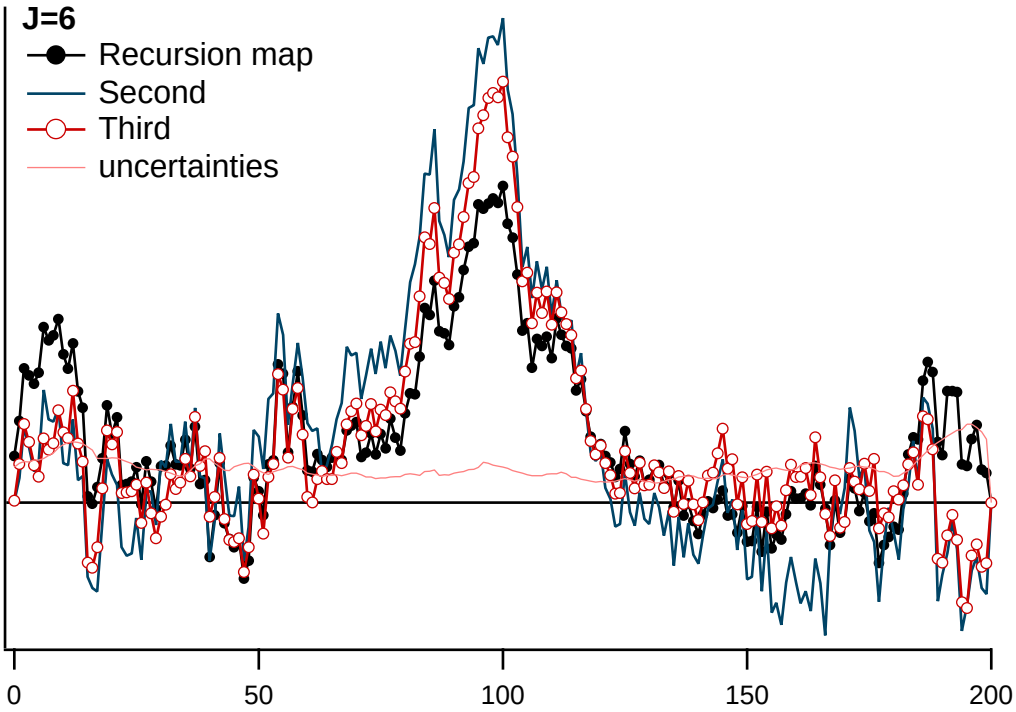

Figure 8-18: J=6 pattern.

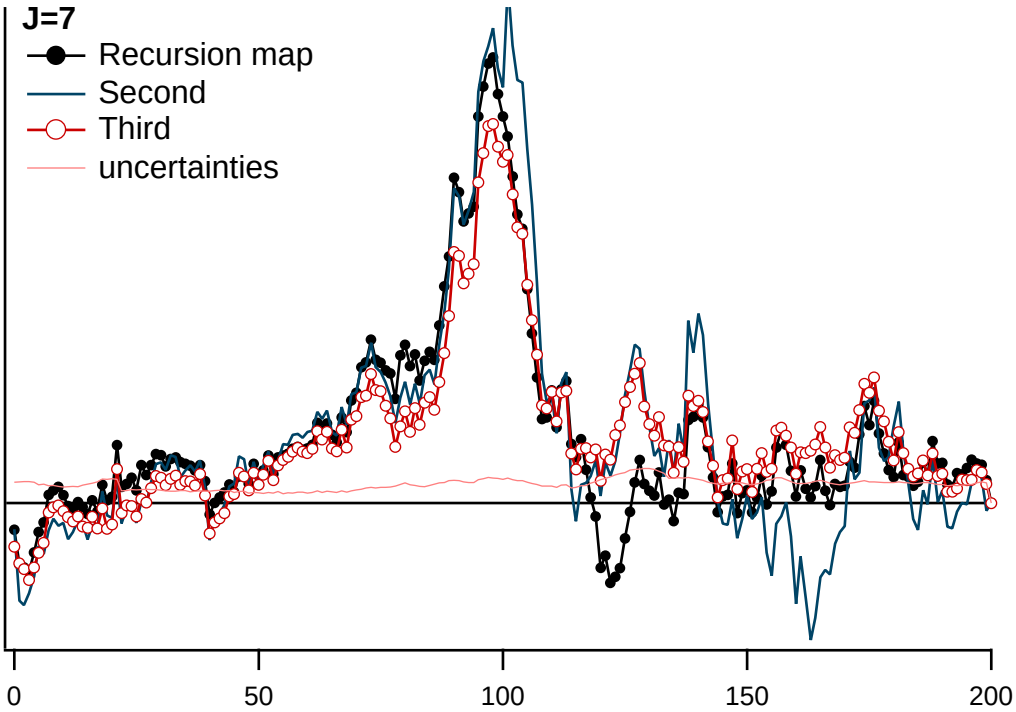

Figure 8-19: J=7 pattern.

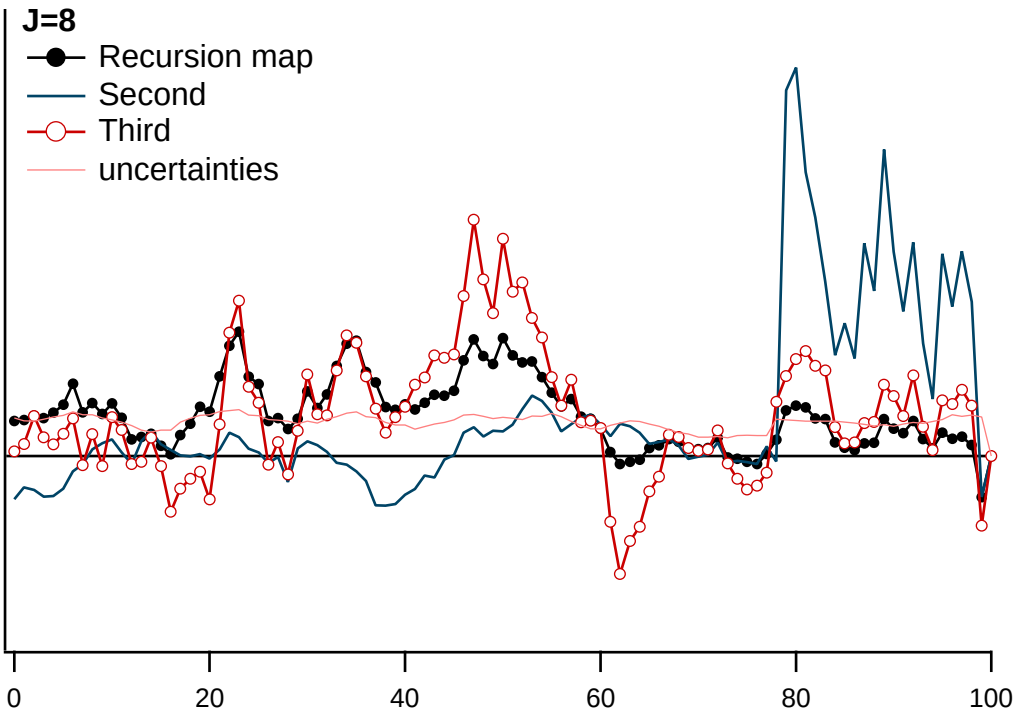

Figure 8-20: J=8 pattern. This pattern is narrower and more uncertain than those of the lower rotational levels.

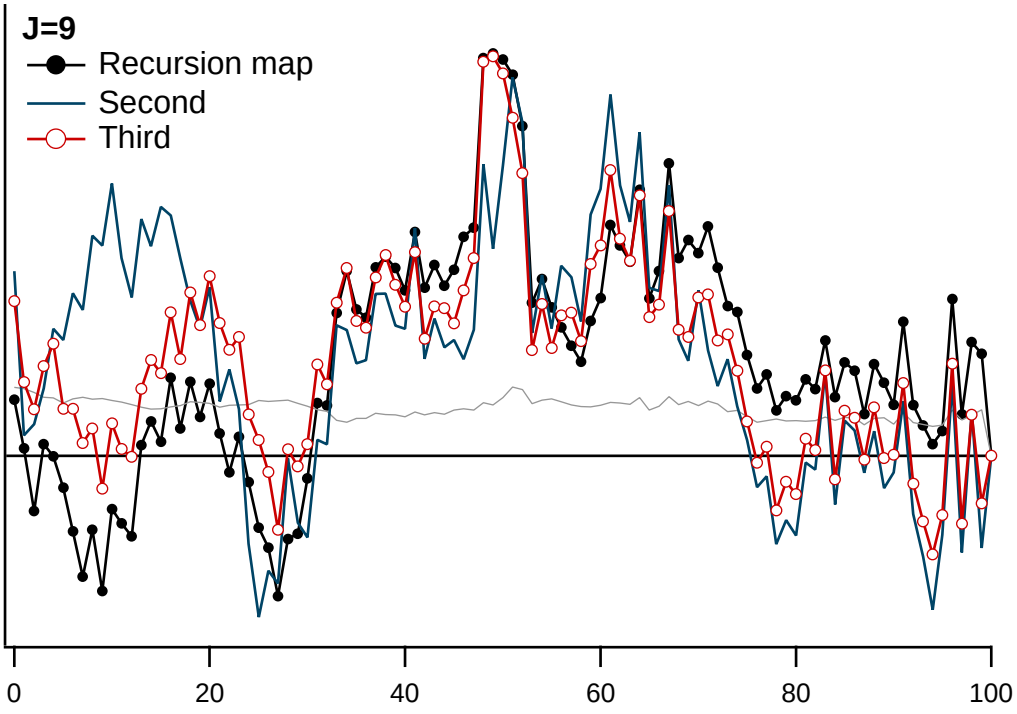

Figure 8-21: J=9 pattern. This pattern is narrower and more uncertain than those of the lower rotational levels.

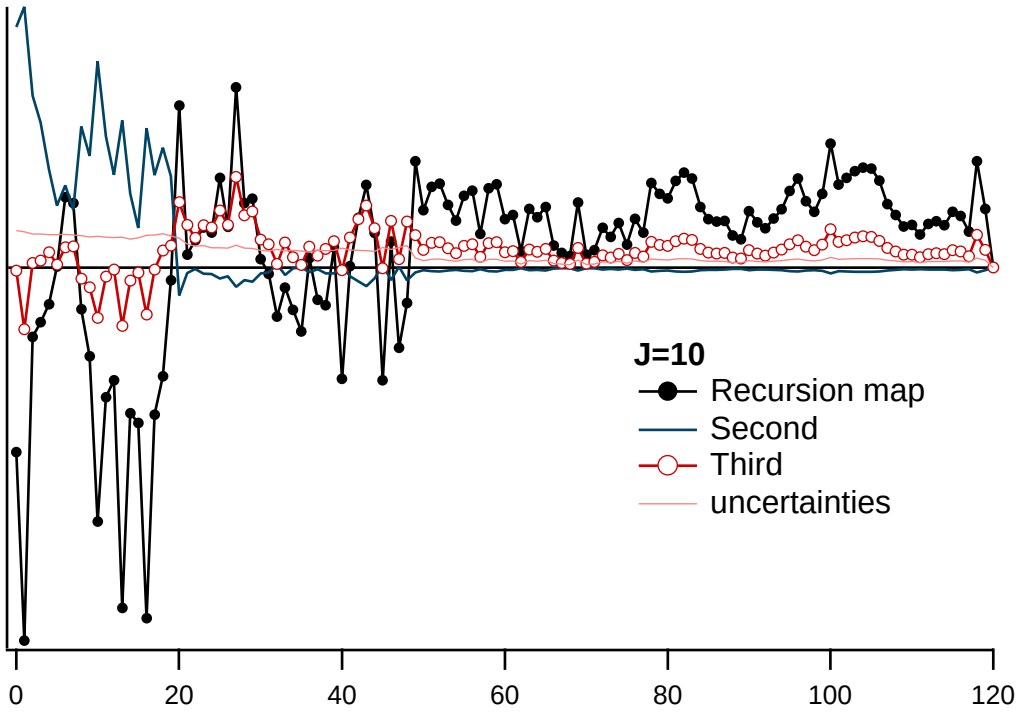

Figure 8-22: J=10 pattern.

fit was selecting a correct weighting function for eq. 8.16. The noise in the experiment was almost entirely shot noise, so the first weighting function was $1/\ \mathrm{I}_{SEELEM}$ ($\sigma_{SEELEM} = \sqrt{I_{SEELEM}}$). The merit function did not include the penalty function for negative going features in the patterns. This, however, did not converge to reasonable patterns. This function heavily weighted small residuals near the baseline, which forced the fit to compensate for very small errors. This produces large residuals and unrealistic patterns with negative features.

To improve the results, the penalty function of negative going features in the patterns was included. The patterns that resulted are shown in Figs. 8-12 through 8-22 and are referred to as "second" since this was the second merit function. They are obviously worse than the patterns without intensities "improved" by non-linear fitting, although the merit function did decrease with these patterns. The weighting function is inappropriate.

The successful weighting function was $1/\ (\sqrt{I_{SEELEM}} + 20)^2$, which accounts for a

small, constant noise level. This, along with the penalty term, produces the patterns shown in Figs. 8-12 through 8-22 in eight iterations. These patterns are referred to as "third." The resulting patterns have fewer negative going features. The residuals are smaller than those that result from the intensities estimated from the recursion maps and are comparable to the noise level in the data. The patterns of the higher Js are unrealistic, but these patterns exceed the uncertainty by only a small amount. These patterns are poorly determined because the corresponding spectral appearances are weak and overlapped near the R-branch head. The final pattern, J=10, is almost flat. Most of this pattern is just above the 1 σ uncertainty level. It is not clear that any of the J=10 rotational level pattern is real. The calculated spectrum that results from these patterns is shown in Fig. 8-23 through 8-30.

The value of 20 in the weighting function is too generous a compensation for the constant noise level. χ^2 equals 111.1, while there are 2991 degrees-of-freedom (knowns minus unknowns). A fit is considered good when χ^2 equals the degrees-of-freedom. 20 is too large a value, which makes the weighting function and χ^2 too small. However, the value of 20 successfully minimizes the influences of small deviations near the baseline.

Despite the overall success of the procedure, a few of the resulting patterns are unsatisfactory. The feature on the left side of J=1 is clearly not correct (Fig. 8-13). As one can see in the spectrum (Fig. 8-30), this should be three lines, not a wide, unresolved feature. This is due to heavy overlapping in the Q-branch. In the J=2 pattern, a spike appears on the right of the pattern (Fig. 8-14) which is intensity from Q(1) that overlaps this pattern when it appears in Q(2). In addition, some of the residuals have systematic variation, as shown in (Fig. 8-27). These problems are due to a violation of the assumption that the patterns are invariant in each appearance. There are some significant changes in the relative intensities of the features in the spectrum. This may be due to detector saturation or related to surface detectivities that are different for the pure acetylene expansion than they are for the acetylene-seeded He expansion. The resulting pattern is the average of the appearances of the pattern weighted by $1/\ (\sqrt{I_{SEELEM}}\ +\ 20)^2$. The weighting accounts for variations

of the patterns that are associated with noise but not the more significant variation that appears in this spectrum. Clearly, if the patterns are not invariant, XAC will not produce accurate results.

An attempt was made to analyze the patterns using a reduced term value plot. Unfortunately, there are too many lines or, conversely, too poor resolution to make much sense of the plot. As discussed in Chapter 7, it is not clear what determines the SEELEM intensity. It is certainly related to the amount of S_1 and T_3 character in the terminal state, but the form of this relation has yet to be experimentally established. Because of this lack of information, one cannot predict how the intensity of a state will change as it tunes through the zero-order bright S_1 basis state as a function of J.

8.5 Conclusions

Extended Auto Correlation can extract patterns from a highly overlapped SEELEM spectrum. Within the limits of data quality, the patterns that result from XAC are optimal in the sense that they minimize both the negative going features in the patterns and the residuals. These patterns can now be subjected to a set of analysis techniques that could reveal the interactions between singlets and background states at his energy.

8.6 Acknowledgments

Thanks to Dr. Matthew Jacobson for helping me understand XCC and for helpful discussions about the XAC problem. Also, thanks to Dr. Stephen Coy for helpful discussions about SVD.

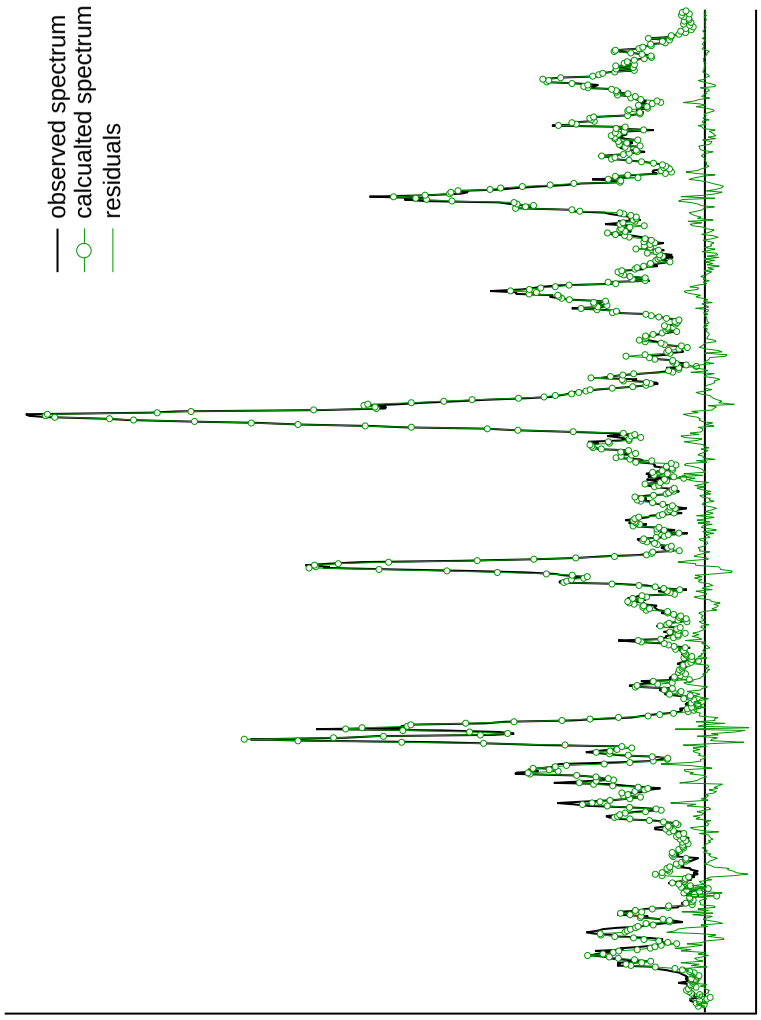

Figure 8-23: The R-branch of the spectrum recorded with a pure acetylene expansion.

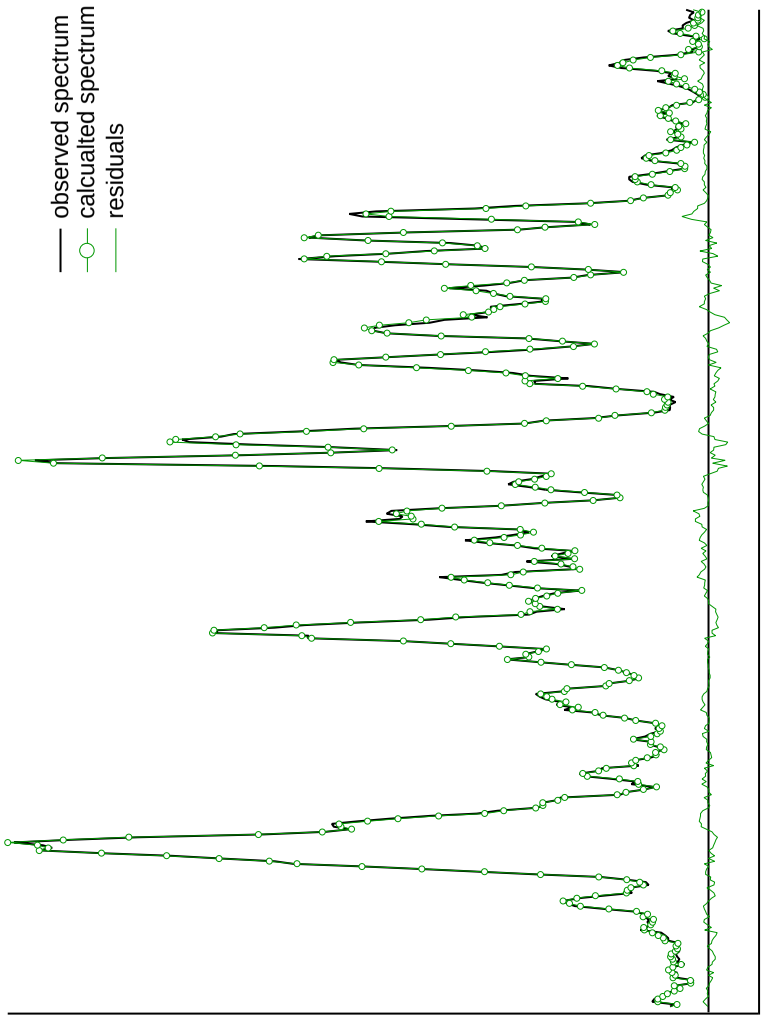

Figure 8-24: The Q-branch of the spectrum recorded with a pure acetylene expansion.

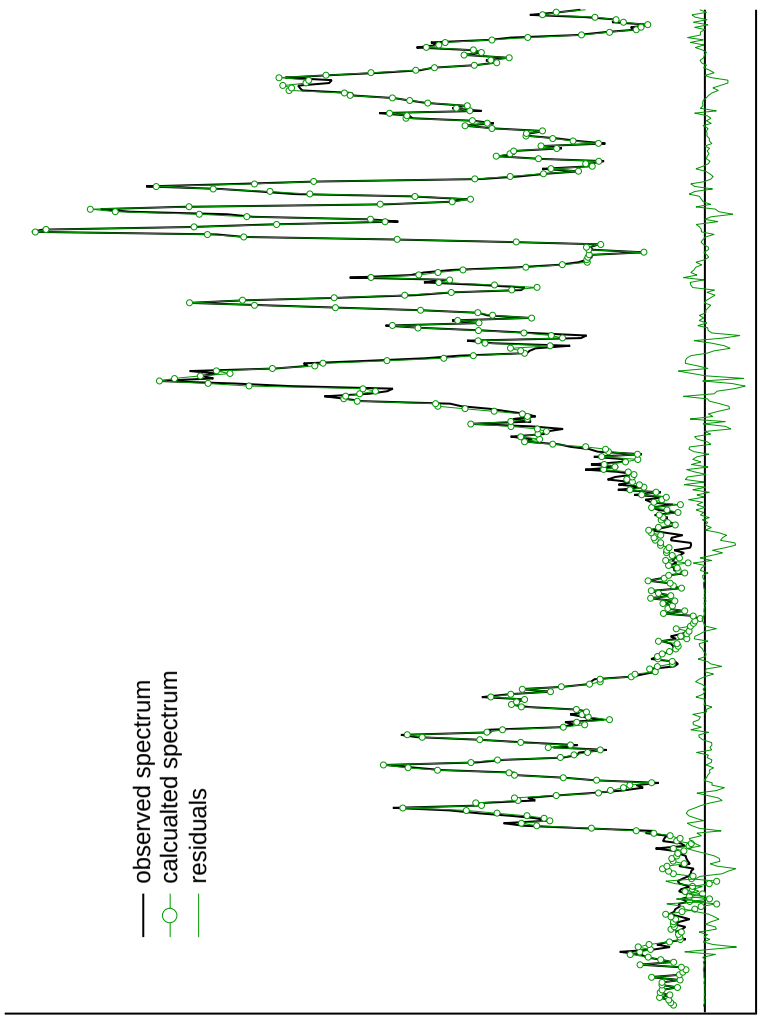

Figure 8-25: The P-branch of the spectrum recorded with a pure acetylene expansion.

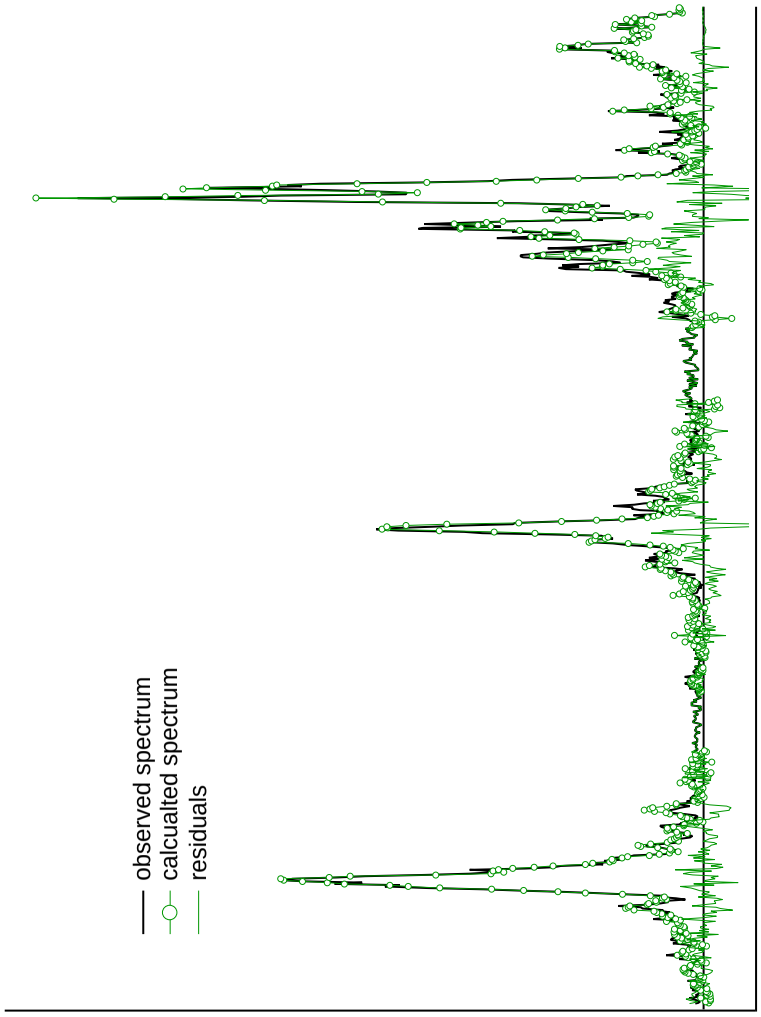

Figure 8-26: The P-branch of the spectrum recorded with a pure acetylene expansion.

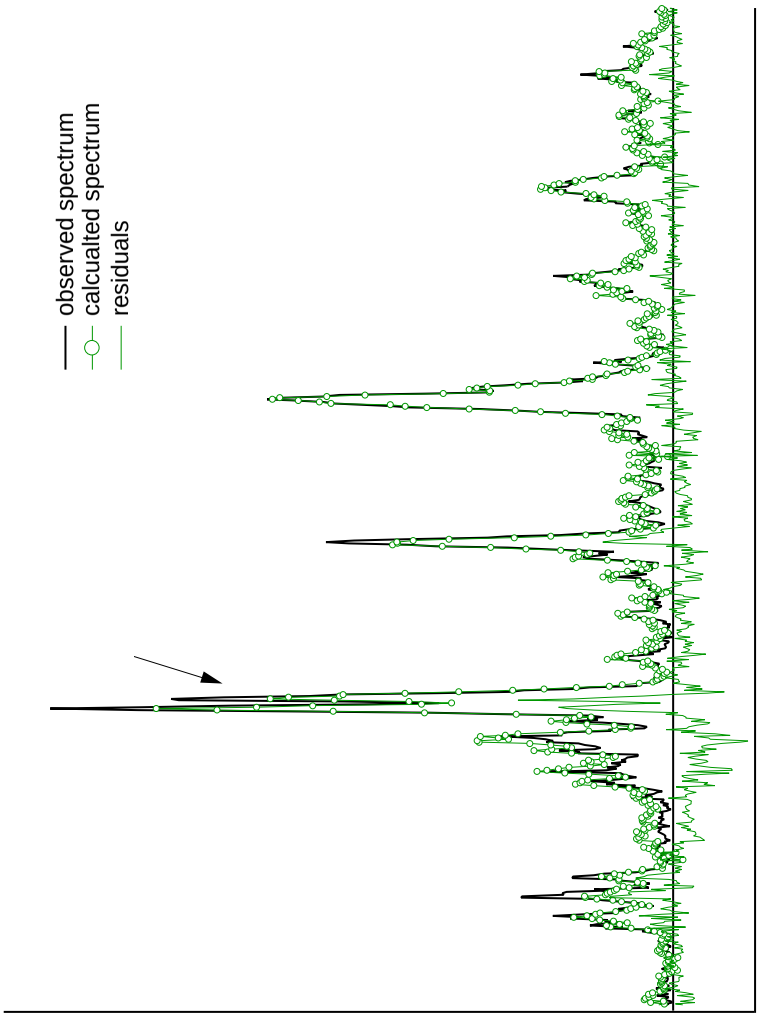

Figure 8-27: The R-branch of the spectrum recorded with an acetylene-seeded He expansion. Note that the patterns for R(2) are not the same here as elsewhere in the spectrum. The strongest lines are much larger here compared with the smaller lines. It is not clear what caused this.

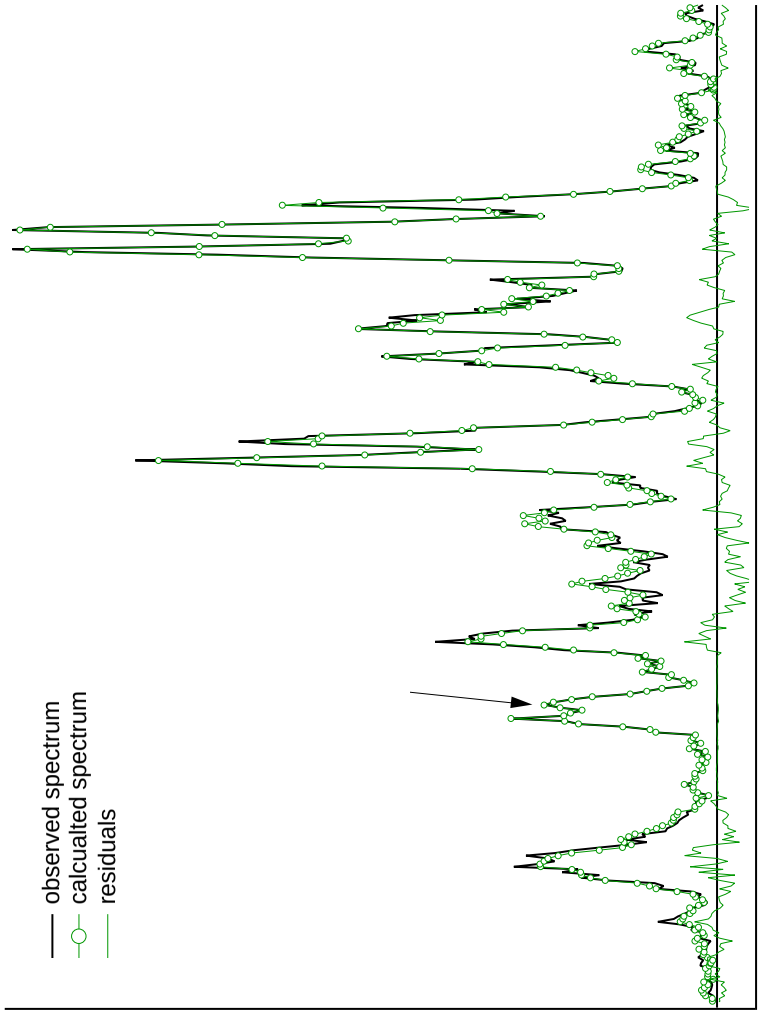

Figure 8-28: The Q-branch of the spectrum recorded with an acetylene-seeded He expansion. Note that the residuals near P(1) are small, which indicates that the region is not over-determined.

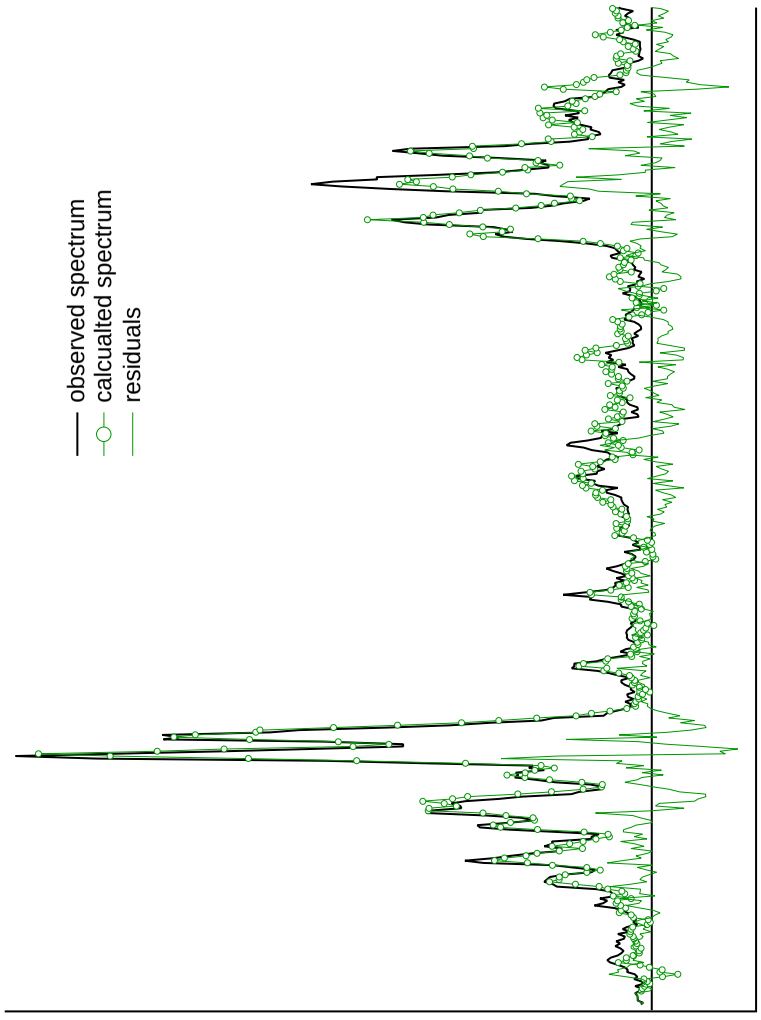

Figure 8-29: The P-branch of the spectrum recorded with an acetylene-seeded He expansion.

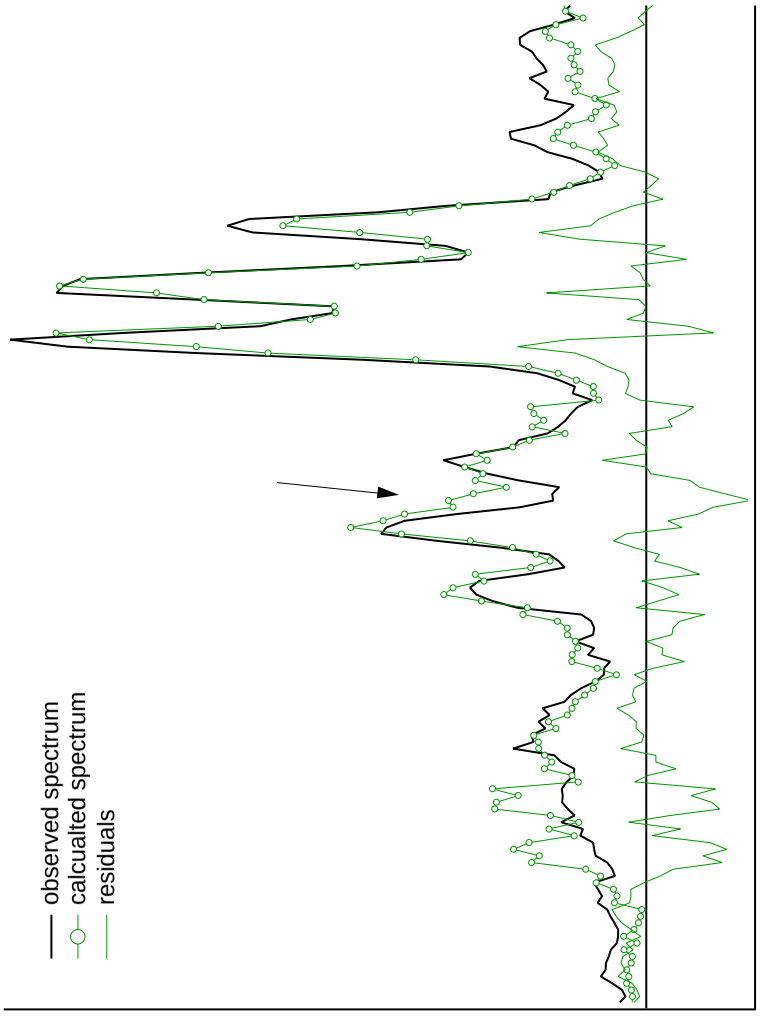

Figure 8-30: The P(2) transition. The observed spectrum clearly shows three resolved lines, but the pattern has an unresolved feature.

Chapter 9

Metastable Photofragments

9.1 The observation of metastable photofragments

Electronically excited fragments produced by multiphoton acetylene dissociation have been detected. Metastable photofragments have been detected in the SEELEM channel, and emission from excited photofragments has been detected in the near infrared. Neither of these signals can be accounted for by a one-photon absorption to highly excited, bound acetylene. The metastable photofragments can be distinguished from metastable acetylene because they arrive at the detector earlier than the intact molecules, as shown in Figs. 9-1, 9-2, 9-3, and 9-4. The dissociation imparts additional kinetic energy to the fragments, so they arrive at the detector in advance of the intact metastable acetylene.

Due to the Jacobian transformation from the frame of the molecules in the expansion to laboratory frame, one normally observes only those fragments that move faster than the molecular beam velocity. The fragments form sphere that expands from the moving position of the parent molecules. A certain solid angle of this sphere is collected as the leading edge of the sphere arrives at the detection surface. The trailing edge arrives much later, when the sphere has expanded, so a smaller solid angle of this sphere is collected by the detection surface.

Electronically excited photofragments have also been detected using the IR detector both in cell and molecular beam experiments. As shown in Fig. 9-5, IR emission

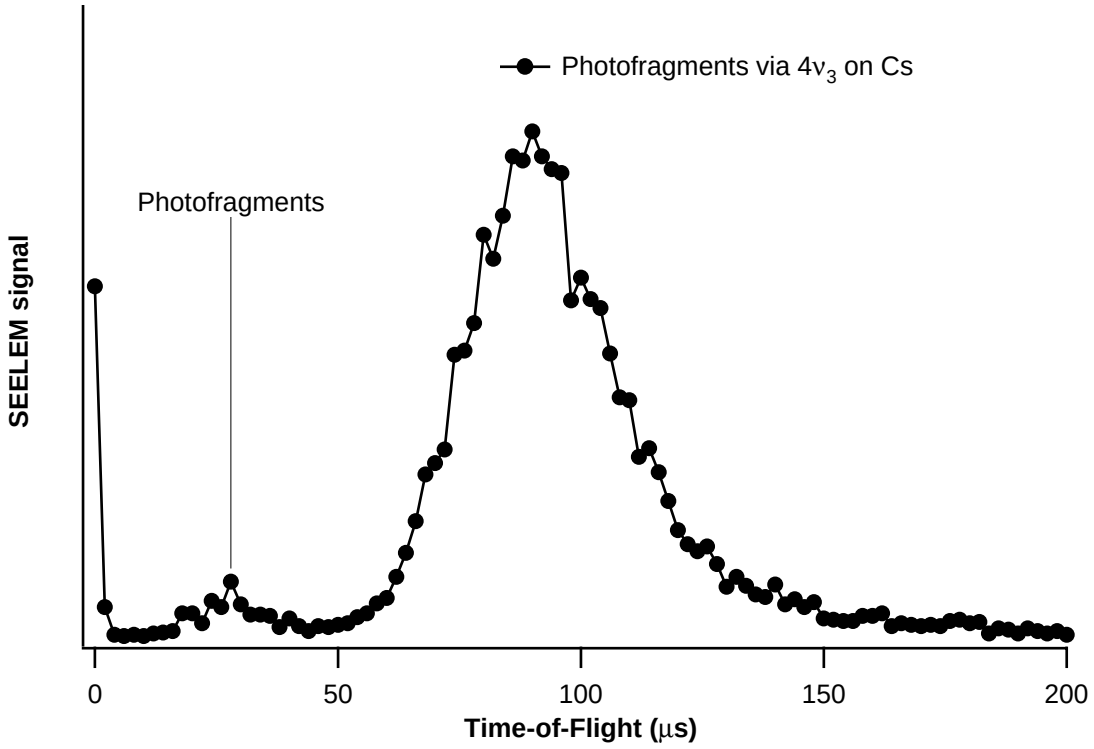

Figure 9-1: TOF profile of Q(1) of $4\nu_3$ ($V_0^4K_0^1$) detected on a Cs surface. The arrival times of metastables at the detection surface are shown relative to the time the excitation laser fires. The initial signal is caused by photoelectrons ejected from the surface by laser scatter or molecular fluorescence. The large peak at 90 μs is formed by intact acetylene metastables excited by a single photon. Metastable photofragments are responsible for the smaller peak at 30 μs.

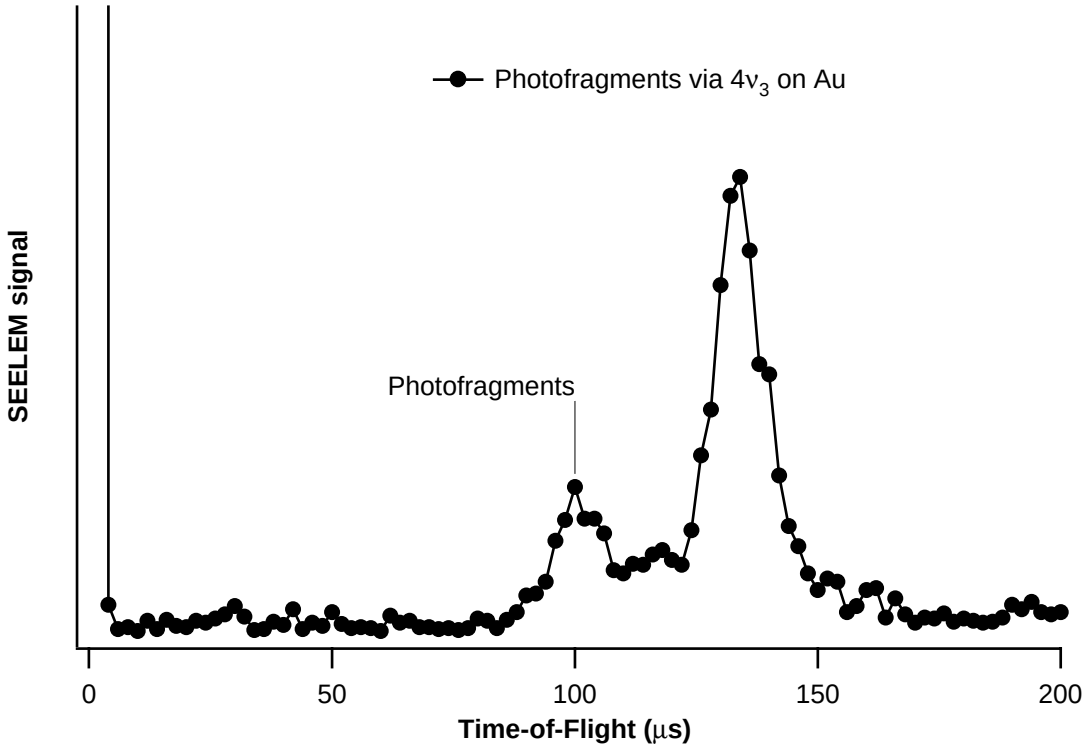

Figure 9-2: TOF profile of Q(1) of $4\nu_3$ ($V_0^4K_0^1$) detected on a Au surface. Intact metastable acetylene, resulting from one-photon excitation, arrives at ~ 140 μs, and metastable photofragments arrive ~ 105 μs after the laser fires. The distinction between this TOF profile and the one in Fig. 9-1 is discussed in the text. This was recorded at UCSB.

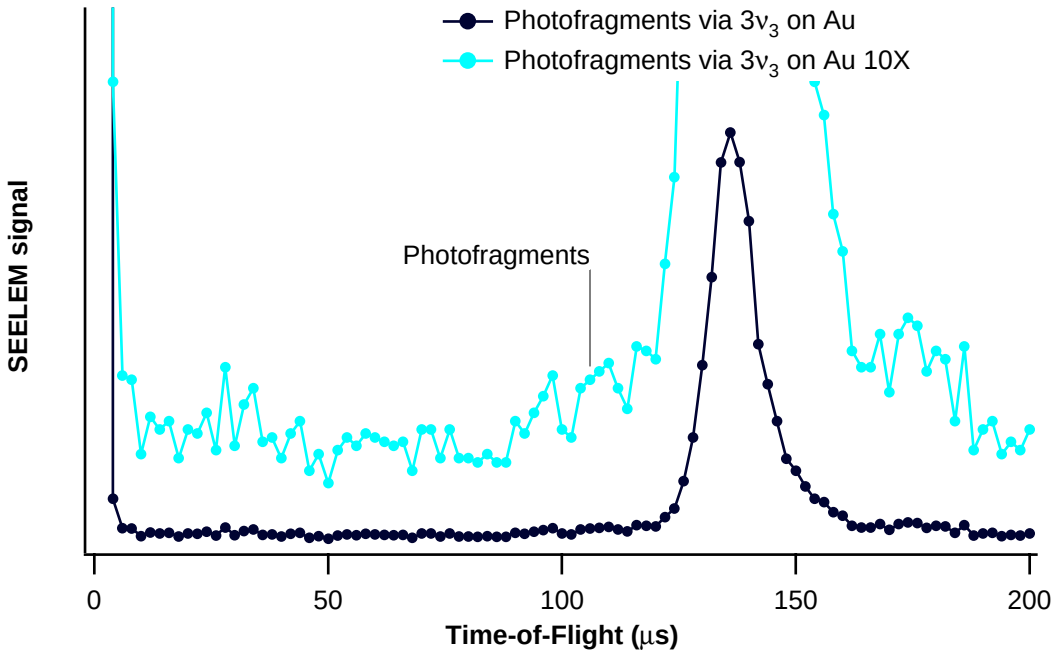

Figure 9-3: TOF profile of R(1) of $3\nu_3$ ($V_0^3K_0^1$) detected on a Au surface. The small signal at the base of the intact metastable peak is the metastable photofragment signal. This metastable photofragment signal can also be seen, perhaps more convincingly, in Fig. 9-1 of Humphrey, *et al.*[79] under somewhat different expansion conditions. This was recorded at UCSB.

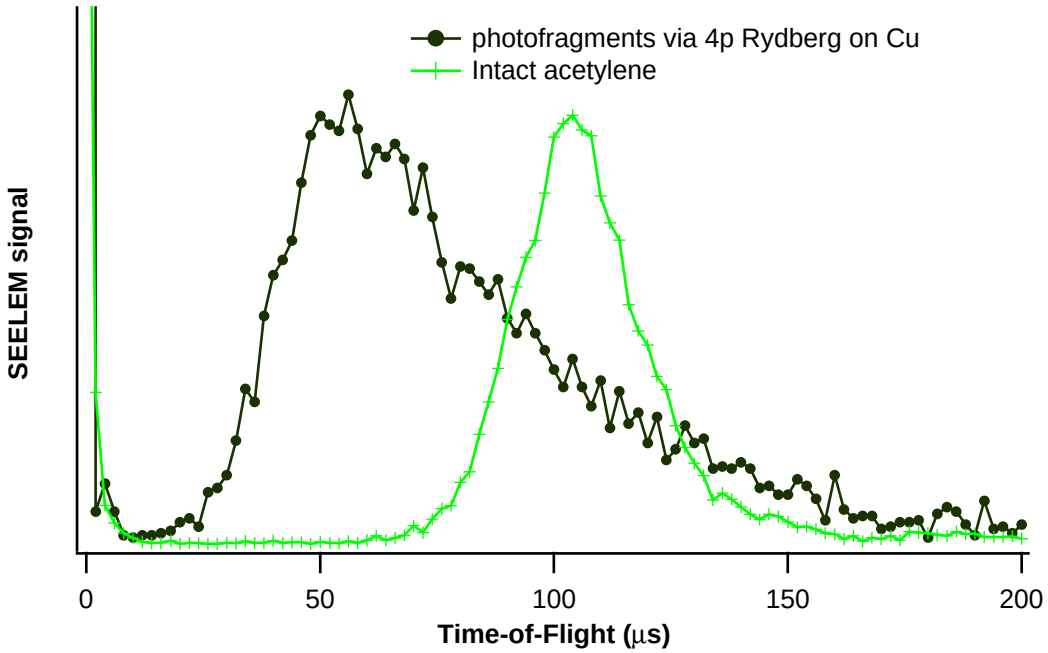

Figure 9-4: TOF profile of the two-photon transition terminating in the $4p$ Rydberg state detected on a Cu surface. This state was observed by Ashfold, *et al.*[9] Since there is no intact acetylene signal, a TOF profile of $3\nu_3$ under the same expansion conditions is shown so that the Rydberg state TOF profile may be compared to the profile created by the expected velocity distribution.

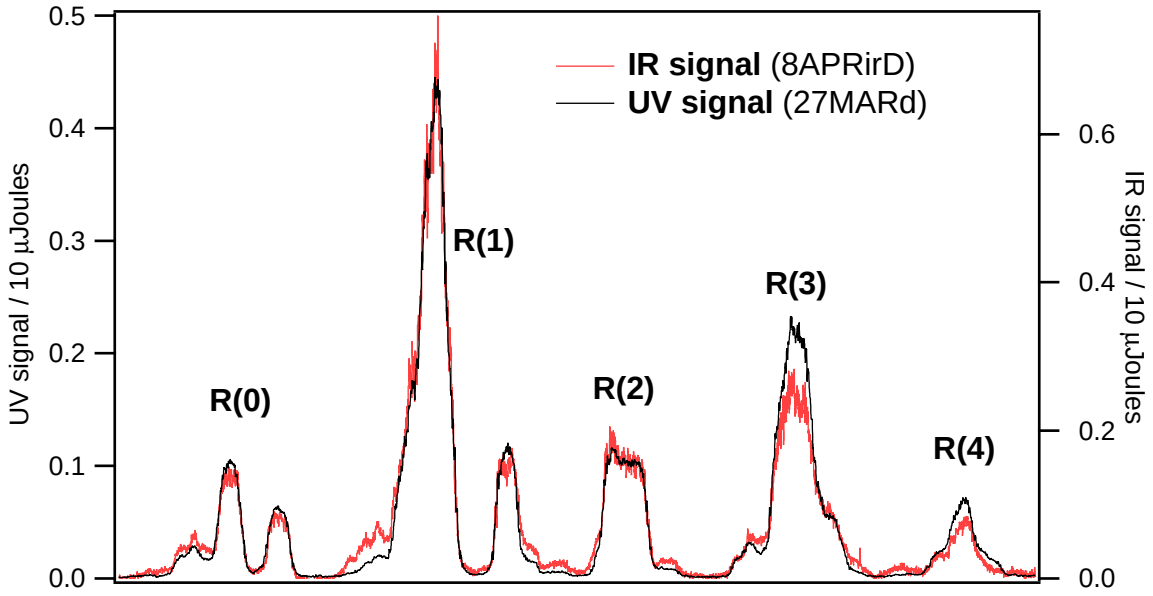

Figure 9-5: IR-LIF and UV-LIF spectra of the R-branch of $3\nu_3$ in the $\tilde{A}$-state of acetylene.

is detected at the same excitation frequencies as is fluorescence in the UV. These spectra were not taken simultaneously, so some intensity differences maybe due to different rotational temperatures. There are other intensity differences with in a single rotational transition, like those shown on the left side of R(1). these may be the result of two effects. IR-producing, two-photon transitions through these states might be enhanced because these states possess some special character that provides good oscillator strength to the dissociating Rydberg states. The second effect may be that some of the UV-LIF is not observed. These states have long lifetimes. These are the states labeled 002, 003, and 004 in Fig. 6-4, and their lifetimes were measured to be > 5 μs, as shown in Table 6.1. It is possible that the UV-LIF signal is lower than the IR-LIF signal because a large fraction of the UV-LIF is emitted after the molecules have moved out of the viewing region of the collection optics.

The IR emission is not the result of a one-photon absorption. While the UV fluorescence has a linear power dependence, the IR emission has a non-linear power

Table 9.1: Observations of metastable and IR-emitting photofragments.

Initial transition	Excitation energy (cm^{-1})	SEELEM detected fragments	detection surface (work function)	IR detected fragments
$4p$ Rydberg	82654	7JUN99	Cu (4.65 eV)	2JUN99
$4\nu_3$	46300	10OCT96	Au (5.1)	24-26APR99
$4\nu_3$	46300	5FEB99	Cs (2.14)	
$3\nu_3$	45300	6OCT96	Au (5.1)	8,15-17ARP99
$2\nu_3$	44300	(no attempt)		24FEB96
$1\nu_3$	42130 (hot band)	none	Cs (2.14)	4JUN99
origin band	42209	none	Cs (2.14)	4JUN99

dependence, so it can be attributed to a two-photon absorption process. Figure 9-6 shows the dependence of the IR-LIF signal on laser energy. Clearly it is non-linear. Fitting this data to the following function resulted in a exponent or 1.67(6) indicating that this signal must be due to at least two photons.

$$IR\ signal\ =\ constant \cdot (laser\ energy)^n \tag{9.1}$$

The exponent is not be equal to 2 perhaps because of some saturation on the second absorption step. In fact, this saturation may be increasing over this laser energy range. Note that the IR signal is a little lower than the fit line at 25 μJ and a little higher at 60 μJ. This may indicate that saturation of the second step is increasing around 60 μJ. The acetylene states at energy of two photons dissociate quickly forming C_2H which is known to emit in the near-IR. IR emission from C_2H photofragments has been observed.[140, 160, 185, 168, 188, 45] Other possible sources of IR-LIF will be discussed below.

Evidence of electronically excited photofragments has been obtained at five excitation frequencies, as shown in Table 9.1. Infrared emission resulted from laser excitation of each $\tilde{A}$-$\tilde{X}$ that we have studied: the origin band, $2\nu_3$, $3\nu_3$, and $4\nu_3$. It is likely that excitation through any of the bands in the $\tilde{A}$-state will result in IR emission. Additionally, excitation of the two-photon transition to a $4p$ Rydberg state results in infrared emission.

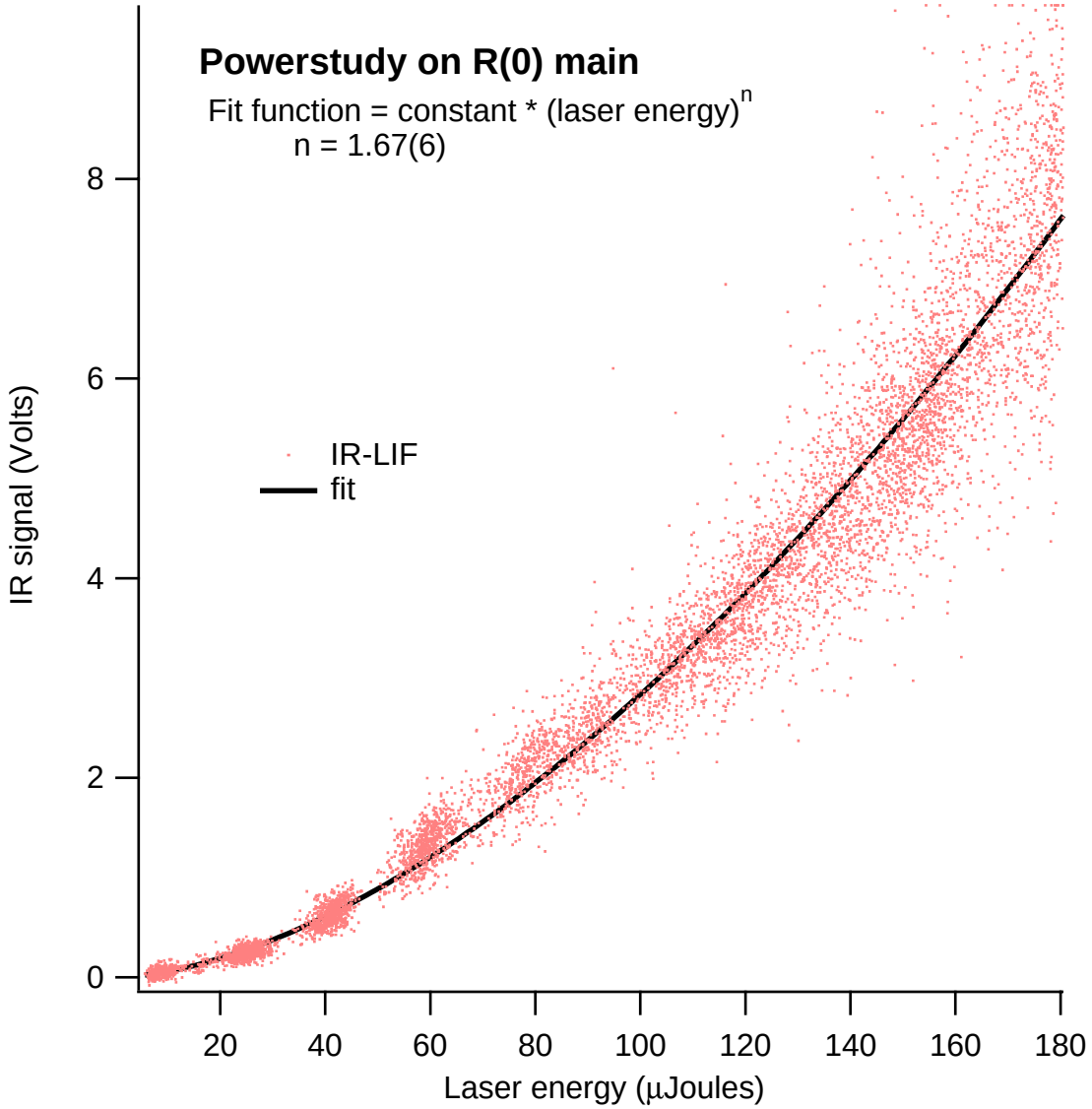

Figure 9-6: The dependence of the IR-LIF signal on laser energy.

Metastable photofragments have been observed at a number of these excitation frequencies, also shown in Table 9.1. Photofragments have been observed on a Cs surface when $4\nu_3$ was excited. They were also observed on a Cu surface when the two-photon transition to the $4p$ Rydberg state was excited. Using Au as a detection surface, metastable photofragments were detected through both $3\nu_3$ and $4\nu_3$ with a Au detection surface at UCSB. None were observed when the laser was tuned to the origin band or $1\nu_3$.

The observation of electronically excited photofragments is interesting for a number of reasons. It implies that SEELEM and IR-LIF spectra have the potential to reveal dissociation pathways and provide other insights into dissociation mechanisms. The SEELEM results are of special photochemical relevance. The observation of electronically excited metastables shows that some fraction of the absorption events results in highly excited photoproducts that sequester chemically-relevant amounts of energy. Photochemists have shown that metastable species play an important role in the chemistry of acetylene after the absorption of a vacuum UV photon.[141, 143, 142, 163, 162, 97, 98, 99, 54, 53, 55] The production of metastable photofragments could have a significant impact on the photochemistry of acetylene.

For example, the hydrogen abstraction reaction

$C_2 + C_2H_2 \rightarrow 2\ C_2H$

is endothermic by $\sim$ 0.8 eV ($\sim$18 kcal./mol.). A photochemist might not consider this reaction in the chain of events following the photolysis of acetylene. However, if a significant number of C_2 molecules that result from photolysis end up in the 1 $^3\Delta_u$ state, the reaction may become important. The 1 $^3\Delta_u$ state of C_2 is probably metastable and lies at an electronic energy of $\sim$ 5.25 eV relative to the C_2 electronic ground state.

$C_2(1\ ^3\Delta_u) + C_2H_2 \rightarrow 2\ C_2H$

is exothermic by -4.45 eV (-102 kcal./mol.), and the long $C_2(1\ ^3\Delta_u)$ lifetime means that the state has plenty of time to collide with an acetylene molecule. The electronic energy maintained in the 1 $^3\Delta_u$ state of C_2 makes this molecule more reactive.

In this chapter, the possible photofragment states that could be responsible for

the observed signals will be examined. Several electronically-excited photofragments could account for either the IR emission or the SEELEM signal. Eliminating all but one of the possibilities for each observable is impossible at present, but it is possible to identify the most likely candidates.

9.2 Analysis

The point of departure for the analysis of the SEELEM-detected photofragments is energy conservation.

$$0 = n \cdot h\nu - E_{\ translational} - E_{\ internal} - E_{\ dissociation} \tag{9.2}$$

where n equals the number of photons absorbed, $E_{translational}$ is the translational energy release upon dissociation, $E_{internal}$ is the energy internal to the photofragments, including rotational, vibrational, and electronic energy, and $E_{dissociation}$ is the energy required to dissociate acetylene into a given set of photofragments. This equation expresses the fact that the energy imparted by the photons is divided between bond fission and the fragments' translational and internal energies.

If the identity of the fragments that are responsible for the signal is known, $E_{translational}$ can be computed from the TOF profile. This allows for the calculation of the $E_{internal}$ of the photofragments by subtracting $E_{dissociation}$ and $E_{translational}$ from the energy of a given number of photons.

To be SEELEM-detectable, the photofragment must be in a state that meets two criteria. The state must have a large amount of electronic energy to remove an electron from the metal surface. Consequently, $E_{internal}$ must be at least as large as the detector surface work function, probably somewhat larger to account for vibrational and rotational energy. This provides us with one criterion for evaluating the possible states.

The second criterion is that the electronic state must have a lifetime in excess of $\sim 20\mu$s. This is the shortest lifetime that would allow for detectable quantities of molecules to remain excited after the molecules have traveled from the excitation

region to the detection surface.

Because we know neither the identity of the fragments nor the number of photons responsible for the signal, the $E_{internal}$ will be calculated for several fragmentation reactions in the case of both two- and three- photon absorption.

Two constraints help identify which states could produce the IR signal. The first is that there must be a sufficient number of photons to exceed $E_{dissociation} + E_{emission}$. The IR detector can detect emission at wavelengths in the range of 800 - 1700 nm (1.5 - 0.7 eV). Two photons are sufficient for this at the frequencies we have used. The second constraint is that the final state must have an allowed transition to an electronic state lower in energy by ~ 1 eV

9.2.1 Possible photofragments

There are several possible sets of fragments that could be produced when acetylene absorbs three photons with wavelengths between 215-240 nm. The most important of these are

$$C_2H_2 + n \cdot h\nu \rightarrow C_2H + H \quad \text{(I)}$$

$$C_2H_2 + n \cdot h\nu \rightarrow C_2 + H_2 \quad \text{(II)}$$

$$C_2H_2 + n \cdot h\nu \rightarrow C_2 + 2H \quad \text{(III)}$$

$$C_2H_2 + n \cdot h\nu \rightarrow C_2 + 2H \quad \text{(IIIa)}$$

$$C_2H_2 + (1\text{-}2) \cdot h\nu \rightarrow C_2H + H + (2\text{-}1) \cdot h\nu \rightarrow C_2 + 2H \quad \text{(IIIb)}$$

$$C_2H_2 + n \cdot h\nu \rightarrow \ 2CH \quad \text{(IV)}$$

$$C_2H_2 + n \cdot h\nu \rightarrow C_2H + H\ (2s) \quad \text{(V)}$$

$$C_2H_2 + n \cdot h\nu \rightarrow C(^1S,\ 2.68\ \text{eV or}\ ^5S,\ 4.18\ \text{eV}) + C(^3P,\ 0\ \text{eV}) + H_2 \quad \text{(VI)}$$

Three photons provide enough energy to produce metastable atoms. Metastable hydrogen in the $2s$ state, which has 10.2 eV of electronic energy, could be produced by reaction V. Metastable carbon atoms could be produced by reaction VI. Reactions V and VI require almost all of the energy imparted by the photons to be used in breaking bonds with little left over for translational, vibrational, or rotational energy of the fragments.

Figure 9-7 shows the energy thresholds of each of the fragmentation reactions, and the electronic energy levels of C_2H, C_2, CH, and a few of the relevant levels in C_2H_2. The dissociation limits for D_0(HCC–H) and D_0(CC–H) were determined by Mordaunt *et al.*[127, 128] and Chiang *et al.*[28] respectively. The other limits were determined using the D_0 of C_2, H_2, and CH from Huber and Herzberg[77]. The acetylene states shown $\sim 45,000$ cm^{-1} represent the ν_3 progression in the $\tilde{A}$-state. The $4p$ Rydberg state corresponding to Fig. 9-5 is also shown at 82,654 cm^{-1}. Figs. 9-12, 9-10, 9-11, 9-8, and 9-9 show the fragment levels in more detail, including the symmetry, dominant configuration, energy, and lifetime (if known) of each electronic state. Some of this information is from experiment and some is from theoretical calculations. Experimentally determined values are printed in black.

Figure 9-7 also depicts the energies reached by one-, two- and three-photon transitions as horizontal lines that extend across the entire figure. The lowest two signify the energies of transitions to the $3\nu_3$ and $4\nu_3$ vibrational levels of the $\tilde{A}$-state. The next shows the energy of the two-photon transition to the $4p$ Rydberg state. The next two show the energy of two-photon transitions through $3\nu_3$ and $4\nu_3$. The upper three lines correspond to the energies of three-photon transitions through the $4p$ Rydberg state, $3\nu_3$, or $4\nu_3$.

9.2.2 $\mathbf{E}_{translational}$

The SEELEM TOF profiles provide information about $E_{translational}$, the translational energy kick of the dissociation event. If the distance between the location where the laser and molecular beams intersect and the detection surface is known, the time between the laser firing and the arrival of the photofragments at the detection surface is a measure of the velocity of the fragments. This allows us to calculate the kinetic energy released by the dissociation as follows. The momentum of the two fragments (C_2H and H, for example) must be equal as required by momentum conservation:

$$m_H \cdot v_H = m_{C_2H} \cdot v_{C_2H} \tag{9.3}$$

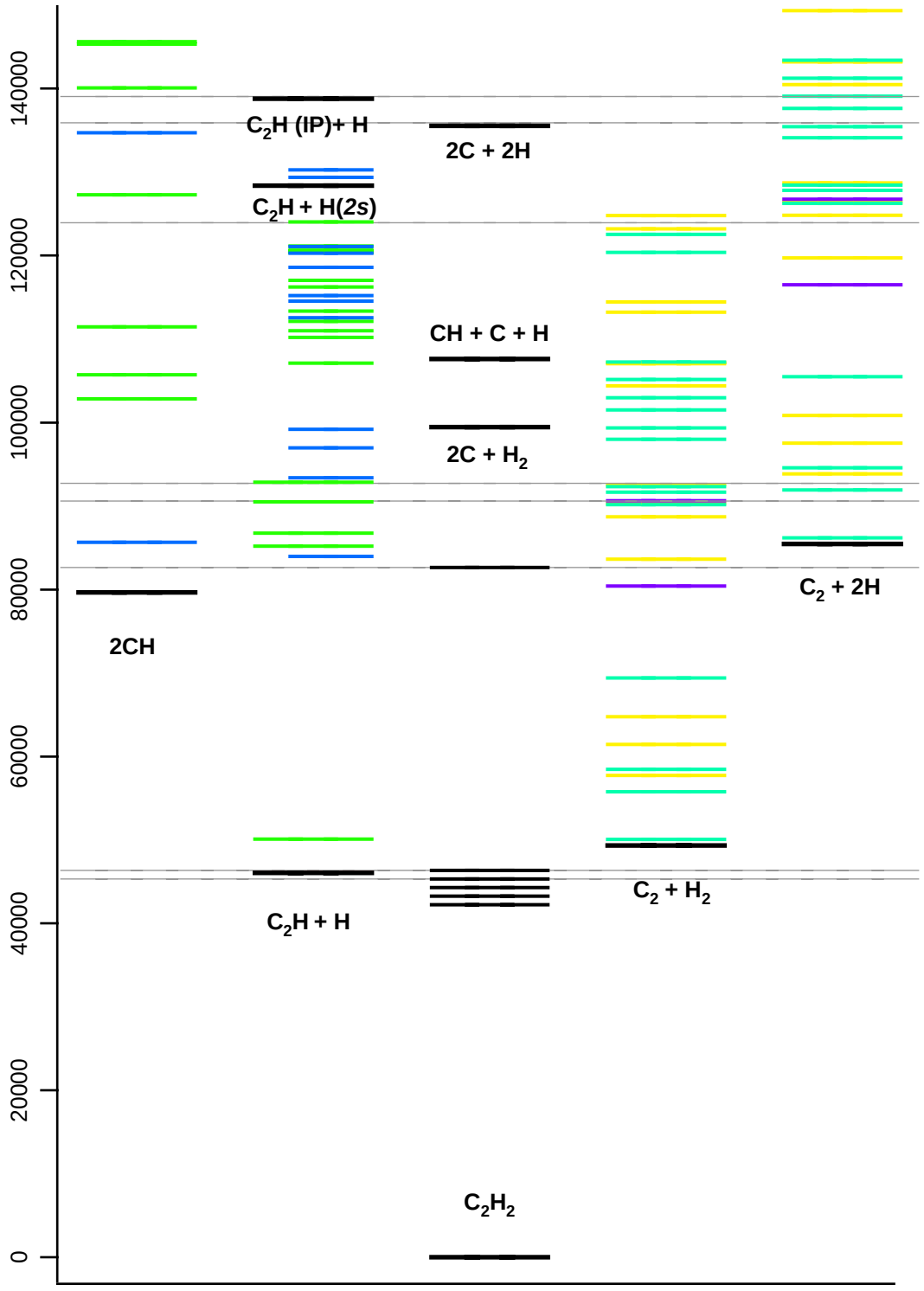

Figure 9-7: Possible photofragments along with the dissociation limits. Details about the photofragment states of CH, C_2, and C_2H are displayed in Figs. 9-12, 9-10, 9-11, 9-8, and 9-9.

or

$$v_H = m_{C_2H}/m_H \cdot v_{C_2H}. \tag{9.4}$$

The kinetic energy released in the dissociation is

$$E_{\ translational} = 1/2 \cdot (m_H \cdot v_H^2) + 1/2 \cdot (m_{C_2H} \cdot v_{C_2H}^2). \tag{9.5}$$

Substituting the expression for momentum conservation yields

$$E_{\ translational} = 1/2 \cdot m_{C_2H} \cdot v_{C_2H}^2 \cdot (m_{C_2H}/m_H + 1). \tag{9.6}$$

If we know the velocity of one fragment and the mass of both, we can determine $E_{translational}$. For a given TOF profile, we can calculate the translational energy release of a dissociation that results in two fragments.

Despite the simplicity of this approach, this method is not considered the best way to extract the translational energy release from the TOF profiles. The peaks that appear in the TOF profiles are the result of the behavior of fragments that have wide distributions of dissociation translational energies and originate from parent molecules with a range of initial velocities. The best way to arrive at the distribution of kinetic energies is to use the forward convolution method described by Morgan, Drabbels, and Wodtke[130, 131]. Rather than implementing this lengthy deconvolution, the photofragment peak maximum and the flight distance will be used to estimate the average velocity of the fragment.

One of the possible photodissociation paths results in three photofragments, C_2 + 2H. The TOF profile provides the velocity of only one of the three fragments. This provides insufficient information to calculate the total kinetic energy released by this dissociation. However, the translational energy release for C_2 + H_2 provides a lower bound to the translational energy release of C_2 + 2H. This can be made clear with a simple picture. The C_2 and the two H-atoms form a plane. The fragmentation occurs at the origin, and the motion of the C_2 fragment defines the x-axis. The momentum of the C_2 must be balanced by the component of the momentum of the H-atoms

Table 9.2: Approximate $E_{translation}$ in eV for five possible reactions.

	intact molecule velocity m/s	fragment velocity m/s	C_2H+H (I) $E_{translation}$	C_2+H_2 (II)	C_2+ 2H (III)	2CH (IV)	C_2H+H($2s$) (V)
$3\nu_3$ (Au)	1450	2080	1.34	0.64	0.64	0.05	0.002
$4\nu_3$ (Au)	1450	1950	0.84	0.40	0.40	0.03	0.001
$4\nu_3$ (Cs)	820	2640	11.18	5.36	5.36	0.45	0.018
$4p$ Ryd. on Cu	820	1580	1.95	0.94	0.94	0.08	0.003

along x. The fragmentation pattern with the lowest kinetic energy occurs when the H-atoms move along the negative x-axis with zero velocity in y. Why? Because any velocity in the y-direction of the H-atoms would increase the total kinetic energy of the fragmentation. With the two H-atoms moving along the negative x-axis, the kinetic energy will be minimized if the velocity of the two H atoms is equal. The case where both H-atoms travel in one direction with the same velocity is like the case with the two H-atoms bound together, which is C_2 + H_2. So the translational energy release calculated for C_2 + H_2 will provide a lower bound of the translational energy release of C_2 + 2H.

9.2.3 $\mathbf{E}_{dissociation}$

The dissociation limits for D_0(HCC–H) and D_0 (CC–H) were determined by Mordaunt, *et al.*[127, 128] and Y.-C. Hsu as reported by Cui and Morokuma[36] respectively. The other limits were determined using the D_0 values of C_2, H_2, and CH from Huber and Herzberg[77]. For example, the dissociation limit for $C_2H_2 \rightarrow$ 2CH is calculated as follows:

$$D_0(HC{-}CH) = D_0(H{-}CCH) + D_0(CC{-}H) + D_0(C{-}C) - 2{\cdot}D_0(C{-}H)$$

Table 9.3 shows the energy remaining for $E_{dissociation}$ for each of the cases under consideration.

Table 9.3: $E_{dissociation}$ in cm^{-1} of the possible photofragmentation reactions.

$C_2H + H$	(I)	46074
$C_2 + H_2$	(II)	49346
$C_2 + 2H$	(III)	85462
2CH	(IV)	79656
$C_2H + H(2s)$	(V)	128333

9.2.4 Previous studies

Several groups have studied acetylene photodissociation in the VUV. The first five of the six reactions mentioned above have been observed, although not all reactions are observed with each excitation scheme. Wodtke and Lee[212] studied acetylene photodissociation at 193.3 nm (51730 cm^{-1}). They used mass spectrometric TOF techniques that unselectively ionized and detected all photofragments. As shown in Table 9.4, they established that one-photon absorption promotes reaction I and that two-photon absorption promotes reaction IIIb. They did not detect products of reaction IV. Their data revealed no products of reaction II resulting from a two-photon absorption. Although a one-photon absorption is very unlikely, given other data, to promote reaction II, C_2 from this reaction would be masked by signal from C_2H which fragments into C_2 and H when ionized. Products of these two reactions cannot be distinguished. The authors were able to set an upper limit of 15 percent to the possible contribution of reaction II to the one-photon signal. Balko, Zhang, and Lee revisited and confirmed these results.[13] They also demonstrated that most of the C_2 formed by reaction IIIb is produced in electronically excited states, probably because of the high excited state density in C_2 at the energy of two 193 nm photons.

McDonald, Baronavski, and Donnelly[120] detected electronically excited CH and C_2 by exciting acetylene with 193 nm light and monitoring the dispersed fluorescence. The power dependence of the signals indicates that these fragments were produced by multi-photon absorption. Emission from excited vibrational states of $C_2(A)$ does not extend beyond $v' = 5$, which indicated that these fragments are produced by reaction III and not reaction II. They also detected $C_2(d)$ emission that could only

Table 9.4: Summary of previous work on the photoproducts of acetylene.

Reaction	Wodtke and Lee[212]	McDonald *et al.* [120]	Han *et al.* [69] one-photon	two-photon	Ukai *et al.*[193] signal starts at
I	1×193 nm	continuum detected	92.3-124 nm	not detected	>100 nm
II	perhaps 1×193 nm	not detected	83.4-95.5 nm $C_2(C,D)$	not detected	90 nm $C_2(C)$
III		$C_2(A)$ 2×193 nm	45.7-92.3 nm	2×193 nm	$C_2(C)$ 78 nm
		$C_2(d)$ 3×193 nm	$C_2(d)$	2×157 nm $C_2(d)$	$C_2(d)$ 89 nm
IIIa	not detected				
IIIb	2×193 nm				
IV	not detected	2×193 nm minor channel	45.7-95.5 nm	2×193 nm 2×157 nm	96 nm
V	...	...	45.7-58.7 nm Balmer	...	78 nm Lyman-α

result from a three-photon absorption. They detected a background continuum that is probably attributable to $C_2H(\tilde{A})$ and a small amount of $CH(A)$ emission. Unlike the experiment of Wodtke and Lee, this experiment was insensitive to the non-fluorescent ground states of these fragments. Okabe, Cody, and Allen[144] conducted a similar experiment that agreed with these conclusions.

Acetylene photofragmentation has been studied in two synchrotron experiments. The excitation energies used in these experiments were comparable to a three-photon absorption at the frequencies we used have been studied in two synchrotron experiments. In the first of these experiments, Han, *et al.* measured the absorption and the fluorescence quantum yield of acetylene at excitation wavelengths of 50-106 nm in a gas cell.[69] They also dispersed the fluorescence resulting from excitation at 13 VUV excitation wavelengths. Emission from $C_2H(\tilde{A})$, $C_2(C, d, D)$, $CH(A, B, C)$, and H Balmer appear in these spectra. They assign the C_2H emission to the $\tilde{B}\rightarrow\tilde{X}$ transition, but it is more likely that the emission originates in high vibrational levels of $C_2H(\tilde{A})$ because the emission appears at an excitation frequency more than 4000 cm^{-1} below the energy of $C_2H(\tilde{B})$ measured by Hsu, *et al.*[28] Emission from each state appears in the spectra at excitation energies just exceeding the required threshold energy with three exceptions. First, emission from $C_2(d)$ does not appear until the excitation energy exceeds the energy required to produce $C_2(d)$ from reaction III. Production of $C_2(d)$ by reaction II is unlikely because of spin conservation. Second, production of $C_2(C, D)$ by reaction II requires excitation energy 15,000 cm^{-1} above the threshold. Han, *et al.* suggested that this is due to the large amount of bending required to bring the two H atoms sufficiently close together in either a *cis*-bent or vinylidene geometry. Finally, the appearance of H-atom Balmer emission required at least 13,000 cm^{-1} of excitation energy above the threshold for the production of H(n=3).

Han *et al.* conducted an interesting comparison. A one-photon excitation and a two-photon excitation that reach the same energy may not produce the same photofragment states. So, they repeated the dispersed fluorescence experiments at two excimer wavelengths: 193 nm and 157 nm. Two-photon absorptions at these

wavelength have equivalent excitation energy as one-photon excitations at 96.5 nm and 78.5 nm. These are close to the 95.5 nm and 76.5 nm one-photon excitation frequencies at which Han *et al.* recorded DF. The two-photon DF spectra show emission from CH(A, B) and $C_2(d)$ due to reaction III, but $C_2(C)$ due to reaction II and $C_2H(\tilde{A})$ are absent. Reaction II may be absent from the 193 nm DF spectrum because the intermediate state is $10\nu_3$ of $C_2H_2(\tilde{A})$ which has a *trans*-bent geometry. As mentioned, *cis*-bending may be required to dissociate via reaction II. The absence of $C_2H(\tilde{A})$ was is not explained.

The second experiment using synchrotron radiation was conducted by Ukai *et al.*[193] They continuously scanned the wavelength of the synchrotron radiation that excited the acetylene as they monitored the resulting fluorescence at specific fragment emission lines. Frequency selection of the synchrotron radiation was accomplished with a vacuum monochromator. They scanned 50-100 nm. Bandpass filters were used to select single emission lines. The experiment resulted in excitation spectra, which show the onset and variation of production of selected photofragments, including $C_2(d)$ (with some interfering $C_2H(\tilde{A})$ emission), $C_2(C)$, CH(A), and H(Lyman-α). The onset of $C_2(d)$ corresponds to reaction III. The onset of $C_2(C)$ corresponds to reaction II, but emission from this state increases by an order of magnitude above the threshold for production of this state via reaction III. The onset of CH(A) and H(Lyman-α) correspond to the threshold of reaction IV and V, respectively. Ukai *et al.* also report absolute absorption cross sections and photoionization quantum yields for excitation wavelengths between 53-93 nm.

Several conclusions can be drawn from these experiments. Wodtke and Lee show that reactions I and IIIb dominate the dissociation of acetylene at 193 nm. McDonald, *et al.* showed that reaction IV could be a minor contributor to acetylene photodissociation and also showed the importance of spin conservation in dictating which states are produced. Han *et al.* showed that reaction II occurs, but not if the $C_2H_2(\tilde{A})$ is used as an intermediate.[69] So we do not expect to observe products of reaction II when exciting the $3\nu_3$ or $4\nu_3$ vibrational levels of the $\tilde{A}$-state, but excitation to the $4p$ Rydberg may create products by reaction II. Han *et al.* and Ukai, *et al.* provide in-

Table 9.5: The states that meet the criteria for SEELEM and IR detectability.

	Fragment SEELEM Cs	-detectable on Au	IR-detectable transitions 800-1700 nm
H_2	...	...	...
C_2H	$1\ ^4\Sigma^+$	high-l, high-n Rydbergs	$\tilde{A}\ ^2\Pi \rightarrow \tilde{X}\ ^2\Sigma^+$ $(1\ ^4A'') \rightarrow (1\ ^4A')$ $(2\ ^4A') \rightarrow (1\ ^4A')$
C_2	$1\ ^5\Pi_g$	$(1\ ^5\Sigma_g^+)$ $(1\ ^3\Delta_u)$, $(1\ ^3\Sigma_u^+)$, $(3\ ^3\Sigma_u^-)$, $(1\ ^3\Phi_g)$ $(1\ ^1\Phi_g)$	$b\ ^3\Sigma_g^- \rightarrow a\ ^3\Pi_u$ $A\ ^1\Pi_u \rightarrow X\ ^1\Sigma_g^+$
CH	...	...	...
H atom	...	$2s$	...
C atom	^1S	^5S	...

formation about which reactions could occur over a wide range of excitation energies. Ukai, *et al.* show that reaction V takes place. There is no evidence for reaction VI, but all the low lying states are metastable. They are not detectable by fluorescence. Wodtke and Lee did not detect C atoms in their mass spectroscopy experiment.

9.2.5 Survey of the fragments

The SEELEM and IR-LIF detectivities of the fragments will be considered in turn. The hydrogen molecule will not be discussed because it has no accessible excited states at the energies of three 215-240 nm photons.[77]. Hydrogen molecule will produce neither metastables nor IR emission at these energies.

C_2H

Ab initio calculations on C_2H have been performed by Cui and Morokuma[36] on the seven lowest doublet states and by Duflot, Robbe, and Flament[46] on 29 of the lowest doublet and quartet states. The results are summarized in Fig. 9-8 for the doublet states and in Fig. 9-9 for the quartet states. The lifetime of the $\tilde{B}$ state was measured by Chiang, *et al.*[28]. The lifetime of the $\tilde{A}$ state was measured by Fletcher, *et al.*[188]. Cui and Morokuma calculated the energies of the lowest 6 doublet states

allowing for bend in the CCH angle. These levels are represented in Figs. 9-8 and 9-9 with longer lines. Duflot, *et al.* calculated both doublet and quartet states, but constrained the calculations to linear geometry.[46] These levels are represented with shorter lines. Energies and lifetimes that have been experimentally determined are shown in black. The rest are taken from theoretical calculations. The thin gray lines show the energies of two and three photons of various frequencies.

None of the doublet states are likely to be SEELEM detectable. The two lowest states in C_2H are the ground $\tilde{X}\ ^2\Sigma^+$ state and the $\tilde{A}\ ^2\Pi$ state at 0.45 eV. Since there are no Φ valence states expected in C_2H, the entire doublet manifold has symmetry-allowed transitions to one of these two states. Accordingly, no doublet states are expected to be metastable.

Although knowledge about the quartet manifold is sparse, it is likely that there is one state that is SEELEM-detectable, the $1\ ^4\Sigma^+$ state. Unfortunately, *ab initio* calculations of the quartet states have been constrained to linear geometries.[46] The valence quartet states are almost certainly not linear. The dominant configuration of these states has an electron in a π^* orbital. The appropriate Walsh diagram (Figure 1 in Part III of reference[203]) for "HAB" molecules like HCC suggests that these states split into two, one that is strongly bent and a higher energy state that is linear. However, Cui and Morokuma's *ab initio,* calculations of the doublet states with the same configuration show that all these doublet states are bent.[36] This includes both components of the $2\ ^2\Pi$ state. Although *ab initio* calculations would be required to be certain, it is reasonable to assume that all of these states have bent equilibrium geometries.

The energy of the $1\ ^4\Sigma^+$ state can be estimated from the *ab initio* calculations. The bent states calculated by Cui and Morokuma have energies that are $\sim$2 eV lower than the corresponding linear states calculated by Duflot, *et al.* It is reasonable that the quartets will be stabilized by a similar amount. This places the lowest quartet, the $1\ ^4\Sigma^+$ state, at $\sim$ 2.7 eV. This will be detected on Cs but not on either Au or Cu.

There are only two other quartet states that might be metastable. These states, the $1\ ^4\Delta$ state at 5.87eV and the $1\ ^4\Sigma^-$ at 6.59, cannot emit to the lower quartet

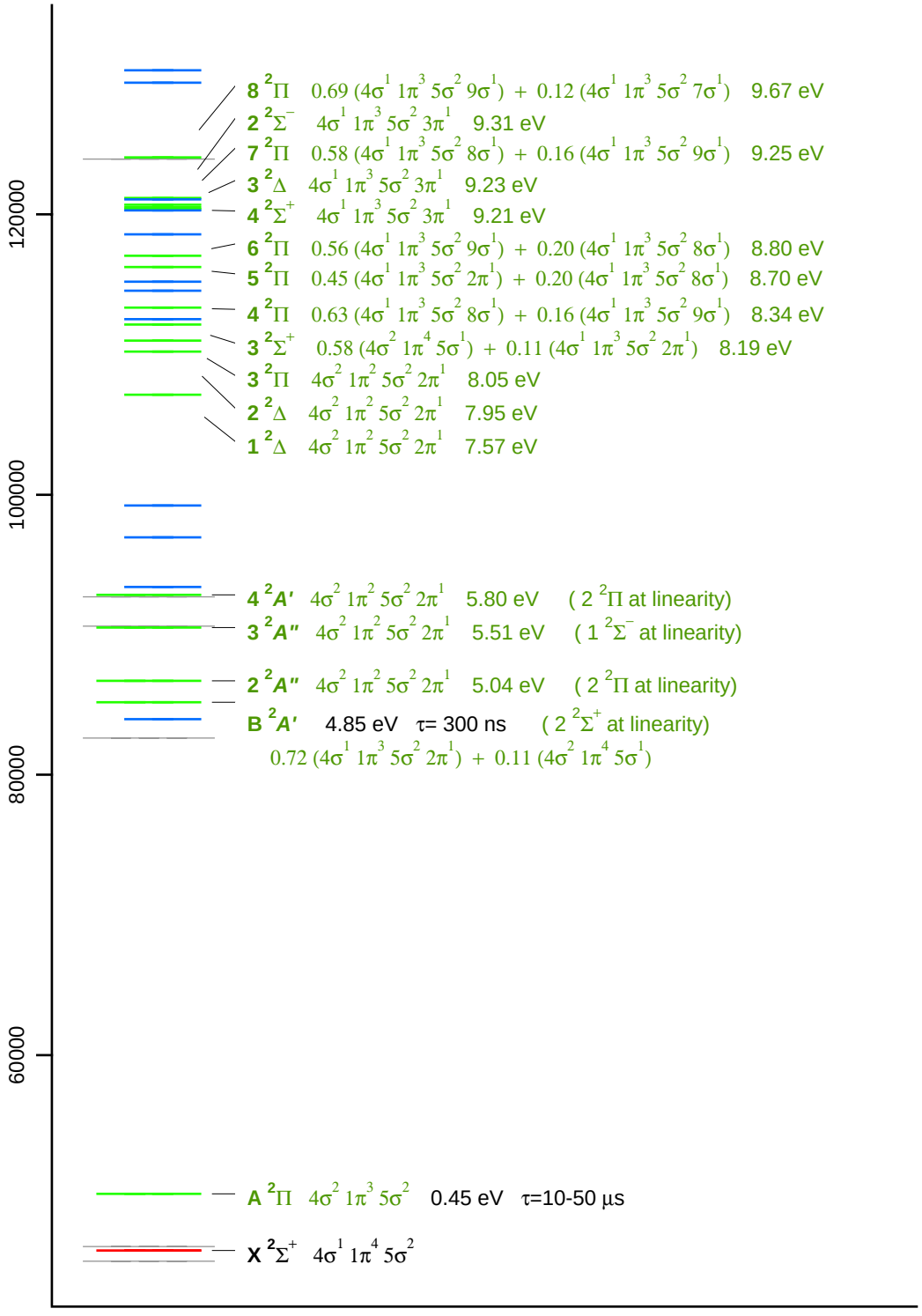

Figure 9-8: The valence doublet states of C_2H, including the symmetries, dominant configurations, electronic energy (T_v), and lifetimes.

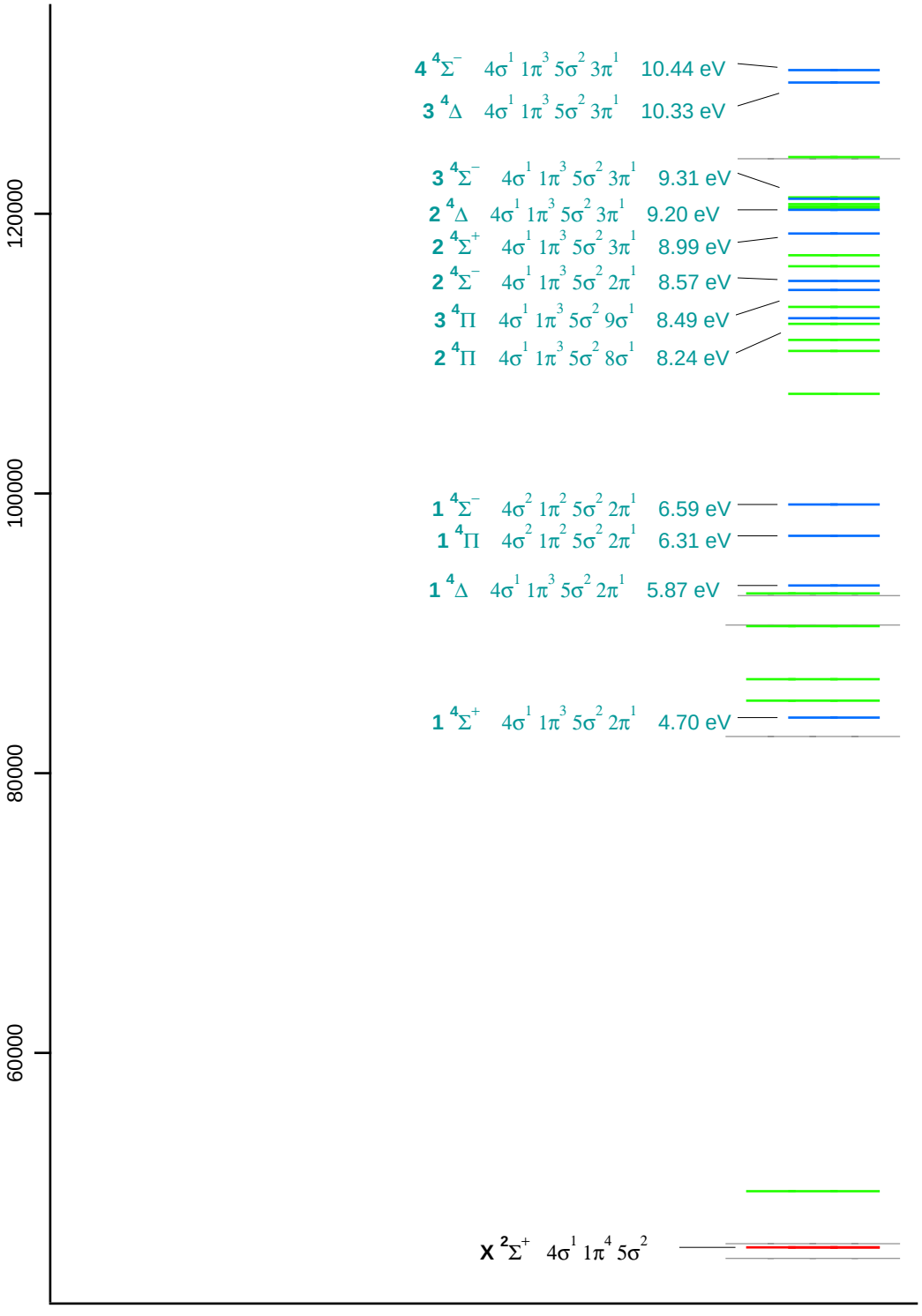

Figure 9-9: The valence quartet states of C_2H, including the symmetries, dominant configurations, and electronic energy (T_v).

states in linear geometry. These states are unlikely to be metastable for two reasons. First, as mentioned above, these states probably have a bent equilibrium geometry. All transitions are symmetry-allowed in the bent, C_s symmetry. Second, these states lie above the dissociation limits of C_2 $a\ ^3\Pi_u$ and $b\ ^3\Sigma_g^+$ states. Because these states have two decay pathways, emission and dissociation, they probably do not live long enough to be detected.

There have been no observations or calculations of sextet states of C_2H. This would require five unpaired electrons, a configuration that will lie at high energy.

C_2H Rydberg states may be accessible by three-photon absorption. Rydberg states have sufficient electronic energy to excite Auger electrons from any surface. Only high-n, high-l states Rydberg states are long-lived, so they exist in a narrow energy region below the ionization potential. Electrons in low-l Rydberg states penetrate the core, so these states are more likely to dissociate or decay radiatively to the valence states. C_2H Rydberg states with $l \geq 4$ will probably be non-penetrating. So these states must have $n \geq 5$, which limits the electronic binding energy of these states to 4400 cm^{-1}. Rydberg states with core vibrational excitation can lie above the ionization limit, but these are unlikely to live long because the core and Rydberg electron can exchange energy which results in autoionization. This additional decay pathway will reduce the state's lifetime. So long-lived Rydberg states exist in a ~ 4400 cm^{-1} region below the ionization potential.

The C_2H ionization potential is poorly determined, but lies at approximately 11.5 eV.[94] This ionization limit is at the energy of a three photon transition through the $4\nu_3$ vibrational level in the $\tilde{A}$-state. These Rydberg states would probably be formed by dissociation of acetylene after a three-photon absorption into C_2H Rydberg states. Rydberg states may be formed when C_2H absorbs additional photons, but these Rydberg states will probably have short lifetimes because the most accessible Rydberg states from the valence states are those that are core-penetrating and, therefore, short-lived. If highly excited acetylene can dissociate into C_2H Rydberg states, Au-SEELEM detectable states may be formed.

So, we reach a conclusion that the only Au-SEELEM detectable states in C_2H

are the Rydberg states only after some degree of speculation. No experiments or detailed calculations have been carried out for the valence quartet states. If there is a Au-SEELEM detectable valence state, it is most likely to be the upper component of the 1 $^4\Delta$ state at 5.87eV. As mentioned, the upper component is more likely to be linear, or near-linear. If it is, then the linear selection rules will continue to be strong propensity rules at small bending angles. This could result in lifetimes for some vibrational levels that are long enough to survive the flight time to the detector. However, this would require two things of the upper component of the 1 $^4\Delta$ state. One, the equilibrium geometry of this state must be very different than the upper component of the 2 $^2\Pi$ state is calculated to be. Two, the state cannot be strongly coupled to the dissociation channels that exist at this energy.

To summarize, C_2H certainly provides one state that would be SEELEM-detectable on Cs. High-l C_2H Rydberg states are detectable on Au.

C_2H has IR emission from the $\tilde{A} \rightarrow \tilde{X}$ transition. Although the 0-0 transition lies at 0.45 eV, outside the range of the IR detector, transitions from higher vibrational states in the $\tilde{A}$-state would be detectable with our detector. In fact, the $\tilde{A} \rightarrow \tilde{X}$ emission extends into the visible, as shown by Han, *et al.* with 124 nm excitation[69] and Suto, *et al.* at a number of excitation frequencies.[185] The quartet manifold may also provide transitions in the IR, but this is hard to assess due, again, to the lack of information about these states. At linear geometry, the 1 $^4\Delta$ state lies 1.17 eV above the 1 $^4\Sigma^+$ state. There are allowed transitions between the bent states that correlate to 1 $^4\Delta$ and the state that correlates to 1 $^4\Sigma^+$. It is likely that the transitions between the 2 $^4A'$ or 1 $^4A''$ states and the lower 1 $^4A'$ state are in the near-IR.

C_2

There are two excellent sources on C_2. Martin has written an exhaustive review of experimental and theoretical work on C_2.[115] Kirby and Liu[93] have calculated the potentials of the lowest 62 states. Figure 9-10 summarizes the relevant information on the singlet and quintet states C_2, and Figure 9-11 summarizes the relevant information on the triplet states C_2. This information is from the review by Martin[115] and Kirby

and Liu[93] with the exception of the lifetime of the B' state, which was measured by Gong, *et al.*[58]. Energies and lifetimes that have been experimentally determined are shown in black. The rest are taken from theoretical calculation. The thin gray lines show the energies of two and three photons of various frequencies assuming a dissociation to C_2 + H_2 (as opposed to C_2 + 2H).

There are many possible SEELEM-detectable states. Only one possibility, however, is a singlet state. The 1 $^1\Phi_g$ state, calculated to lie at 7.11 eV above the ground state, has no symmetry-allowed transitions to lower states. However, this unobserved state may not be metastable because it lies above the first dissociation limit at 6.2 eV. Otherwise, the singlet manifold has no SEELEM-detectable metastable states. The four lowest states (X, A, B, and B') are too low in energy to be detected on a Cs surface. Higher-lying singlet states either have measured lifetimes that are too short (C, D, and E) or have symmetry-allowed, one-electron transitions to lower states.

The triplet manifold of C_2 may have a number of SEELEM-detectable states. The lowest five triplet states either have too little energy to be detected on Cs or their lifetimes are too short to reach the detector. There are four higher states that might be SEELEM-detectable but they have not been observed. Two of these are the 1 $^3\Delta_u$ and 1 $^3\Sigma_u^+$ states at 5.25 eV and 5.33 eV, respectively. These states are calculated to have very shallow potentials by Kirby and Liu[93]. If they have bound levels, they might have long lifetimes. While they both have symmetry-allowed transitions to the d-state, the dominant configurations require that the transitions occur via two-electron transitions. Although other configurations are certainly mixed into these states, the lifetimes might be long enough for SEELEM detection. The other two states, the 3 $^3\Sigma_u^-$ at 6.05 eV and the 1 $^3\Phi_g$ state at 6.13 eV, have symmetry-allowed transitions to lower states, but the transitions are either in the near-IR or are two-electron transitions. These states might have lifetimes in excess of 10 μs.

The quintet manifold of C_2 has two bound states, the 1 $^5\Pi_g$ at 3.79 eV and the 1 $^5\Sigma_g^+$ at 5.12 eV. The 1 $^5\Pi_g$ state is certainly detectable on Cs. The 1 $^5\Sigma_g^+$ state is calculated is have a shallow potential. If it has bound levels, they would be metastable and detectable on Au. It should be noted that these states cannot by produced via

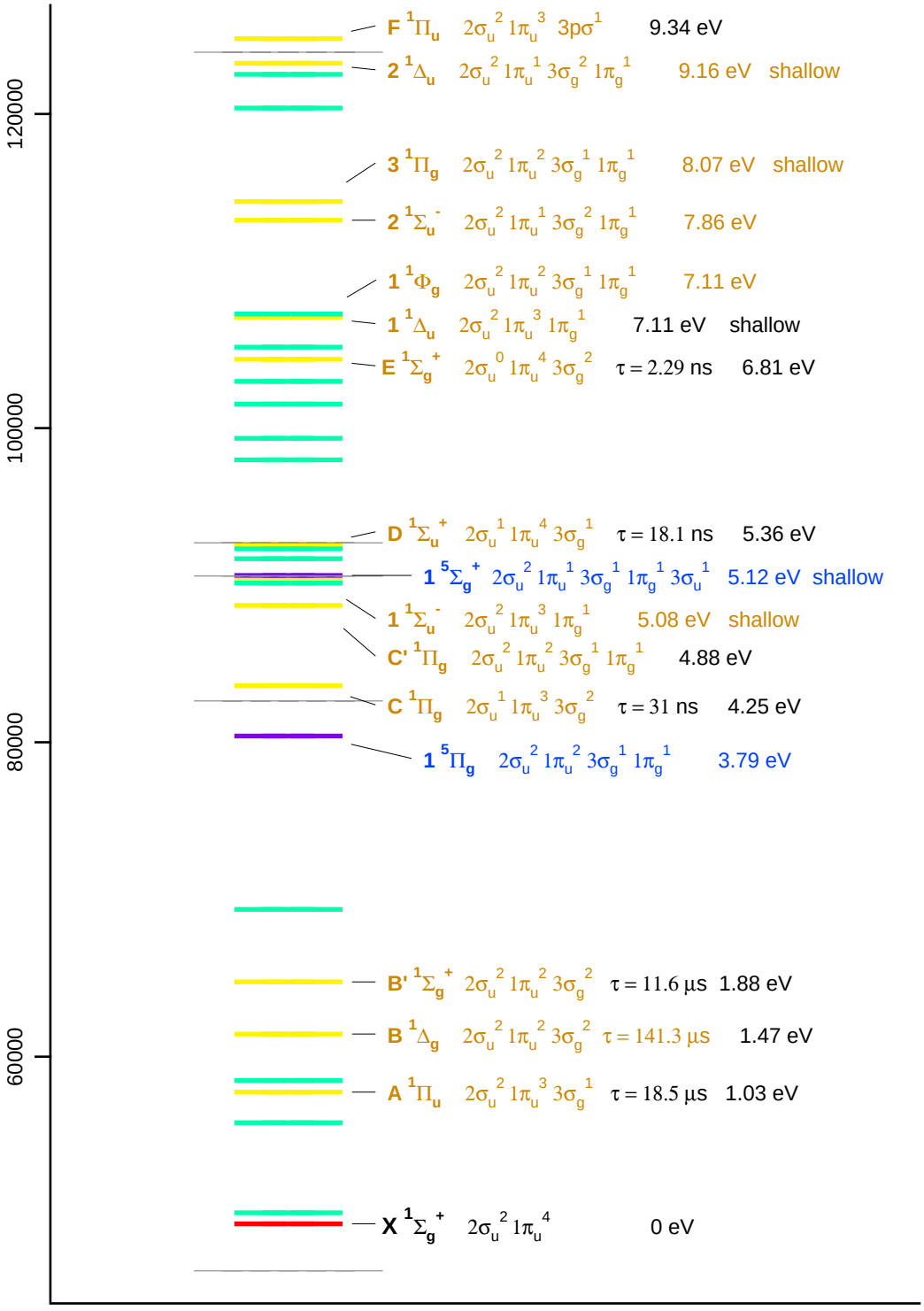

Figure 9-10: The valence singlet and quintet states of C_2, including the symmetries, dominant configurations, electronic energy (T_v), and lifetimes.

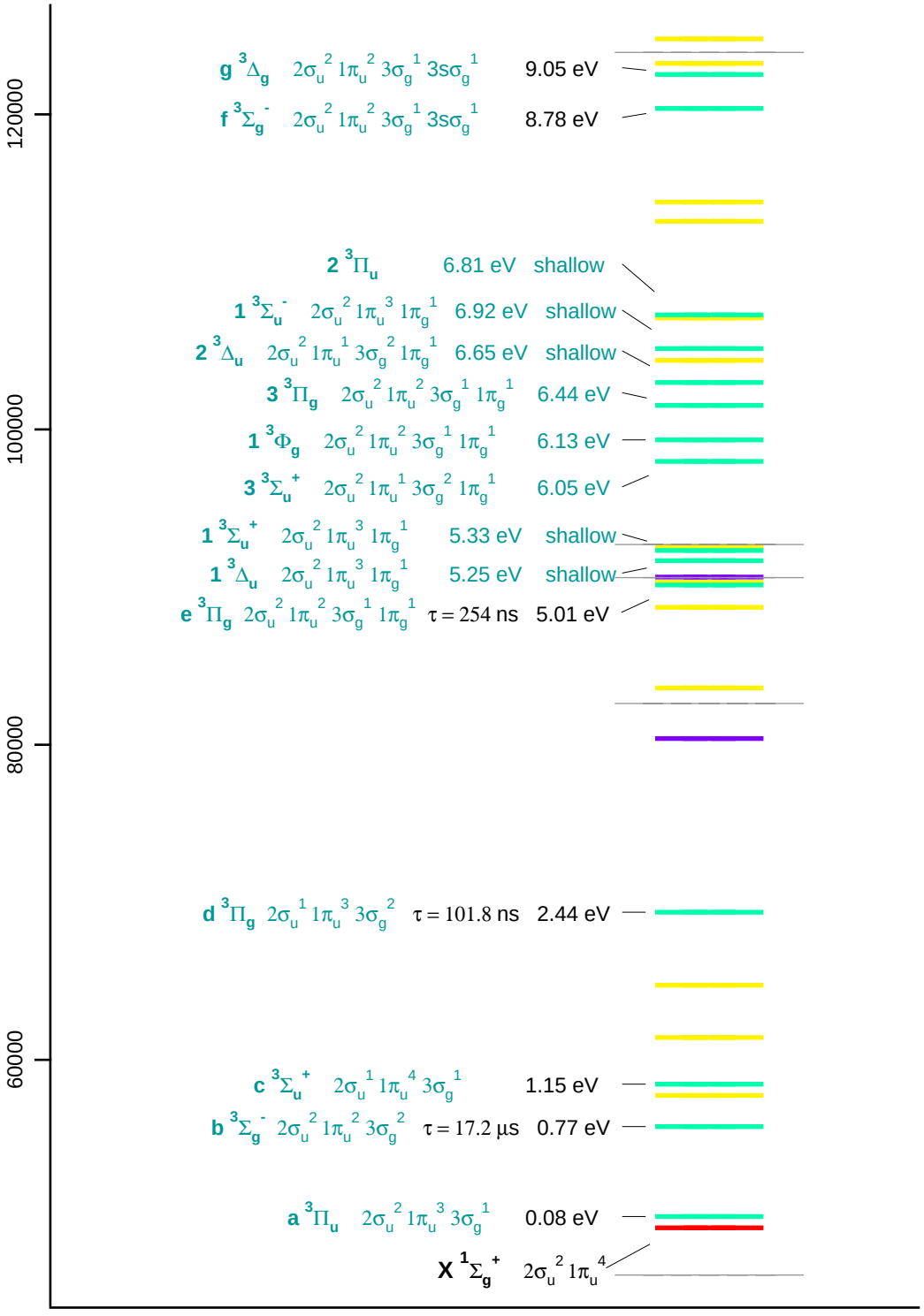

Figure 9-11: The valence triplet states of C_2, including the symmetries, dominant configurations, electronic energy (T_v), and lifetimes.

reaction IIIb at some excitation frequencies. If the first photon can only produce the two lowest C_2H states, which are doublets, subsequent photons can only excite C_2H doublet states. C_2H doublets spin-correlate to singlet and triplet C_2 product states, not to these quintet states.

The C_2 ionization potential is 12.15 eV[77], so only Rydberg states with $n^* < 3.6$ produced by reaction II are accessible at the highest excitation frequency we use. These low-n states are likely to have short lifetimes because of both predissociation and emission.

In summary, there is one singlet, four triplets, and a quintet state that might be detectable on Au or Cu. None of these states has been observed, so the lifetimes and energies of these states have yet to be experimentally measured. There is a quintet state that is certainly detectable on Cs but not on Au. The quintet state has not been observed, but it is unquestionably long-lived since it is the lowest state of the quintet manifold.

C_2 provides two transitions in the IR between low-lying electronic states. The 0-0 transition of the $b\ ^3\Sigma_g^- \rightarrow a\ ^3\Pi_u$ transition lies at 0.69 eV, while the $A\ ^1\Pi_u \rightarrow X\ ^1\Sigma_g^+$ transition lies at 1.03 eV.

CH

The best source of information on CH is a recent paper by Kalemos, Mavridis, and Metropoulos[89]. The levels of CH are summarized in Fig. 9-12. The information in Fig. 9-12 is drawn from Kalemos, *et al.*[89] with the exception of the lifetimes. The lifetimes of the A, B, C, and D states are from Ortiz *et al.*[145], Kumar *et al.*[1], Ubachs, *et al.*[192], and Li, *et al.*[105] respectively. These lifetimes are of the ground vibrational state in each electronic state. Energies and lifetimes that have been experimentally determined are shown in black. The rest are taken from theoretical calculations. The thin gray lines show the energies of two and three photons corresponding to transitions through $3\nu_3$, $4\nu_3$ and the two-photon transition to the $4p$ Rydberg state.

Kalemos, *et al.* conducted *ab initio* calculated potential curves of all the states

correlating to the lowest five dissociation limits and compared the results to experimental data. Their work shows that CH has several electronically excited states accessible at the three photon level. However none of these states is likely to provide either SEELEM or IR signal. As shown in Fig. 9-12, the lowest doublet state is $^2\Pi$, so emission from all of the valence doublet states to the ground state is symmetry allowed. Those doublet states for which lifetimes have been measured have lifetimes shorter than one microsecond. There are only three quartet valence states. The a-state has too little energy to be detectable on any metal, the b-state is purely dissociative, and the c-state has an allowed transition to the a-state. There is a single valence sextet state which is purely dissociative. The CH ionization potential is 10.64 eV,[77] so the Rydberg states are not accessible at the excitation frequencies we use.

CH is unlikely to be the source of any emission in the near-IR. All transitions terminating in or between low-lying valence states (electronic energy less than 5 eV) have transition energies greater than 2 eV (625 nm).

Hydrogen atom

The excited states of H atom are well known[135], and a number of long-lived states exist. In particular, the $2s$ state cannot emit to the $1s$ ground state because of the $\Delta l = \pm 1$ selection rule. The $2s$ state has an excitation energy of 10.2 eV. If the $2s$ state is produced as readily as is the $2p$ state that Ukai *et al.* detected[193], the $2s$ state should be detectable on any surface. Because of the small mass of the atom, this metastable will arrive at the detection surface well in advance of intact acetylene metastables.

Detecting the $2s$ state is complicated by its extreme vulnerability to electric fields. The $2s$ state can be mixed with the nearly degenerate $2p$ state by a small electric field. A simple quantum mechanical calculation shows that the lifetime of the $2s$ state will be shortened to 10 μs by a field of 7 Volts/cm due to the Stark mixing of $2p$ character into the eigenstate. This mixed state would emit at 121 nm. The survival of the $2s$ state is dependent on the fields along the flight path and the velocity of the H atom fragment.

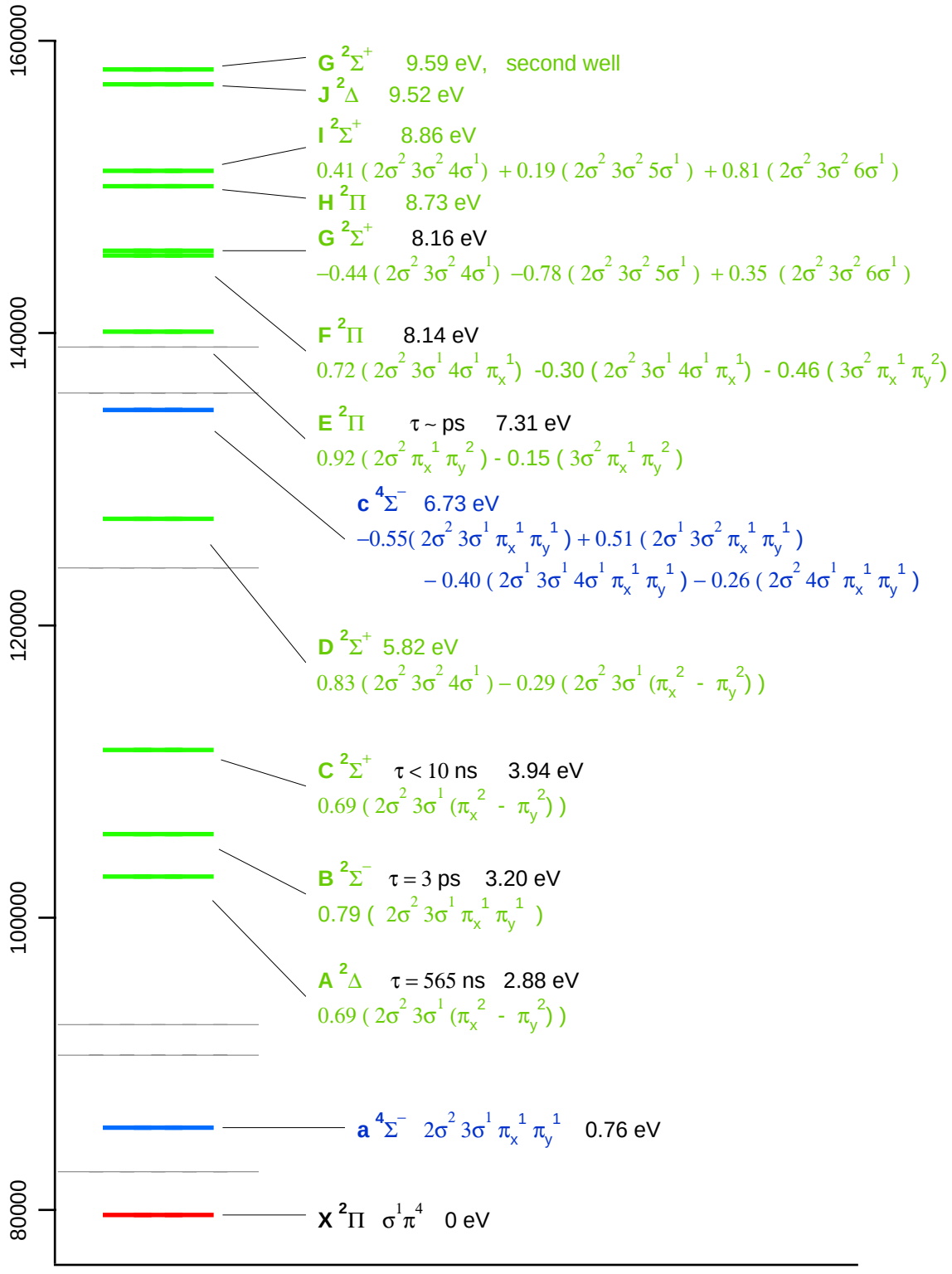

Figure 9-12: The valence states of CH, including the symmetries, dominant configurations, electronic energy (T_v), and lifetimes if measured.

In our apparatus, some of the H($2s$) atoms would emit before they arrive at the detector. The ion deflector usually has an electric field of 8 Volts/cm. The field inside the repeller varies as a function of location due to the geometry of the charged surfaces, but an estimate of 10 Volts/cm is fair. The lifetime of H($2s$) as it passed through these regions would be short, on the order of μs, but the H atom is moving quickly. If $E_{translational}$ resulting from reaction V was 0.5 eV, the H atom would be moving at 9.5 mm/microsecond. The electric fields strongly affect about a 50 mm length of the flight path, so the atom would move through this region in ~ 5 μs. This is roughly equivalent to the lifetime of the Stark-mixed state. So many of the atoms would emit before they reached the detection surface.

Even if a large fraction of the excited atoms did not make it to the surface, many of the emitted photons would. Since the non-zero electric fields are located fairly close to the detection surface, the detection surface would capture a large solid angle of the emission. Electrons ejected from the surface via the photoelectric effect would produce signal. Whether the H($2s$) atoms emit or not, they should appear somewhere in the SEELEM TOF profile in our apparatus.

9.3 SEELEM signal assignment

What photofragment states are responsible for the SEELEM metastable signal? Table 9.6 shows the $E_{internal}$ remaining after the $E_{dissociation}$ and $E_{translational}$ are subtracted from the energy of two- and three-photons. A reaction must result in an $E_{internal}$ that exceeds the work function of the detection surface used to record the TOF profile. None of the observations can be accounted for by two-photon excitation. All of the metastable photofragments must be due to at least three photons.

The photofragments observed in the $3\nu_3$ TOF profile using a Au detection surface (Fig. 9-3) are probably the result of one of two reactions. Reaction III produces one or more of the three lower Au-detectable excited states of C_2. These states are the $1\ ^3\Delta_u$ at 5.25 eV, the $1\ ^3\Sigma_u^+$ at 5.33 eV, and the $1\ ^5\Sigma_g^+$ at 5.12 eV. As mentioned, the 5.61 eV $E_{internal}$ calculated for reaction III is an upper limit. The average $E_{internal}$

Table 9.6: $E_{internal}$ in eV of the possible photofragmentation reactions.

2 photons	$C_2H + H$ (I)	$C_2 + H_2$ (II)	$C_2 + 2H$ (III)	2CH (IV)	$C_2H + H(2s)$ (V)
$3\nu_3$ on Au ($\phi = 5.1$ eV)	4.18	4.47	-0.006	1.30	-4.68
$4\nu_3$ on Au	4.94	4.97	0.49	1.58	-4.42
$4\nu_3$ on Cs ($\phi = 2.1$ eV)	-5.39	0.01	-4.47	1.17	-4.44
$4p$ Rydberg on Cu ($\phi = 4.65$ eV)	2.59	3.19	-1.28	0.29	-5.67
3 photons	$C_2H + H$ (I)	$C_2 + H_2$ (II)	$C_2 + 2H$ (III)	2CH (IV)	$C_2H + H(2s)$ (V)
$3\nu_3$ on Au	9.80	10.09	5.61	6.92	0.94
$4\nu_3$ on Au	10.68	10.72	6.24	7.33	1.33
$4\nu_3$ on Cs	0.35	5.76	1.28	6.92	1.31
$4p$ Rydberg on Cu	7.71	8.32	3.84	5.42	-0.54

is lower. Accordingly, very little vibrational excitation can exist in these fragments. These states, however, are calculated to have shallow potentials, which could not support much vibrational excitation.[93]

Reaction I could produce Au-detectable C_2H Rydberg states if highly excited acetylene can dissociate to C_2H Rydberg states.

The other reactions are much less likely. Reaction II does not occur when $C_2H_2(\tilde{A})$ is used as an intermediate state. Reaction V is unlikely because the metastable photofragments are moving too slowly. If reaction V were responsible for the signal, $E_{translational}$ would account for only 0.01 percent of the energy imparted by the photons. This energy partitioning seems unreasonable.

The photofragments observed in the $4\nu_3$ TOF profile using a Au (Fig. 9-2) and a Cs (Fig. 9-1) detection surface prove much more difficult to explain. The photofragments that appear in the Au TOF profile do not appear in the Cs TOF profile even though Cs has a much lower work function than Au. One would expect that the photofragments that appear in the $3\nu_3$ TOF profile would also appear in the $4\nu_3$

TOF profiles, which is excited with only ~ 0.4 eV more excitation energy.[1] But they do not.

Several factors might explain why fragments that appear in the Au TOF profile do not appear in the Cs TOF profile, but none of these are overwhelmingly convincing. The two TOF profiles were taken in different vacuum chambers, so the surface poisoning may have affected detectivity of the surface differently. Or the Au-detectable photofragments might be vulnerable to some kind of quenching that is present in the MIT apparatus and not in the UCSB apparatus. The two TOF profiles were recorded with different laser fluencies and polarizations. It is possible that the two sets of fragments are produced through multiphoton process with different numbers of absorbed photons. Or the laser polarization may have affected the observed photofragments. The Au TOF profile was recorded with the laser polarized along the molecular beam, while the Cs TOF profile was recorded with the laser polarized perpendicular to the free jet. Zare discussed the angular distribution of photofragments in Applications 6 and 13 of his book.[216]

Another problem is that those photofragments that do appear in the Cs TOF spectrum are moving very quickly. If the photofragment signal in the Cs TOF profile is due to C_2 molecules produced by reaction II, $E_{translational}$ would be 5.37 eV, or about a third of the available energy. If the signal is due to excited H atoms produced by reaction V, $E_{translational}$ is less than 0.1 percent of the total available energy. Neither of these options seems reasonable. Reaction III is not energetically possible after a three-photon absorption.

Clearly, more work is needed to clarify the source of the signals that appear in the $4\nu_3$ TOF profile.

Unlike the other photofragment signals, the photofragment signal appearing in

[1] It should be pointed out that reaction IIIb proceeds differently through $4\nu_3$ than it does through $3\nu_3$. One-photon absorption into $3\nu_3$ produces no photofragments because this excitation energy is below the first dissociation limit. Reaction IIIb would require three photons, two for the first dissociation and one for the second dissociation, if $3\nu_3$ were the intermediate state. $4\nu_3$ is above the first dissociation limit. The first dissociation of reaction IIIb can happen with the absorption of only one photon, leaving two photons to accomplish the second dissociation. Although the dissociation rate of $4\nu_3$ is slow compared to the laser pulse length ($4\nu_3$ has a lifetime of ~ 300 ns) this might change the variety of photofragments that are produced by reaction IIIb.

the $4p$ Rydberg TOF profile (Fig. 9-4) strongly diminishes as a function of voltage on the ion deflectors. At a voltage difference of 100 volts (40 Volts/cm), the signal has diminished by a factor of 10. It is not clear what could cause this. Ionized acetylene would be strongly deflected by such a field and never reach the detector. This excitation energy is too low to produce H($2s$).

The photofragments observed in the $4p$ Rydberg TOF profile using a Cu detection surface may be the result of reaction II which produces one or more of the six Cu-detectable excited states of C_2 discussed above. Reaction II is a possibility for this signal because $C_2H_2(\tilde{A})$ is not used as an intermediate. C_2H Rydberg states could also be responsible, and Rydberg state Stark-mixing may explain the electric field dependence.

Again, the other reactions are not likely. Reaction III is not energetically possible after a three-photon absorption. Reaction V is unlikely because the metastables photofragments are moving too slowly.

9.4 IR signal assignment

Of the two possible sources of IR shown in Table 9.5, the C_2H $\tilde{A}$-$\tilde{X}$ emission is preferred. Three factors argue for this conclusion.

a) This only requires two photons at all of the observed excitation wavelengths. Nothing rules out the production of IR emission by an absorption of three or more photons, but it would be surprising if two-photon-excited $\tilde{A}$-$\tilde{X}$ emission were not observed.

b) Another source of IR emission from a two-photon absorption would be from C_2 produced by reaction II. As mentioned, reaction II is not observed when $C_2H_2(\tilde{A})$ is used as an intermediate.

c) The last source of IR emission from a two-photon absorption would be from C_2 produced by reaction IIIa or b. This is only energetically allowed for the excitation wavelength corresponding to $4\nu_3$ excitation. If this were important, we would expect to see a dramatic increase in emission when exciting through $4\nu_3$. We do not observe

this such an increase.

9.5 Future experiments

Clearly, more SEELEM TOF profiles should be recorded using other detection surfaces and other excitation frequencies. The use of a skimmer and a double, differentially pumped vacuum chamber should result in much narrower velocity distributions. The lifetimes of the metastables would help identify the metastable photofragments. Power studies would place a lower bound on the number of photons required to produce the metastable photofragments.

The dispersed fluorescence at these excitation frequencies has been studied in our lab, but these experiments have been conducted without focusing the laser beam. It would be interesting to see if photofragment emission could be detected in a cell with a laser focused to strengthen multiphoton transitions. The results would probably be similar to observations by McDonald, *et al.*[120] and Han, *et al.*[69], but we would be using longer wavelength excitation.

Bibliography

[1] Kumar A., Hsiao C. C., Hung W. C., and Lee Y. P. Highly predissociative levels of CH $B\ ^2\Sigma^-$ state detected with two-color resonant four-wave mixing spectroscopy. *J. Chem. Phys.*, (109)3824–3830, 1998.

[2] Evan Abramson, Robert W. Field, Dan Imre, K. K. Innes, and James L. Kinsey. Fluorescence and stimulated emission $S_1 \rightarrow S_0$ spectra of acetylene: Regular and ergodic regions. *J. Chem. Phys.*, (83)453–465, 1985.

[3] Evan Abramson, Carter Kittrell, James L. Kinsey, and Robert W. Field. Excitation spectroscopy of the acetylene $\tilde{A}$-$\tilde{X}$ transition in the 220 nm wavelength region. *J. Chem. Phys.*, (76)2293–2295, 1982.

[4] Evan H. Abramson. *Molecular Acetylene in States of Extreme Vibrational Excitation*. Ph.D. Thesis, Massachusetts Institute of Technology, 1985.

[5] George W. Adamson. *The Spectroscopy of the Formyl Radical*. Ph.D. Thesis, Massachusetts Institute of Technology, 1994.

[6] C. C. Addison. *The Chemistry of the Liquid Alkali Metals*. John Wiley and Sons, New York, 1984.

[7] A. P. Alivisatos, D. H. Waldeck, and C. B. Harris. Nonclassical behavior of energy transfer from molecules to metal surfaces: Biacetyl (^{3}nΠ^*)/Ag(111). *J. Chem. Phys.*, (82)541, 1985.

[8] Neil W. Ashcroft and N. David Mermin. *Solid State Physics*. Saunders College Publishing, Orlando, Florida, 1st edition, 1976.

[9] M. N. R. Ashfold, B. Tutcher, B. Yang, Z. K. Jin, and S. L. Anderson. *Gerade* Rydberg states of acetylene studied by multiphoton ionization and photoelectron spectroscopy. *J. Chem. Phys.*, (87)5105, 1987.

[10] H. Ashkenas and F. S. Sherman, In *Rarefied Gas Dynamics, 4th Symposium, Vol II.* , J. H. de Leeuw, editor, page 84. Academic Press, New York, 1966.

[11] P. W. Atkins. *Physical Chemistry*. W. H. Freeman and Company, New York, 4th edition, 1990.

[12] P. Avouris, W. M. Gelbart, and M. A. El-Sayed. Nonradiative electronic relaxation under collision-free conditions. *Chem. Rev.*, (77)793, 1977.

[13] B. A. Balko, J. Zhang, and Y. T. Lee. 193 nm photodissociation of acetylene. *J. Chem. Phys.*, (94)7958–7966, 1991.

[14] Israela Becker and Ori Cheshnovsky. The decay of triplet pyrazine and pyrazine-D_4 in supersonic jets. Isotope effects. *J. Chem. Phys.*, (101)3649, 1994.

[15] Peter F. Bernath. *Spectra of Atoms and Molecules.* Oxford University Press, New York, 1^{st} edition, 1995.

[16] K. Besocke, B Krahl-Urban, and H. Wagner. Dipole moments associated with edge atoms; a comparative study on stepped Pt, Au, and W surfaces. *Surf. Sci.*, (68)39–46, 1977.

[17] Philip R. Bevington and D. Keith Robinson. *Data Reduction and Error Analysis for the Physical Sciences.* McGraw-Hill, Inc., New York, 2nd edition, 1992.

[18] Mordechai Bixon and Joshua Jortner. Intramolecular radiationless transitions. *J. Chem. Phys.*, (48)715–726, 1968.

[19] F. Bozso, J. T. Yates Jr., J. Arias, H. Metiu, and R. M. Martin. A surface Penning ionization study of the CO/Ni(111) system. *J. Chem. Phys.*, (78)4256–4269, 1983.

[20] M. Brueckner, B. Heinz, and H. Morgner. Molecular-orientation in organic monolayers probed by UPS and MIES (metastable induced electron-spectroscopy). *Surf. Sci.*, (319)370–380, 1994.

[21] E. H. S. Burhop. *The Auger effect and other radiationless transitions.* Cambridge University Press, Cambridge, 1952.

[22] B. L. Burrows, A. T. Amos, and Z. L. Miskovic S. G. Davison. Many-electron theory of Auger surface-ion neutralization. *Phys. Rev. B*, (51)1409–1419, 1995.

[23] A. Campion, A. R. Gallo, C. B. Harris, H. J. Robota, and P. M. Whitmore. Electronic energy transfer to metal surfaces: a test of classical image dipole theory at short distances. *Chem. Phys. Lett.*, (73)447, 1980.

[24] Jack Cariou and Paul Luc. *Atlas Du Spectre D'Absorption de la Molecule de Tellur.* Technical report, Laboratoire AIME-Cotton CNRS II 91405 Orsay (France), 1980.

[25] R. R. Chance, A. Prock, and R. Silbey. Molecular fluorescence and energy transfer near interfaces. *Advances in Chemical Physics*, (37)1, 1978.

[26] P. Y. Cheng, S. S. Ju, M. Y. Hahn, and H. L. Dai. Intersystem crossing of C_2H_2 (S_1) induced by Ar at different orientations: A van der Waals complex study. *Chem. Phys. Lett.*, (190)109–114, 1992.

[27] P. Y. Cheng, L. Lapierre, S. S. Ju, P. Derose, and H. L. Dai. Orientation dependence in collision-induced electronic relaxation studied through van der Waals complexes with isomeric structures. *Z. Phys. D*, (31)105–115, 1994.

[28] W. Y. Chiang and Y. C. Hsu. Laser spectroscopy of CCH in the 36,600-39,700 cm^{-1} region. *J. Chem. Phys.*, (111)1454–1461, 1999.

[29] A. Cobas and W. E. Lamb Jr. On the extraction of electrons from a metal surface by ions and metastable atoms. *Phys. Rev.*, (65)327, 1944.

[30] H. Conrad, G. Ertl, J. Kuppers, W. Sesselman, and H. Haberland. Deexcitation mechanisms in metastable He-surface collisions. *Surf. Sci.*, (100)L461–L466, 1980.

[31] H. Conrad, G. Ertl, J. Kuppers, W. Wang, K. Garard, and H. Haberland. Penning-ionization electron spectroscopy of chemisorbed CO. *Phys. Rev. Lett.*, (42)1082–1086, 1979.

[32] S. L. Coy, S. D. Halle, J. L. Kinsey, and R. W. Field. Pressure-induced rotational energy-transfer in H_2CO $\tilde{A}\ ^1A_2$ $\nu_4 = 1$: Dipolar M-dependence with no single-collision elastic contribution. *J. Mol. Spec.*, (153)340–375, 1992.

[33] Stephen L. Coy, Matthew P. Jacobson, and Robert W. Field. Identifying patterns in multicomponent signals by extended cross correlation. *J. Chem. Phys.*, (107)8357, 1997.

[34] J. C. Van Craen, M. Herman, R. Colin, and J. K. G. Watson. The $\tilde{A}$-$\tilde{X}$ band system of acetylene - analysis of medium-wavelength bands, and vibration-rotation constants for the levels $n\nu_3'$ (n = 4-6), $\nu_2' + n\nu_3'$ (n = 3-5), and $\nu_1' + n\nu_3'$ (n = 2, 3). *J. Mol. Spec.*, (111)185–197, 1985.

[35] J. C. Van Craen, M. Herman, R. Colin, and J. K. G. Watson. The $\tilde{A}$-$\tilde{X}$ band system of acetylene - bands of the short-wavelength region. *J. Mol. Spec.*, (119)137–143, 1986.

[36] Qiang Cui and Keiji Morokuma. *Ab initio* MO studies on the photodissociation of C_2H_2 from the S_1 (^1A_u) state. II. Mechanism involving triplet states. *Chem. Phys. Lett.*, (272)319, 1997.

[37] Qiang Cui and Keiji Morokuma. *Ab initio* molecular orbital studies on the structure, energies and photodissociation of the electronic exited states of C_2H. *J. Chem. Phys.*, (108)626, 1998.

[38] Qiang Cui, Keiji Morokuma, and John F. Stanton. *Ab initio* MO studies on the photodissociation of C_2H_2 from the S_1 (^1A_u) state. I. Non-adiabatic effects and S-T interaction. *Chem. Phys. Lett.*, (263)46, 1996.

[39] R. J. Cvetanovic and D. L. Singleton. Comment on the evaluation of the Arrhenius parameters by the least squares method. *Int. J. Chem. Kinet.*, (9)481–488, 1977.

[40] R. J. Cvetanovic and D. L. Singleton. Comment on the evaluation of the Arrhenius parameters by the least squares method. *Int. J. Chem. Kinet.*, (9)1007–1009, 1977.

[41] W. Edwards Deming. *Statistical Adjustment of Data.* Wiley and Sons, Inc., New York, 1st edition, 1943.

[42] Daniel Demoulin. The shapes of some excited states of acetylene. *Chem. Phys.*, (11)329–341, 1975.

[43] Marcel Drabbels, Johannes Heinze, and W. Leo Meerts. A study of the singlet-triplet perturbatios in the $\tilde{A}\ ^1A_u$ state of acetylene by high resolution *uv* spectroscopy. *J. Chem. Phys.*, (100)165, 1994.

[44] Marcel Drabbels, Christopher G. Morgan, and Alec M. Wodtke. The spin-forbidden $a\ ^4\Pi(\nu = 13 - 15)$ and $b\ ^4\Sigma^-(\nu = 3)$ -$X\ ^2\Pi(\nu = 0)$ bands of nitric-oxide - a new scheme for quantum state-specific high-resolution kinetic-energy measurements. *J. Chem. Phys.*, (103)7700–7707, 1995.

[45] S. Drucker, J. P. O'Brien, P. Patel, and R. W. Field. The effects of triplet perturbers on photophysical processes in the $\tilde{A}\ ^1A_u$ state of acetylene. *J. Chem. Phys.*, (106)3423, 1997.

[46] D. DuFlot, J-M. Robbe, and J-P. Flament. *Ab initio* potential energy surfaces for $C_2H \rightarrow C_2 + H$ photodissociation. *J. Chem. Phys.*, (100)1236, 1994.

[47] F. B. Dunning, R. D. Rundel, and R. F. Stebbings. Determination of secondary electron ejection coefficients for rare gas metastable atoms. *Rev. Sci. Instrum.*, (46)697, 1975.

[48] P. Dupré, R. Jost, M. Lombardi, P. G. Green, E. Abramson, and R. W. Field. Anomalous behavior of the anticrossing density as a function of excitation energy in the C_2H_2 molecule. *Chem. Phys.*, (152)293, 1991.

[49] Patrick Dupré. Study of Zeeman anticrossing spectra of the $\tilde{A}\ ^1A_u$ state of acetylene molecule(C_2H_2) by Fourier transform: product $\rho_{vib}\langle V\rangle$ and isomerization barrier. *Chem. Phys.*, (196)239, 1995.

[50] Patrick Dupré and Peter G. Green. Characterization of a large singlet-triplet coupling in the a state of the acetylene molecule. *Chem. Phys.*, (212)555, 1993.

[51] Patrick Dupré, Peter G. Green, and Robert W. Field. Quantum beat spectroscopic studies of Zeeman anticrossings in the $\tilde{A}\ ^1A_u$ state of acetylene molecule(C_2H_2). *Chem. Phys.*, (196)211, 1995.

[52] S. Dushman and J. M. Lafferty. *Scientific Foundations of Vacuum Technique.* Wiley and Sons, Inc., New York, 2nd edition, 1962.

[53] Askar Fahr and Allan H. Laufer. Extinction coefficient of $H_2CC(^3B_2)$ at 137 nm. *J. Chem. Phys.*, (83)908–910, 1985.

[54] Askar Fahr and Allan H. Laufer. Photodissociation of vinyl chloride. *J. Phys. Chem.*, (89)2906–2909, 1985.

[55] Askar Fahr and Allan H. Laufer. Quantum yield of vinylidene ($^3B_2$) from the vacuum uv photolysis of acetylene and ethylene. *J. Photochem.*, (34)261–266, 1986.

[56] Robert S. Freund. Ph.D. Thesis, Harvard University, 1965.

[57] W. Ronald Gentry. Low-energy pulsed beam sources, In *Atomic and Molecular Beam Methods, Volume 1.* , Giacinto Scoles, editor, page 54. Oxford University Press, New York, 1988.

[58] M. X. Gong, Y. H. Bao, R. S. Urdahl, and W. M. Jackson. LIF measurements of radiative lifetimes of the $C_2(B\ ^1\Sigma_g^+)$ state. *Chem. Phys. Lett.*, (217)210–215, 1994.

[59] Peter G. Green. *Acetylene near dissociation: Novel effects of external fields.* Ph.D. Thesis, Massachusetts Institute of Technology, 1989.

[60] Peter G. Green, James L. Kinsey, and Robert W. Field. A new determination of the dissociation energy of acetylene. *J. Chem. Phys.*, (91)5160–5163, 1989.

[61] H. D. Hagstrum. *Phys. Rev.*, (91)543, 1953.

[62] H. D. Hagstrum. Instrumentation and experimental procedure for studies of electron ejection by ions and ionization by electron impact. *Rev. Sci. Instru.*, (24)1123, 1953.

[63] H. D. Hagstrum. Auger ejection of electrons from tungsten by noble gas ions. *Phys. Rev.*, (96)325, 1954.

[64] H. D. Hagstrum. Theory of Auger ejection of electrons from metals by ions. *Phys. Rev.*, (96)336, 1954.

[65] H. D. Hagstrum. *Phys. Rev.*, (104)1516, 1956.

[66] H. D. Hagstrum. *Phys. Rev.*, (31)897, 1960.

[67] H. D. Hagstrum. Studies of adsorbate electronic structure using ion neutralization and photoemission spectroscopies, In *Electron and Ion Spectroscopy of Solids.* , J. Vennik L. Fiermans and W. Dekeyser, editors, page 273. Plenum Press, New York, 1978.

[68] H. D. Hagstrum. Excited-atom deexcitation spectroscopy using incident ions. *Phys. Rev. Lett.*, (43)1050, 1979.

[69] J. C. Han, Chao Ye, Masako Suto, and L. C. Lee. Fluorescence from photoexcitation of C_2H_2 at 50-106 nm. *J. Chem. Phys.*, (90)4000, 1989.

[70] Yoshiya Harada, Shigeru Masuda, and Hiroyuki Ozaki. Electron spectroscopy using metastable atoms as probes for solid surfaces. *Chem. Rev.*, (97)1897–1952, 1997.

[71] M. W. Hart, M. S. Hammond, F. B. Dunning, and G. K. Walters. Spin-polarized metastable-atom deexcitation spectroscopy: A new probe of the dynamics of metastable-atom-surface interactions. *Phys. Rev. B*, (39)5488–5491, 1989.

[72] John C. Hemminger. Ph.D. Thesis, Harvard University, 1976.

[73] John C. Hemminger, Brian G. Wicke, and William Klemperer. Delocalization of electronic energy in the lowest triplet states of molecules. *J. Chem. Phys.*, (65)2798, 1976.

[74] Robert C. Hilborn. Einstein coefficients, cross sections, f values, dipole moments, and all that. *Am. J. Phys.*, (50)982, 1982.

[75] H. Hotop. Detection of metastable atoms and molecules, In *Atomic, Molecular, and Optical Physics: Atoms and Molecules.* , F. B. Dunning and Randall G. Hulet, editors, page 191. Academic Press, San Diego, 1996.

[76] Jon T. Hougen. The calculation of rotational energy levels and rotational line intensities in diatomic molecules. Technical report, National Bureau of Standards, 1970. Monograph 115.

[77] K. P. Huber and G. Herzberg. *Molecular Spectra and Molecular Structure: IV. Constants of Diatomic Molecules.* Van Nostrand Reinhold Co., New York, 1979.

[78] T. R. Huet, M. Godefroid, and M. Herman. The $\tilde{A}$ electronic state of acetylene - geometry and axis-switching effects. *J. Mol. Spec.*, (144)32–44, 1990.

[79] Susan J. Humphrey, Christopher G. Morgan, Alec M. Wodtke, Kevin L. Cunningham, Stephen Drucker, and Robert W. Field. Laser excited metastable states of acetylene in the 5.5-5.7 eV region. *J. Chem. Phys.*, (107)49, 1997.

[80] C. K. Ingold and G. W. King. Excited states of acetylene. Part IV. description and analysis of the near-ultra-violet absorption spectra of acetylene and dideuteroacetylene: Nature of the excited state. *J. Chem. Soc.*, ()2725, 1953.

[81] Matthew P. Jacobson. *Spectroscopic Patterns Encode Unimolecular Dynamics.* Ph.D. Thesis, Massachusetts Institute of Technology, 1999.

[82] Matthew P. Jacobson, Stephen L. Coy, and Robert W. Field. Extended cross correlation: A technique for spectroscopic pattern recognition. *J. Chem. Phys.*, (107)8349, 1997.

[83] Matthew P. Jacobson and Robert W. Field. Acetylene at the threshold of isomerization. *J. Phys. Chem. A*, (104)3073–3086, 2000.

[84] Matthew P. Jacobson, Christof Jung, Howard S. Taylor, and Robert W. Field. State-by-state assignment of the bending spectrum of acetylene at 15,000 cm^{-1}: A case study of quantum-classical correspondence. *J. Chem. Phys.*, (111)600–618, 1999.

[85] D. M. Jonas, S. A. B. Solina, X. Zhao, and R. W. Field. High resolution vacuum ultraviolet stark measurement of the dipole moment of $\tilde{A}$-state $^1A''$ HCN. *J. Chem. Phys.*, (96)7209, 1992.

[86] R. T. Jongma, T. Rasing, and G. Meijer. 2-dimensional imaging of metastable CO molecules. *J. Chem. Phys.*, (102)1925–1933, 1995.

[87] Willis E. Lamb Jr. and Robert C. Rutherford. Fine structure of the hydrogen atom. Part I. *Phys. Rev.*, (79)549, 1950.

[88] S. S. Ju, P. Y. Cheng, M. Y. Hahn, and H. L. Dai. Isomeric structures of the electronically excited acetylene Ar complex: Spectroscopy and potential calculations. *J. Chem. Phys.*, (103)2850–2862, 1995.

[89] A. Kalemos, A. Mavridis, and Metropoulos. An accurate description of the ground and excited states of CH. *J. Chem. Phys.*, (111)9536–9548, 1999.

[90] Hideto Kanamori. Hydrocarbonated radicals with a C=C core. In *53rd International Symposium on Molecular Spectroscopy*, 1998. Talk WA02.

[91] Kunifusa Kayama and James C. Baird. Spin-orbit effects and the fine structure in the $^3\Delta_g$-ground state of oxygen. *J. Chem. Phys.*, (46)2604–2618, 1967.

[92] James T. Kindt, John C. Tully, Martin Head-Gordon, and Maria A. Gomez. Electron-hole pair contributions to scattering, sticking, and surface diffusion: CO on Cu(100). *J. Chem. Phys.*, (109)3629, 1998.

[93] K. Kirby and B. Liu. The valence states of C_2: A configuration interaction study. *J. Chem. Phys.*, (70)893–900, 1979.

[94] A. G. Koures and L. B. Harding. *Ab initio* examination of the electronic excitation spectrum of CCH. *J. Chem. Phys.*, (95)1035–1040, 1991.

[95] W. J. Lafferty and A. S. Pine. Spectroscopic constants for the 2.5 and 3.0 μm bands of acetylene. *J. Mol. Spec.*, (141)223, 1990.

[96] Don Lancaster. *The TTL Cookbook*. Howard W. Sams & Co., Indianapolis, Indiana, 1st edition, 1974.

[97] Allan H. Laufer. An excited state of acetylene: Photochemical and spectroscopic evidence. *J. Chem. Phys.*, (73)49–52, 1980.

[98] Allan H. Laufer. The formation of the vinylidene radical as an intermediate in the combination of triplet methylene. *J. Chem. Phys.*, (76)945–948, 1982.

[99] Allan H. Laufer and Yuk L. Yung. Equivalence of vinylidene and C_2H_2 - calculated rate-constant for vinylidene abstraction from CH_4. *J. Phys. Chem.*, (87)181–183, 1983.

[100] Warren D. Lawrance and Alan E. W. Knight. Direct deconvolution of extensively perturbed spectra: the singlet-triplet molecular eigenstate spectrum of pyrazine. *J. Phys. Chem.*, (89)917–925, 1985.

[101] Warren D. Lawrence and Alan E. W. Knight. Reply to comment on "Direct deconvolution of extensively perturbed spectra: the singlet-triplet molecular eigenstate spectrum of pyrazine". *J. Phys. Chem.*, (95)7557–7558, 1991.

[102] H. Lefebvre-Brion and F. Guerin. Calculation of the radiative lifetime of the a $^4\Pi$ state of nitric oxide. *J. Phys. Chem.*, (49)1446–1447, 1968.

[103] Hèléne Lefebvre-Brion and Robert W. Field. *Perturbations in the Spectra of Diatomic Molecules*. Academic Press, Orlando, Florida, 1st edition, 1986.

[104] Kevin K. Lehmann. Comment on "Direct deconvolution of extensively perturbed spectra: the singlet-triplet molecular eigenstate spectrum of pyrazine". *J. Phys. Chem.*, (95)7556–7557, 1991.

[105] Xinghua Li and Yuan-Pern Lee. Highly predissociative levels of the $D\ ^2\Pi$ state of CH studied with the two-color resonant four-wave mixing technique. *J. Chem. Phys.*, (111)4942–4947, 1999.

[106] David R. Lide, editor. *CRC Handbook of Chemistry and Physics*. CRC Press, Boca Raton, FL, 72nd edition, 1991–92.

[107] Hans Lischka and Alfred Karpfen. *Ab initio* calculations on the excited states of π-systems. I. Valence excitations in acetylene. *Chem. Phys.*, (102)77–89, 1986.

[108] James M. Lisy and William Klemperer. Electric deflection studies of metastable acetylene. *J. Chem. Phys.*, (72)3880, 1980.

[109] P. Löffler, E. Wrede, L. Schnieder, J. B. Halpern, W. M. Jackson, and K. H. Welge. Dissociation dynamics of acetylene Rydberg states as a function of excited state lifetime. *J. Chem. Phys.*, (109)5231–5246, 1998.

[110] J. K. Lundberg, Yongqin Chen, J.-P. Pique, and R. W. Field. Ultraviolet optical double-resonance study of the predissociated $\tilde{C}'\ ^1A_g$ state of acetylene. *J. Mol. Spec.*, (156)104–122, 1992.

[111] James K. Lundberg. *Double resonance studies of electronically excited acetylene.* Ph.D. Thesis, Massachusetts Institute of Technology, 1992.

[112] James K. Lundberg, David M. Jonas, Bhavani Rajaram, Yongqin Chen, and Robert W. Field. Rotationally resolved ultraviolet ultraviolet double-resonance study of the nonplanar $\tilde{E}$ state of acetylene. *J. Chem. Phys.*, (97)7180–7196, 1992.

[113] Karsten Malsch, Rupert Rebentisch, Petra Swiderek, and Georg Hohlneicher. Excited states of acetylene: a CASPT2 study. *Theor. Chem. Acc.*, (100)171–182, 1998.

[114] Ts. S. Marinova and P. Stefanov. Interaction of acetylene with an oxygen-covered Cu(100) surface. *Surf. Sci.*, (219)490, 1989.

[115] Margarita Martin. C_2 spectroscopy and kinetics. *J. Photochem. Photobiol. A*, (66)263–289, 1992.

[116] N. J. Mason and W. R. Newell. A state selective metastable detector. *Meas. Sci. Technol.*, (2)568–570, 1991.

[117] H. S. W. Massey. *Proc. Camb. Phil. Soc.*, (26)386, 1930.

[118] H. S. W. Massey. *Proc. Camb. Phil. Soc.*, (27)460, 1931.

[119] S. Masuda, H. Hayashi, and Y. Harada. Spatial-distribution of the wave-functions of a graphite surface studied by use of metastable-atom. *Phys. Rev. B*, (42)3582–3585, 1990.

[120] J. R. McDonald, A. P. Baronavski, and V. M. Donnelly. Multiphoton-vacuum-ultraviolet laser photodissociation of acetylene: emission from electronically excited fragments. *Chem. Phys.*, (33)161, 1978.

[121] David R. Miller. Free jet sources, In *Atomic and Molecular Beam Methods, Volume 1.* , Giacinto Scoles, editor, page 14. Oxford University Press, New York, 1988.

[122] William H. Miller. *Chem. Phys. Lett.*, (4)627, 1970.

[123] William H. Miller. Theory of Penning ionization. I. Atoms. *J. Chem. Phys.*, (52)3563, 1970.

[124] William H. Miller and Henry F. Schaefer III. Theoretical treatment of Penning ionization - He($1s2s\ ^1S,\ ^3S$) + H($1s\ ^2S$)*. *J. Chem. Phys.*, (53)1421, 1970.

[125] John H. Moore, Christopher C. Davis, and Michael A. Coplan. *Building Scientific Apparatus.* Addison-Wesley, Reading, Mass., 2nd edition, 1989.

[126] John H. Moore, Christopher C. Davis, and Michael A. Coplan. *Building Scientific Apparatus.* Addison-Wesley, Reading, Mass., 2nd edition, 1989.

[127] David H. Mordaunt and Michael N. R. Ashfold. Near ultraviolet photolysis of C_2H_2: A precise determination of D_0(HCC-H). *J. Chem. Phys.*, (101)2630, 1994.

[128] David H. Mordaunt, Michael N. R. Ashfold, Richard N. Dixon, Peter Löffler, Ludger Schnieder, and Karl H. Welge. Near threshold photodissociation of acetylene. *J. Chem. Phys.*, (108)519, 1998.

[129] Christopher G. Morgan. *A New Method for the Determination of Correlated Product State Distributions in a Photodissociation Reaction: Ketene at 308 and 351 nm.* Ph.D. Thesis, University of California, Santa Barbara, 1997.

[130] Christopher G. Morgan, Marcel Drabbels, and Alec M. Wodtke. The correlated product state distribution of ketene photodissociation at 308 nm. *J. Chem. Phys.*, (104)7460–7474, 1996.

[131] Christopher G. Morgan, Marcel Drabbels, and Alec M. Wodtke. State-specific neutral time-of-flight of CO from ketene photodissociation at 351 nm: The internal energy distribution of $CH_2(\tilde{X}\ ^3B_1)$. *J. Chem. Phys.*, (105)4550–4555, 1996.

[132] Michael D. Morse. Supersonic beam sources, In *Atomic, Molecular, and Optical Physics: Atoms and Molecules.* , F. B. Dunning and Randall G. Hulet, editors, page 21. Academic Press, San Diego, 1996.

[133] Neil R. Avery. Adsorption and reactivity of acetylene on a Cu(110) surface. *J. Am. Chem. Soc.*, (107)6711, 1985.

[134] A. Niehaus. Spontaneous ionization in slow collisions, In *The Excited State in Chemical Physics, part 2, Vol 45.* , J. Wm. McGowan, editor, page 84. Academic Press, New York, 1981.

[135] National Institute of Standards and Technology, http://physics.nist.gov.

[136] Jonathan P. O'Brien. *Acetylene: Dispersed Fluorescence Spectroscopy and Intramolecular Dynamics.* Ph.D. Thesis, Massachusetts Institute of Technology, 1997.

[137] Nobuaki Ochi and Soji Tsuchiya. Quantum beat spectroscopy of Zeeman splitting and level anticrossing of rotationally selected acetylene ($\tilde{A}\ ^1A_u\ 3\nu_3$) under weak magnetic-fields. *Chem. Phys. Lett.*, (140)20–25, 1987.

[138] Nobuaki Ochi and Soji Tsuchiya. Rovibronic level structure of electronically excited acetylene ($\tilde{A}\ ^1A_u$) in a supersonic jet as studied by laser-induced fluorescence and Zeeman quantum beat spectroscopy. *Chem. Phys.*, (152)319–336, 1991.

[139] Ronald W. Ohse, editor. *The Handbook of Thermodynamic and Transport Properties of Alkali Metals.* Blackwell Scientific Publications, 1985.

[140] H. Okabe. Photodissociation of acetylene and bromoacetylene in the vacuum ultraviolet: Production of electronically excited C_2H and C_2. *J. Chem. Phys.*, (62)2782–2787, 1975.

[141] H. Okabe. Photochemistry of acetylene at 1470 Å. *J. Chem. Phys.*, (75)2772–2778, 1981.

[142] H. Okabe. Photochemistry of acetylene. *Can. J. Chem.*, (61)850–855, 1983.

[143] H. Okabe. Photochemistry of acetylene at 1849 Å. *J. Chem. Phys.*, (78)1312–1317, 1983.

[144] Hideo Okabe, R. J. Cody, and J. E. Allen Jr. Laser photolysis of C_2H_2 and CF_3C_2H at 193 nm: Production of $C_2(d\,^3\Pi_g)$ and $CH(A\,^2\Delta)$ and their quenching by Xe. *Chem. Phys.*, (92)67–73, 1985.

[145] M. Ortiz and J. Campos. Lifetimes of excited states of CH. *Physica B+C (Amsterdam)*, (114)135–139, 1982.

[146] P. Auger. The compound photoelectric effect. *J. Phys. Radium*, (6)793, 1925.

[147] Kent F. Palmer, Michael E. Mickelson, and K. Narahari. Rao. Several infrared bands of $^{12}C_2H_2$ and studies of the effects of vibrational-rotational interactions. *J. Mol. Spec.*, (44)131–144, 1972.

[148] Costas Papaliolios. *Excitation of metastable states of nitrogen and CO by electron impact.* Ph.D. Thesis, Harvard University, 1965.

[149] Avigdor Persky, Edward F. Greene, and Aron Kuppermann. Formation of positive and negative ions on rhenium, oxygenated tungsten, hafnium, lanthanum hexaboride, and thoriated tungsten surfaces. *J. Chem. Phys.*, (49)2347–2357, 1968.

[150] William H. Press, Saul A. Teukolsky, William T. Vetterling, and Brian P. Flannery. *Numerical Recipes in FORTRAN.* Cambridge University Press, Cambridge, UK, 2nd edition, 1992.

[151] J. M. Price, A. Ludviksson, M. Nooney, M. Xu, R. M. Martin, and A. M. Wodtke. Time-of-flight measurements of single rovibrational states of CO. *J. Chem. Phys.*, (96)1854–1857, 1992.

[152] RCA. *Photomultiplier Tubes.*

[153] Robert S. Freund. Dissociation by electron impact of oxygen into metastable quintet and long-lived high-Rydberg atoms. *J. Chem. Phys.*, (54)3125–3141, 1971.

[154] Robert S. Freund. Dissociation of CO_2 by electron impact with the formation of metastable $CO(a\,^3\Pi)$ and $O(^5S)$. *J. Chem. Phys.*, (55)3569–3577, 1971.

[155] Robert Von Trebra and Tad H. Koch. DABCO stabilization of coumarin dye lasers. *Chem. Phys. Lett.*, (93)315, 1982.

[156] Fred Rosebury. *Handbook of electron tube and vacuum techniques.* Addison-Wesley, Reading, Mass., 1st edition, 1965.

[157] David R.Penn and Peter Apell. Theory of spin-polarized metastable-atom-deexcitation spectroscopy - Ni-He. *Phys. Rev. B*, (41)3303–3315, 1990.

[158] J. Ruiz and M. Martin. Application of the truncated singular value decomposition method to the obtention of rovibrational population distributions from electronic spectra of diatomic molecules. *Computers Chem.*, (4)417, 1995.

[159] S. Andersson and U. Jostell. Electron structure of Na and K adsorbed on Ni(100). *Surf. Sci.*, (46)625, 1974.

[160] Y. Saito, T. Hikida, T. Ichimura, and Y. Mori. Fluorescence of excited ethynyl radicals produced by pulsed vacuum ultraviolet photolyses of C_2H_2, C_2D_2, and C_2HBr. *J. Chem. Phys.*, (80)31–35, 1984.

[161] G. J. Scherer, Y. Chen, R. L. Redington, J. L. Kinsey, and R. W. Field. An unsuspected Fermi perturbation in the acetylene $\tilde{A}\ ^1A_u\ 3\nu_3$ level. *J. Chem. Phys.*, (85)6315, 1986.

[162] K. Seki and H. Okabe. Photochemistry of acetylene at 193.3 nm. *J. Phys. Chem.*, (97)5284–5290, 1993.

[163] Kanekazu Seki, Nobuaki Nakashima, Nobuyuki Nishi, and Minoru Kinoshita. Photochemistry of acetylene at 193 nm: Two pathways for diacetylene formation. *J. Phys. Chem.*, (85)274–279, 1986.

[164] W. Sesselmann, B. Woratschek, G. Ertl, J. Kuppers, and H. Haberland. Penning ionization electron-spectroscopy of molecular adsorbates on Pd and Cu surfaces. *Surf. Sci.*, (146)17–42, 1984.

[165] C. David Sherrill, George Vacek, Yukio Yamaguchi, Henry F. Schaefer III, John F. Stanton, and Jürgen Gauss. The $\tilde{A}\ ^1A_u$ state and the T_2 potential surface of acetylene: Implications for triplet perturbations in the fluorescence spectra of the $\tilde{A}$ state. *J. Chem. Phys.*, (104)8507–8515, 1996.

[166] Yang Shi and Toshinori Suzuki. Formation of metastable triplet acetylene from the $\tilde{A}(^1A_u)$ state near the dissociation threshold. *J. Phys. Chem.*, (102)7417–7419, 1998.

[167] David P. Shoemaker, Carl W. Garland, and Joseph W. Nibler. *Experiments in Physical Chemistry.* McGraw-Hill, Inc., New York, 5th edition, 1989.

[168] F. Shokoohi, T. A. Watson, H. Reisler, F. Kong, A. M.. Renlund, and C. Wittig. Photolytic production of C_2H- collisional quenching of $\tilde{A}\ ^2\Pi$ - $\tilde{X}\ ^2\Sigma^+$ infrared-emission and the removal of excited C_2H. *J. Phys. Chem.*, (90)5695–5700, 1986.

[169] Kermit C. Smyth, James A. Schiavone, and Robert S. Freund. Dissociative excitation of N_2 by electron impact: Translational spectroscopy of long-lived high-Rydberg fragment atoms. *J. Chem. Phys.*, (59)5225, 1973.

[170] Ofer Snè and Ori Cheshnovsky. Surface ejection of electrons by laser-excited metastables of anthracene derivatives. *Chem. Phys. Lett.*, (130)53, 1986.

[171] Ofer Sne and Ori Cheshnovsky. Triplet selectivity in surface ejection of electrons by laser-excited metastables of aniline. *Chem. Phys. Lett.*, (146)216, 1988.

[172] Ofer Sneh, Aviv Amirav, and Ori Cheshnovsky. The branching of nonradiative processes in isoquinoline. *J. Chem. Phys.*, (91)3532, 1989.

[173] Ofer Sneh, Aviv Amirav, and Ori Cheshnovsky. The decay of triplet pyrazine in supersonic jets. *J. Chem. Phys.*, (91)7331, 1989.

[174] Ofer Sneh and Ori Cheshnovsky. Triplet state interrogation in supersonic beams by surface electron ejection. *Isr. J. Chem.*, (30)13, 1990.

[175] Ofer Sneh and Ori Cheshnovsky. Dynamics of triplet states in beam-isolated benzaldeyde. *J. Phys. Chem.*, (95)7154, 1991.

[176] Ofer Sneh and Ori Cheshnovsky. Triplet states dynamics in isolated molecules. *Jerusalem Symp. Quantum Chem. Biochem.*, (24)359, 1991.

[177] Ofer Sneh and Ori Cheshnovsky. The decay of triplet pyrazine and methylpyrazine in supersonic jets. Substitution effects. *J. Chem. Phys.*, (96)8095, 1992.

[178] Stephani Ann B. Solina. *Intramolecular Dynamics of Acetylene*. Ph.D. Thesis, Massachusetts Institute of Technology, 1996.

[179] Gabor A. Somorjai. *Introduction to Surface Chemistry and Catalysis*. John Wiley & Sons, inc., New York, 1st edition, 1994.

[180] John F. Stanton, private communication.

[181] J.C. Stephenson, J. A. Blazy, and D. S. King. Spectroscopy and collisional quenching rates for $\tilde{A}$ C_2H_2 ($\nu_3' = 0, 1, 2$). *Chem. Phys.*, (110)31–38, 1984.

[182] Richard C. Stern. *Molecular beam spectra of metastable ^{12}CO and ^{13}CO*. Ph.D. Thesis, Harvard University, 1968.

[183] Charles G. Stevens and John C. D. Brand. Angular momentum dependence of first- and second-order singlet-triplet interactions in polyatomic molecules. *J. Chem. Phys.*, (58)3324–3330, 1973.

[184] Frank Stienkemeier, private communication.

[185] Masako Suto and L. C. Lee. Quantitative photoexcitation and fluorescence studies of C_2H_2 in vacuum ultraviolet. *J. Chem. Phys.*, (80)4824–4831, 1984.

[186] Toshinori Suzuki, Yang Shi, and Hiroshi Kohguchi. Detection of metastable triplet acetylene produced by intersystem crossing from the excited $\tilde{A}(^1A_u)$ state. *J. Chem. Phys.*, (106)5292–5295, 1997.

[187] Attila Szabo and Neil S. Ostlund. *Modern Quantum Chemistry: Introduction to Advanced Electronic Structure Theory*. Dover Publications, Mineola, New York, 1st, revised edition, 1996.

[188] T. Rick Fletcher and Stephen R. Leone. Photodissociation dynamics of C_2H_2 at 193 nm: Vibrational distributions of the CCH radical and the rotational state distributions of the $\tilde{A}(010)$ state by time-resolved fourier transform infrared emission. *J. Chem. Phys.*, (90)871, 1989.

[189] K. Tanigawa and H. Kanamori. unpublished data.

[190] K. Tanigawa and H. Kanamori. High-resolution study of triplet acetylene. In *50th International Symposium on Molecular Spectroscopy*, 1995. Talk FD03.

[191] J. R. Tatarczuk. Gateable delay gate generator. *Rev. Sci. Instrum.*, (43)930, 1972.

[192] W. Ubachs, G. Meyer, J. J. TerMeulen, and A. Dymanus. Hyperfine-structure and lifetime of the C $^2\Sigma^+$, v = 0 state of CH. *J. Chem. Phys.*, (84)3032–3041, 1986.

[193] Masatoshi Ukai, Kosei Kameta, Ryo Chiba, Kazunori Nagano, Noriyuki Kouchi, Kyoji Shinsaka, Yoshihiko Hatano, Hironobu Umemoto, Yoshiro Ito, and Kenichiro Tanaka. Ionizing and nonionizing decays of superexcited acetylene molecules in the extreme-ultraviolet region. *J. Chem. Phys.*, (95)4142, 1991.

[194] A. L. Utz, J. D. Tobiason, E. Carrasquillo M., L. J. Sanders, and F. F. Crim. The direct observation, assignment, and partial deperturbation of the ν_4 and ν_6 vibrational fundamentals in $\tilde{A}\ ^1A_u$ acetylene (C_2H_2). *J. Chem. Phys.*, (98)2742–2753, 1993.

[195] P. H. Vaccaro, A. Zabludoff, M. E. Carrera-Patiño, J. L. Kinsey, and R. W. Field. High precision dipole moments in $\tilde{A}\ ^1A_2$ formaldehyde determined via Stark quantum beat spectroscopy. *J. Chem. Phys.*, (90)4150, 1989.

[196] Patrick H. Vaccaro. *Spectroscopy and kinetics of highly excited formaldehyde*. Ph.D. Thesis, Massachusetts Institute of Technology, 1986.

[197] George Vacek, C. David Sherrill, Yukio Yamaguchi, and Henry F. Schaefer III. The anomalous behavior of the Zeeman anticrossing spectra of $\tilde{A}\ ^1A_u$ acetylene: Theoretical considerations. *J. Chem. Phys.*, (104)1774–1778, 1996.

[198] George Vacek, J. Russell Thomas, Bradley J. DeLeeuw, Yukio Yamaguchi, and Henry F. Schaefer III. Isomerization reactions on the lowest potential energy hypersurface of triplet vinylidene and triplet acetylene. *J. Chem. Phys.*, (98)4766–4775, 1993.

[199] J. H. Van Vleck. *Rev. Mod. Phys.*, (23)213, 1951.

[200] W. Ronald Gentry and Clayton F. Giese. Ten-microsecond pulsed molecular beam source and a fast ionization detector. *Rev. Sci. Instrum.*, (49)595–600, 1978.

[201] W. T. Raynes. *J. Chem. Phys.*, (41)3020, 1964.

[202] D. H. Waldeck, A. P. Alivisatos, and C. B. Harris. Nonradiative damping of molecular electronic excited states by metal surfaces. *Surf. Sci.*, (158)103, 1985.

[203] A. D. Walsh. The electronic orbitals, shapes, and spectra of polyatomic molecules. Part III. HAB and HAAH molecules. *J. Chem. Soc. (London)*, ()2288–2296, 1953.

[204] Sheng-Wei Wang and G. Ertl. Theory of Penning ionization of adsorbed CO by metastable helium ($2\ ^1$S, $2\ ^3$S) beams. *Surf. Sci.*, (93)L75, 1980.

[205] J. K. G. Watson, M. Herman, J. C. van Craen, and R. Colin. The $\tilde{A}$-$\tilde{X}$ band system of acetylene: Analysis of long-wavelength bands, and vibration-rotation constants for the levels $n\nu_4''$ (n = 0-4), $n\nu_3'$ (n = 0-3), and $\nu_2' + n\nu_3'$(n = 0-2). *J. Mol. Spec.*, (95)101–132, 1982.

[206] Harold W. Webb. The metastable state in mercury vapor. *Phys. Rev.*, (24)113, 1924.

[207] H. R. Wendt, H. Hippler, and H. E. Hunziker. Triplet acetylene: Near infrared electronic absorption spectrum of the *cis* isomer, and formation from methylene. *J. Chem. Phys.*, (70)4044, 1979.

[208] H. R. Wendt, H. Hippler, and H. E. Hunziker. Triplet acetylene: Near infrared electronic absorption spectrum of the *cis* isomer, and formation from methylene. *J. Chem. Phys.*, (70)4044, 1979.

[209] Ross W. Wetmore and Henry F. Schaefer III. Triplet electronic states of acetylene: *cis* and *trans* structures and energetics. *J. Chem. Phys.*, (69)1648–1654, 1978.

[210] P. M. Whitmore, A. P. Alivisatos, and C. B. Harris. Distance dependence of electronic energy transfer to semiconductor surfaces: $^3n\Pi^*$ pyrazine/GaAs(110). *Phys. Rev. Lett.*, (50)1092, 1983.

[211] P. M. Whitmore, H. J. Robota, and C. B. Harris. Mechanism for electronic energy transfer between molecules and metal surfaces: a comparison of silver and nickel. *J. Chem. Phys.*, (77)1560, 1982.

[212] Alec M. Wodtke and Y. T. Lee. Photodissociation of acetylene at 193.3 nm. *J. Phys. Chem.*, (89)4744–4751, 1985.

[213] B. Woratschek, W. Sesselman, J. Kuppers, G. Ertl, and H. Haberland. Electron-spectroscopy of alkali-metal surfaces by deexcitation of metastable He atoms. *Surf. Sci.*, (180)187–202, 1987.

[214] Yukio Yamaguchi, George Vacek, and Henry F. Schaefer III. Low-lying triplet electronic states of acetylene: *cis* $^3B_2$ and $^3A_2$, *trans* ^3B_u and ^3A_u. *Theoret. Chim. Acta*, (86)97, 1993.

[215] Q. Y. Yang, K. J. Maynard, A. D. Johnson, and S. T. Ceyer. The structure and chemistry of CH_3 and CH radicals adsorbed on Ni(111). *J. Chem. Phys.*, (102)7734–7749, 1995.

[216] Richard N. Zare. *Angular Momentum.* Wiley, New York, 1988.

[217] M. Zen. Accommodation, accumulation and other detection methods, In *Atomic and Molecular Beam Methods, Volume 1.* , Giacinto Scoles, editor, page 254. Oxford University Press, New York, 1988.

[218] M. Zubek and G. C. King. A hot ribbon detector for metastable atoms. *J. Phys. E: Sci. Instrum.*, (15)511, 1982.